Surface Acoustic Wave driven Ferromagnetic Resonance in FeRh

Kavilen Vythelingum

Surface Acoustic Wave driven Ferromagnetic Resonance in FeRh

M. Ashwin Kavilen Pillay VYTHELINGUM

Thèse de doctorat de Sorbonne Université préparée à l'Institut des Nanosciences de Paris (INSP - UMR 7588)

École doctorale n°: 397 - Physique et Chimie des Matériaux

Spécialité de doctorat: Physique

Soutenue le 30 Septembre 2024
à Paris, France

Devant un jury composé de:

Président du Jury	**M. CHERIF Mourad Salim**	Laboratoire des Sciences des Procédés et des Matériaux (LSPM) - Université Sorbonne Paris Nord
Rapporteur	**M. HAGE-ALI Sami**	Institut Jean Lamour (IJL) - Université de Lorraine
Rapporteur	**M. RANNO Laurent**	Institut Néel - Université Grenoble Alpes
Examinatrice	**Mme. DUPUIS Véronique**	Institut Lumière Matière (iLM) - Université Claude Bernard Lyon 1
Co. Directrice de thèse	**Mme. GOURDON Catherine**	Institut des Nanosciences de Paris (INSP) - Sorbonne Université
Co. Directrice de thèse	**Mme. THEVENARD Laura**	Institut des Nanosciences de Paris (INSP) - Sorbonne Université

SORBONNE UNIVERSITÉ
CRÉATEURS DE FUTURS
DEPUIS 1257

À mes trois Mamans:

Pamela, Leena, Malini

et Raj

Projet financé par l'ED 397-Sorbonne Université

Project title : Strain control of antiferromagnets

PhD student: VYTHELINGUM Kavilen Pillay Ashwin

Supervisors: GOURDON Catherine & THEVENARD Laura

Laboratory: Institut des Nanosciences de Paris (INSP) UMR 7588

Project Description : The context of this project is the storage of digital information. Magnetic coding of information, e.g. in hard-disks, has so far relied on bistable ferromagnetic (FM) states, "north"/"south" sub-micronic magnetic grains coding for "0" and "1" bits . They are easy to manipulate with magnetic fields, but are also for the same reason unfortunately sensitive to stray fields, stemming for instance from bit-to-bit interactions. To bypass these issues, there is now a keen interest in using antiferromagnets (AF) for the magnetic coding of information [1]. These materials are composed of two magnetic sublattices of opposite magnetizations M1 =-M2. The idea is to encode data ("0" and "1" states") onto two orthogonal directions of the Néel vector L = M1 - M2. The total zero magnetization conveniently renders AFs pretty insensitive to magnetic fields, but also makes them difficult to manipulate. We are thus implementing a novel strategy, relying on magnetostriction: the coupling of strain and magnetic moments. We use the dynamic strain provided by GHz surface acoustic waves (SAWs), i. e. propagating coherent phonons [2]. The main objective is to gauge the possibilities SAWs offer as opposed to the traditional excitation of AF dynamics with radio-frequency (RF) fields, in terms of coupling efficiency, frequency, tunability, or zoology of excited modes. In the longer term this scheme would limit Joule dissipation (and associated spurious temperature-gradient related effects) as strain will be excited by electrical fields, and allow alternative AF data storage design using focusing, interference, wave-front shaping and waveguiding effects, or remote accessing of bits, thanks to the weak attenuation of SAWs.

The interaction of electrically excited SAWs with magnetization excitations (magnons) has been evidenced in several ferromagnetic materials, including magnetic semiconductors, on which we have shown that SAWs can drive the ferromagnetic resonance, and achieve magnetization switching [3,4,5]. Controlling antiferromagnets with strain has instead been very little explored, although their magnetoelasticity is well documented [5].

SAW-driving of AF dynamics, and the resulting possible manipulation of AF static states will be explored on two very different well-chosen systems, both bypassing in a different way the main bottleneck of addressing collinear antiferromagnets: their near-total lack of macroscopic stray field and magnetization. One is a ferrimagnet (Gd1-xCox) which can behave dynamically as an antiferromagnet but maintains a detectable magnetization, and the other is a particular antiferromagnet, FeRh, transitioning via strain to a FM phase at TAF-FM around room temperature.

Spin-phonon coupling in GdCo: For selected compositions ferrimagnetic GdCo alloys exhibit two characteristic temperatures. At Tm the magnetizations of the two antiferromagnetically coupled sublattices are equal and opposite, giving zero net magnetization. At Ta, the spin densities of the two sublattices are equal and opposite, giving an AF-like dynamical behavior, but the total magnetization remains finite [7]. We will study the interaction of SAWs with the magnetic sublattices, varying continuously from an FM-like dynamic behavior to an AF-like

behavior with temperature, and establishing the optimal conditions for a resonant excitation of the dynamics. We will compare our results with the dynamics obtained by inductive excitation to assess the benefits of SAW excitation.

Towards L vector switching in FeRh: The robustness of AFs to external magnetic fields also makes it very difficult to switch between two AF states. In FeRh, similarly to heat assisted magnetic recording, one can bring the system in the FM phase, switch the magnetization, which leads to a L-vector switching by 90° after relaxation to the AF state. So far, the most significant results concerning L-switching in FeRh [8,9] were obtained by temperature cycling under large fields (0.3-9T) . Relying on the equivalence of stress and temperature for this magneto-structural transition we will investigate how a local and transient AF-FM transition can be triggered by SAWs.

References:

[1] T. Jungwirth et al., http://www.nature.com/articles/nnano.2016.18

[2] P. Delsing et al., https://iopscience.iop.org/article/10.1088/1361-6463/ab1b04

[3] P. Kuszewski et al., https://link.aps.org/doi/10.1103/PhysRevApplied.10.034036

[4] I. Camara at al, https://link.aps.org/doi/10.1103/PhysRevApplied.11.014045

[5] M. Kraimia et al.,https://link.aps.org/doi/10.1103/PhysRevB.101.144425

[6] H. Gomonay, https://iopscience.iop.org/article/10.1088/0953-8984/14/15

[7] C.Kim et al. http://www.nature.com/articles/s41563-020-0722-8

[8] T. Moriyama et al. http://aip.scitation.org/doi/10.1063/1.4931567

[9] X. Marti et al. http://www.nature.com/articles/nmat3861

Abstract

Remote excitation of **ferromagnetic resonance (FMR)** via **magneto-elasticity**, using **piezoelectrically** generated **surface acoustic waves (SAWs)**, provides an attractive route for the manipulation of magnetic states, magnetisation switching, non-reciprocal interactions, novel **spintronic** architectures, and offers realistic applications for on-chip information processing and storage. To achieve resonant SAW-FMR, the frequency and wave-vector of the SAW must match those of the **Spin-Wave (SW)**, and there must be a non-zero magneto-elastic torque acting on the magnetic moments. Typically, the first two conditions are met by: (i) using a **hard axis of magnetic anisotropy** and applying an external magnetic field to soften the SW eigen-frequencies, or (ii) by generating high-frequency SAWs in **magnetically isotropic** samples. However, in certain scenarios (absence of a magnetic hard-axis, lithographic limitations in achieving high SAW frequencies), these conditions cannot be fulfilled. Part of this thesis proposes an alternative method to soften the SW eigen-frequencies by using the **magnetic coercivity** of FeRh thin films.

FeRh, for near equi-atomic concentration, undergoes a **first-order magneto-structural phase transition** from a low-temperature **antiferromagnetic (AFM)** phase to a high-temperature **ferromagnetic (FM)** phase. Advantage is taken of the strong variation of the coercivity in the region of phase coexistence. This thesis investigates two samples: **crystalline** FeRh on MgO and **polycrystalline** FeRh on GaAs. Using **magneto-linear dichroism (MLD)** in the visible range, we characterised and confirmed that the FeRh thin film on MgO exhibits a biaxial magnetic anisotropy. Despite that, most results were obtained on FeRh/GaAs. We developed the first implementation of electrically generated SAWs on FeRh. The interaction of the SAWs with the magnetic FeRh layer was analysed by measuring the variations in SAW **amplitude** and **relative phase** (or velocity). Both **resonant** and **non-resonant** SAW-FeRh interactions were explored. Using **fixed-field temperature** ramps across the AFM-FM transition, we found that the relative phase variations exhibited a hysteresis similar to the temperature-dependent magnetisation. By modelling the SAW propagation, using the elastic constants obtained from Brillouin light scattering and picosecond acoustics, we showed that this hysteresis originated from a difference in SAW velocities between the AFM and FM phases. The amplitude variation revealed a complex relationship depending on the frequency and the FeRh FM phase fraction. **Fixed-temperature field** ramps, on the other hand, revealed SAW-FMR resonances. By modelling this interaction, it was shown that this results from the softening of SW eigen-frequencies at the coercivity. The local coercivity was precisely measured using **Longitudinal Magneto-Optical Kerr (LMOKE)** Microscopy and observed to match the resonance field value. This SAW-FMR resonance was followed across the phase transition and showed the same temperature dependency as the coercivity. **Angular SAW-FMR** measurements, i.e. measurements with varying angle between the SAW propagation direction and the magnetic field, revealed unexpected results. The magneto-elastic interaction is non-zero at all measured angles, while some angles exhibit double resonance field values. A numerical model, based on the SAW back-action, was developed to study both the origin of the angular dependency and the double resonance field values.

Additionally, we improved the existing experimental setup, coupling the electrical generation of SAWs to the synchronised optical detection of the dynamical magneto-elastic interaction. This synchronisation is now ensured by a Master generator and two slaves, leading to SAW excitation no longer limited by the laser repetition rate.

Résumé

Ce travail se situe dans le contexte de l'excitation à distance de la **résonance ferromagnétique** (**FMR**), en utilisant des ondes acoustiques de surface (**SAWs- Surface Acoustic Waves**) générées **piézo-électriquement** via le couplage **magnéto-élastique**. Cela offre une voie attractive pour la manipulation des états magnétiques, le basculement de l'aimantation, les études d'interactions non-réciproques, les nouvelles architectures spintroniques, et des applications concrètes pour le traitement et le stockage de l'information sur puce. Pour atteindre une résonance SAW-FMR, il est nécessaire d'égaler les fréquences et les vecteurs d'ondes des SAWs et des ondes de spin (**Spin Waves- SWs**), et d'avoir un couple magnéto-acoustique non-nul agissant sur les moments magnétiques. Généralement, les deux premières conditions sont remplies en : (i) utilisant un **axe difficile d'anisotropie magnétique** et en y appliquant un champ magnétique externe afin de diminuer les fréquences propres des SWs, ou (ii) en générant des SAWs à haute fréquence dans des échantillons **magnétiquement isotropes**. Cependant, dans certains cas (absence d'axe difficile magnétique, limitations lithographiques), ces conditions ne peuvent pas être satisfaites. Cette thèse propose une méthode alternative pour abaisser les fréquences propres des SWs en utilisant la **coercivité** magnétique de films minces de FeRh.

Le **FeRh** équi-atomique possède une transition de phase magnéto-structurale de premier ordre, passant d'une phase **antiferromagnétique (AFM)** à basse température, à une phase **ferromagnétique (FM)** à haute température. Dans cette étude, nous avons étudié deux échantillons : du FeRh **cristallin** sur MgO et du FeRh **polycristallin** sur GaAs. En utilisant un dispositif de **dichroïsme magnétique linéaire** dans le visible, nous avons caractérisé et confirmé que le film mince de FeRh sur MgO présente bien une anisotropie magnétique biaxiale. Nous avons ensuite mise en évidence la première génération électrique des SAWs sur FeRh. Les **interactions SAW-FMR** ont été analysées en mesurant les **variations d'amplitude** et de **phase relative** (ou de vitesse). Pour l'échantillon de FeRh polycristallin, qui nous a fournis la majorité des résultats, nous avons exploré les interactions SAW-FMR **résonantes** et **non résonantes**. Les conditions de résonance ont été atteintes par des balayages de **température** et/ou de **champ magnétique**. Pour des balayages en température à champ fixé, nous avons observé que : (i) les variations de phase relatives présentaient une hystérèse similaire aux données de magnétométrie, et (ii) les variations d'amplitude révélaient une relation complexe entre la fréquence et la proportion de FeRh ferromagnétique présente à une température. Des interactions à la fois résonantes et non résonantes ont été documentées. D'autre part, les rampes en champ à température fixes ont révélé une résonance SAW-FMR, avec des croisements de fréquence au champ coercitif. Ces croisements ont été bien modélisés comme une diminution de la fréquence propre des ondes de spin autour de la coercivité, le champ de résonance suivant alors la même dépendance en température que la coercivité. Nous avons aussi fait des mesures de résonance **SAW-FMR angulaires**, c.-à-d. en variant la direction du champ par rapport à la direction de propagation des SAWs. Des résultats inattendus ont été révélé. Premièrement, nous avons mesuré des résonances à tout angle - c'est-à-dire que le couple magnéto-acoustique n'est jamais nul, et nous avons constaté la présence de doubles champs de résonance à certains angles. Afin de comprendre ces comportements, nous avons développé un modèle numérique en se basant sur le modèle du rétro-interaction de la SAW sur la couche magnétique.

Enfin, nous avons amélioré le dispositif expérimental existant qui permettait la génération électrique et la détection synchronisée optique des SAWs. Il fonctionne désormais à quelconque fréquence, et n'est plus limité aux multiples de la fréquence de répétition du laser.

Contents

Remerciements

Faire une thèse, c'est s'engager dans un long voyage semé d'embûches. C'est emprunter des chemins inconnus, trébucher sur des cailloux de doute, mais aussi découvrir des paysages insoupçonnés et savourer des instants d'émerveillement.

À Laurent, Sami, Mourad et Véronique,
Merci d'avoir accepté d'être membres de mon jury de thèse et pour vos relectures précieuses. Je suis profondément reconnaissant de votre engagement et de l'attention que vous avez portée à ce travail.

À ma famille, mes racines et mon refuge,
Neetya, Raj, Pamela, Leena, Malini, Geerish, Mayen et Nicole: dans votre amour et votre soutien inébranlables, j'ai trouvé la force de poursuivre ce voyage. Vos encouragements ont été les phares guidant mon navire à travers les tempêtes. Merci pour tout ce que vous avez sacrifié pour que je puisse réaliser ce rêve.

À Adilah, Angelika, Aicha, Lamya et Nouhaila,
Vous êtes les piliers de ce parcours. Votre soutien constant et votre présence lumineuse m'ont permis de surmonter les obstacles et de continuer d'avancer. Ce voyage n'aurait pas été le même sans vous. Je vous porte dans mon cœur et serai éternellement reconnaissant pour l'amour et la force que vous me donnez.

À Valia, Tristan, Marie, Laurent, Bumedijen et Pauline,
Merci pour votre soutien inestimable, aussi bien scientifique qu'humain, tout au long de cette thèse et au-delà. Vous avez été bien plus que des collègues : des mentors et des sources d'inspiration. Il est rare que les permanents soient aussi bienveillants avec les doctorants, et pour cela, je vous en suis particulièrement reconnaissant. Restez tels que vous êtes, car c'est ainsi que vous enrichissez la vie de ceux qui ont la chance de vous rencontrer.

À Jean-Michel, Ma plus belle rencontre de l'année. Merci pour ton aide précieuse, ton soutien constant et ta sagesse. Tu as été, et continues d'être, une source d'inspiration, éclairant mon chemin à chaque étape. J'ai la chance de pouvoir compter sur toi!

À Catherine, Merci de m'avoir permis de me développer et de me surpasser. Votre dévouement, notamment en corrigeant le manuscrit même pendant les Jeux Olympiques, a été essentiel à la finalisation de cette thèse. Vous m'avez guidé avec rigueur et perspicacité dans les aspects les plus complexes de ce travail. Je vous suis profondément reconnaissant pour vos conseils et la passion que vous avez su transmettre tout au long de ce voyage.

À Victor et Anatole, Mes mousquetaires de bureau. Merci pour vos discussions passionnées sur la politique et bien au-delà, et pour m'avoir écouté me plaindre sur mes échantillons. Merci pour ces trois ans bien animés.

À Djoudi, Moundji et Robin, Merci pour les bons moments passés ensemble. Vous avez apporté une énergie précieuse et une amitié qui ont rendu ces trois années bien plus humaines. Merci d'avoir rendu le travail de thèse moins solitaire.

À Mathieu, Maxime, Florent, Silbé, Laura et Vincent L., Merci pour votre aide précieuse, que ce soit sur les manips, l'interfaçage, les expériences ou les calculs. Vous avez transformé des défis en opportunités, et vos contributions ont apporté une dimension nouvelle à ce parcours. J'ai beaucoup appris à travers nos échanges.

À Faith Z., Merci de m'avoir accueilli au LSPM. Ce fut un véritable plaisir de collaborer avec toi et de découvrir à quel point chaque laboratoire a ses propres cultures et dynamiques.

À mes collègues de l'INSP, Les Supers Nanos! et d'ailleurs: Kaouther, Charlie, Eliane, Lucille, Guillaume, Antoine, Hugo, Sergei, Juan, Chabane et tant d'autres, vous avez été des compagnons précieux tout au long de ce voyage. Merci pour votre bonne humeur, les pizzas/raclettes nights qui ont rendu cette aventure plus douce.

Et enfin, à toutes les idées, aux rêves, et à cette rose qu'il a fallu cultiver avec soin. Car, comme Saint-Exupéry l'écrit si justement : « C'est le temps que tu as perdu pour ta rose qui fait ta rose si importante. » (Le Petit Prince, 1943).

Introduction

The first physical observations of magnetic effects date around 600 BC, when Greek philosopher Thales of Miletus observed the attraction of Iron to Lodestones, and famously quoted "**the magnet has a soul..**" [1]. However, it was not until the late 18^{th} century that a comprehensive understanding of "this soul" began to emerge, with the advent of modern **Physics** and subsequently **Quantum Mechanics**. Research in **Magnetism** has revolved significantly around the most familiar form of magnetic ordering: **Ferromagnetism (FM)**, which is characterised by the parallel alignment of magnetic moments and the associated spontaneous magnetisation. The transition from bulk material studies to the exploration of magnetic phenomena in thin films, which began in the early 1960s, led to the development of **Spintronics** — a field leveraging electron spin for information processing. This shift reflects a broader trend in contemporary research, promising faster and more energy-efficient technologies for the storage, manipulation and processing of information, compared to conventional charge-based electronics [2]. The discovery of the **Giant Magneto-Resistance (GMR)** in the late 1980s by Albert Fert and Peter Grünberg, which in due course earned them the Nobel Prize in Physics in 2007, marked a pivotal moment for this field [3], [4]. The GMR effect is a quantum mechanical phenomenon, observed in thin film structures composed of alternating ferromagnetic and non-magnetic layers [5]. When the magnetisation of the magnetic layers are aligned parallel to each other, the electrical resistance of the structure is relatively low. Conversely, when they are anti-parallel, the resistance is significantly higher. This significant change in electrical resistance has revolutionised data storage technology, leading to the development of **high-density hard disk drives (HD-HDD)**, **Magnetic Random Access Memory (MRAM)** and more recently **Spin-Transfer Torque MRAM (STT-MRAM)** [6]–[10]. Further exploration into the dynamics of spin has led to the emergence of **Magnonics**, a sub-field of spintronics. Magnonics focuses on the manipulation of magnons, which are quanta of **Spin Waves (SWs)** or more precisely, the collective excitation of magnetic moments in a material. The study of magnons offers a pathway to novel computing paradigms, where information is encoded in the phase and amplitude of spin waves rather than on the electronic charge [11], [12]. Magnonics is particularly appealing due to the diverse range of phenomena it encompasses, from the fundamental physics of spin wave propagation to practical applications in communication and data processing [13], [14]. Spin waves can exhibit dynamics for frequencies ranging from the gigahertz (GHz) to terahertz (THz) regimes, making them suitable for a variety of technological applications. Moreover, the wavelength of spin waves can be manipulated through the material's magnetic properties (anisotropy, saturation magnetisation, damping etc.), and geometric constraints (confinement, patterning, periodicity etc.), allowing for highly localised and re-configurable magnonic circuits [15]. A significant element in the field of magnonics is the development of techniques to generate and control spin waves. One such technique is the **Acoustic Wave-Ferromagnetic Resonance**, which uses acoustic strain fields to drive SW magnetisation dynamics via **Magneto-Elasticity** [16]. Today, **Surface Acoustic Waves (SAWs)**, which are acoustic waves propagating along the top surface of a material medium is at the fore-front for SW manipulation. Research into **SAW-Ferromagnetic Resonance, SAW-FMR** has demonstrated its effectiveness in interacting with spin waves in various magnetic materials such as: Ni [17]–[19], GaMnAs [20], Fe [21], YIG among many others; for promoting domain walls [22] and skyrmion [23] motions and for SAW-driven spin-pumping phenomenon [24]. SAWs are typically excited via **piezoelectric** effect, where **Interdigitated-Transducers (IDTs)** convert electric fields into mechanical strain fields, or via **thermo-elastic** effect, where a rapid heating and subsequent thermal expansion generates strain field dynamics. The team at the INSP has the expertise to do both, and has subsequently reported SAW-driven magnetisation switching [25], [26], SAW-driven coercivity reduction

[27] and the optical probing of linear and non-linear SAW-FMR dynamics via **Magneto-Optical Kerr Effects (MOKEs)** on the ferromagnetic semiconductor GaMnAs [26], [28]. In 2020, the small group decided to investigate SAW-driven **Antiferromagnetic (AFM)** dynamics on two distinct magnetic materials: **GdCo** and **FeRh**.

GdCo is a Ferrimagnetic alloy composed of two unequal magnetic sub-lattices, which for selected composition exhibit two characteristic temperatures: T_{MC} and T_{AC}. At the magnetic compensation temperature T_M, the two anti-ferromagnetically coupled sub-lattices are equal and opposite, giving a net zero magnetisation. At the angular compensation temperature, the spin densities of the two sub-lattices are equal and opposite, giving an AFM-like dynamical behaviour, but with finite net magnetisation. Part of the 1st year was devoted to the first experimental evidence of SAW generation on GdCo/LNO structures, and the establishment of optical conditions for the resonant excitation of both FM-like and AFM-like magnetisation dynamics. Although much work has been undertaken on this material, the FM and AFM dynamics with respect to temperature could not be demonstrated experimentally. Unfortunately, only one 5nm-thick GdCo sample was available during the PhD. Consequently, these findings are not included in this manuscript.

FeRh is a unique material known for exhibiting a first-order magnetic phase transition going from the AFM to FM phases near room temperature. In the AFM phase, the net zero magnetisation renders AFMs largely insensitive to magnetic fields, but also makes them difficult to manipulate. Initially, this project was devised to implement a novel way to act on the AFM phase using SAWs. The main objectives were to gauge the possibilities of controlling the AFM static states via magneto-elasticity, surpassing the net zero magnetisation obstacle (c.f. Projet Financé). However, the lack of epitaxial FeRh/MgO samples, to test lithography protocols for SAW generation, prompted the growth of Polycrystalline FeRh/GaAs at the INSP. SAW-FMR interaction on the polycrystalline FeRh constitutes the majority of results presented in this manuscript.

Typically, **SAW-FMR** involves matching the frequency and wave-vector of the SAWs to the SWs. This is generally obtained either:
(i) In **anisotropic** magnetic materials where the magnetic properties vary depending on the direction of the applied magnetic field. By applying the magnetic field along the **hard axis** (the direction in which it is most difficult to magnetise the sample), the SW eigen-frequency is reduced, or **softened**. This reduction in the SW eigen-frequency allows easier matching between the SAW and SW frequencies.
(ii) In **isotropic** magnetic materials, which have uniform magnetic properties in all directions, achieving frequency matching requires the use of **high-frequency SAWs**. However, piezoelectric transducers operating at high frequencies can face challenges such as increased losses, decreased coupling efficiency, more complex fabrication processes and might pose challenges in practical implementation.

Here, we proposed an alternative approach for the softening of SW eigen-frequencies around the **local coercive fields**. By-passing the need for high SAW frequencies or the presence of a magnetic hard axis, this will allow the SAW-FMR interaction for arbitrarily low SAW frequencies and any effective anisotropy. This original method offers a promising avenue for improving the application and effectiveness of SAW-FMR techniques on a wider range of magnetic materials.

The manuscript is organised as follows. In Chapters 1 and 2, a general overview of the FeRh material is given, followed by the description and characterisation of the FeRh samples and the introduction to the optical setups. This is followed by Chapters 3 to 5 which covers the theoretical aspects, essential for understanding the SAW-FMR interaction. Then, Chapters 6 to 8 deal with SAW-FMR experiments and the subsequent data analysis for temperature and/or magnetic field variation. Finally, in Chapter 9 is presented an improvement of the existing SAW-FMR optical detection setup, for future applications.

Part I
FeRh, Samples and Setups

Chapter 1

Iron-Rhodium

Objectives

In this chapter is provided a comprehensive overview of the metallic alloy of FeRh. FeRh is a fascinating material, as it undergoes for near equi-atomic concentration, a first-order magnetic phase transition going from the low-temperature AFM phase to the high-temperature FM phase. This transition is accompanied by changes in its lattice, electronic and magnetic degrees of freedom. Exploring those properties are important to understand how to act on the meta-magnetic FeRh. A detailed examination of how extrinsic and intrinsic factors like applied magnetic fields, pressure and dimension can induce and control the phase transition are presented. This provide the readers with a thorough understanding of FeRh's unique characteristics, and offers valuable insights into how these factors can be leveraged to tailor the properties of FeRh for specific applications.

Contents

1 Magnetic Order

Since the discovery and the attempts to apprehend the fundamentals of magnetism by W. Gilbert [1540-1603], C.F. Gauss [1777-1855], C. Coulomb [1736-1806], C. Oersted [1777-1851], A.M. Ampere [1775-1836], M. Faraday [1791-1869], J.C. Maxwell [1831-1879] and many others, a lot of progress has been made. The existence of an atomic magnetic moment is related to the movement of electrons around the nucleus and thus to its electronic structure. The subsequent discovery of the intrinsic spin of the electron by G.E. Uhlenbeck [1900-1988] and S. Goudsmit [1902-1978] in 1925, further revolutionised the understanding of magnetism, highlighting that the spin of the electron contributes significantly to the magnetic properties of atoms. Consequently, due to Coulomb repulsion and Pauli exclusion principle, two neighbouring magnetic moments interact with each other by a so-called exchange coupling. Depending on the symmetry and the overlap of the electron spin states, this exchange parameter can be either negative or positive. Magnetism as considered in this manuscript, consists of a large assembly of magnetic moments - the micro-magnetic approximation[1], whereby the full exchange interaction results from all the moment pairs aligned parallel or anti-parallel to establish a magnetic order. Two major magnetic orders exist: Ferromagnetic (FM) and Antiferromagnetic (AFM). Figure [1.1], is a representation of the magnetic moments, for field-saturated samples in the two classes.

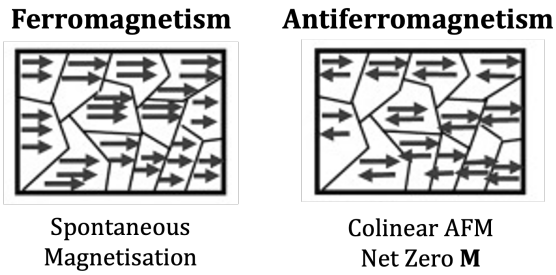

Figure 1.1: There are two classes of magnetic order: ferromagnetic (FM) and antiferromagnetic (AFM). The magnetic moments within a material, represented by arrows, are grouped into magnetic domains, which are separated by magnetic domain walls. For a FM, in the absence of an external magnetic field, the moments align spontaneously within their domains, resulting in spontaneous magnetisation. This is the typical characteristic of FM materials. When a strong enough magnetic field is applied, it can suppress the magnetic disorder, causing all magnetic moments to align collinearly with the field. In some antiferromagnetic materials, however, the net magnetisation remains zero even in the presence of a magnetic field. This can be illustrated by a collinear AFM with a sublattice system composed of two magnetic moments. If a field strong enough to suppress the AFM exchange interaction is applied, the magnetic moments rotate and are all aligned with the field.

Ferromagnetism- FM: Ferromagnetic materials possess a spontaneous magnetisation in the absence of a magnetic field. The magnetic moments or spins are aligned in the same direction, resulting in a long-range order. By convention, the exchange parameter is taken to be positive. The regions within which magnetic moments align with each other are called magnetic domains, and are separated by domain walls. When an external magnetic field is applied, all the magnetic moments align parallel to the field. The spontaneous magnetisation vanishes at the Curie Temperature, T_C, and the FM order disappears. The material thus becomes paramagnetic. A non-linear response of magnetisation with field is illustrated on figure [1.2], commonly referred to as the magnetic hysteresis loop. It begins at zero-field and

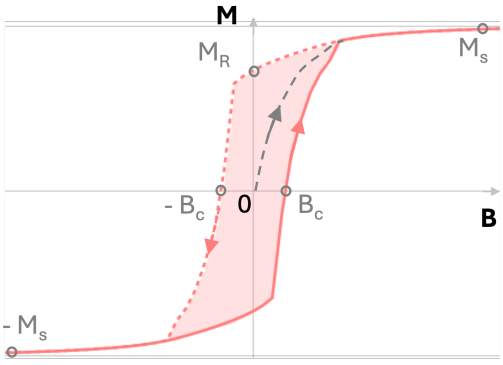

Figure 1.2: Typical hysteresis loop. M_S is the saturation magnetisation, M_R the remanence and B_C the coercive fields.

[1]The length scales considered are large enough for the atomic structure of the material to be ignored, yet small enough to resolve magnetic structures such as domain walls.

zero magnetisation (in grey), and increases with increasing field value and reaches a maximum at saturation magnetisation, M_S. When the field is decreased, the magnetisation decreases and at zero-field value, this time, the corresponding remaining magnetisation of the sample is called magnetic remanence, M_R. This magnetisation finally reaches a net zero value at an opposing directed field value called coercivity, - B_C, and starts to increase in the opposite direction up to opposing saturation, - M_S, and identically on the way back. Coercivity is a crucial parameter in magnetic materials, and in understanding this manuscript.

Magnetic coercivity can originate from both intrinsic and extrinsic factors. Intrinsic origins are tied to the fundamental properties of the material itself, such as its crystalline structure, magnetic anisotropy, and exchange interactions. Magnetic anisotropy, for instance, is a critical intrinsic factor, determining how easily the material magnetisation can be reoriented. Materials with high magnetic anisotropy, like cobalt (72 kA/m)[29] or Hard Disk-drive (HDD) recording medium CrCoPt (140 kA/m)[30], exhibit high intrinsic coercivity[2] because their domains are strongly aligned along specific crystallographic directions, making reorientation difficult. Extrinsic origins of coercivity, on the other hand, are influenced by factors external to the material's inherent properties, including defects, magnetic grain size, and domain wall pinning. For example, the presence of impurities or structural defects can impede the movement of domain walls, thus increasing coercivity. Similarly, materials with fine grain structures often exhibit higher coercivity due to the grain boundaries acting as barriers to domain wall movement. An example of this is the use of nano-crystalline alloys in permanent magnets, where the refined grain size enhances coercivity by restricting domain wall motion [32].

Antiferromagnetism- AFM: A magnetic material exhibits Antiferromagnetic order when two neighbouring magnetic moments are anti-parallel to each other. This leads to zero net spontaneous magnetisation. When an external field is applied, it must compete with the AFM exchange interaction (negative) in order for the magnetic moment to align with it. There are two primary types of ordering: collinear and non-collinear. In collinear antiferromagnets, spins are aligned directly opposite to each other. This can be observed in materials like manganese oxide (MnO). In contrast, non-collinear antiferromagnets exhibit more complex spin arrangements where the spins do not align along a single axis but instead form angles with each other. This type of ordering is seen in materials such as hematite (Fe_2O_3), where the spins can adopt a triangular configuration [33]. Likewise, the stability of AFM order is highly dependent on temperature, and the antiferromagnetic order vanishes at a critical temperature, known as the Néel temperature, T_N. Similar to FM, the AFM material becomes paramagnetic above this critical temperature.

Ferrimagnetism- FerriM: A ferrimagnet is a type of magnetic material containing two or more different magnetic populations with different magnetic properties called sub-lattices. The moments of each sub-lattice are ferromagnetically coupled, whereas the moments of two different sub-lattices are coupled antiferromagnetically. This results in a net magnetic moment because the opposing magnetic moments of the sub-lattices do not completely cancel out each other. Ferrimagnets typically exhibit spontaneous magnetisation like FM but have a lower net magnetisation due to the partial cancellation of magnetic moments. Key characteristics of FerriM are the presence of a magnetic and angular compensation points respectively. At the magnetic compensation point, the net magnetisation becomes zero because the opposing moments cancel each other. At the angular compensation point, the angular moments cancel each other leading to magnetic precession-free dynamics [34]. Examples of FerriM are GdCo (which has been studied during this PhD- but not present in the manuscript) and Yittrium Iron Garnet (YIG).

2 Metallic FeRh

First studied more than eight decades ago by Fallot *et al.* [35], interest in FeRh has rarely dwindled, primarily due to the remarkable feature that it has a phase transition going from the AFM-to-FM

[2] This is in contrast with soft ferrite e.g $Ni_{0.5}Zn_{0.5}Fe_2O_4$, where the coercivity is 1.6-7.6 kA/m [31]

phase in close proximity to room temperature. Understanding and harnessing this first-order phase transition has been the focus of various research endeavours aimed at exploiting its potential, both for fundamental research and practical technological applications. An up-to-date state-of-the art on the latter is given at the end of this chapter.

The settled binary phase diagram of the bulk $Fe_{1-x}Rh_x$ alloy with respect to the Rhodium concentration is given on Figure [1.3]-**Left**. Compiled by Swartzendruber *et al.* [36], it describes all possible magnetic states and crystallographic structures of bulk FeRh. For temperatures above 1963°C, all $Fe_{1-x}Rh_x$ compounds are in the liquid phase, while Fe-rich compounds exhibit liquid phases down to temperatures close to 1538°C. Note that for near-pure Fe content ($x < 6\%$), a high-temperature δ body-centred cubic (BCC) phase exists. These phases are circumscribed by the ubiquitous paramagnetic (PM) face-centred cubic (FCC) state, denoted by γ, end phase of solid solubility. α, on the other hand, is the low-temperature and high Fe content BCC ferromagnetic (FM) phase, found at temperatures below the Curie point, T_C. An α-to-γ transition is of martensitic nature[3]. A transition between paramagnetic and ferromagnetic phases is continuous, meaning the change in magnetisation is gradual. Even though this phase diagram is rich in physics, the focus of this manuscript lies close to the atomic equilibrium of FeRh, i.e for $\mathbf{Fe_{\approx 0.5}Rh_{\approx 0.5}}$.

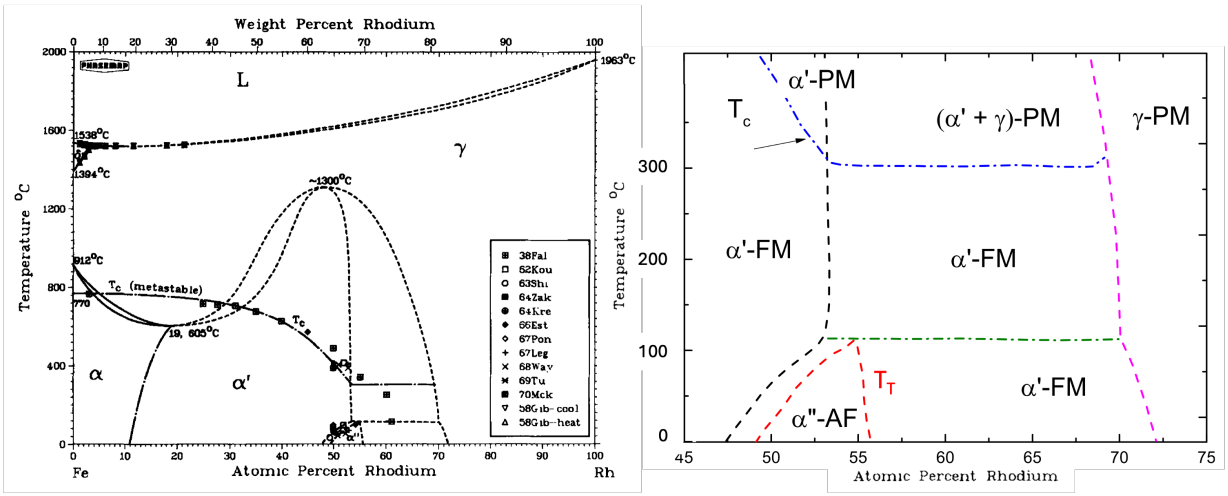

Figure 1.3: Left: Phase diagram of the Fe-Rh binary compound. Note the existence of Paramagnetic, Ferromagnetic and Antiferromagnetic FeRh depending on the Rhodium concentration in the alloy. Adapted from [36]. **Right**: Truncated reproduction of the binary-phase diagram around near equilibrium chemical components. For temperatures close to room temperature and up to $\approx$ 130°C, the existence of the AFM FeRh phase is strictly related to a Rhodium concentration of ($0.48 \leqslant x < 0.56$): $Fe_{1-x}Rh_x$ [37].

Figure [1.3] **Right**- shows the truncated phase diagram around equi-atomic concentration depicting the most important equilibrium phases of FeRh. Both the α'-FM phase and α''-AFM phase have ordered CsCl crystallographic structure- usually denoted as B2 (or in Crystallographic Space Group: $Pm3m$), and are separated by a thermodynamic first-order[4] FM-to-AFM phase transition. These transitions are characterised by the coexistence of the two phases at the transition temperature, with both phases in equilibrium. The red dotted line borders this AFM phase which is present at temperatures less than $\lessapprox$ 130°C. Moreover, at 0°C, the existence of the AFM-phase occurs exclusively for a narrow Rhodium atomic concentration of ($Fe_{1-x}Rh_x$: $0.48 \leqslant x < 0.56$), whereas outside of this range, metallic FeRh exhibits the α'-FM CsCl-type structure without phase transition [38]. Across the AFM-to-FM phase transition, the B2-CsCl cubic structure is conserved, but there is an increase in the unit cell. In thin films, the phase diagram and phase lines have not been definitively established, so the presence of small amounts of secondary α or γ phases can be measured even in near equi-atomic films [39]. However,

[3] A martensitic phase transition occurs when a material undergoes a rapid metastable phase change from one crystal structure to another under certain conditions such as temperature or stress, without the diffusion of atoms.

[4] A first-order thermodynamic phase transition is where a system undergoes a sudden change at a critical point, typically characterised by a discontinuity in one or more thermodynamic properties.

for near equi-atomic concentration, it is clearly established that FeRh goes from a low-temperature AFM-phase to a high-temperature FM-phase. Exploring this transition is the starting point of this manuscript.

2.1 Properties of the AFM-FM phase transition

Early diffractometry measurements have showcased the strong interplay between magnetic and lattice degrees of freedom and the high symmetry cubic crystallographic structure. Indeed, neutron diffraction in the AFM phase measured that the Fe atoms have a local magnetic moment of $\mu_{\mathrm{Fe}}^{\mathrm{AFM}} = 3.3\ \mu_{\mathrm{B}}$ while the Rhodium atoms exhibit zero magnetic moments[40]–[42]. Figure [1.4], is a schematic representation of the B2 FeRh unit cell structure in the AFM state. The central grey atom depicts the Rh element while the outer-magnetised atoms represent the Fe elements. Two AFM orders of the unit cells are possible. The left cell depicts an inter-plane type-I AFM interaction. Here the Fe atoms are anti-ferromagnetically coupled through successive {001} planes, while exhibiting ferromagnetic coupling within the plane. Only the AFM coupling is represented on the diagram. Alternatively, the right cell illustrates the type-II unit cell. Here the Fe atoms are anti-ferromagnetically coupled through successive {111} planes and ferromagnetically coupled intra planes. First-principles band-structure calculations revealed that the type-II-AFM configuration is more stable energetically [43], [44], and coexists with FM solutions over a wide range of cell volume.

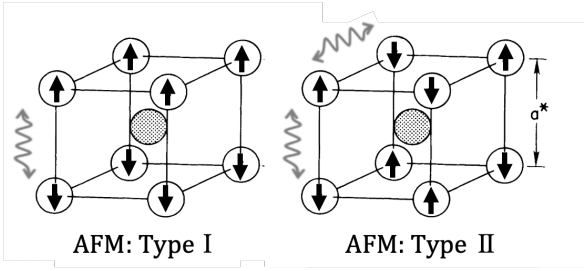

Figure 1.4: Spin configuration of the AFM-FeRh CsCl cubic unit cell. The Fe and Rh atoms are respectively depicted as open and grey-filled spheres while the arrows show the spin alignment. Note that the Fe atoms occupy the outer corners of the unit cell-atomic positions $(0,0,0)$- while the Rh atoms the central location- atomic positions $\left(\frac{1}{2},\frac{1}{2},\frac{1}{2}\right)$. Type-I describes successive {001} planes AFM coupling, while Type-II shows successive {111} planes AFM coupling between Fe atoms. Adapted from [43].

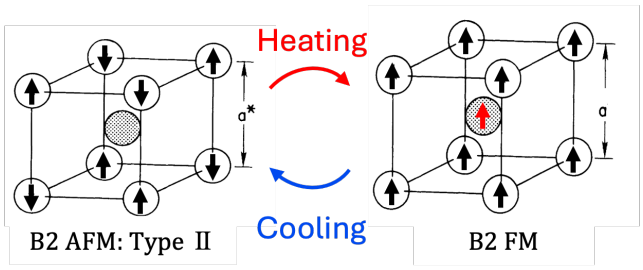

Figure 1.5: Moruzzi et al. showed using band structure calculations that Type-II is the ground state of the AFM phase. Note that in the Type-II-AFM unit cell, the magnetic moments are present on the Fe atoms only. By heating the equiatomic FeRh element, it goes from the AFM-to-FM phase. In the FM phase, the central Rh atom is now magnetised. Moreover, the cell volume changes and there is a 1% increase in the cubic cell volume across the transition for Bulk FeRh. Adapted from [43].

As the FeRh is heated, its magnetic properties transition from AFM to FM order. Figure [1.5] is a representation of the cubic cell across the phase transition. In the FM phase, the Rh atom acquires a magnetic moment equalling to $\mu_{\mathrm{Rh}}^{\mathrm{FM}} = 0.9\ \mu_{\mathrm{B}}$, while the Fe atoms moments decrease slightly to $\mu_{\mathrm{Fe}}^{\mathrm{FM}} = 3.2\ \mu_{\mathrm{B}}$ [38]. This temperature-induced zero-pressure AFM-to-FM phase transition does not affect the CsCl-type structure but results in a 1% increase in the bulk crystallographic volume and 0.3% increase in the lattice cell parameter: a [45]–[47]. Furthermore, a substantial change in entropy (16-25 $\mathrm{Jkg^{-1}K^{-1}}$ [41], [48]) and electrical conductivity accompanies this first order phase transition.

Figure [1.6] are the temperature dependence of **(a)** magnetisation and **(b)** electrical resistivity across the AFM-to-FM phase transition measured by Kouvel *et al* [40]. As the latter is first-order, **(a)** shows a sharp transition occurring around 350 K. The closed and open symbols respectively denote the heating and cooling branches respectively. The Curie temperature befalls at 675 K. The right axis illustrates the temperature dependence of the magnetic susceptibility, χ. Note that here, is represented $1/\chi$, in dotted line. For temperatures above $\mathrm{T_C}$, the FeRh behaves like a paramagnetic sample and $1/\chi$ diverges. For $\mathrm{T} \leqslant \mathrm{T_C}$, Curie-Weiss law is applicable. **(b)** on the other hand, shows the evolution of the electrical conductivity measured by conventional potentiometric techniques. An abrupt decrease

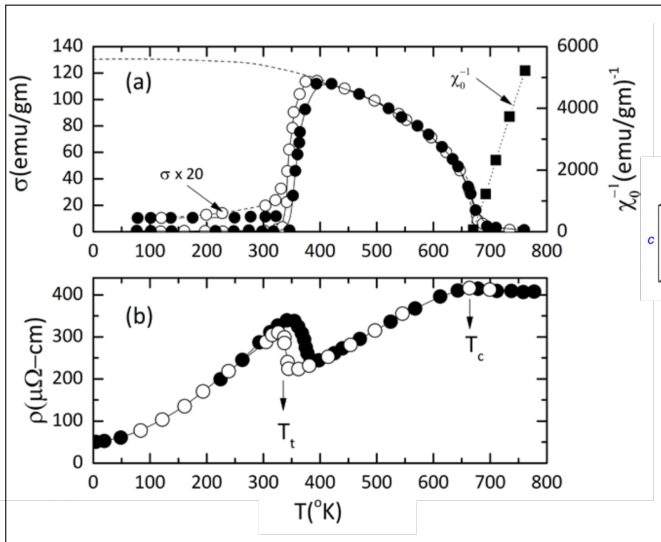

Figure 1.6: **(a)**:Magnetometry measurement with respect to temperature on bulk polycrystalline FeRh. The closed symbols represent the heating ramp, while the open symbols represent the cooling ramp. In dotted line is represented the reciprocal magnetic susceptibility, χ, with the axis on the right side. Note the existence of an abrupt increase in magnetisation around 350 K and the Curie temperature measured at 675 K. **(b)** Transport measurement on the same bulk FeRh sample. An abrupt decrease in electrical resistivity measurements in-line with the first-order phase transition is seen. Here, a 45% decrease across the AFM-to-FM transition is recorded. Adapted from [40].

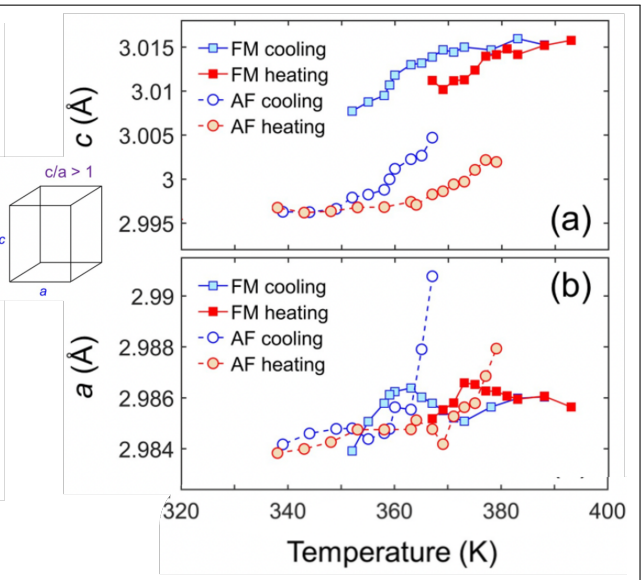

Figure 1.7: Temperature dependence of the out-of-plane **(a)**, and in-plane lattice parameter **(b)**, for both AFM and FM phases for a 84 nm-thick FeRh thin film grown on MgO. The c parameter shows well separated values between the AFM and FM phases. For thin-films, the out-of-plane lattice expansion accounts for the majority of volume increase across the transition. The out-of-plane parameter increases by 0.67%. On the other hand, the in-plane parameter increases monotonously, and have only a 0.13% increase across the AFM-to-FM phase transition. Adapted from [49].

of 40% at the transition is noted [40]. This is due to the electronic band structure also being altered by the AFM-FM transition. Furthermore, a thermal hysteresis is noted for both the magnetometry and transport measurements. Similarly, Lommel prepared and studied alternately deposited Fe and Rh layers up to 140-to-180 nm-thickness [50]. He showed that FeRh films also exhibited thermal hysteresis both for the magnetisation and electrical resistivity, while keeping the same high symmetry ordered B2 crystal structure. The thin film overall magnetic moment was about one third of the bulk, while the resistivity half of the bulk sample.

X-ray diffractometry by Zakharov *et al.*[47], showed that the lattice parameter also exhibits an abrupt increase at transition. The author measured an out-of-plane lattice expansion of 0.3% across the AFM-to-FM phase transition on bulk polycrystalline FeRh. More recently, Zhou *et al.* revealed a giant lattice parameter change of 0.67% on 100 nm-thick FeRh layer grown on MgO [51]. This was attributed to a distortion of the FeRh lattice structure due to the growth relationship between the film and the substrate and the finite sizing nature of thin films. On average, the transition usually present a thermal hysteresis of 10-15°C for epitaxial FeRh thin films, for example on MgO (FeRh(001) on MgO(001)), Sapphire (FeRh(111) on Al_2O_3(0001)) [52], Strontium Titanate (FeRh(001) on $SrTiO_3$(001)) or Lanthanum Aluminate (FeRh(001) on $LaAlO_3$(001)) [53]. On figure [1.7] are represented the out-of plane c, (fig. **(a)**) and in-plane a, (fig. **(b)**) lattice parameter for a 48 nm-thick FeRh grown on MgO with respect to temperature. Both follow monotonic trend with increasing temperatures. There is an increase of 0.67% for the out-of-plane components between the AFM and FM phases. For the in-plane, this variation is limited to 0.13%, due to the compressive in-plane stress exerted by the MgO substrate. As said above, the AFM-to-FM FeRh phase transition is also accompanied by a substantial change in entropy. Several groups have tried to explain the origin of this phase transition, and in doing so has investigated the entropy at the transition. The aim of the next section is to understand the origin of this first-order magneto-structural phase transition.

Thermodynamic phase transition

In order to fully understand the AFM-to-FM phase transition, a review of thermodynamics is necessary. Any thermodynamic phase transition, in the presence of a magnetic field, can be understood using Landau theory [54]. The Gibbs free energy G, can be written in terms of the internal energy U, volume V, temperature T, magnetisation M, magnetic field B, and entropy S:

$$G\left(T,B\right)=U-TS-MB \tag{1.1}$$

The Gibbs energy differential can thus be written as:

$$dG=dU-TdS-SdT-MdB-BdM \tag{1.2}$$

The first principle of thermodynamics states that: $\mathrm{dU}=\delta Q+\delta W=TdS+BdM$. This differential accounts for the heat transfer to the system and the work-done by the system and by the magnetic field respectively. Hence, equation [1.2] can be written as:

$$dG=-SdT-MdB=\frac{\partial G}{\partial T}_{|\mathrm{B}}dT+\frac{\partial G}{\partial B}_{|\mathrm{T}}dB \tag{1.3}$$

By simple identification,

$$S=-\left(\frac{\partial G}{\partial T}\right)_{\mathrm{B}}\quad\text{and}\quad M=-\left(\frac{\partial G}{\partial B}\right)_{\mathrm{T}} \tag{1.4}$$

As FeRh has a first-order phase transition, this imply that there is a discontinuity in the first derivative of the free energy. This discontinuity is observed on the measurement of the entropy and the magnetisation. Moreover, the second law of thermodynamics relates to the specific heat at constant B, as:

$$C_{\mathrm{B}}=T\left(\frac{\partial S}{\partial T}\right)_{\mathrm{B}}=-T\left(\frac{\partial^2 G}{\partial T^2}\right)_{\mathrm{B}} \tag{1.5}$$

Using the Maxwell's relation,

$$\left(\frac{\partial S}{\partial B}\right)_{\mathrm{T}}=-\left(\frac{\partial M}{\partial T}\right)_{\mathrm{B}}\quad\longrightarrow\quad\frac{\partial T_{\mathrm{TR}}}{\partial B}=-\frac{\Delta M}{\Delta S} \tag{1.6}$$

This relation helps in understanding how changes in the magnetic field affect the transition temperature $\mathrm{T_{TR}}$, given the changes in magnetisation ΔM, and entropy ΔS. The specific heat and the entropy are the two main thermodynamic parameters needed to understand the mechanism behind the AFM-to-FM transition, as elaborated below.

2.2 Origin of the magneto-structural phase transition

Despite having sparked intense scientific curiosity, leading to numerous theories and experiments aimed at unravelling the underlying mechanism, the origin of this enigmatic magneto-structural phase transition remains debatable to this day. One early explanation, proposed by Zakharov *et al.* in 1964 [47], is rooted in the phenomenological theory of Kittel [55]. It was postulated that the exchange coupling parameter governing this type of first-order AFM-FM transition is a linear function of the lattice parameter and changes sign at a critical value, corresponding to the volume increase occurring at transition. However, subsequent studies calculated a large change in entropy at the transition [41], [56], casting doubt on the adequacy of the exchange-inversion model, in explaining the transition.

Instead, it was proposed that the transition is driven by factors related to electronic band structure, in particular the fine structure [57]. Tu *et al.* supported this view by highlighting the significant difference in electronic specific heats between the AFM and FM phases, suggesting a change in entropy of band electrons as the primary driver of the transition, and the excess magnetic entropy stabilises the FM phase [58]. It was recorded that the electronic specific heat of the FM phase is four-times greater than in the AFM phase. That being said, investigation of the specific heat for samples with Iridium doping, led to too high values to arise from electronic specific heat only at low temperature [59]. This extra contribution to the specific heat was thus interpreted as fluctuation in the exchange fields due

to thermal excitation of magnetic moments. Building upon these findings, Gruner *et al.* put forward a novel hypothesis, suggesting that competition between AFM Fe-Fe and FM Fe-Rh exchange interactions connected to a two magnetic spin states[5] of Rhodium are at the origin of the meta-magnetic transition [60]. The Fe-Fe sub-lattice switches from AFM to FM exchange. The additional entropy from the two-states lowered the FM Gibbs free energy level to that of the AFM thus driving the transition. The feasibility of this mechanism to the FeRh compound was thus verified theoretically by Monte Carlo calculations and underscored the need to include all degrees of freedom and their corresponding thermal dependencies.

First principles calculations, by Gu *et al.*, posit that magnon excitation predominantly propel the AFM-to-FM transition, rather than pure electronic band modifications [48], while the addition of transport and thermodynamics highlight the role of Rh hybridisation with surrounding Fe atoms as source of the transition [61], [62]. They concluded that the non-zero Rhodium magnetic moment in the FM state, resulted in an increase in the magnetic degree of freedom and the total entropy, which consequently stabilises the FM state akin to [58]. Recently Cooke *et al.*, performed broad temperature measurements on epitaxial FeRh films, in order to break down electronic, magnetic and lattice contributions to the specific heat [63]. It was shown that the largest contribution is of magnetic origin, while the smallest contribution was in fact of electronic origin. However, this assertion is in contradiction to an even recent paper by Wolloch *et al.* which states that lattice, electronic and magnetic degrees of freedom contribute in roughly equal magnitude at the transition [46]. Nevertheless, this paper reveals the sensitivity of FM lattice to uniaxial strain, which is entirely absent in the AFM phase.

Alternative theoretical frameworks have spotlighted electronic structure disparities between the AFM and FM phases as pivotal in driving the transition. Koenig *et al.* suggested that fluctuations in the density of states at the Fermi level, between the AFM and FM states, serve as the primary impetus behind the transition [64]. This found support in the experimental observations of a pseudo-gap formation at the Fermi level in the AFM state [65]. Conversely, Barker *et al.* model of atomistic spin dynamics demonstrated that the lattice exchange has the same symmetry as an effective 4-spins interactions[6], and pointed the crucial role of this exchange interactions in describing the transition [67]. Finally, Polesya *et al.* [68] and Staunton *et al.* [69] pushed for a more nuanced contribution of stochiometry and Fe-Fe exchange parameter as the magnetic degree of disorder driving the transition.

In summary, the mechanism driving AFM-FM phase transition in FeRh remains a debatable issue. Moreover, as it is experimentally challenging to observe the variation in the magnetic and lattice system simultaneously, these inconsistencies will likely linger. Nevertheless, one can summarise out of this vast literature that all three degrees of freedom contribute to the transition, with the Rh atoms playing a crucial role either singly or under hybridising effect with the Fe atoms.

2.3 Influencing the AFM-FM phase transition

Even though the origin is still debatable, understanding the parameters influencing the transition is a crucial step towards using FeRh alloys for possible functional applications. Figure [1.3] demonstrated the importance of composition and temperature on the transition. These parameters can be classified as intrinsic or extrinsic, with extrinsic being magnetic field, pressure and temperature, while intrinsic refers to chemical tuning and composition and sizing (or dimensions).

Influence of Magnetic Field

The presence of an external magnetic field around the transition temperature disrupt the AFM order, while favouring the FM order. As such, it is easily understood that a magnetic field stabilises the

[5] The two magnetic spin states refers to the AFM Fe-Fe interaction and the FM Fe-Rh interaction. The Hamiltonian used in their Monte-Carlo simulation is able to distinguish between these two spins states of the Fe and Rh atoms.

[6] A 4-spin interaction refers to the interaction between four nearest neighbour interaction in the B2 structure. A chain-like structure between neighbouring Fe and Rh atoms can be seen as one of the spins associated with an Fe atom, another with a Rh atom, and the remaining two with additional iron atoms [66].

FM phase and decreases the transition temperature by reducing the thermodynamic energy barrier needed for the phase transition. Kouvel *et al.* studied this influence and came up with a decrease in transition temperature of - 8.2 KT^{-1} for bulk FeRh, while keeping the width of the thermal hysteresis [41]. Likewise, Maat *et al.* examined the influence of field on 110 nm-thick FeRh thin films grown on single-crystal Magnesium Oxide, MgO(001), and Sapphire, Al_2O_3(0001) [70]. Figure [1.8]**(a-c)** is the magnetometry measurement of the phase transition under different field values on the 110 nm-thick thin film. Figures **(a)** and **(b)** show the heating and cooling ramps respectively for different fields. It can be observed that both branches shift to lower temperatures for increasing field values. Fig. **(c)** is the transition temperature versus field dependency for the FeRh on MgO sample. A transition rate of - 8 KT^{-1} was calculated. This is very similar to bulk FeRh. It confirms the FM phase stabilisation, reduction in transition temperature and constant width of the hysteresis seen in bulk FeRh. For FeRh on Sapphire, a transition rate of - 9 KT^{-1} was calculated. This difference was attributed to different strained nature of FeRh grown on MgO or Al_2O_3.

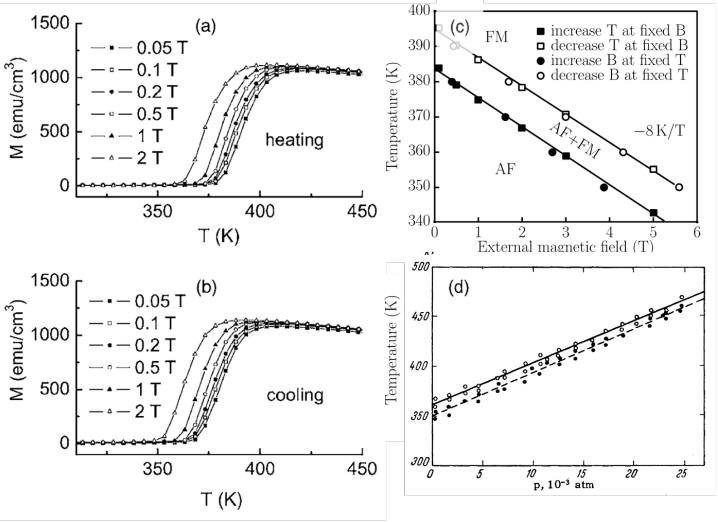

Figure 1.8: Temperature dependence of magnetisation for **(a)** heating branch, **(b)** cooling branch under different field values for a 110nm-thick FeRh grown on MgO. **(c)** Transition temperature versus magnetic field phase diagram established from **(a)** and **(b)** curves showing a shift in phase transition temperature of $\partial T/\partial B = -8$ KT^{-1} for FeRh on MgO single-crystal substrate. Adapted from [70]. (d) Transition temperature dependence to pressure established on bulk FeRh. Adapted from [47].

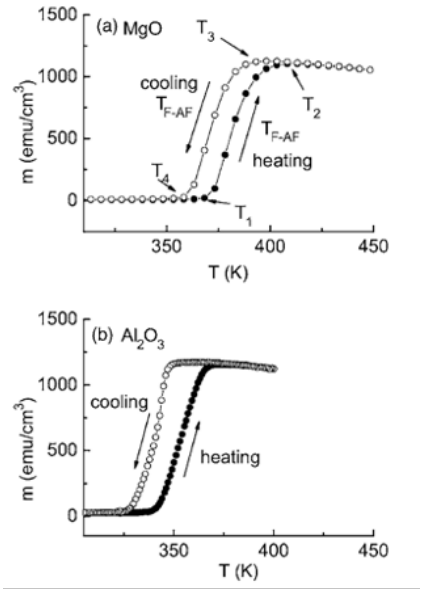

Figure 1.9: Temperature dependence of epitaxially grown 110 nm-thick FeRh on **(a)** MgO **(b)** on Sapphire substrates respectively. In-plane expansion resulted in a stabilisation of the FM phase, while in-plane compression stabilises the AFM phase. Adapted from [70].

Influence of Pressure

Likewise, the influence of pressure can be investigated. Two types of pressure stem out in this category: Hydrostatic (or isotropic) pressure and stress. Zakharov *et al.* examined bulk FeRh under different hydrostatic pressure and showed an increase in transition temperature of 4.33 K bar^{-1} [47], while Wayne *et al.* observed a decrease of -2 K bar^{-1} for tensile stress [71]. Conversely, for epitaxial thin film, Maat *et al.* deposited FeRh on substrates with different lattice parameter. This lattice mis-match resulted in the FeRh film being clamped on its substrate and subjected to either in-plane compressive or tensile strain [70]. As FeRh has a magneto-structural phase transition, the importance of lattice parameter between FeRh and the substrate is fundamental. The MgO (Sapphire) substrate referred above resulted in respectively in-plane compression (expansion), and out-of-plane expansion (compression) respectively. Figure [1.9] is the magnetisation versus temperature curves for the 110 nm-thick FeRh grown on MgO- IP compression **(a)** or Al_2O_3 **(b)**- IP expansion. It is seen that the transition occurs at lower temperature on the Sapphire substrate. However, it was measured that the unit cell volume of the FeRh film was the same in the two substrates, implying that the transition is not primarily determined by the volume of the unit cell. Ceballos *et al.* further studied the influence

of FeRh thickness on the strain effect by growing films of thickness 10, 15, 22 and 100 nm on cubic substrates [72]. It was thus concluded that mismatch with the substrate causes lattice distortions and affect the transition features. In-plane expansion of the FeRh film stabilises the FM phase and reduced the transition temperature, while an in-plane compression stabilises the AFM phase, delaying the transition. Moreover, the abrupt nature for the 22 nm-thick film indicated that compressive lattice mismatch in thinner film actually suppresses the transition. These conclusions were confirmed by Xie *et al.* on several other oxides such as $SrTi0_3$, MgO and $LaAlO_3$ [53].

Influence of Dimension

Indeed, the amount (be it thickness or patterning) of FeRh undeniably influences the phase transition. Ko *et al.* investigated the transition temperatures and coercivity of $Fe_{39}Rh_{61}$ nano-particles with the average size of 3–5 nm, and demonstrated that finite sizing affect the cooling and heating branches differently [73]. Likewise, for 10 nm-thick nano-structures, the cooling branch was measured to be 3-4 times broader than the heating branch. This effect was seen as a resultant of a substantial increase in strain relaxation at the periphery of the nano-structures leading to strong lattice gradient with an AFM core and FM shell [73], [74]. Following on that, Uhlíř *et al.* patterned several FeRh films into varying width stripes of rectangular or square shapes and performed resistivity and reflectivity measurements on the latter [75]. It was observed that the stripes exhibit different behaviours when heated or cooled down. During heating, the electrical resistivity varied gradually with a broad transition, while for stripes ≈ 0.5 μm wide, the cooling resulted in sudden jumps in resistance. They explained this difference by the asymmetry in the long-range FM order that persists through disorder, while the short-range AFM order is easily hampered by defects or grain boundary effectively restricting AFM domain size. Similar results and confirmation of the asymmetry between the cooling and heating branches on the magnetisation was measured eventually [52]. Moreover, by varying and decreasing the FeRh patterns, it was observed that the coercive field increases, as the possible nucleation sites for magnetisation reversal decreases.

Hence, the ability to tune the magneto-structural transition of FeRh, by a variety of internal or external parameters, makes FeRh a rich source for studying the lattice, magnetic and electronic degrees of freedom on a fundamental base, but also holds promise for a plethora of technological applications. In the next section, the reader is introduced to the state of the art of possible technological applications using FeRh.

3 State of the art: Technological applications of FeRh

The concomitant magnetic, resistivity, lattice and entropic changes across the first-order phase transition, has attracted the attention of several scientists in using FeRh for diverse technological applications. In order to evaluate any possible applications, three different factors are to be considered. These include: cost and supply; integration; repeatability and predictability. Firstly, the high cost and scarcity of rhodium might hamper applications using high volume of FeRh material. Secondly, FeRh devices must show ease of integration with existing technologies or need to serve as foundational block for new technological framework. Finally, any FeRh applications must show resilience and repeatability in the input-output. Addressing these challenges is crucial for the successful implementation of FeRh in practical applications and ensuring that the material's unique properties can be fully leveraged for realistic applications.

Heat-Assisted Magnetic Recording Hard Disk Drive: HAMR-HDD

Since the beginning of the digital age, the amount of data generated, processed, and used by society keeps on increasing exponentially. Yet, 90% of the data are stored in data centres in the form of hard disk drives (HDD), as they still offer the lowest cost per terabyte of stored information [79], [80]. Mass storage is more important than ever, and companies big and small are in a race to monetise these precious information. Hence, the need to develop and deploy storage solutions that deliver optimal

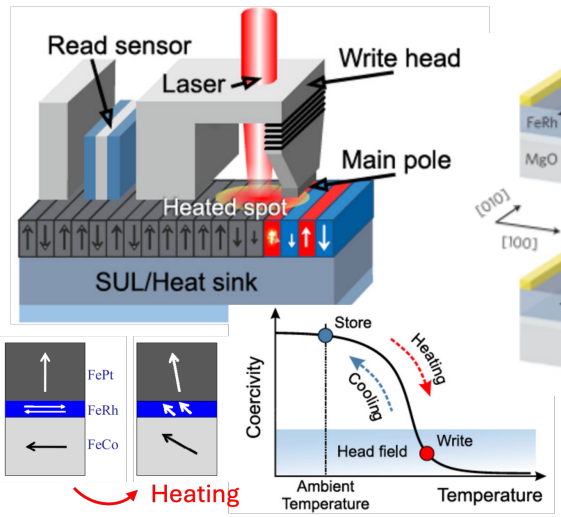

Figure 1.10: Top: Typical HAMR recording media. The laser heat the recording media to induce a phase transition. the recording is possible using the magnetic field and a rapid cooling. Adapted from [76]. **Bottom**: Influence of FeRh to reduce the coercivity due to exchange interaction with FePt in the trilayer configuration. Adapted from [77].

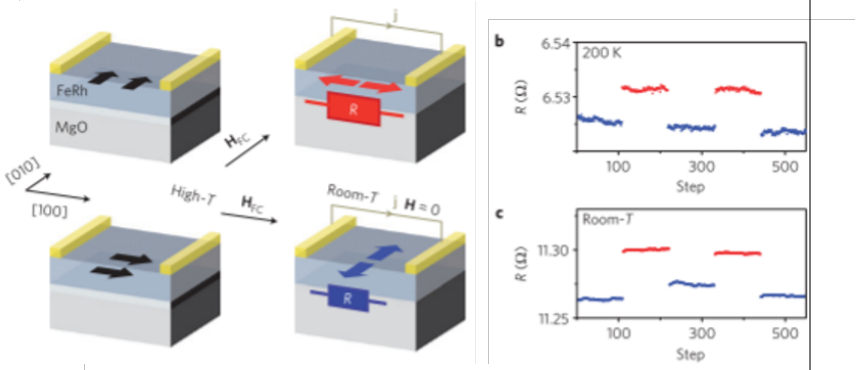

Figure 1.11: Schematic representation of the anisotropic magneto-resistance AMR memory. **(a)-(1-2)**: The magnetic field is applied in the High Temperature FM phase to align all the magnetic moments. **(a)-(3-4)**: Two routes are possible for writing and storing the information while cooling to the AFM phase, and depends on whether the magnetic field is applied parallel (red) or perpendicular (blue) to the AMR read-out current. A two-level system is thus possible both in the FM phase for coding, and the AFM phase for storing. **(b)-(c)**: Two stable values of resistivity are recorded at Room temperature and 200 K (pure AFM phase). Adapted from [78].

performance for the lowest possible cost and highest energy efficiency is a matter of paramount technological importance. As such, three important parameters are considered here: The write-ability and readability of the given information and the thermal stability of the storage system, i.e. data must be retained for long period of time so that it can be retrieved only when required.

One way to circumvent the influence of this magnetic recording trilemma, is to use Heat Assisted Magnetic Recording or HAMR. HAMR is seen as the future of information storing, as it is believed to extend the areal density from 1.2-1.5 Tbit/in^2 in commercial Perpendicular Magnetic Recording, PMR-HDD to up to 4 Tbit/in^2 [81], [82]. Conventional HAMR uses FePt as recording media, and a laser pulse is used to assist the writing in binary system, i.e. in "0" and "1" bits, by heating locally the media up to T_C[7], followed by a rapid thermal cooling. By heating the media, its coercivity is reduced making writing easier. As the FePt cools down, the coercivity increases back and sufficient thermal and magnetic stability is recovered for information storage. Figure [1.10]-**Top** is a representation of the HAMR head and media, laser heated spots and the FePt media. However, such high Curie temperature and thus high writing temperature poses significant challenges. Consequently, Thiele *et al.* proposed adding an additional FeRh layer, and harness its near room temperature phase transition instead [83]. Figure [1.10]-**Bottom** is the proposed FePt/FeRh bilayer as the composite HAMR media. In this configuration, the FeRh AFM state stabilises the FePt layer via exchange bias, while the FM phase has shown to reduce the HAMR coercivity by eight-fold following the transition [46], [76], bypassing the high Curie temperature. Recently, Zhou *et al.* further developed the concept and proposed an exchange switchable FePt/FeRh/FeCo trilayer with higher heating efficiency [77].

Anisotropic Magneto Resistance- Magnetic Random Access Memory: AMR MRAM

The need of a two-level system for coding information as "0" and "1" bits was stabilised by the magnetic energy barrier between the up-magnetised and down-magnetised domains in HAMR. An alternative way is to use the change in electrical conductivity accompanying the FeRh first-order phase transition. The existence of a field-stabled anisotropic magneto-resistance, AMR, was demonstrated in the

[7] The Curie temperature of FePt is ≈ 600°C.

FM and AFM phases of FeRh [78], [84]. AMR[8] is the physical phenomenon whereby the electrical resistivity of a magnetic material depends on the orientation of the magnetic field with respect to its crystallographic structure. Using a high epitaxial biaxial anisotropy FeRh grown on MgO system, Marti *et al.* demonstrated a two-level system based on AMR [78]. In other words, they showed that information can be written onto two perpendicular directions in the FM phase, which will then be stored onto two perpendicular directions in the AFM phase. Figure [1.11] is a schematic illustration of the FeRh AFM-AMR resistor memory functionality in a writing and reading configuration. Starting in the AFM phase, the resistor is first heated above the transition temperature to the FM phase. A large external magnetic field is then applied, so as to align all the magnetic moments parallel to the field. Note here, that two perpendicular directions are possible owing to the cubic symmetry of the 100 nm-thick FeRh grown on MgO. Fig. **(c)** shows the two AMR read-out states in the FM phase. The resistor is then field-cooled to the AFM phase. Depending on which directions of the applied field is chosen, the canting effect of the magnetic moments when reaching the AFM phase gives two orthogonal directions[9] having slightly different resistance level, as shown on **(b)**. This difference in resistance level is due to the AMR effect, whereby the magnetic moments are parallel or perpendicular to the electrical current. A maximum of 1.8% and 1.4% in AMR values in the FM and AFM phases respectively were measured, while retaining repeatability. Moreover, as the AFM phase has no net magnetisation, the memory resistor model was field-resistant up to 9 T which set up a reliable precedence for operational AFM memory storage.

However, to perform the writing, there is a need to heat the FeRh/MgO sample to temperatures above the AFM-FM transition, in this case around 400°K. This can be be a major obstacle for technological integration. The following year, Moriyama *et al.* established a step-by-step prototype for the write-read operations for a FeRh-based AFM memory avoiding the need to change the external temperature [85]. As a matter of fact, the AFM-to-FM transition was assisted by the Joule heating of the resistor for a current up to 12 mA [86]. Then using the same applied field and cooling procedure, they obtained a two-level MRAM-type sequence based on anisotropic magneto-resistance. The stability of the sequence was verified and tested with satisfactory results over 50 cycles. As such, the FM phase serves as a means to write the information, while the AFM phase can be seen as storing or hiding that information thanks to its net zero magnetisation.

Electric-field driven strain control of magnetism

Previously, it has been demonstrated that pressure, influences greatly the transition with in-plane compressive strain stabilising the AFM phase and tensile strain the FM phase respectively. Cherifi *et al.* [87], Bennett *et al.* [88], Chen *et al.* [89] and Liu *et al.* [90], investigated the possibility to control, modulate and enhance these effects. Epitaxial FeRh films were deposited on different piezoelectric substrates, such as $BaTiO_3$ and PMN-PT. Applying an electric field on piezoelectric materials causes the substrate to be deformed, and in so doing induces additional strains on the FeRh deposited layer.

Figure [1.12] is the voltage or electric field[10] dependence of the magnetisation of a 22 nm-thick FeRh layer grown on $BaTiO_3$. Note the reversible butterfly-type shape of the magnetisation. By applying an electric voltage, the magnetisation decreases. For small electric voltage values, a giant change of magnetisation can be observed: $\approx$ 20% for 20 V [87]. The inset is the resistivity versus temperature curves for zero and non-zero electric field value. An increase of the transition temperature is observed for the non-zero electric field. More precisely, a 26 K increase was measured for an electric field value of 2 kV cm^{-1} [90]. This 2 kV cm^{-1} resulted in an FeRh unit cell volume variation as large as $\approx$ 1.13%. This breakthrough created opportunities for electric AFM-to-FM induced transition, leading to on-off switching of FM state for low-energy Random-Access Memory applications [91].

[8] AMR = $\frac{\rho_{\parallel}-\rho_{\perp}}{\rho_{\parallel}}$, where $\rho_{\parallel}$ and $\rho_{\perp}$ are respectively the resistivity for the spin axis parallel or perpendicular to the current.

[9] This direction is known as the Néel Vector. In an antiferromagnetic material, the Néel vector, $\vec{L}$ is defined as: $\vec{L} = \vec{M}_1 - \vec{M}_2$.

[10] $\mathbf{E} = -\nabla \cdot V$

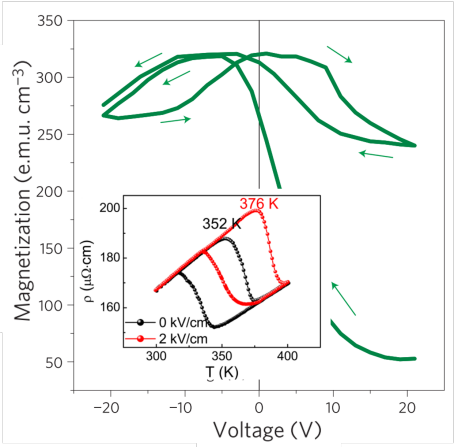

Figure 1.12: Magnetisation dependence on electric voltage for a 22 nm-thick FeRh grown on BTO at a temperature of 385 K. Adapted from [87]. **Inset**: Thermal dependence of resistivity across the phase transition for two electric field values, for a 35 nm-thick FeRh on BTO system. The piezoelectric strains triggered by a 2 kV cm^{-1} electric field value results in an increase of the magneto-structural phase transition temperature by 26 K. Adapted from [90].

Control of the AFM-FM transition using optical pulses

Likewise, Mei *et al.* reported an approach of leveraging photo-thermal effects to manipulate magnetic patterns in FeRh across the magnetic phase transition [92]. This work hopes to offer a novel approach to control ferromagnetic structures and patterning. Figure [1.13] is the Photo-thermal Nernst[11] experimental observation of an on-demand, write and read sequence on a 35 nm-thick FeRh grown on MgO. Starting at room temperature in the AFM phase, a high-fluence laser is used to heat locally the FeRh layer. By controlling the laser pulse duration, energy, and focus, precise patterns of FM regions can be written onto the AFM background. These patterns can be of arbitrary shapes and sizes, allowing for high-resolution magnetic patterning. The written FM regions can be erased by cooling the material below room temperature, causing the FeRh to revert to its AFM state. The use of optical pulses to control the AFM-FM transition in FeRh represents a significant advancement in magnetic material manipulation. The precise, reversible, and high-resolution control enabled by the laser pulses, at the nanometre scale, opens up new possibilities for applications in data storage and advanced magnetic devices, making FeRh a model material for testing future technological developments.

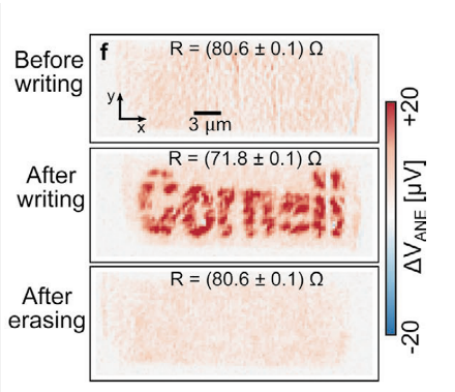

Figure 1.13: Images showing the sub-micronic ultrafast patterning of the FeRh sample. Single pulses of 14 mJ/cm^2 enough to induce phase transition. This writing can be fully erased by cooling the sample and no discernible damaged can be seen after erasing. [92]

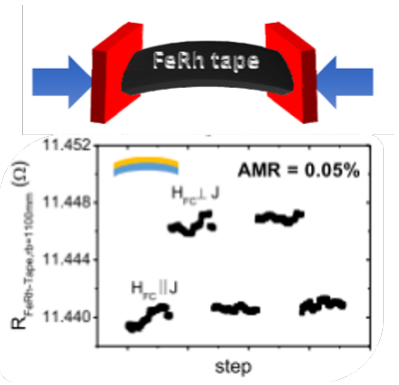

Figure 1.14: Sketch of the flexible FeRh-Tape structure grown on a Hastelloy™tape previously buffered with a MgO- textured layer. A resistance contrast, similar to Marti *et al.* model is visible when applying the magnetic field, illustrating the data storing ability and bending resistance. The FeRh tape showed no significant damage after 100 bending cycles. [94]

[11]The Nernst effect is a thermo-electric phenomenon whereby a transverse electric field is generated perpendicular to both an applied temperature gradient and a perpendicular magnetic field in a conductive material.[93]

Flexible AFM-FM memory tapes

Finally, a much more surprising application of FeRh is the integration of FeRh films onto flexible substrates, such as MgO-coated Hastelloy™[12] tapes as developed by Fina *et al.* [94]. Figure [1.14]-**Top:** shows an FeRh layer grown on a Hastelloy™layer. Here, they have demonstrated that FeRh films on flexible tapes can endure significant bending without losing their magnetic integrity. Using Scanning Electron Microscopy (SEM) measurements, no significant damage was observed on the 57 nm × 25 mm × 12 mm, even after 100 bending cycles. Figure [1.14]-**Bottom:** illustrates the resistance measured for a bent FeRh-tape while a current is applied parallel (low resistance state) or perpendicular (high resistance state) to the magnetic field. The difference in resistance showcases the data storing capabilities of of FeRh on flexible substrates and opens the perspective of application in flexible electronic devices, such as wearable technology.

Discussion

As developed throughout this chapter, FeRh is a fascinating material known for exhibiting a first-order magnetic phase transition. Several groups, have acted on this phase transition in order to harness the properties of FeRh. As seen, these typically involved applying a magnetic field, changing the chemical composition, patterning or voltage-controlled static strain. However, the effect of dynamic strain fields is in reality untapped and offer a promising avenue for controlling the magneto-structural phase transition of FeRh. This is explored in this manuscript. Here, dynamical strains in the form of Surface Acoustic Waves (SAWs) and at sub-GHz frequencies are generated using piezoelectricity. Relying on magneto-striction, which is the coupling between strains and magnetic moments, we aim to act on the magnetic phase transition. This effect, could allow for both anisotropic and volume magnetostrictive effects, as well as an exploration of the interaction of strain with the AFM and FM phases and/or AFM-FM domain walls. Furthermore, we leverage the potential of SAWs and explore the possibility of SAW-Ferromagnetic Resonance (SAW-FMR). This involves matching the frequencies of SAWs to the spin-wave (SW) frequencies of the FeRh layer. The extreme sensitivity of f_{SW} and of the magneto-elastic torque is investigated, both experimentally and numerically.

Chapter Summary

1. FeRh undergoes a magneto-structural phase transition from the low-temperature AFM phase to the high-temperature FM phase.

2. Across the phase transition, the cubic structure is conserved but is accompanied by an increase of 1% of the unit cell volume and an increase of 0.7% for the out-of-plane lattice parameter for FeRh thin films (generally epitaxial).

3. The presence of an external magnetic field around the transition temperature disrupt the AFM order, while favouring the FM order. Similarly, in-plane expansion of the FeRh film stabilises the FM phase and reduce the transition temperature, while an in-plane compression stabilises the AFM phase, delaying the transition.

[12] Hastelloy™is a term used to describe nickel metal that has been alloyed to increase resistance to corrosion.

Chapter 2

Samples, Characterisations, Electrical and Optical experimental setups

Objectives

This chapter outlines the experimental techniques and samples used in this thesis. Detailed descriptions of the growth processes, properties, and characterisation methods for Crystalline Sample A (FeRh/MgO) and Polycrystalline Sample B (FeRh/GaAs) are presented. This enables the reader to appreciate the specific methods and conditions required to achieve the crystallographic and magnetic properties. The reader is then introduced to the magneto-optical techniques such as Magneto-Optic Kerr Effect (MOKE) and Magnetic Linear Dichroism (MLD); as well as to the various experimental setups used for characterising the samples with respect to magnetic field and temperature. These are essential for the subsequent data analysis chapters.

Contents

1 Fabrication of FeRh samples

As described in the previous chapter, the existence of the AFM-to-FM magneto-structural phase transition depends on the chemical composition of the FeRh alloy. Historically, bulk FeRh samples were obtained either by melting Fe and Rh cores together at fusion temperatures $\approx$ 1500°C [45], [47], or by chemical reduction under hydrogen gas [42], and cooled near room-temperature for the appearance of the AFM phase. In the late 60s, R. C. Wayne discovered the influence of thermal treatments on the first-order phase transition [71]. These included annealing, i.e. heating the FeRh material to high temperatures $\approx$ 400-700°C, to relieve residual fusion stress and promote crystallisation, followed by either slow cooling or rapid quenching. Around the same time, J. M. Lommel experimented with the preparation of FeRh films using different techniques such as alternate layer deposition, co-deposition and sputtering [95]. Further research on FeRh thin films fabrication showed the importance of the annealing process for the formation of the ordered CsCl-type FeRh crystalline structure [37], [96]. These can be summarised as follows. Annealing of FeRh thin films improves crystallographic structure and micro-structures. Larger grains can lead to a more uniform phase transition, while smaller grains introduce more pinning sites that hamper domain wall motion. Furthermore, annealing reduces magnetic hysteresis, promotes sharper and well-defined phase transitions and can fine-tune the transition temperatures. However, although annealing is a critical parameter in the fabrication of FeRh layers, it will not be the focus of this chapter. Instead, the discussion will revolve around the crystallographic nature and subsequent characterisation of the two samples used in this manuscript. The two samples are: (*i*) a crystalline 50 nm-thick FeRh grown on MgO (001) substrate, denoted as **Crystalline Sample A: FeRh/MgO** and (*ii*) a polycrystalline 270 nm-thick FeRh grown on GaAs (001) substrate, denoted as **Polycrystalline Sample B: FeRh/GaAs**. The project was initially based on high quality crystalline FeRh/MgO samples. However, the lack of readily available epitaxial samples (as per the Ph.D. project), for testing lithographic protocols for SAW generation, prompted an alternative growth on GaAs at the INSP. This polycrystalline FeRh/GaAs reduced the lithography steps for achieving SAW devices from 7-to-1, although reorienting the whole Ph.D. work from SAW-driven FeRh-based magnetic coding and spin-pumping phenomena. Below is described the growth and characterisation of the two samples. Schematic representations and summaries of every experiment undertaken on either sample are presented at the end of this section.

1.1 Growing method: Magnetron Sputtering

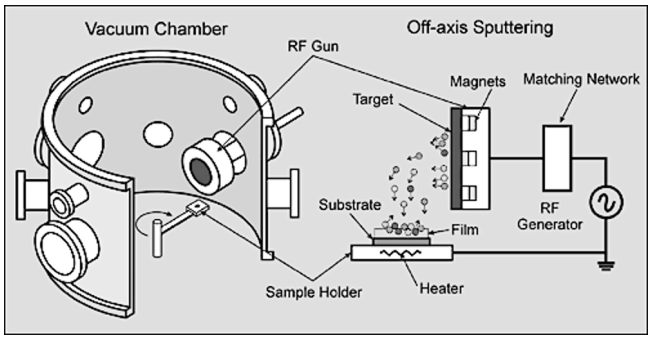

Figure 2.1: Magnetron sputtering machine. The target and substrate are placed in a vacuum chamber where argon gas is introduced. The power supplies used in magnetron sputtering can be categorised as DC or RF, among others. Here is represented the RF source, which when the RF power is applied, creates a plasma that sputters atoms from the targets onto the substrate. This method allows for precise control over the deposition rate and film thickness. Adapted from [97]

Although the growth were performed at two different locations, as discussed below, the two samples were fabricated using the same growth technique, which is the magnetron sputtering. Figure [2.1] is a schematic representation of the sputtering technique. The Fe and Rh targets or an FeRh target and the substrates (MgO or GaAs) are placed in the sputtering chamber, and the latter is filled with a gas (typically Argon) at a low base pressure $\approx 10^{-4} - 10^{-3}$ mbar, to remove air and contaminants. The substrate is placed opposite the target(s). When a high power (50-100 W) is applied to the target, a

potential difference ionises the argon gas, creating a plasma. The plasma is confined near the target by a magnetic field, which enhances ionisation and sputtering efficiency. High-energy argon ions bombard the target, ejecting atoms that travel through the chamber and deposit onto the substrate, forming a thin film. This increased plasma density, in contrast to conventional sputtering, leads to higher quality in the FeRh thin film deposited. Typical deposition rates are between 0.03 nm/s on MgO [49], to 0.07 nm/s for GaAs [98]. Note that the GaAs and MgO substrates were respectively at room temperature and 450°C during deposition. Following the sputtering process, the two samples were annealed at high temperatures ≈ 780°C for 60 min (MgO) or 90 min (GaAs).

1.2 Crystalline Sample A: FeRh/MgO

The nominal 50 nm-thick epitaxial FeRh grown on MgO (001), was prepared by J. Arregi and V. Uhlíř at the CEITEC facility[1] in the Czech Republic, using DC magnetron sputtering. A 1.5 nm-thick Pt capping layer was deposited after cooling down the sample below 120°C as a protective layer against oxidisation. Figure [2.2] is the θ-2θ X-Ray diffraction, XRD scans **[(a)]** and X-Ray Reflectivity, XRR scans **[(b)]** of a typical crystalline sample grown by this group. These data were provided by CEITEC or adapted from [52]. The XRD scan for FeRh/MgO shows high texture quality. The well-defined and high intensity FeRh (001), (002), and (003) peaks, indicate that the FeRh film has a high degree of crystallinity and that the atoms are well-ordered in a regular lattice structure. Moreover, the presence of only these (00l) diffraction peaks without additional, unexpected signal suggests that the film is highly oriented with B2 symmetry. This means that the FeRh film is growing epitaxially on the MgO substrate with its out-of-plane [001] coinciding with the MgO [001] axis, and its [110] axis coinciding with the in-plane [100] MgO axis. The XRR scans, on the other hand, reveals a planar uniform growth of the FeRh layer. Using $d = \lambda_{XRR}/(2\Delta\theta \cos\theta)$, and $\lambda = 1.54$ nm, the FeRh thickness was calculated to be 47 nm.

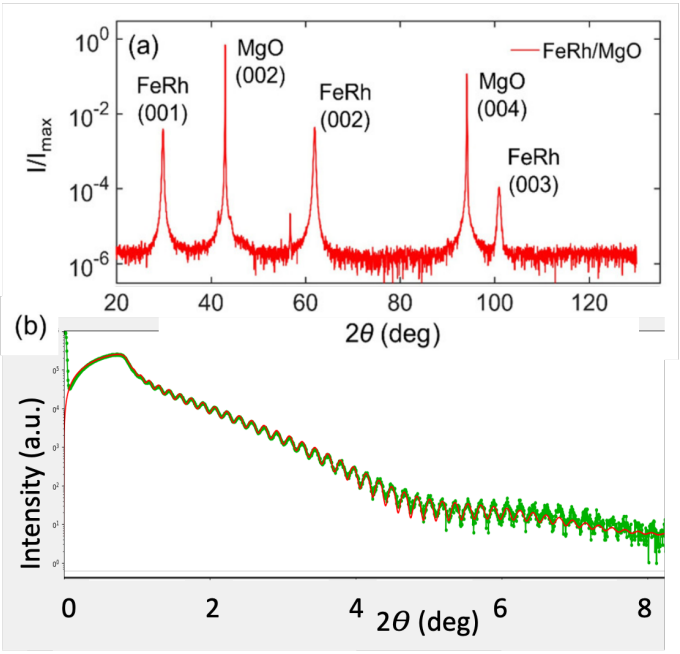

Figure 2.2: **(a)**:Typical XRD scan of a 50 nm-thick FeRh on MgO sample. Clear and sharp diffraction peaks are observed showing a high quality epitaxial growth. Adapted from [52]. **(b)**: XRR scans showing smooth planar growth surface of the FeRh layer. From this data, it can be calculated that the FeRh layer is 47 nm-thick. (Courtesy J. Arregi)

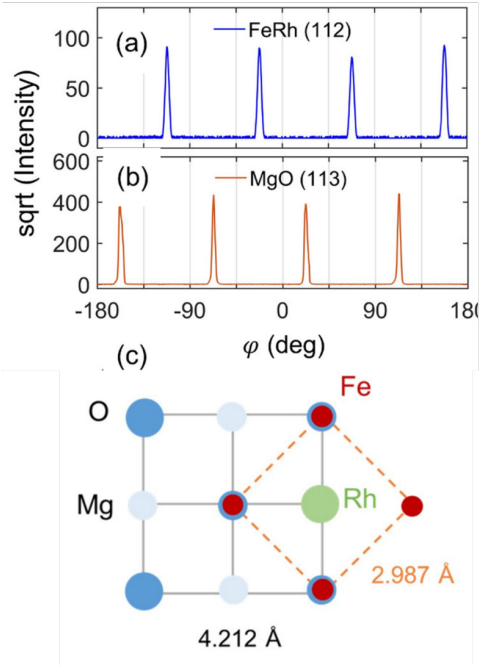

Figure 2.3: **(a-b)** Azimutal XRD scans performed on FeRh and MgO while rotating the sample. There is a clear 45° angular shifts between the diffraction peaks. This is a signature of a 45° in-plane rotation of the lattice for the FeRh growth on MgO. **(c):** Schematic representation of the film and lattice unit cells and the lattice parameter matching. Adapted from [49].

[1] CEITEC BUT, Brno University of Technology, Purkyňova 123, 612 00 Brno, Czech Republic

Figures [2.3][**(a-b)**] represent the ϕ-XRD scans, also known as azimutal scans [49]. These are obtained by monitoring the MgO(113) and FeRh(112) diffraction peaks while rotating the sample. A clear 45° shift is observed between the FeRh film and the MgO substrate. This rotation is explained by the epitaxial lattice matching. B2 FeRh has a lattice parameter of $\approx$ 2.98Å as seen on figure [1.7] and epitaxial MgO has a lattice parameter of $\approx$ 4.2Å. In order for the FeRh lattice parameter to match that of the substrate, it grows at 45° to the MgO. As such, for the 50-nm thick layer, the lattice mismatch between the FeRh and MgO is reduced to 0.3% only [52]. Figure [2.2][**(c)**] is a representation of each atom in the FeRh-MgO compound, and the rotation of the crystal structures between the FeRh and MgO layers. Similar rotation of 45° of the FeRh lattice has been observed on $SrTiO_3$ [53].

1.3 Polycrystalline Sample B: FeRh/GaAs

Despite the high epitaxial growth quality of FeRh on MgO, the lack of sufficient epitaxial FeRh/MgO samples, prompted a re-orientation of the PhD on alternative substrates. Piezo-electricity refers to the ability of materials to generate an electric charge in response to applied mechanical stress; this phenomenon will be thoroughly explained in Chapters [4] and [5]. Al_2O_3 (sapphire) emerged as a suitable candidate due to its compatible lattice parameters, as noted in prior studies [52], [70]. However, neither magnesium oxide nor sapphire exhibit piezoelectric properties, which are essential for the generation of acoustic waves. To overcome this limitation, it was proposed to use a piezoelectric substrate. Gallium Arsenide (GaAs) was chosen for this purpose, as it had previously been used bythe lab and for its good acoustic properties [24], [26]. This choice allowed for the direct generation of acoustic waves without the need for additional piezoelectric coupling layers.

The growth of FeRh on GaAs was undertaken by D. Nguyen (during his Post-doctoral contract), and L. Thevenard at the INSP. Since the existence of the AFM-to-FM phase transition depends strictly on a near equiatomic concentration of Fe and Rh elements, and since an equi-atomic FeRh target was not available, a particular technique called graded composition growth was chosen and the growth was possible using the magnetron sputtering machine described above [99]. This method involves creating a gradient in the stoichiometry, typically from iron-rich to rhodium-rich, across the length of the FeRh film grown over the GaAs wafer. To obtain a graded composition of a FeRh film, a 25×55 mm^2 Rh foil is placed over half of a 75 mm diameter Fe target. This ensures that different parts of the sample see different ratio of Fe and Rh during the sputtering process. As such, several samples should have the correct chemical composition for the phase transition to occur.

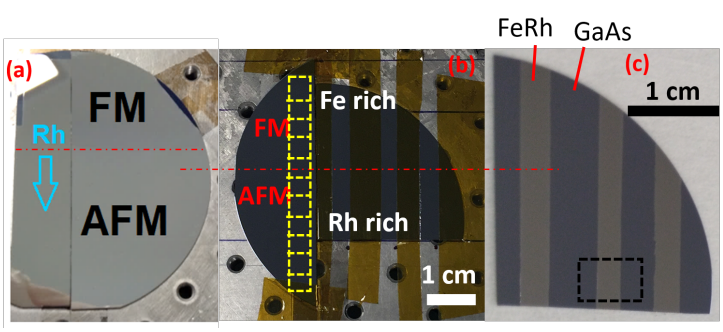

Figure 2.4: Graded composition growth: (a) Difference in reflectivity at room temperature, for the graded composition sample going from top-higher Fe concentration to down-higher Rh concentration, evidencing the transition from FM to AFM phase. This is a 2" wafer. (b) Graded composition growth with the Kapton tape for shadow masking. This allows to have vertical strips regions of GaAs only and FeRh/GaAs. (c) Dotted black rectangle represents the Sample B used in the manuscript. The yellow boxes are smaller samples used for magnetometry measurements.

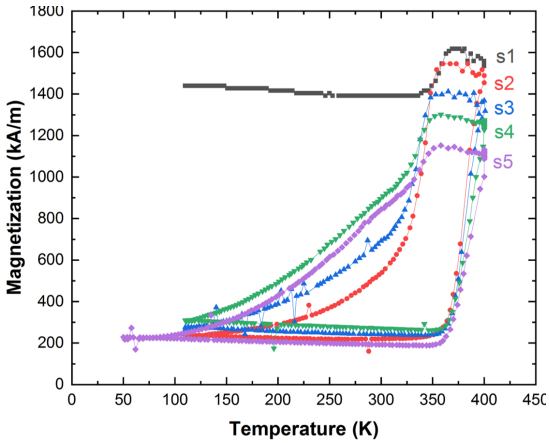

Figure 2.5: Magnetometry measurements on the different yellow boxes. The top-most box, of fig. [2.4]**(b)**-denoted here as S1 always exhibit FM phase, while the thermal asymmetry is present for all samples. Note the residual ferromagnetic fraction still present at very low temperature, in the AFM phase.

Figure [2.4] are images of 3 different FeRh/GaAs substrates at room temperature. On fig. **(a):** a clear

difference in reflectivity is seen on the figure between the part of the sample exhibiting FM phase, and the part exhibiting AFM phase at room temperature. As the Rhodium concentration varies vertically, different parts of the grown FeRh have different magnetic phases at room temperature. AFM and FM phases of FeRh have different electronic band structures and thus different reflectivity [100]. Fig. **(b)** represents the GaAs substrate used in this manuscript. Here, to avoid a lithography etching step, part of the sample is masked with a Kapton tape. This leaves the masked area of the GaAs wafer free of the FeRh layering. Following the growth by sputtering, stripe regions of GaAs and FeRh/GaAs are thus obtained, as shown on the fig. **(c)**. Interdigitated Transducers (IDTs) - used to generate Surface Acoustic Waves (SAWs) - are then deposited on the piezoelectric GaAs parts (this will be discussed in more details in chapter [4]. The dotted black rectangle represents the sample denoted as Polycrystalline Sample B: FeRh/GaAs, used in the rest of the manuscript. It has a dimension of 10×5.6 mm^2, with the horizontal length of the FeRh part ≈ 3.3 mm. The yellow boxes are smaller 2.5 mm square FeRh test samples with different Rh concentrations used for magnetometry measurements. Figure [2.5] shows the different VSM measurements for the different FeRh test samples, represented by the yellow boxes previously. For S1 (the highest yellow box in fig. [2.4-**(b)**], the sample remains in the ferromagnetic phase down to 100 K. The other samples show a very asymmetric thermal hysteresis, with an antiferromagnetic phase at low temperatures, albeit a significant residual magnetisation ≈ 200 kA/m. This might be related to the thickness of the FeRh layer. Here, the FeRh is 270 nm-thick. One reason might be that the top or bottom layers remain in the FM phase at all temperatures. For the former this might be due to dead AFM layers close to the top, resulting in the top-most layer being independent of adjacent AFM exchange interactions, while for the latter, this might be a result of the consequent lattice mis-match between the FeRh ≈ 2.98 Å and the GaAs substrate ≈ 5.65 Å. Likewise, it might be that over the 270-nm FeRh, the vertical Rh concentration varies, resulting in part of the layer not having the correct stochiometry for the existence of the AFM phase. The further away are the yellow boxes from the Fe-rich region, the more asymmetric is the thermal hysteresis. Nevertheless, this difference in lattice parameter prompt the FeRh to be polycrystalline.

XRD scans were performed at the INSP by J.-E. Duvauchelle, D. Nguyen and Y. Zheng and are represented on figure [2.6]. Several peaks corresponding to FeRh, Ta, and GaAs are identified, with the GaAs substrate peaks being prominent at GaAs (002) and (004), indicating that the substrate is crystalline. The presence of several FeRh peaks, not multiple of each other with non-zero (hk0) Miller planes, indicates a polycrystalline nature for this FeRh film. This crystal structure is due to a too large lattice mismatch between FeRh and GaAs ≈ 5.65 Å. The resulting FeRh layer is therefore non-epitaxial and relaxed. Additional in-plane and out-of-plane rocking XRD scans concluded that no preferred texture was visible, either in the plane or out-of-plane, meaning the 270-nm-thick FeRh grown on GaAs was purely polycrystalline.

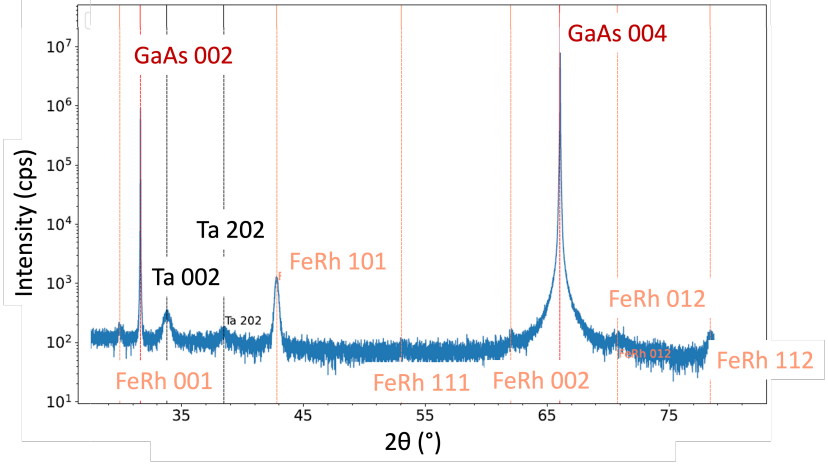

Figure 2.6: XRD scans of the FeRh grown on GaAs substrate. Several low intensity broad diffraction peaks are visible for the FeRh, accompanied with high intensity sharp peaks for GaAs. The substrate is well-ordered and crystalline, but the FeRh film does not inherit this crystalline quality.

During the growth process, an additional layer of 100 nm-thick Tantalum was deposited between the FeRh and GaAs layers, in order to prevent intermixing of Fe and Ga and the appearance of FeGa [101]. In the rest of the manuscript, the sample used out of the graded composition growth, matches to the S2 of fig. [2.5]. The Rhodium concentration varies parallel to the Kapton-generated FeRh/GaAs strips.

1.4 Static magnetic characterisation of FeRh samples

Magnetisation versus temperature curves were taken using a SQUID (Superconducting Quantum Interference Device) Magnetometer. Figure [2.7] represents the M-T curve for the crystalline 47 nm-thick FeRh grown on MgO, while fig. [2.8] gives the M-T curve for the polycrystalline FeRh grown on GaAs. Starting on the left, the AFM-FM phase transition is relatively sharp, symmetrical and occurs over a narrow temperature range of ≈ 50°C both for the heating (red) and cooling (blue) curves. The warming and cooling branches are centred around 80°C and 60°C respectively. The magnetisation saturates for temperatures above 100°C with a magnetisation of ≈ 1100 kA/m. On the other hand, the AFM phase is recovered for all temperatures below 20°C. A residual magnetisation of ≈ 90 kA/m is present in the AFM phase. This implies that a small residual part, ≈ 8%, of the FM layer at low temperatures.

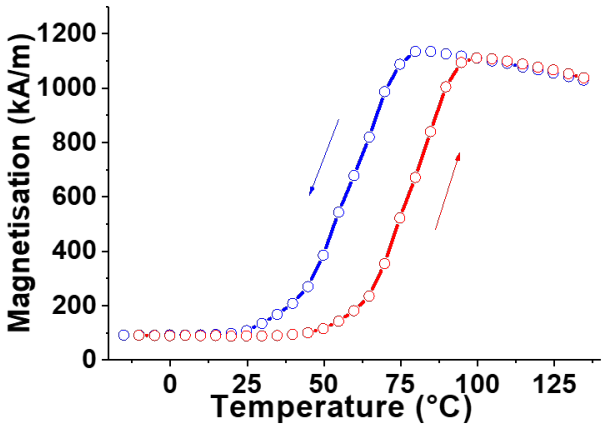

Figure 2.7: VSM measurement on Crystalline Sample A: 47 nm-thick FeRh grown on MgO. Fabrication courtesy of J. Arregi and V. Uhlíř, CEITEC

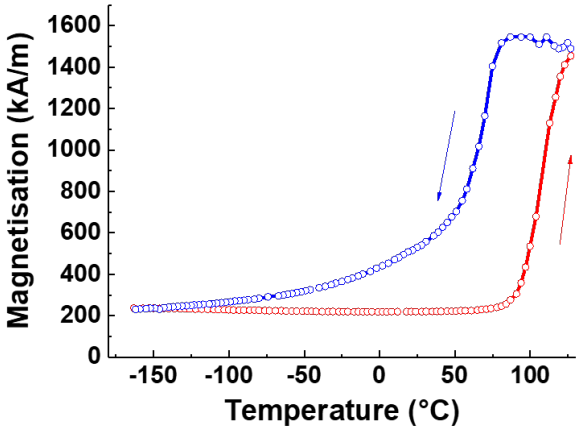

Figure 2.8: SQUID measurement on Polycrystalline Sample B: 270 nm-thick FeRh grown on GaAs. Fabrication courtesy of D. Nguyen at the INSP

For the polycrystalline FeRh, a huge asymmetry is present between the heating and cooling ramps. The hysteresis loop is also wider, indicating a more gradual and possibly more heterogeneous phase transition. This is characteristic of its polycrystalline nature and the presence of multiple grains and defects. For the heating ramp, the transition begins at 80°C, with 104°C the temperature midway through the transition. On the cooling ramp, the transition begins around 80°C, and reaches AFM phase at -110°C. The saturation magnetisation at high temperature is ≈ 1500 kA/m, while the residual magnetisation in the low-temperature AFM phase is ≈ 230 kA/m, which accounts for ≈ 15% of the AFM layer still in the FM phase. The first reason for the broad asymmetry may be defects or grain boundaries, that make the transition more gradual. The second one might be related to the fabrication process. As the Rh concentration is varied, it might be that part of the layer does not have the correct stoechiometry for the AFM phase to exist. Moreover, the 270 nm thickness of the FeRh film on GaAs means there is a greater volume of material, potentially leading to more significant variations in the rhodium concentration over the thickness of the layer, compared to the thinner 50 nm film on MgO. Thicker films can support more complex domain structures, with larger and more varied domains contributing to the asymmetry [102], [103].

1.5 Schematic representation of the two patterned FeRh samples

The two patterned FeRh samples are schematically represented on figure [2.9]. As will be discussed in the following chapters, this thesis revolves around the interaction and resonance of Surface Acoustic Waves (SAWs) with Spin Waves (SWs). In order to generate the SAWs, Interdigitated Transducers (IDTs) are lithographically deposited onto piezoelectric substrates. Fig. **(a)** shows the Crystalline Sample A: FeRh/MgO. Note that the MgO substrate is not piezoelectric. Hence, an additional 200 nm-thick piezoelectric Zinc oxide (ZnO) layer is sputtered onto a 50 nm-thick SiO_2. This additional Silicon Dioxide layer is used to assist the growth of ZnO onto MgO. Note that the ZnO layer is removed for the SAW propagation path between the 2 IDTs. The resulting SiO_2 layer covering the FeRh film, thus acts as an anti-reflective coating which increases ($\nearrow$ 5%) the optical contrast between the AFM and FM phases. This increases the contrast for reflectivity was measured and calculated by A. Chavatte during his M1 internship (2020). The complete fabrication process is listed below, resulting in a minimum of 7-different fabrication steps:

CEITEC, Czech Republic
1. Sputtering of FeRh on the MgO.

INSP, France - Courtesy of L. Becerra
2. Dry-etching of the FeRh layer to obtain a central mesa.
3. Deposition of SiO_2 layer.
4. Deposition of ZnO layer.
5. Etching of ZnO.
6. Deposition of transport Ti/Au contact (not shown).
7. Deposition by IDTs

On the other hand, the fabrication process of the Sample B, consists of a single step, and is represented on the fig. **(b)**. Indeed, as GaAs exhibits piezoelectric properties, the IDTs are deposited directly onto the GaAs substrate, in an FeRh free region (regions covered by the Kapton tape c.f. fig. [2.4]).

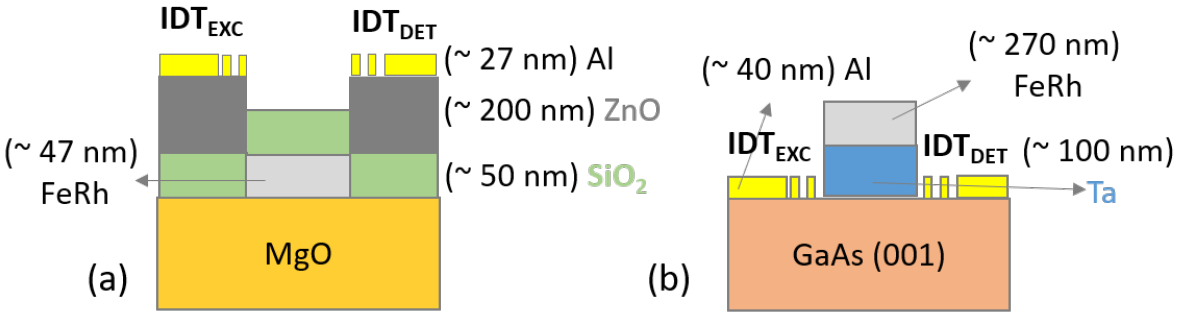

Figure 2.9: Schematic representation of the Sample A and Sample B, respectively grown on MgO and GaAs. For Sample A, denoted by **(a)**, the Interdigitated Transducers are deposited on a piezoelectric ZnO layer, which in turn grows on a SiO_2 layer. This 3-layers configuration is necessary to be able to generate surface acoustic wave on the magnetic FeRh layer, as the MgO substrate is non-piezoelectric. The 47 nm-thick FeRh layer is grown directly on the MgO, resulting in a 45° rotation in lattice structure for better lattice parameter matching. Note, A. Chavatte has previously measured that the absence of the ZnO layer on top of the FeRh layer, improve the reflectivity between the AFM and FM phases by 12%. For Sample B, the GaAs substrate is piezoelectric. Hence, the IDTs are deposited directly on the GaAs substrate. This reduces the number of fabrication steps and the number of different layers, but the FeRh layer is now polycrystalline. Note that the 270 nm-thick FeRh layer is grown on top a 100-nm thick Tantalum layer to prevent the mixing of Fe and Ga into FeGa.

Here, a summary is provided of each experiment performed on either sample, as they will be encountered by the reader in this manuscript.

Crystalline Sample A: FeRh/MgO

1. **Reflectivity measurement to investigate the AFM-FM domains**
   ⇒ Evaluate the typical domain size on a crystalline FeRh sample (c.f. Chapter [2]).
2. **Magnetic-Linear Dichroism (MLD) to determine the direction of the in-plane easy-axis**
   ⇒ Discriminate beween two contradictory results found in the literature: one giving an easy axis along <100> and one along <110> (c.f. Chapter [2]).
3. **Measurement by Brillouin Light Scattering (BLS) and Picosecond acoustic**
   ⇒ Determination of the elastic constants of FeRh in the AFM and FM phases. (c.f. Chapter [4]). Note that this was undertaken by D. Ourdani (Post-Doc) on a 200 nm-thick FeRh on MgO sample (not illustrated in this manuscript).
4. **Farnell-Adler model of SAW propagation on the SiO_2/FeRh/MgO tri-layer**
   ⇒ Mathematical model and numerical resolution of a SAW propagation and SAW dispersion on the tri-layer system for a propagation along the [100] direction of MgO for crystalline FeRh using BLS and picosecond data (c.f. Chapter [4]).
5. **Electrical SAW generation on FeRh thin films (c.f. Chapter [4])**
   ⇒ First experimental evidence of all-electrical generation and detection of Surface Acoustic Waves (SAWs) on FeRh thin films (c.f. Chapter [4]).
6. **SAW-assisted magnetic phase transition**
   ⇒ Investigation of whether SAWs can influence the AFM-FM transition temperatures (c.f. Chapter [6]).

Polycrystalline Sample B: FeRh/GaAs

1. **Longitudinal Magneto-Optical Kerr Experiment (L-MOKE)**
   ⇒ Investigation of the coercive field (c.f. Chapter [2]), remanence and the ferromagnetic domains (c.f. Chapter [7]).
2. **Farnell-Adler model of SAW propagation on the FeRh/Ta/GaAs tri-layer**
   ⇒ Mathematical model and numerical resolution of a SAW propagation and dispersion on the tri-layer system for a propagation along the [110] direction of GaAs for Polycrystalline FeRh (c.f. Chapter [4]).
3. **Probing the AFM-FM phase transition using SAWs**
   ⇒ SAW amplitude attenuation and velocity variation are measured across the phase transition with aim to look for interaction and/or investigate the transition (c.f. Chapter [6]).
4. **SAW-FMR measurement for different orientation of the magnetic field**
   ⇒ Investigation of the SAW-FMR interaction for the magnetic field applied parallel to the direction of propagation of the SAW and for different angular directions (c.f. Chapter [7]).
5. **Discussion and modelling of SAW-FMR interaction**
   ⇒ Presentation of a complete Mathematical model and numerical resolution for the SAW-FMR interaction with aim to understand the measured experimental data, while taking into consideration the presence of magnetic hysteresis (c.f. Chapter [5], and [7])

The reader is now introduced to the magneto-optical effects (namely L-MOKE and MLD), useful to characterise the magnetic samples and to follow the surface acoustic wave interaction with the magnetic FeRh layer.

2 Magneto-Optical effects

When a light beam, consisting of E- and B-fields, passes through or reflects off a magnetic material, it can be influenced by the magnetisation or by a magnetic field. These interactions are known as Magneto-Optical (MO) effects. At the heart of these effects lies the ability of magnetic materials to alter the polarisation state of light in response to an applied magnetic field. Discovered in 1845 by M. Faraday [1791-1867], the Faraday effect is one among several magneto-optical effects, and describes the rotation of polarisation of light when propagating through a magnetic material. Magneto-optical effects offer high sensitivity to magnetic fields, and enables the development of devices for detecting magnetic field variations in various applications, including navigation, aerospace, and medical diagnostics [104]. Here, the magnetisation is always in a stationary regime, i.e varies very slowly with respect to the electric field of light.

2.1 Faraday, Kerr and Magnetic Linear Dichroism Effects

Faraday Effect

Magneto-optical effects depend on the geometric configuration. For the Faraday effect, as a linearly polarised light propagates through a transparent dielectric material medium, parallel to an applied external magnetic field B, its polarisation changes. Figure [2.10] is a schematic representation of a linearly polarised light- here vertically polarised. Upon a propagation through the medium, a rotation of the linear polarisation is measured by the detector. This rotation angle, denoted by θ_F, is directly proportional to the magnitude of the magnetic field, the distance propagated through the material L, and the Verdet[2] constant, V [105]. If the magnetic field is reversed, the rotation in polarisation of the incident light is then - θ_F. This characterises the non-reciprocity of the Faraday effect.

$$\theta_F = V\,B\,L \tag{2.1}$$

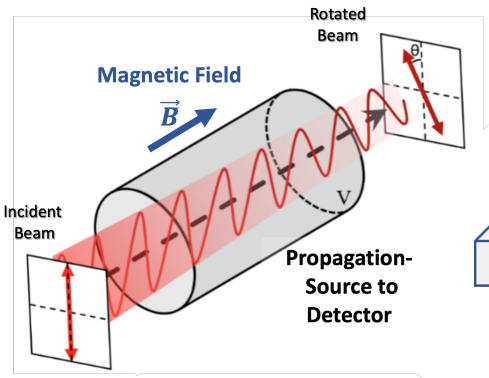

Figure 2.10: Faraday Configuration- Transmission geometry. A linearly polarised light travels through a transparent dielectric medium and parallel to an external magnetic field. The detector measures a rotation in the polarisation after the medium.

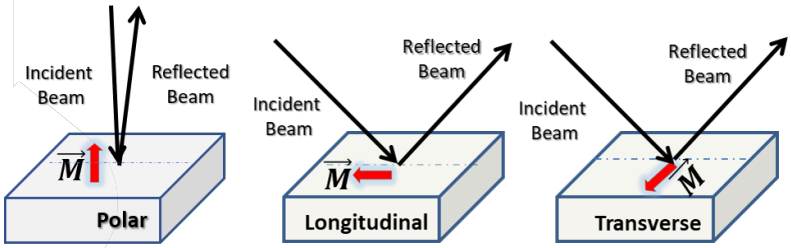

Figure 2.11: Schematic representation of the three Magneto-optical Kerr Effects in reflection geometry. **(a)**: In the polar Kerr effect, the polarisation of the incident light beam is affected by the out-of-plane component of magnetisation. **(b)**: For the Longitudinal Kerr, it is the in-plane component of magnetisation parallel to the plane of incidence of light. **(c)**: For the Transverse Kerr, it is the in-plane component of magnetisation perpendicular to the plane of incidence of light.

Kerr Effects

A similar effect has been observed by J. Kerr [1824-1907], in 1877. Unlike the Faraday effect, the Kerr effects are present in reflection geometries, as illustrated on figure [2.11]. Indeed, Kerr rotation experiments involve illuminating the surface of a magnetic material with polarised light and detecting the reflected light's polarisation state. There are three main Kerr effects depending on the material magnetisation and incident light beam configurations.

- **Polar Kerr** whereby the polarisation of a linearly polarised and incident beam is rotated proportionally to the out-of-plane component of magnetisation. Typically, after reflection, there is a rotation and an ellipticity in the reflected beam.

[2]The Verdet constant is an intrinsic property of a transparent medium, and is related to the dispersion of its optical index and the light wavelength. For YIG: V = 380 rad T^{-1} m^{-1} at λ = 780 nm [105].

- **Longitudinal Kerr** whereby the rotation of polarisation of an obliquely incident beam is dependent on the in-plane component of magnetisation, in the plane of incidence of light.
- **Transverse Kerr** has a similar geometry to Longitudinal MOKE, except that the magnetisation is perpendicular to the plane of incident of the light. Note that Transverse MOKE does not exist for perpendicularly polarised (denoted as s) light beam (with respect to plane of incidence).

MLD Effects

Magnetic Linear Dichroism (MLD) is a phenomenon observed in certain materials where the refractive index depends on the orientation of the material's magnetisation with respect to the polarisation direction of the light. When a linearly polarised light is reflected off a magnetic material, the light refractive index differs depending on whether the polarisation direction aligns parallel or perpendicular to its magnetisation. Note that the MLD rotation is proportional to the magnetisation $\mathbf{M}^2$. The MLD effect generally produces a smaller polarisation rotation compared to the Kerr effects in the visible range.

2.2 Analytical Formulae for Magneto-Optical Effects

A light beam propagating in a continuous magnetic medium can be described using Maxwell's equations, and the medium's response to the latter can be described using the dielectric permittivity tensor, ϵ. Since the MLD effect is quadratic, second order terms are included in the magneto-optical interaction. For a cubic magnetic material, the dielectric tensor is written as [106], [107]:

$$\epsilon(\omega) = \epsilon_{\mathrm{r}} \begin{bmatrix} 1 & -i\,Q\,m_{\mathrm{z}} & i\,Q\,m_{\mathrm{y}} \\ i\,Q\,m_{\mathrm{z}} & 1 & -i\,Q\,m_{\mathrm{x}} \\ -i\,Q\,m_{\mathrm{y}} & i\,Q\,m_{\mathrm{x}} & 1 \end{bmatrix} + \begin{bmatrix} O_1\,m_{\mathrm{x}}^2 & O_2\,m_{\mathrm{x}}\,m_{\mathrm{y}} & O_2\,m_{\mathrm{x}}\,m_{\mathrm{z}} \\ O_2\,m_{\mathrm{x}}\,m_{\mathrm{y}} & O_1\,m_{\mathrm{y}}^2 & O_2\,m_{\mathrm{y}}\,m_{\mathrm{z}} \\ O_2\,m_{\mathrm{x}}\,m_{\mathrm{z}} & O_2\,m_{\mathrm{y}}\,m_{\mathrm{z}} & O_1\,m_{\mathrm{z}}^2 \end{bmatrix} \tag{2.2}$$

where ϵ_{r} is the relative dielectric constant of the material, Q the Voigt parameter[3] and m_{i} the magnetisation unit vector. The second part of the matrix element characterises the second order MO effect namely: Voigt effect, and $\mathrm{O_i}$ is the quadratic Voigt constant.

2.2.1 Kerr Geometries

The Fresnel reflection matrix, $\mathbb{R}$, accounts for the polarisation of light and its interaction at an interface between two optically different media, in the reflection geometry, with r_{ps} the ratio of the incident p-polarised **E**-field to the reflected s-polarised **E**-field, is given as [108]–[110]:

$$\begin{bmatrix} E_{\mathrm{r,p}} \\ E_{\mathrm{r,s}} \end{bmatrix} = \begin{bmatrix} r_{\mathrm{pp}} & r_{\mathrm{ps}} \\ r_{\mathrm{sp}} & r_{\mathrm{ss}} \end{bmatrix} \cdot \begin{bmatrix} E_{\mathrm{i,p}} \\ E_{\mathrm{i,s}} \end{bmatrix} \tag{2.3}$$

The complex Kerr effects for the p- and s-polarisation are defined as:

$$\Theta_{\mathrm{K}}{}^{\mathrm{p}} \equiv \theta_{\mathrm{K}}{}^{\mathrm{p}} + i\,\kappa_{\mathrm{K}}{}^{\mathrm{p}} \equiv \frac{r_{\mathrm{sp}}}{r_{\mathrm{pp}}} \tag{2.4}$$

$$\Theta_{\mathrm{K}}{}^{\mathrm{s}} \equiv \theta_{\mathrm{K}}{}^{\mathrm{s}} + i\,\kappa_{\mathrm{K}}{}^{\mathrm{s}} \equiv \frac{r_{\mathrm{ps}}}{r_{\mathrm{ss}}} \tag{2.5}$$

with θ_{K} the Kerr rotation and κ_{K} the Kerr ellipticity.

i Longitudinal L-MOKE configuration

Inoue *et al.* measured the temperature dependence of the Kerr rotation with respect to the photon energy, on FeRh thin films epitaxially deposited onto MgO substrates [111]. Using their data, and knowing that the light source used in our L-MOKE experiment, c.f. [3.2], is 635 nm, the Voigt coefficient for FeRh in the FM phase (at T = 125°C) is calculated to be : Q = - 0.055 - i 0.060.

[3] Q describes the strength of the magneto-optical effect and is directly proportional to the magnetisation: ($Q \propto M$)

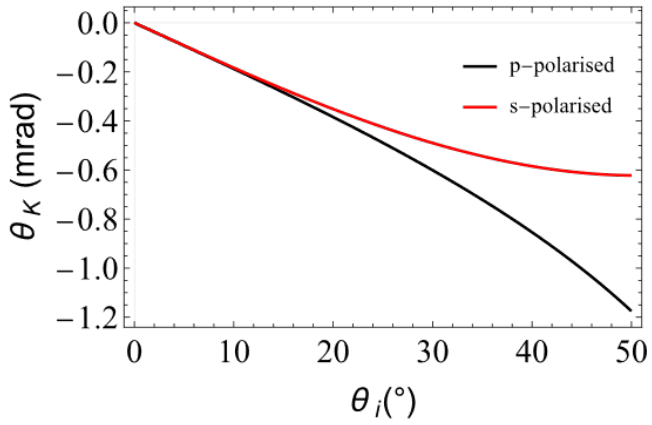

Figure 2.12: Calculated Kerr rotation with respect to the incident angle at 635 nm, for a p-polarised or s-polarised incident light beam. As shown in the following section, the maximum obtainable incident angle on our setup is ≈ 20°. Hence, the maximum observable is ≈ 0.4 mrad, which is a very small rotation.

Figure [2.12] shows the calculated evolution of the LMOKE rotation with respect to the angle of incidence of the incoming light beam, for P-Polar and S-polar respectively. At normal incidence, $\theta_i = 0°$, it can be seen that no rotation is possible. Part of section [3.2], consists in maximising the angle of incidence as the latter is constrained by the sample being placed inside the cryostat, and by the numerical aperture of the microscope objective being used.

2.2.2 Magnetic Linear Dichroism

Using Maxwell's equations and looking for plane wave solutions describing the light propagation in the medium, yields the following equation:

$$n^2\vec{E} - \vec{n}\left(\vec{n}\cdot\vec{E}\right) = \left[\epsilon\left(\omega\right)\right]\vec{E} \tag{2.6}$$

where the vector n is defined as: $\vec{n} = \vec{k}\ \mathrm{c}\ /\ \omega$.
Solving this equation gives two eigenvalues: $n_{||}$ and $n_{\perp}$, which correspond to the two values of the refractive indices for incident polarisation parallel and perpendicular to the in-plane magnetisation. This results in a birefringence, similar to a linearly polarised light passing through a wave-plate.

The MLD-induced rotation can be calculated from the eigen-vectors and is given by:

$$\delta\beta = \theta_{\mathrm{MLD}} = \frac{E_{\mathrm{r},\perp}}{E_{\mathrm{r},||}} = \underbrace{\frac{\left(n_{||} - n_{\perp}\right)}{\left(1 - n_0^2\right)}}_{P_{\mathrm{MLD}}} \sin\left[2\ \left(\beta - \varphi_0\right)\right] \tag{2.7}$$

with β and ϕ_0 are the angles between the polarisation of the incident light and the in-plane magnetisation with respect to the x-axis of the coordinate system, and $\delta\beta$ the MLD rotation. The Voigt effect is maximum for the incident polarisation oriented at 45° to the static magnetisation.

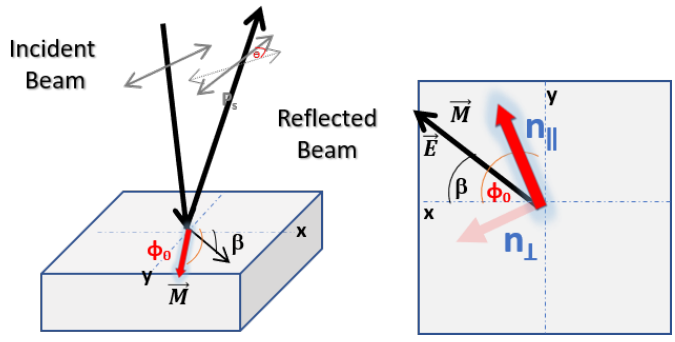

Figure 2.13: Incident light beam reflected off a magnetic sample. As the refractive indices are different for an incident light polarised parallel or perpendicular to the in-plane magnetisation, there is a birefringence in the reflected light, and hence an induced rotation of polarisation: θ_{MLD}. The incident light makes an angle β with the x-axis and the magnetisation an angle ϕ_0.

3 Experimental Setup and Techniques

In this section, the reader is introduced to the experimental setup used during this thesis. A focus is made here on the static optical detection of magneto-optical interactions. However, it should be noted that this is not the complete setup used in this manuscript. The acoustic measurements setup is introduced in Chapter [4], while the dynamical aspects of magneto-optical and magneto-acoustics are covered in Chapter [9].

Three different measurements can be performed out of one optical setup. As said before, the metallic alloy of FeRh undergoes a first-order phase transition with respect to temperature. The first measurement consists of a real-time reflectivity of the FeRh surface. Indeed, as discussed before, the AFM and FM phases of FeRh have different electronic band structure, and consequently different reflectivity. By following the variation in the FeRh reflectivity, the AFM-FM phase transition can be characterised in real time. Then the focus is directed towards magneto-optical effects namely: the Longitudinal Magneto-Optical Kerr Effect for the determination of the coercivity and the Magnetic Linear Dichroism for the proof of a biaxial anisotropy in ferromagnetic crystalline FeRh.

3.1 Reflection Microscopy Imaging- Focus adjustment

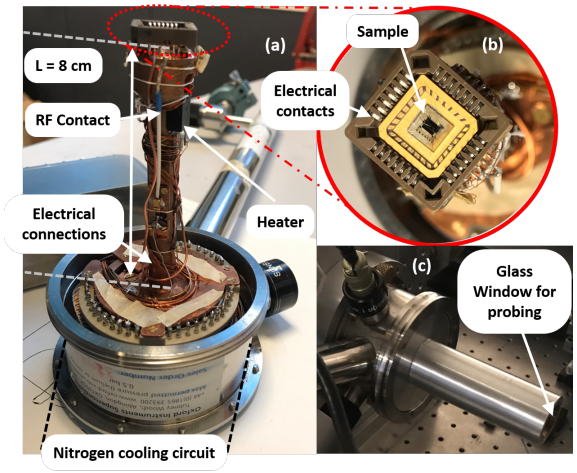

Figure 2.14: **(a)** Picture of the cryostat without the cover at room temperature. The copper pillar has a length of 8 cm. **(b)** Picture of the clipped in sample - here the crystalline FeRh film over its transparent MgO substrate on a yellow chip holder- connected to the electrical RF ports. **(c)** Closed under-test cryostat

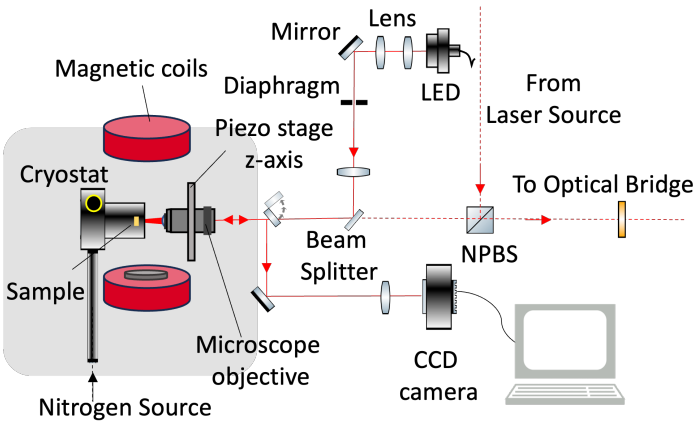

Figure 2.15: Experimental Setup for static optical detection. The microscope objective is fixed onto an adjustable piezoelectric stage, which allows z-axis motion. This ensures that the focal point of the microscope objective always lies on the FeRh surface and compensates for the contraction or dilatation of the cryostat pillar.

Reflection microscopy requires the collection of light beams that are reflected from the surface of a sample subsequent to their passage through a microscope objective. This method facilitates the observation and analysis of the surface characteristics of the sample. Figure [2.14] provides better understanding of the internal configuration of the cryostat and the immediate vicinity encompassing the sample. As depicted in Figure [2.14**(a)**], the sample is positioned atop a copper pillar having a room-temperature length of 8 cm. This pillar serves two purposes. First this allows to place the sample between the magnetic poles of an electromagnetic coil. Secondly, the copper pillar serves as a cold finger from the Nitrogen cooling circuit, situated at the circular end of the cryostat, to the sample placed atop. This cooling circuit, made up of a thin-capillary tube is supplied by a continuous flow of liquid Nitrogen. Coupled with the electric heater at the other end of the pillar, they serve as thermal sources for temperature variation and control. Furthermore, as described in details in Chapter [4], acoustic waves are generated in our setup. Figure [2.14**(b)**] is a picture of the sample (here the FeRh film is deposited over the transparent $ZnO/SiO_2/MgO$ stack, c.f. fig. [2.9]), placed within its holder (maroon). The magnetic film is the dark square at the centre. The holder is connected to a system

of electric and radio-frequency circuitry that feeds the sample in order to generate and detect acoustic waves. Micro-bonding procedures are essential for establishing connections between lithographically fabricated electrical contacts on the sample and the wired connections of the sample-holder. Once the cryostat is closed with the sample under study, the sole means of probing its surface is through the aperture situated at the end of the elongated pillar support, as shown in Figure [2.14**(c)**]. For that, an optical setup is used.

Figure [2.15] is a schematic representation of the experimental setup employed for surface reflectivity measurement. A LED source ($\lambda = 635$ nm), is precisely focused onto the back-focal plane of the microscope objective by a set of lenses and mirrors. This arrangement ensures homogeneous illumination, (Köhler illumination), of the sample inside the cryostat. The light beam reflected off the sample is then directed towards an Andor CCD camera, (0.3 μm/pixel, for a magnification of ≈ 20), for further analysis, through the same objective. The microscope objective is mounted on a movable z-plane piezoelectric stage. As the magnetic phase transition of FeRh is of interest in this manuscript, the sample undergoes cyclic temperature variations ranging from approximately -50°C to 140°C. Consequently, the copper pillar undergoes repeated contractions and expansions during each of these cycles. To maintain consistent focus on the sample surface throughout the experiment, real-time adjustments are made using the piezoelectric stage.

Two microscope objectives are used in the setup: a Mitutoyo objective with a working distance of 20 mm and focal length of 9.9 mm and a Leitz objective with a frontal distance of 12.5 mm and a focal length of 10 mm, both with Numerical aperture of 0.40, where both have a depth of field[4] of only a few microns. The process of focal adjustment relies on the thermal expansion coefficient of copper and the careful calibration of voltage input/output to the focusing z-displacement stage. The piezoelectric stage allows for adjustments of up to a maximum of 300 μm, which is enough to cover for the thermal expansion and contraction of copper during a whole temperature cycle.

3.1.1 Reflectivity Measurement

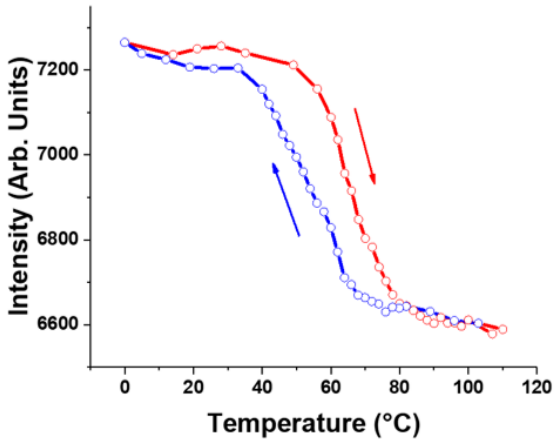

Figure 2.16: Reflectivity curve versus temperature for the Sample A.

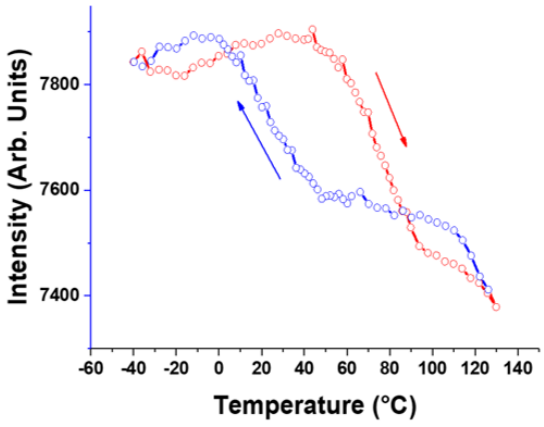

Figure 2.17: Reflectivity curve versus temperature for the Sample B.

Contrary to SQUID measurement, which averages on the whole sample, reflectivity only probe the top layers, $\approx$ 10-15nm. Figures [2.16] and [2.17] shows the reflectivity versus temperature curves for the FeRh grown on MgO and GaAs respectively. For the Crystalline Sample A: FeRh/MgO, two well defined intensity plateau are observed. This is not the case for the Polycrystalline Sample B: FeRh/GaAs, where the thermal AFM-FM hysteresis is accompanied by two smaller hysteresis. The origin of the smaller hysteresis loops is discussed below. Both curves show a reduction in the reflectivity when going from the AFM-to-FM phase. In the case of the MgO substrate, this reduction is $\approx 9.3\%$,

[4]The depth of field refers to the range of distance that appears acceptably sharp in an image.

while in the case of the GaAs, this is ≈ 5.4%. These values are higher than what is measured by Saidl *et al.* at 633 nm, ≈ 2.5%. The origin of this difference in reflectivity of the AFM and FM phases are due to the different electronic band structure, most notably at the Fermi level [112], [113].

3.1.2 Appearance of ice-islands

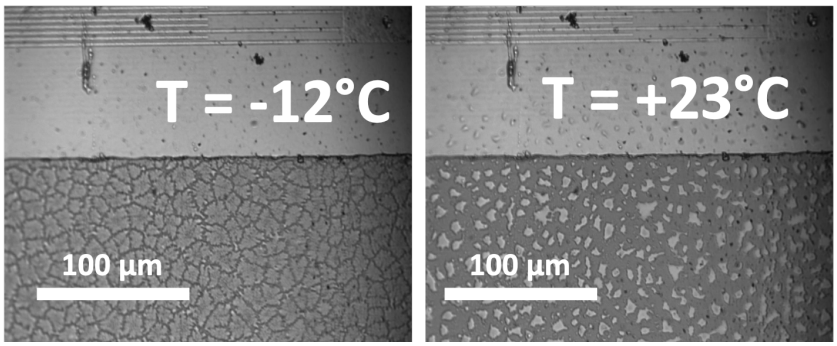

Figure 2.18: Reflectivity imaging showing the appearance of Ice-Islands close to 0°C.**(a)** taken below at -12°C where an ordered system is observed. **(b)** melting causes dislocation of the ice islands

As said and seen before, FeRh undergoes a first-order phase transition with the fully AFM phase close to 0°C and in the negative temperatures, on sample B. However, as the temperature ramps are performed from approximately - 50°C to 140°C, appearances of ice islands typically around 0°C, has been observed. Figure [2.18] are typical images of the surface taken using the reflection microscopy imaging setup. Note the uniform illumination over the whole image, and the appearance of the ice islands or organic pollution. The melting and visual disappearance of the latter are investigated. As the ice-islands have different refractive indices, they introduce unwanted reflective features on the sample's surface, which can obscure the true reflectivity signal originating from the FeRh under study. Moreover, the presence of these ice crystals alters dynamically the surface morphology and texture. This might affect the propagation of acoustic wave travelling on the layer. Hence, considerate efforts have been put towards minimising the presence of these ice islands or organic substances. These included thorough cleaning of the cryostat, the addition of active charcoal elements and careful purging with argon gas. Although these surface impurities have been effectively reduced and rendered visually invisible in later experiments, there remains a lingering suspicion regarding the remaining presence of water vapour and influence on acoustic wave propagation, particularly during experiments conducted in the proximity of 0°C.

3.2 Longitudinal Magneto-Optical Kerr Microscopy

As described above, the LMOKE configuration is sensitive to the in-plane magnetisation parallel to the plane of the incident light. Figure [2.19] is a schematic representation of the LMOKE setup consisting of the same optical elements as above with an addition of a diaphragm aperture, an HN-32 pair of polariser-analyser and a removable Bertrand lens (second lens in front of the Camera). The polariser is used to have a linearly polarised light either strictly vertical (S-Polar) or strictly horizontal (P-polar).

As seen in figure [2.12], in order to observe Kerr rotation, the incident light beam must not be normal to the surface. The diaphragm aperture is placed on a mechanical stage and used to off-centre the light beam, and ensures that it enters near the edge of the microscope objective. The incident angle in the LMOKE geometry is thus oblique and is ≈ 20°. Larger angular values are deemed impossible due to the sample being enclosed inside the cryostat and in between the magnetic coils. Moreover, the LMOKE experiment is extremely sensitive to light polarisation and stray light. To mitigate these factors, the setup is meticulously enclosed to minimised external influences. However, as the microscope objective is made up of a series of spherical lenses, there is a risk of the latter depolarising the incident light beam. One way to check the polarisation of this incident light is to cross its reflection with the analyser. The light is then made to pass through the polarisation cross of the objective. For that the

Bertrand lens is used.

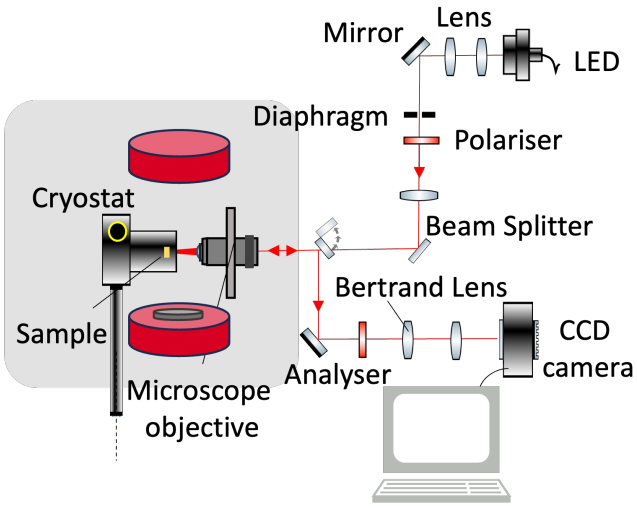

Figure 2.19: LMOKE Experimental Setup. A linearly polarised light is, made to pass through a diaphragm aperture and to the surface of the sample through the objective. Following interaction with the magnetic FeRh, the reflected light is sent towards an analyser and to the CCD camera. Two lenses are seen in front of the CDD camera in the diagram. In normal LMOKE measurement, only one is present. The second lens is placed only when in Bertrand configuration.

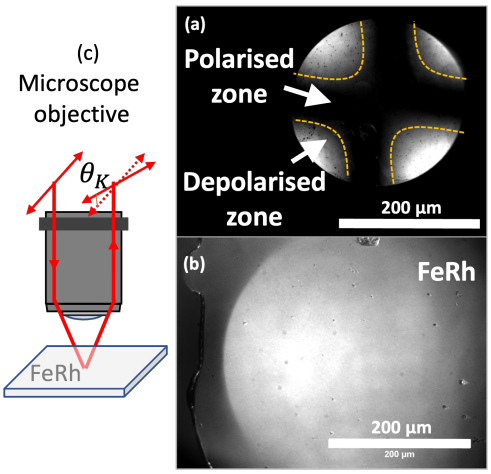

Figure 2.20: **(a)**: CCD image of the back-focal plane of the microscope objective, (in this case- Mitutoyo), in the Bertrand configuration, showing the polarisation cross. Note the existence of a polarised and depolarised zones. The incoming light from the LED is made to pass through one of the edge within the polarised zone- delimited by the yellow markings. **(b)**: LMOKE microscopy image of the FeRh surface. **(c)**: Schematic representation of the microscope objective, when a linearly polarised light passes through the objective and reflects off the FeRh sample. The reflected light undergoes a Kerr Rotation.

Figure [2.20**(a)**] is an image in the Bertrand configuration. In the presence of the second lens, the aperture diaphragm is conjugated with the back focal plane of the objective and the Andor camera. A cross-like shape is seen. This represents the region where the linearly polarised light can pass without being depolarised. For all LMOKE measurements, it has been ensured that the linearly polarised light goes through one edge of the cross. **(b)** represents a microscopic image of the FeRh layer in the polariser-analyser configuration, without the Bertrand lens, meaning after crossing the analyser at 90° to the polariser, and using only one lens in front of the camera. **(c)** is a schematic representation of the microscope objective. The linearly polarised light is made to pass near the edge of the entrace pupil of the objective. Following the interaction with the FeRh layer, the light undergoes a Kerr rotation. The signal is thus obtained by analysing cross-polarisation with the CCD camera and the software.

3.2.1 Measurement of the local coercivity

This magneto-optical technique is used to determine the local coercivity of the FeRh grown on GaAs layer, i.e. Sample B. Figure [2.21] represents the optical configuration of the LMOKE experiment. The procedure for a LMOKE measurement consists in scanning the field from + B_{MAX} (the saturation magnetisation), to - B_{MAX} and back. The magnetisation then parallel to the field until - B_{MAX}, where the field reverses direction again. A typical measurement of the LMOKE signal is presented in figure [2.22]. The striking feature is that the hysteresis is squared, a feature of sharp transition, meaning that magnetisation remains in the direction of the initially applied field until the opposing field is strong enough to overcome the local anisotropy field or and/or pinning field.

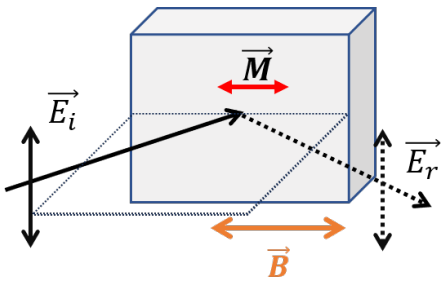

Figure 2.21: LMOKE configuration with the linear polarisation of light and direction of the magnetic field. For this configuration, the interaction is maximised.

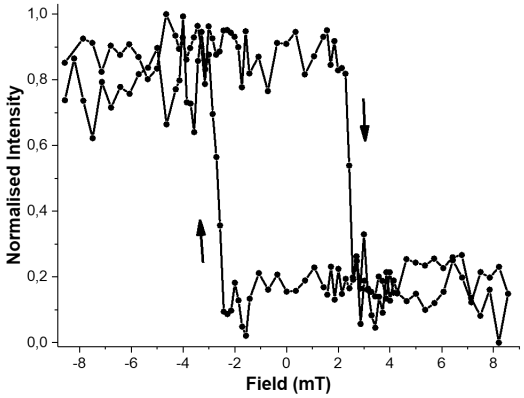

Figure 2.22: Typical L-MOKE measurement signal, here at 130°C in the fully FM phase. Very small contrast is observed- 0.37%. The mean coercivity is measured to be 2.7 mT.

The L-MOKE measurement is repeated while varying the temperature from the high-temperature FM phase down to the AFM-phase. The temperature dependence of the coercivity with respect to temperature is represented on figure [2.23]. It is observed that the coercivity is constant down to ≈ 80°C, which corresponds to the beginning of the transition on the cooling ramp as gathered from the SQUID measurement- figure [2.8]. The increase in coercivity, on the other hand, can be understood by considering the FM fraction in the transition. As we decrease the temperature, the ratio of the FM phase volume over the total volume decreases. Consequently, less nucleation centres are available, making it more and more difficult for switching to occur. The coercivity is an important parameter in this thesis and will be discussed in more details in chapters [5] and [7].

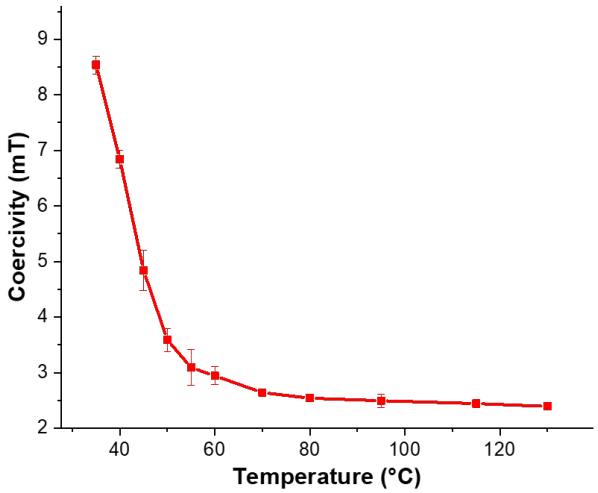

Figure 2.23: Evolution of the coercivity with respect to temperature on Polycrystalline Sample B. Constant value of the coercivity for temperature going from the fully FM phase, down to temperature close to the FM-to-AFM phase transition. Then a sharp increase in the coercivity is recorded.

3.3 Magnetic Linear Dichroism

Bulk Fe has a cubic magnetic anisotropy with <100> being the easy axes [114]. Epitaxial Fe, on the other hand, has a different symmetry. This is exemplified by Fe(001) thin films grown on GaAs(001). The Fe thin-film has now an in-plane biaxial anisotropy along [100] and [010] due to magneto-crystalline anisotropy while the [001] is now a hard axis due to shape anisotropy. As no definite anisotropy is ratified for FeRh thin films, it is believed to be somehow similar to Fe. Marti *et al.* stated that a 100 nm-thick FeRh layer grown on MgO has a biaxial in-plane magnetic anisotropy with the crystallographic

<110> being easy axes [78], while Mariager *et al.* [115] came to the conclusion that a 47 nm epitaxial FeRh thin-film has no preferred in-plane easy axis. The aim of this experiment is to determine the orientation of the easy axes (between <100> and <110>) of our crystalline Sample A:FeRh/MgO. Knowing the magnetic anisotropy is the easiest route for SAW-FMR interaction.

3.3.1 Experimental Setup

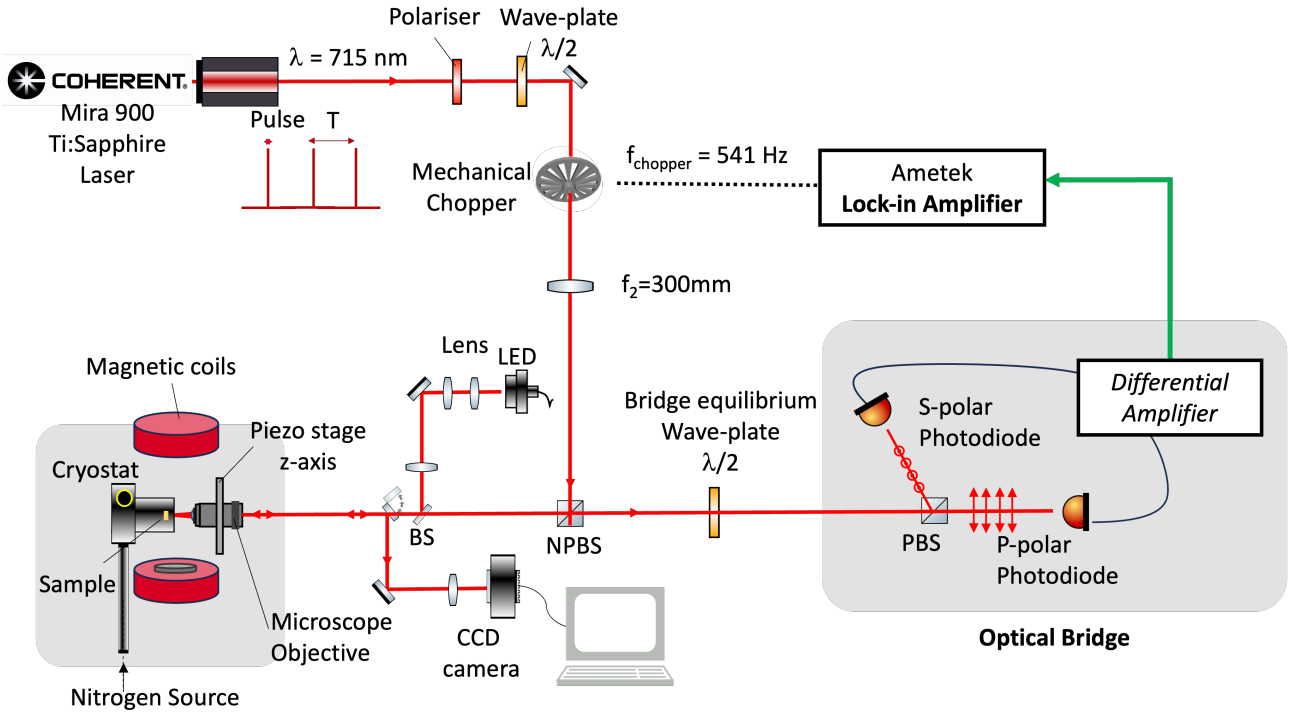

Figure 2.24: Magnetic Linear Dichroism Experimental Setup

Magnetic Linear Dichroism (MLD) is a second form of magneto-optical phenomenon used in this manuscript. This has been employed to determine the magnetic anisotropy of crystalline FeRh. Figure [2.24] illustrates the optical arrangement employed in the MLD experiment. The Coherent femtosecond Titanium:Sapphire laser, pumped by a solid-state **Verdi** laser, emits 200 fs light pulses with a repetition rate of 75 MHz, at a wavelength of $\lambda = 714$ nm. The light beam is linearly polarised and made to pass through a half-wave plate. This allows subsequent variation of the polarisation direction, denoted as β (c.f. figure [2.25]). The beam is then made to go through a mechanical chopper operating at a frequency of 514 Hz, which modulates the probe signal, and towards the microscope objective via a Non-Polarising Beam-splitter (NPBS). Figure [2.25] represents the FeRh sample. The linearly polarised light directed at an angle β to the x-axis is reflected off the surface. The reflected light is rotated by an angle θ_{MLD}. This light beam is reflected and recollected by the objective and directed towards the optical diode bridge through the NPBS.

Operational principle of the optical bridge

The bridge is composed of a second half-wave plate placed in front of a Calcite Glan-Taylor polarisor (PBS), and two photo-diodes connected to a differential amplifier. The operational principles governing the MLD experiment and optical bridge can be outlined as follows. Before an acquisition, the bridge needs to be balanced. A linearly polarised light is sent on the sample via the microscope objective and reflected off the FeRh surface. This reflected light is sent to the optical bridge and the half-wave plate is adjusted such that the light polarisation reaching the PBS cube is at a 45° angle from its axes. The linearly polarised light beam is thus separated into two components, namely the Horizontal component (P-polar) and the Vertical component (S-Polar). The bridge-equilibrium wave-plate is then adjusted until both photo-diodes collect equal intensities which is then fed to the differential amplifier

that amplifies their voltage difference. Prior to any measurement it should ensured that the difference between the diode signals is around zero, effectively eliminating common mode noise. This serves as the reference signal and the bridge is balanced. When the magnetic field is scanned, the polarisation of the reflected signal off the sample is rotated by θ_{MLD}. When this signal reaches the PBS cube, the signal measured by the differential amplifier deviates from zero due to the unbalanced state of the bridge. The lock-in amplifier electronically multiplies the measured signal with the reference signal at f_{MOD} at (514 Hz), integrates and returns the in phase and out of phase components of the bridge signal.

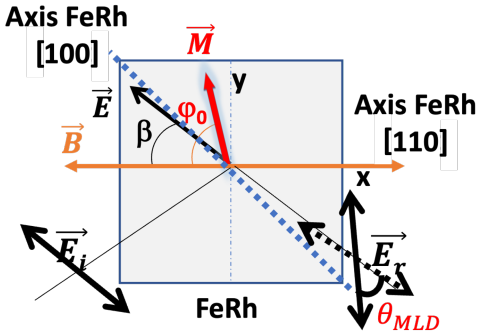

Figure 2.25: Incident and reflected laser beam on the FeRh surface. The linearly polarised incident light makes an angle β with the $<110>$ axis, and the magnetisation an angle ϕ_0.

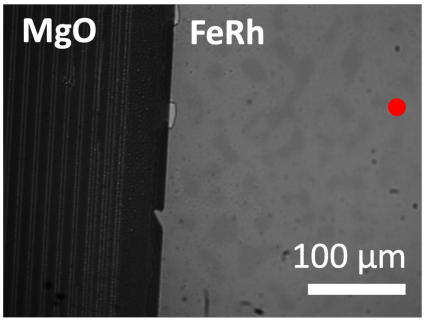

Figure 2.26: The incident laser spot schematically represented here, as a red dot, typically exhibits Gaussian shaped distribution, characterised by a Full Width at Half Maximum (FWHM) of approximately 8 pixels, corresponding to a spatial extent of 1.76 μ m.

3.3.2 Working Protocol for MLD measurement

Using the theoretical framework explained before, the MLD experiment consists in performing magnetic ramps from + B_{MAX} to - B_{MAX} and back to + B_{MAX}, for different values of the incident light polarisation angle β. The MLD rotation is then recovered using the optical bridge.

The MLD study was performed in the FM phase, i.e. heated up to 90°C. The magnetic field is applied in the plane of the sample and along the x-axis (parallel to the <110> crystallographic axis of FeRh) or at an angle of - 45° from the + x-axis (parallel to the <100> crystallographic axis of FeRh). Figure [2.25] gives a schematic representation of the in-plane magnetic field (in orange), the direction of magnetisation of the sample (in red) and the angle of the linearly polarised light (black) with respect to the x-axis. $<100>$ direction represents the expected easy-axes of magnetisation. The MLD causes a birefringence parallel and perpendicular to the direction of magnetisation, and affects differently the reflected light.

3.3.3 Results

Horizontal Magnetic Field

The magnetic field is varied from - 50 mT, along the x-axis, to + 50 mT, and back to the initial value of - 50 mT. Figure [2.27] shows the three sets of data obtained from this measurements. Fig. [**(a)**]- shows the experimental signal obtained from the optical diode bridge. The signal is centred around the zero field value but is asymmetrical. From this asymmetry, it can be deduced that the raw signal is made up of an odd and an even contribution which are of two different magneto-optical origins: An odd-function, Longitudinal MOKE signal and an even function, the MLD signal. The separation of the two signals is done by considering two functions: $F^{\nearrow\searrow}(x)$[5] and $G^{\nearrow\searrow}(x)$[6] respectively:

[5] x being a nondescript argument
[6] $\nearrow\searrow$ implies here the increasing and decreasing of the field magnitude in the cycle for eg.

Odd- LMOKE Contribution : $F^{\nearrow}_{\mathrm{LMOKE}}(x) = -F^{\searrow}_{\mathrm{LMOKE}}(-x)$

Even- MLD Contribution : $G^{\nearrow}_{\mathrm{MLD}}(x) = G^{\searrow}_{\mathrm{MLD}}(-x)$

With: $\theta^{\nearrow}_{\mathrm{ROT}}(x) = G^{\nearrow}_{\mathrm{MLD}}(x) + F^{\nearrow}_{\mathrm{LMOKE}}(x)$ and $\theta^{\searrow}_{\mathrm{ROT}}(x) = G^{\searrow}_{\mathrm{MLD}}(x) + F^{\searrow}_{\mathrm{LMOKE}}(x)$

which corresponds to the rotations recorded while increasing and decreasing the field only.

The pure odd and even contributions can be calculated from:

$$G^{\nearrow}_{\mathrm{MLD}}(x) = \frac{1}{2}[\theta^{\nearrow}_{\mathrm{ROT}}(x) + \theta^{\searrow}_{\mathrm{ROT}}(-x)] \qquad G^{\searrow}_{\mathrm{MLD}}(x) = \frac{1}{2}[\theta^{\nearrow}_{\mathrm{ROT}}(-x) + \theta^{\searrow}_{\mathrm{ROT}}(x)] \tag{2.8}$$

$$F^{\nearrow}_{\mathrm{LMOKE}}(x) = \frac{1}{2}[\theta^{\nearrow}_{\mathrm{ROT}}(x) - \theta^{\searrow}_{\mathrm{ROT}}(-x)] \qquad F^{\searrow}_{\mathrm{LMOKE}}(x) = \frac{1}{2}[\theta^{\searrow}_{\mathrm{ROT}}(x) - \theta^{\nearrow}_{\mathrm{ROT}}(-x)] \tag{2.9}$$

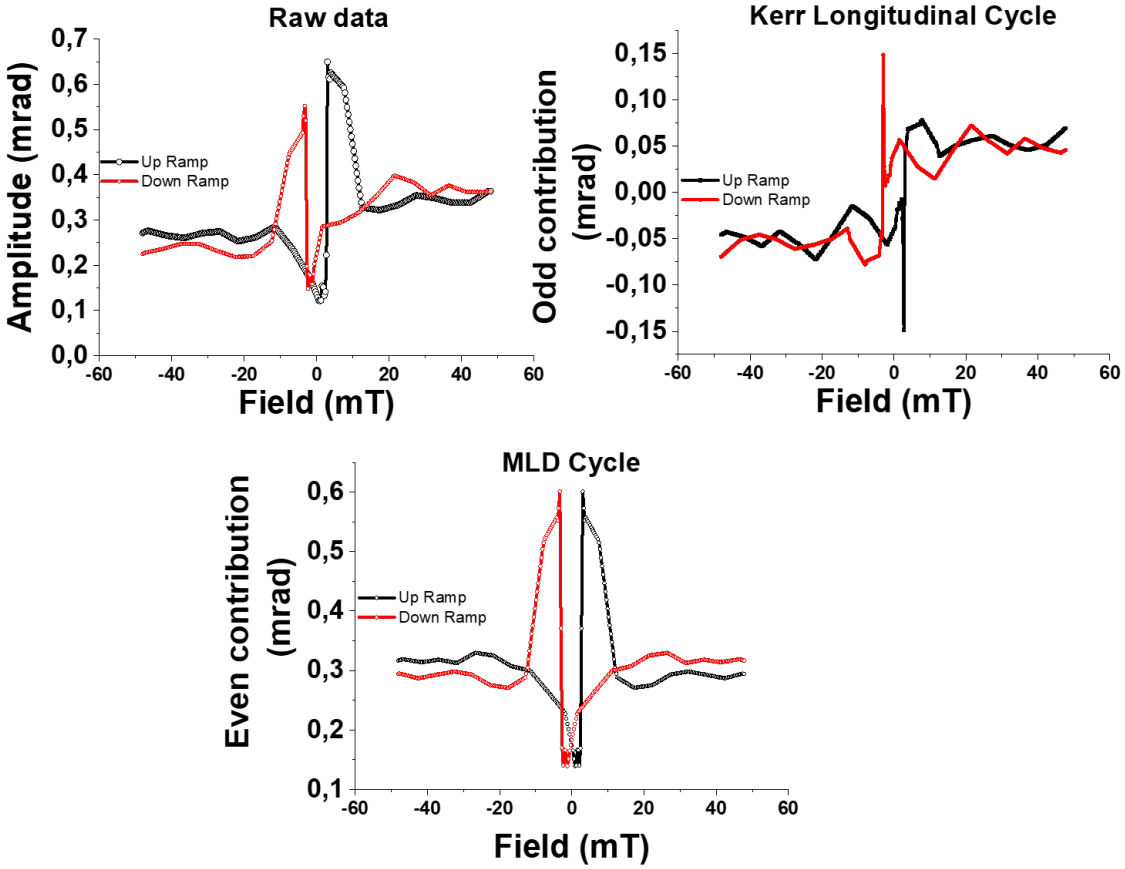

Figure 2.27: Results for the magnetic field applied horizontally, i.e. parallel to the <110> crystallographic axis of FeRh

The main contribution in figure [2.27(a)] comes from an even signal, i.e. the MLD signal, and is represented on figure [**(b)**]. From the plot, it can be seen that for the increasing field (Up Ramp), a slow rotation of (- 0.13 mrad) from - 12 mT to 2.4 mT, is followed by a quick rotation of (+ 0.43 mrad) from 2.4 mT to 3 mT and back to stationary (0.3 mrad) value at 13.5 mT up to the saturating field value. The decreasing field value from 50 mT is symmetrical. Figure [**c**] shows the smaller contribution of the LMOKE signal. For the Up ramp, a consequent rotation (+ 0.04 mrad) is seen from 2.7 mT to 3.4 mT only. This is ten times less than calculated, which is okay since we are at 0° incidence. Notice that these rotations occur around the same field value. It implies a change in the in-plane optical dichroism, whereby suggesting a switching of the in-plane magnetisation.

Figure [2.28] shows the schematic representation of the in-plane magnetisation rotation corresponding to the FeRh thin-film having an easy-axis along the <100>. A field of - 50mT almost along [-1-10],

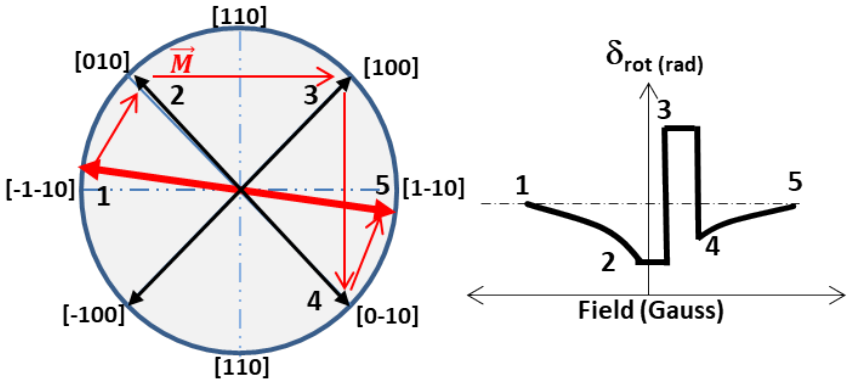

Figure 2.28: Expectation MLD cycle for EA: <100> and light polarisation along [-1-10]

is strong enough to overcome the magneto-crystalline anisotropy. The magnetisation is forced by the field. As the field magnitude is decreased, the magnetisation direction rotates until it aligns along the easy axis. This corresponds to steps 1 to 2. As the field decreases to zero, it is energetically favourable to stay along the [010] direction. For positive field, the system realigns itself so that the magnetisation switches to the [100] direction (step 2 to 3). However, since it is energetically more favourable for the magnetisation to be close the the field (smaller angle), the system prefers to align itself along the [0-10] direction. For further increase in the field, the magnetisation will align along the field (close to [1-10]). The MLD signal is shown schematically in Fig. [2.28].

For a light polarisation along [-1-10]. From step 1 to 2 the angle between the polarisation and magnetisation $(\phi_0 - \beta)$ goes from zero to $\pi/4$ and the $\sin 2(\phi_0 - \beta)$ term of the MLD signal increases from zero to 1. When magnetisation switches from step 2 to 3 this makes the $\sin 2(\phi_0 - \beta)$ term go from 1 to -1, generating an abrupt step in the MLD signal. Step 3 to 4 again changes the value of the $\sin 2(\phi_0 - \beta)$ term from -1 to 1, generating a second step. Finally from step 4 to 5 the signal goes back to zero.

Magnetic Field at -45°

Systematic repetition of the experiment was performed for several geometries ranging from changing the direction of the applied-in-plane magnetic field as well as varying the polarisation of the incident linearly polarised light (β). Recall that the MLD signal varies as:

$$\delta\theta_{\mathrm{MLD}} = P_{\mathrm{MLD}}\, sin(2(\phi_0 - \beta))$$

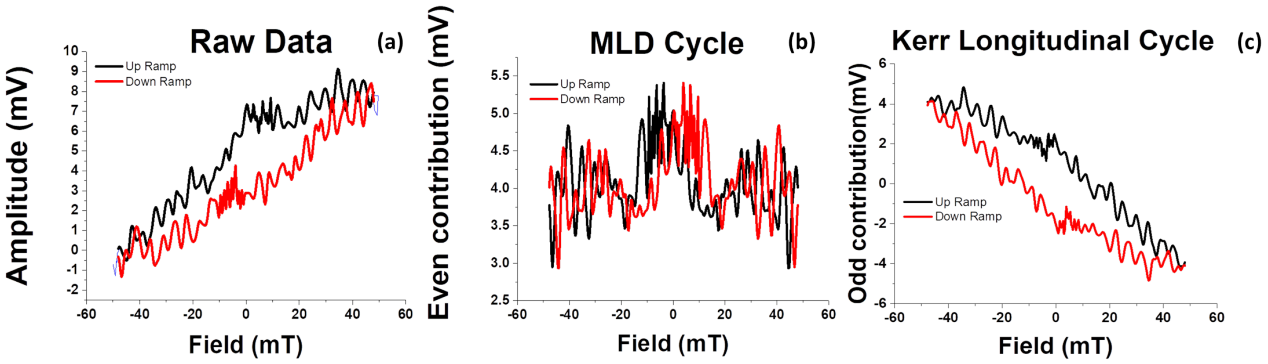

Figure 2.29: Results for the magnetic field applied at - 45°, i.e. parallel to the <100> crystallographic axis of FeRh

Figure 2.29, is an example of one of the multiple experiments performed. Here, the magnetic field was applied - 45° from the horizontal axis, while the incident light polarisation is at $(\beta = 45°)$. As it can be seen, there is no rotation-related signals from the measurements. Figure 2.29 [a] and [c] show

certain slopes which corresponds to some electronic drift in our measured signals. This means that the field is along an easy axis. As the field is scanned the magnetisation switches from [010] to [100] to [0-10] and the $\sin 2(\phi_0 - \beta)$ of the MLD signal remains zero.

Conclusion: The MLD experiment has revealed the easy axes of the crystalline FeRh grown on MgO in the FM state is, along its crystallographic <100> directions. Moreover, contrary to the arguments put forward by Mariager *et al.* [115], it has been demonstrated that FeRh has indeed a bi-axial magnetic anisotropy.

Chapter Summary

1. The chapter details the fabrication processes and characterisation techniques employed for the two FeRh samples investigated in this thesis. This includes an in-depth discussion of the methods used to prepare and analyse the samples. A full description of the experiments performed on either sample was given to help the reader.

2. A concise description of the Magneto-Optical Kerr Effect (MOKE) techniques is provided, highlighting their relevance and application in the subsequent chapters. This section serves to familiarise the reader with the fundamental principles and practical uses of MOKEs.

3. The optical setups used in the experiments, including reflectivity measurements, Longitudinal Magneto-Optical Kerr Effect (LMOKE), and Magnetic Linear Dichroism (MLD), are thoroughly described. Measurements of the temperature dependence of LMOKE on polycrystalline sample B, revealed an increase of the coercivity with respect to temperature when going from the fully FM phase to the AFM-FM phase transition. Measurements of the MLD on crystalline sample A showed that FeRh grown on MgO has an easy axis along the <100> crystallographic direction in the FM phase.

Part II
Theoretical Concepts

Chapter 3

Magnetic Resonance

Objectives

The objective of this chapter is to provide a comprehensive introduction of magnetic resonance, emphasising both the theoretical foundations and practical applications. It begins by exploring the key magnetic energy terms that influence the behaviour and stability of magnetic systems. The chapter then introduces the Landau-Lifshitz-Gilbert (LLG) equation, essential for describing magnetisation dynamics, and to understand the spin-wave modes.

Contents

1 Magnetic energy terms

The origin of any magnetic phenomenon can be traced back to the fundamental quantum mechanical nature of an electron's magnetic moment, μ, and its relationship to the spin, **S**, and angular momentum, **L**. These intrinsic electronic properties within ions or atoms give rise to the magnetic moments; governing macroscopic magnetic behaviour, and the magnetic response under the influence of an external magnetic field. Similar to any physical entity, a magnetic system tends to minimise its total free energy as this represents a state of stability and equilibrium. This section provides an introductory overview of the principal magnetic free energy terms.

1.1 Zeeman energy

The Zeeman energy term, named after Dutch Physicist Pieter Zeeman [1865-1943] [116], describes the interaction between a magnetic material fundamental constituents, the magnetic moments, and an externally applied magnetic field. It originates from a splitting in the electronic energy bands structure under the influence of a field. Energy-wise, the Zeeman energy term favours the alignment of the magnetic moments, or the macroscopic magnetisation, **M**, with the applied magnetic field, **B**. The Zeeman free energy is formulated as:

$$E_{\mathrm{Z}} = -\int_{\mathrm{V}} \mathbf{B}\cdot\mathbf{M}\,\mathrm{dV} \tag{3.1}$$

Coordinate system

In the rest of this manuscript, the spherical coordinates are privileged. The direction cosines are recalled here in the {x,y,z} reference frame.

$$\begin{pmatrix}\alpha_{\mathrm{x}}\\ \alpha_{\mathrm{y}}\\ \alpha_{\mathrm{z}}\end{pmatrix} = \begin{pmatrix}\sin(\theta)\ \cos(\phi)\\ \sin(\theta)\ \sin(\phi)\\ \cos(\theta)\end{pmatrix} \tag{3.2}$$

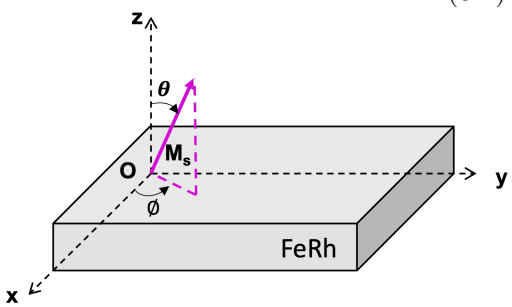

Figure 3.1: Reference frame {M_s, θ, ϕ}

1.2 Magneto-crystalline energy

The magneto-crystalline anisotropy (MCA) arises from the dependence of the magnetic energy on the crystallographic arrangement of atoms within a material. Multiple mechanisms contribute to the MCA term, namely the spin-orbit-coupling anisotropy arising from the hybridisation of magnetic orbitals and crystal field splitting of atomic orbitals, and the lattice strain anisotropy resulting from growth or lattice defects, among others. In order to minimise the free energy, the magnetisation expresses the tendency to lie along specific directions, referred to as the Easy Axes (E.A) of magnetisation, while avoiding some other directions, the Hard Axes (H.A). The existence of one or both directions depends on the existence and sign of the anisotropy constants, K

Similar to crystallographic point groups that can be expressed in either two-, three-, four- or six-fold symmetries, the contributions to the magneto-crystalline anisotropy energy respect group symmetries and are written in terms of the direction cosines.

- Uniaxial MC anisotropy directed colinearly to α_{i}: $E_{\mathrm{U}} = -K_{\mathrm{U}}\,\alpha_{\mathrm{i}}^2$
- Cubic MC anisotropy: $E_{\mathrm{C}} = K_0 + K_{\mathrm{C}_1}\left(\alpha_{\mathrm{x}}^2\,\alpha_{\mathrm{y}}^2 + \alpha_{\mathrm{y}}^2\,\alpha_{\mathrm{z}}^2 + \alpha_{\mathrm{z}}^2\,\alpha_{\mathrm{x}}^2\right) + K_{C_2}\left(\alpha_{\mathrm{x}}^2\,\alpha_{\mathrm{y}}^2\,\alpha_{\mathrm{z}}^2\right) + ...$

where K_{U} is the first uniaxial anisotropy constant and $K_{\mathrm{C}_{1,2}}$, respectively the first and second order cubic anisotropy constants. Note that inter-facial contributions to the MCA are not considered in this manuscript. By minimising the MCA energy, one can obtain the easy and hard axes of magnetisation.

1.3 Magneto-static energy

The magneto-static energy arises due to the internal distribution of magnetic moments and magnetic dipoles within a magnetic material and at its interfaces or surfaces, in the absence of time-varying magnetic fields. As the magnetic moments generate a magnetic field, self-interaction lead to the creation of a demagnetising field that tends to oppose the magnetisation, leading to an overall decrease in the total magnetisation. In general, the demagnetising field can be expressed in terms of the scalar potential, Φ, the surface, $\mu_0 M_\mathrm{s} (\mathbf{m} \cdot \mathbf{n})$[1], and volume, $\mu_0 M_\mathrm{s} (\nabla \cdot \mathbf{m})$, magnetic charges respectively [117]:

$$\mathbf{H}_\mathrm{d}(\mathbf{r}) = -\nabla\Phi(\mathbf{r}) = -\frac{1}{4\pi}\nabla\left[\int_\mathrm{V} \frac{-M_\mathrm{s}(\nabla\cdot\mathbf{m}(\mathbf{r}'))}{|\mathbf{r}'-\mathbf{r}|}V' + \int_\mathrm{S} \frac{M_\mathrm{s}(\mathbf{m}(\mathbf{r}')\cdot\mathbf{n})}{|\mathbf{r}'-\mathbf{r}|}S'\right]$$

For simple geometries and $\mathbf{M}$ uniform, the demagnetising field can be written in terms of the demagnetisation tensor $\underline{\underline{\mathbf{N}}}$, where $\mathbf{H}_\mathrm{d} = -\underline{\underline{\mathbf{N}}} \cdot \mathbf{M}$. The magneto-static energy density is thus:

$$E_\mathrm{DEMAG} = -\frac{1}{2}\mu_0 \int_\mathrm{V} \mathbf{M}\cdot\mathbf{H}_\mathrm{d}\, dV \tag{3.3}$$

In the case of a magnetic thin film infinite in the x and y directions, the demagnetisation tensor is of the following form:

$$\underline{\underline{\mathbf{N}}} = \begin{pmatrix} N_\mathrm{xx} & N_\mathrm{xy} & N_\mathrm{xz} \\ N_\mathrm{yx} & N_\mathrm{yy} & N_\mathrm{yz} \\ N_\mathrm{zx} & N_\mathrm{zy} & N_\mathrm{zz} \end{pmatrix} = \begin{pmatrix} 0 & 0 & 0 \\ 0 & 0 & 0 \\ 0 & 0 & 1 \end{pmatrix}$$

Equation [3.3] is thus simplified as:

$$E_\mathrm{DEMAG} = \frac{\mu_0}{2} {M_\mathrm{s}}^2 {m_\mathrm{z}}^2 \tag{3.4}$$

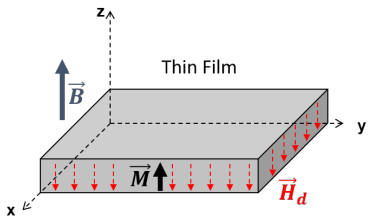

Figure 3.2: Schematical representation of a magnetic thin film out-of-plane magnetised and the existence of the demagnetising field, opposing the magnetisation.

1.4 Exchange energy

The exchange energy term originates from the exchange interactions between neighbouring magnetic moments in a magnetic material. Specifically, it is a result of the Pauli exclusion principle [118], which states that two electrons with the same spin, S_i, cannot possess identical quantum state in an atom. It is responsible for stabilising ordered magnetic states, by favouring the alignment of magnetic moments. The exchange energy term can be obtained by generalising the Heisenberg Hamiltonian [119] over all $[i, j]$ pairs of spins as:

$$E_\mathrm{EX} = -\frac{1}{2} J_\mathrm{EX} \sum_{\langle i,j\rangle} \mathbf{S}_\mathrm{i}\cdot\mathbf{S}_\mathbf{j}$$

where, J_EX, denotes the exchange integral, which is strictly positive for ferromagnetic interactions and strictly negative for antiferromagnetic interactions.
In the continuum distribution or micro-magnetic formalism, this exchange energy can be written in terms of the exchange stiffness, $A_\mathrm{EX} = J\, S^2\, n/\mathrm{a}$, where n, denotes the number of first neighbours and a, the lattice parameter. As such, the exchange contribution to the free energy density is written as:

$$E_\mathrm{EX} = \mu_0\, \mathbf{h}_\mathrm{EX}\cdot\mathbf{m} = A_\mathrm{EX}\, |\nabla_\mathrm{m}|^2 \tag{3.5}$$

2 Landau-Lifshitz-Gilbert equation

Proposed independently by Landau and Lifshitz (1935)[120] and completed by Gilbert (1955)[121], the Landau-Lifshitz-Gilbert equation is a major equation that governs the magnetisation dynamics.

[1] $\mathbf{n}$ is the normal to the plane

Magnetisation dynamics, describe the torque-driven motion of magnetic moments. The generalised LLG formulation is given by [122]:

$$\begin{aligned}\frac{d\mathbf{M}(\mathbf{r},t)}{dt} &= -|\gamma|\mathbf{M}\times\mu_0\mathbf{H}_{\text{eff}} + \frac{\alpha}{M_s}\mathbf{M}\times\frac{d\mathbf{M}}{dt} \\ &= |\gamma|\mathbf{M}\times\nabla_{\mathbf{M}}\mathrm{E} + \frac{\alpha}{M_s}\mathbf{M}\times\frac{d\mathbf{M}}{dt}\end{aligned} \tag{3.6}$$

where $d\mathbf{M}/dt$ represents the rate of change of the magnetisation vector, describing its precession about the effective magnetic field $\mathbf{H_{eff}}$. γ denotes the gyromagnetic constant[2], which is given by the ratio of the magnetic to the angular momentum of the electron. The effective field given by: $\mu_0\,\mathbf{H}_{\text{eff}} = -\nabla_{\mathbf{M}}\mathrm{E}$, is the functional derivative of the total free energy underpinning the magnetic system. The dimensionless Gilbert damping parameter α, quantifies the strength of the damping term hampering magnetisation dynamics. Figure [3.3] depicts the two right-hand side terms of the LLG equation. The first cross-product describes the precession; i.e. sketches out how the magnetic moment precesses around the effective magnetic field indefinitely, analogous to a spinning top influenced by an external torque, while the second cross-product gives an energy dissipation, which describes the relaxation and stabilisation towards the direction of the effective field.

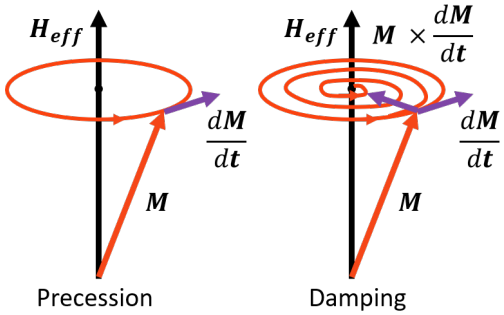

Figure 3.3: Schematic representation of the magnetisation dynamics. On the left, the magnetic moment precesses about the effective field indefinitely. On the right, the damping torque dissipates energy and the magnetisation spirals towards the effective field.

Sources of the driving field are any physical phenomenon that induces a temporal variation of the effective field seen by the magnetisation. Typical examples are micro- or RF-fields, spin-currents or time-dependent magneto-strictive effects. The damping, on the other hand, arises as a transfer of energy from the spin system to any reservoir such as magnon-phonon, magnon-electron or magnon-magnon interactions. Two classes of mechanisms describe the damping: intrinsic and extrinsic damping. This is exemplified, for the former as related to the spin-orbit interaction [123], [124] and causes spin-mixing[3], while the latter revolves mostly around structural inhomogeneities such as impurities, surface or volume non-uniformities and lattice mismatch due to strain, or scatterings [125], among others.

2.1 Spin-Waves or Magnons

From equation [3.6], magnetisation is defined for a space- and time- dependent precession of the magnetic moment. The solutions of this equation describe the collective precessional motion of magnetic moments, or more particularly Spin Waves (SWs). They were first predicted by F. Bloch [1905-1983] [126]. Spin-Waves, or in corpuscular theory- Magnons, are dynamic eigen-excitations of the magnetic order, whereby the associated frequency f_{SW} and wavelength (λ_{SW}) are fixed by the strength of the long-range magnetic dipole-dipole and the short-range exchange interactions. For usual ferromagnets, Fe, Co, Ni etc; the SW frequencies typically fall within the sub-GHz to several tenths of GHz [114]. Figure [3.4] is an illustration of the precession of a spin-wave with the associated λ_{SW}.

[2] By convention, throughout this manuscript, γ is assumed to be strictly positive

[3] In the presence of spin-orbit coupling, the spin states identified as 'up' and 'down' cease to be stationary eigen-states of the system.

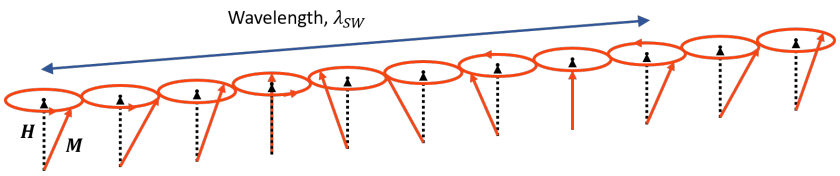

Figure 3.4: Schematic representation of a Spin-wave propagation. Note the motion of individual magnetic moments.

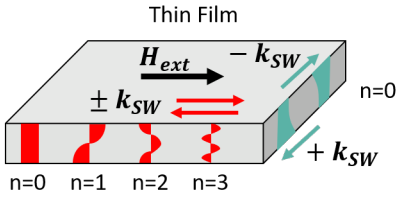

Figure 3.5: Surface (green) and Volume (red) SW propagation in the thin-film geometry.

2.1.1 Zoology of Spin-Waves

For magnetic thin films, the presence of magnetic surface charges results in the generation of additional dynamic demagnetising fields, leading to a more diverse SW spectrum. Figure [3.5], shows for the small wave-vector approximation $k_{\mathrm{SW}}d = 0$[1], two kinds of SW propagating in a thin-film configuration. The red-labelled volume SW exhibit an infinite number of thickness modes, where the SW amplitude oscillates periodically throughout the film's thickness. These mode frequencies are influenced by the film thickness resulting in a series of harmonics [127], while the surface SW modes are evanescent in the film thickness.

Figure [3.6], is a schematic representation of the dispersion relation for different magnetic configuration and two harmonics. In the case of out-of-plane magnetised film, we have the existence of the isotropic forward volume magneto-static waves (FVMSW). On the other hand, for in-plane magnetised films, the SW modes depend on the direction of SW propagation. If the latter is parallel to the direction of static magnetisation, we have the backward volume magneto static wave (BVMSW), and conversely for wave-vector perpendicular to $\mathbf{H}_{\mathrm{EXT}}$, we have the existence of magneto static surface wave (MSSW), commonly referred to as the Damon-Eshbach mode. This wave is chiral, with its amplitude decreasing exponentially from the film surface [128]. As briefly mentioned above, dipolar interaction dominates the dispersion curves for k_{SW} that are small or on par with the inverse film thickness. The BVMSW exhibits negative group velocity while the FVMSW and MSSW modes exhibit positive group velocities. At higher wavevectors, characterised by the prevalence of isotropic exchange interaction, the MSSW mode can be seen to transform into one of the volume modes.

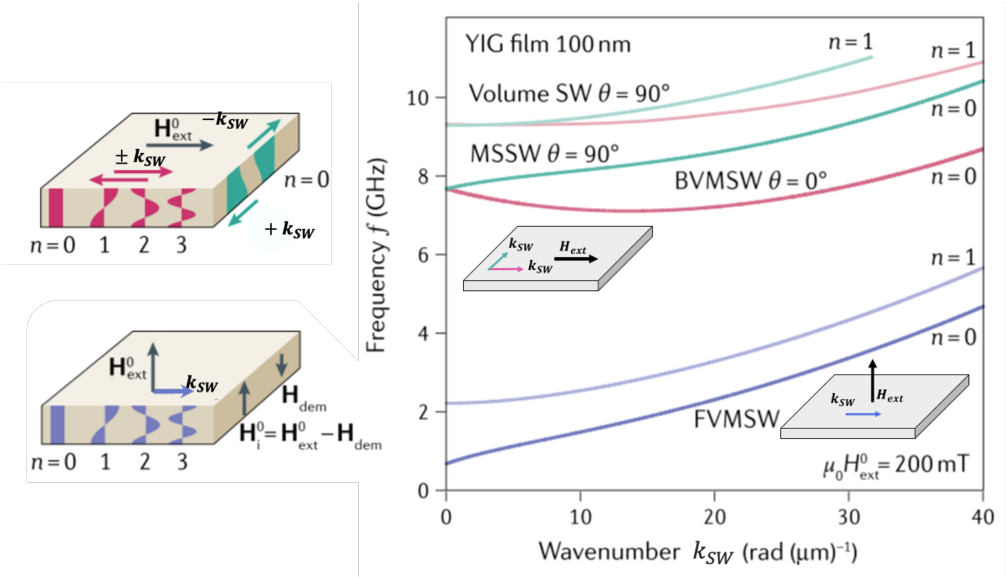

Figure 3.6: Spin-wave spectra for different configuration in the case of a 100 nm-thick YIG film and $\mu_0 \mathrm{H}_{\mathrm{EXT}} = 200$ mT. Adapted from [127].

3 Magnetic Resonance

The rich properties and tunability of SWs, along with careful material selection, have opened up a wide range of applications, from fundamental research to practical implementations. This section opens by laying the general framework for calculating the eigen spin-wave frequency and the corresponding eigen modes. Then, the reader is introduced to the excitation, detection and manipulation techniques surrounding spinwaves.

3.1 Eigen-frequency

The LLG equation [3.6] written in the spherical reference frame $\{\mathrm{M_s}, \theta, \phi\}$ becomes:

$$\frac{d\mathbf{M}(\mathbf{r},t)}{dt} = |\gamma|\mathbf{M} \times \nabla_{\mathbf{M}}\mathrm{E} + \frac{\alpha}{M_\mathrm{s}}\mathbf{M} \times \frac{d\mathbf{M}}{dt}$$

$$\begin{pmatrix} \dot{M}_\mathrm{s} \\ M_\mathrm{s}\dot{\theta} \\ M_\mathrm{s}\sin\theta\dot{\phi} \end{pmatrix} = \gamma \begin{pmatrix} M_\mathrm{s} \\ 0 \\ 0 \end{pmatrix} \times \begin{pmatrix} \nabla_{M_\mathrm{s}} E \\ \frac{1}{M_\mathrm{s}}\nabla_\theta E \\ \frac{1}{M_\mathrm{s}\sin\theta}\nabla_\phi E \end{pmatrix} + \frac{\alpha}{M_\mathrm{s}} \begin{pmatrix} M_\mathrm{s} \\ 0 \\ 0 \end{pmatrix} \times \begin{pmatrix} \dot{M}_\mathrm{s} \\ M_\mathrm{s}\dot{\theta} \\ M_\mathrm{s}\sin\theta\dot{\phi} \end{pmatrix} \tag{3.7}$$

The norm of the magnetic moment is considered independent of time and space. This implies that $\dot{M}_\mathrm{s} = 0$ and $\nabla_{\mathrm{M_s}} = 0$. If the magnetic oscillations are small such that: $\theta = \theta_0 + \delta\theta$ and $\phi = \phi_0 + \delta\phi$, equation [3.7] can be reduced to:

$$\begin{cases} \dot{\delta\theta} = -\dfrac{\gamma}{M_\mathrm{s}\sin\theta_0}\nabla_\phi E - \alpha\sin\theta_0\,\dot{\delta\phi} \\ \dot{\delta\phi} = \dfrac{\gamma}{M_\mathrm{s}\sin\theta_0}\nabla_\theta E + \dfrac{\alpha}{\sin\theta_0}\,\dot{\delta\theta} \end{cases} \tag{3.8}$$

where

$$\begin{cases} \nabla_{\theta|_{\theta=\theta_0}} E = E_{\theta\theta}\,\delta\theta + E_{\theta\phi}\,\delta\phi \\ \nabla_{\phi|_{\phi=\phi_0}} E = E_{\phi\phi}\,\delta\phi + E_{\theta\phi}\,\delta\theta \end{cases}$$

Oscillatory solutions of the form $\delta\theta = \delta\theta_0\, e^{i\omega t}$ and $\delta\phi = \delta\phi_0\, e^{i\omega t}$ are considered. The determinant of the coupled equations [3.7] yields the complex angular frequency ω:

$$\omega = \frac{1}{\sqrt{1+\alpha^2}}\sqrt{\left(\frac{\gamma^2}{\sin^2\theta_0}\right)\left(E_{\phi\phi}E_{\theta\theta} - {E_{\theta\phi}}^2\right) - \frac{\alpha^2\,\gamma^2\,{H_\alpha}^2}{4(1+\alpha^2)}} + i\frac{\alpha\,\gamma\,H_\alpha}{2(1+\alpha^2)} \tag{3.9}$$

where $H_\alpha = E_{\theta\theta} + \frac{E_{\phi\phi}}{\sin^2\theta_0}$

3.2 SW excitation and detection techniques

Exciting spinwaves involves inducing collective precession of magnetic moments within the material. Several techniques exist in the literature with the most common being cavity and broadband ferromagnetic resonance (FMR), Brillouin Light Scattering (BLS), Spin-polarised current and magneto-striction among others.

Cavity FMR

In an FMR experiment, a weak oscillating radio-frequency (RF) or microwave field is used to put into precession the magnetic moments. By gradually adjusting the applied magnetic field or the oscillating frequency, the eigen SW frequency is matched and resonance conditions- equality of SW frequency and wave-vector, are matched, thereby energy is absorbed from the wave source driving precession. For several decades, FMR spectroscopy has been conducted using microwave cavities [129], [130]. This setup is highly sensitive as it exploits resonant amplifications of the small FMR signals through the cavity. Figure [3.7], is a representation of a magnetic sample in a cavity-FMR setup. However, these microwave cavity resonators are tuned to operate at a single resonance frequency, fixed by the dimensions of the cavity. These frequencies are typically 9, 36 and 115 GHz.

Broadband-FMR

The broadband FMR (BB-FMR) is an inductive method used during the thesis to characterise magnetisation dynamics [131]. This technique consists of a microwave strip-line or a coplanar waveguide (CPW), onto which the sample is placed, and connected on both ends to a Vector Network Analyser. Magnetic precession is induced by the magnetic field generated by microwave current flowing through the strip-line. The FMR response of the sample is measured by a frequency sweep at fixed field. As the VNA functions as both the signal source and receiver, scattering parameters in transmission and in reflection, representing proxy strength of the microwave magnetic absorption, are collected during a typical measurement. Nowadays, broadband FMR (BB-FMR) readily allows for the continuous measurements of frequencies up to several tenths of GHz (typically $\approx$ kHz to 40 GHz). However, due to the absence of resonant amplification, BB-FMR typically exhibits lower sensitivity compared to cavity-FMR [132].

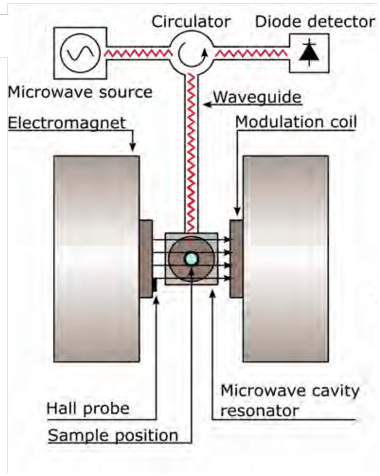

Figure 3.7: Schematic representation of the Cavity-FMR technique. The alternating μ-wave is guided onto the sample in the cavity. The electromagnet serves as field sweep favouring resonant conditions. Adapted from [133].

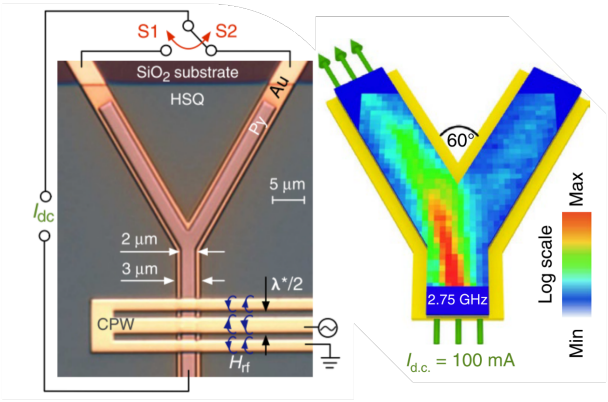

Figure 3.8: Investigation of SW with BLS on a YIG sample. **Left:** Microscope image displaying a 2D Y-shaped spin-wave multiplexer alongside the microwave antenna-CPW and leads for direct current connections. Blue arrows illustrate the oscillating fields surrounding the antenna useful for SW controlled dispersion and propagation. **Right:** 2D BLS intensity map of SW propagation at 2.75 GHz excitation. Adapted from [134].

Brillouin Light Scattering: BLS

Brillouin Light Scattering (BLS), spectroscopy is a powerful technique, relying on the inelastic scattering of light, for studying spin waves (SWs) and other elemental excitation in materials, such as phonons. It is based on the difference in frequency/wave-vector between the incident and the outgoing radiation off a magnetic surface, resultant of an absorption/emission of a magnon. One of the foremost advantage of BLS lies in its remarkable sensitivity, particularly adept at discerning weak signals emanating from thermally excited incoherent magnons, even within ultra-thin magnetic materials [135]. Nowadays, advancements in Fabry-Perot (FP) interferometry have notably improved the signal-to-noise ratio, with the typical frequency range going from 3-to-300 GHz and typical SW wave-vectors are 3-to-23.6 μm^{-1}. BLS provides information about temporal, spatial and phase evolution of SWs in magnetic systems. Figure [3.8] is diagram showing a microscopic image of microwave CPW-antenna and its Y-shaped track or multiplexer and the corresponding BLS intensity map. As the SWs have an anisotropic dispersion relation parallel and perpendicular to the equilibrium magnetisation, the SWs propagate on either one of the Permalloy track. **Right**: shows the spin-waves travelling on the left branch. By playing on this anisotropic dispersion relation SW can be used for gating or multiplexing among others [134]. In this manuscript, the excitation of spin-waves is made by interaction with surface acoustic waves, via magneto-elastic effect. As the wave propagates, its associated strains (or deformations) vary and so does its magneto-elastic energy. From this energy are derived magneto-elastic

effective fields that drive magnetisation dynamics governed by the Smit-Beljers equation, c.f. Chapter [5].

3.3 Magnonics

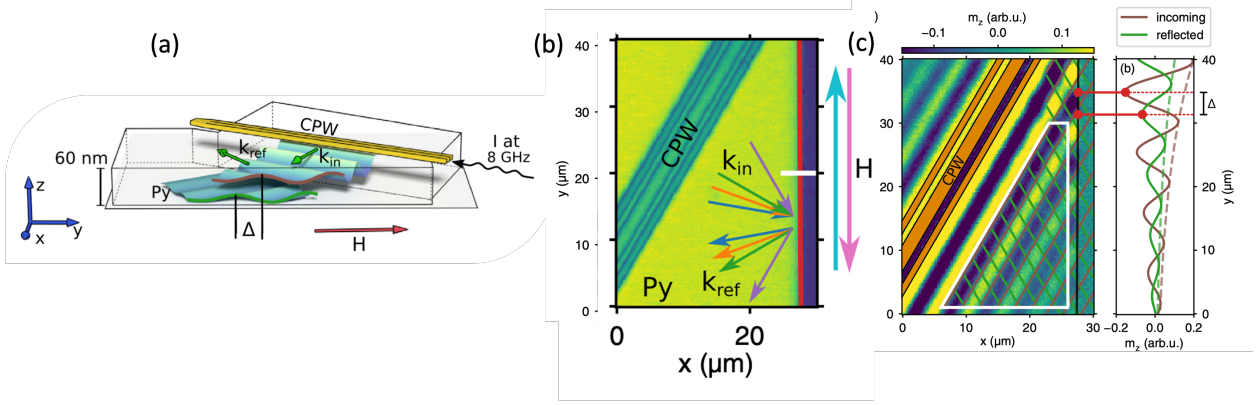

Figure 3.9: **(a)**: Sketch of CPW exciting the SWs at a 30° angle. **(b)-(c)**: Upon reflection, the interference pattern is represented with a phase shift synonymous of a total internal reflection. Adapted from [136].

The rise of spintronics and the use of spin-polarised currents, with respect to conventional electronics has in the process, ushered the development of a sub-field: Magnonics. Specifically, magnonics is the spinwave-based approach to information storage, manipulation and transmission. The large variety of simple techniques available for the excitation and detection of SW concomitant to the easy control of their dispersion relation, by adjusting magnetic field, altering geometry and material composition, and temperature, has sparked interest for a multitude of potential applications. One major advantage of using SW for signal processing is provided by their wave nature. Indeed, as they are waves, they can be reflected [137], diffracted [138], focused and made to interfere [139]. Figure [3.9], is a measurement of the phase shift following Damon-Esbach SW mode exhibiting total internal reflection in a 60nm-thick Py layer. As the incoming SW is reflected off the edges at an angle of 30°, larger than the critical angle, the SW undergoes a total internal reflection. The reflected SW has a phase shift with respect to its incoming counterpart and thus interferes constructively or destructively in space. This interaction is observed using time-resolved scanning Kerr microscopy where the Kerr signal is proportional to the dynamic out-of-plane magnetisation component m_z. Figure [3.10] on the other hand, is a representation of a SW-based spectrum analyser. The SWs are generated by the microstrip antenna as seen on the **Left**, and propagate towards the diffraction gratings. These diffract and focus the SWs towards the readout. **Right**: is the simulated snapshot of the SWs and their corresponding spatial diffraction patterns. It can be seen that the SWs exhibit similar patterns to electro-magnetic waves.

Figure 3.10: **Left:** Schematic representation of a spinwave-based spectrum analyser on a YIG film. The latter uses a microstrip antenna along the serrated edge of a magnetic film, serving both, as a source of SWs and a concave diffraction grating. The curved grating focuses SWs of different frequencies into distinct spatial points, where nano-scale inductive antenna array detects them. **Right:** Micromagnetic simulation snapshot showing the colour map of propagating SWs and interference patterns. Results shows that SWs behave similar to linear waves interference. Adapted from [140].

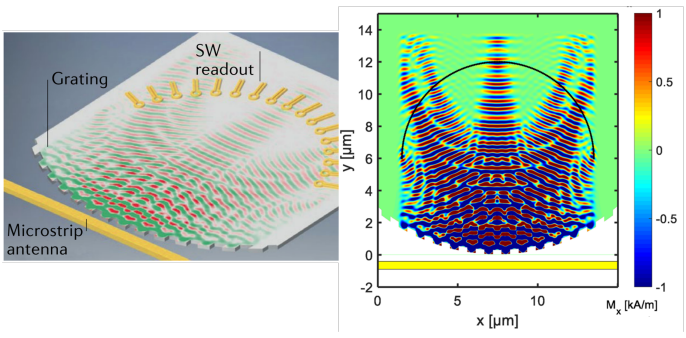

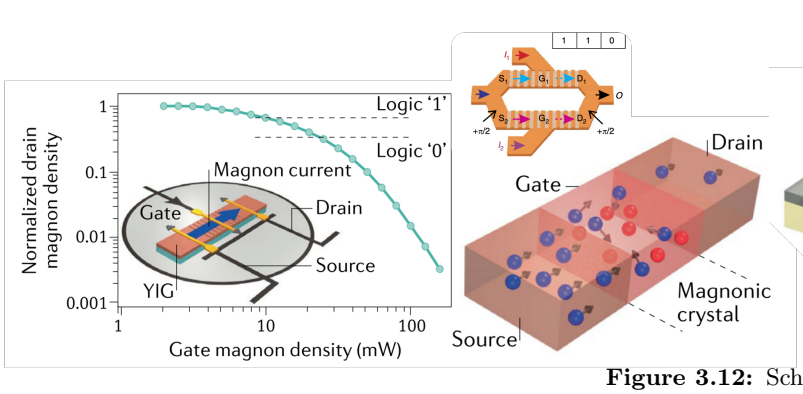

Figure 3.11: Schematic of the magnon transistor. Top: It is based on a YIG film with an array of parallel grooves on its surface. Magnons are generated into the source, scattered and detected at its drain using microstrip antennas. The high degree of gate magnon localisation inside the crystal consequently leads to high scattering probabilities. Bottom: The horizontal dashed lines define the drain density levels corresponding to '1′ and '0′ for logic gating. Adapted from [13].

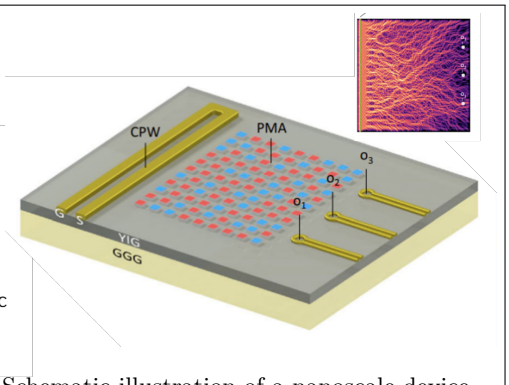

Figure 3.12: Schematic illustration of a nanoscale device where input signals are processed through the propagation and interference of spin waves in a magnetic thin film. The configuration of small PMA magnets on top of the film determines the scattering and routing of these waves, enabling complex computational tasks to be performed. **Top:** shows specific points where the intensity of the spin waves is detected. These points correspond to the areas where the system is designed to read the computation outputs. This work shows the potential of integrating wave-based computing and magnetic materials to achieve highly interconnected, low-power neuromorphic functions. Adapted from [141].

Likewise, a promising endeavour for using spin-waves in computing technology and data processing involves exploiting the additional, phase-related, degree of freedom [11]. Controlled manipulation of amplitude and phases enables the design of interference-based SW logic gates[142], splitters, phase shifters and transistors [13], possibly bypassing the needs of tens of conventional Complementary Metal-Oxide Semiconductor (CMOS)[4] components. Figure [3.11] is an example of a magnon-based transistor. It consists of a grooved YIG-film crystal, serving as the gate, source, and drain regions. Magnons injected into the gate modulate the flow of magnon current from the source to the drain through non-linear scattering. This modulation allows the YIG film to act as a switch depending on the drain magnon density, enabling basic logical operations without electric signals. Figure [3.12] illustrates the design and function of a neural network made using non-linear SW interference. The SWs are generated using the CPW, and directed towards a grid of perpendicular magnetised nanodots. The up or down magnetic configurations of the latter alter the SWs propagation and its intensity at different points away from the CPW. This magnetic grid-like structure can thus direct the waves to specific output points, effectively performing operations like matrix multiplication or pattern recognition.

Commonly used materials include polycrystalline metallic films of Permalloy ($Ni_{81}Fe_{19}$, $\alpha_{Py} \approx 10^{-5}$) [143] and single-crystal films of Yttrium Iron Garnet (YIG[5], $\alpha_{YIG} \approx 10^{-5}$) [12], known for their low magnetic damping. Ferromagnetic Heusler compounds, which offer high spin polarisation, saturation magnetisation, and Curie temperature and CoFeB composites exhibit promising characteristics for magnonic applications [127].

[4]CMOS components are fundamental building blocks of modern integrated circuits, widely used in various electronic devices

[5]$Y_3Fe_50_{12}$ is an outstanding material for magnonics, owing to its uniquely low magnetic damping, due to the zero orbital moments of the magnetic ions:

Chapter Summary

1. In this chapter, the reader has been introduced to the equation governing magnetisation dynamics, the LLG equation, and the corresponding magnetic energy terms driving precession. The general solution of the SW eigen-frequency has been developed. This will be useful in Chapter [5].

2. In the second part of the chapter, the reader is introduced to SW excitation and detection techniques and to some application of SW in spintronic devices.

Chapter 4

SAW Theory

Objectives

This chapter introduces the basic concepts around Acoustic waves, or more particularly Surface Acoustic Waves. This is essential for understanding strain relation to FMR. Then, using BLS and pico-second acoustics, the experimental determination of the complete set of FeRh elastic constant is given. This serves as the foundation for introducing the Farnell-Adler method, which is the principles in calculating the acoustic modes and acoustic velocities for layer-on-substrates structures. The chapter concludes by explaining the concept of piezoelectricity and the SAW generation using the IDTs, before the schematic description of our all electrical SAW generation and detection setup is given.

Contents

1 Acoustic Waves

Chapter [1] pointed out the influence of hydrostatic pressure and strains on the magneto-structural phase transition of FeRh. By strains, it was firstly demonstrated the influence of static strain originating from the growth-induced lattice mismatch between thin FeRh films and their substrate and the effect of an electric field over a piezoelectric substrate, in driving giant magnetisation change. A step forward consists in studying dynamic strains, or in other words, time- and space-varying regions of compression and expansion. One such example is the acoustic wave. Acoustic waves or sound waves, are mechanical vibrations that transport energy from one point to another. However, acoustic waves (AWs) are not limited to sound waves, but consist of a whole frequency spectrum ranging from seismic waves, generated during earthquakes in the Hertz regime, through well-known human hearing and ultrasound frequency ranges and up to the hypersound regimes where frequencies are well above the 1 gigahertz. Figure [4.1], is a representation of the acoustic spectrum and the commonly associated frequencies and major examples associated to each frequency regime. In this manuscript, the focus is made on acoustic or elastic waves in the frequency range going from $\sim$ 100 MHz to $\sim$ 1 GHz.

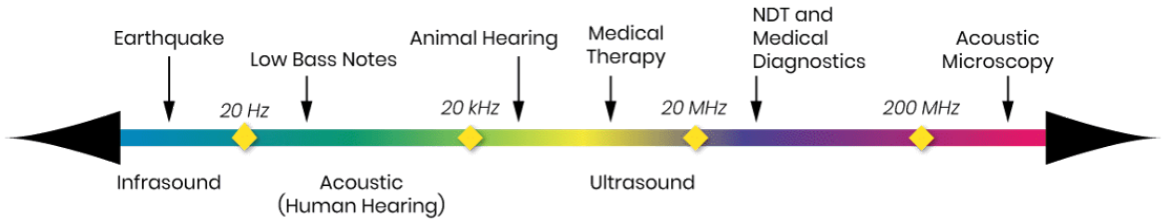

Figure 4.1: Typical frequency Spectrum of acoustic waves spanning from infrasonic frequencies below 20 Hz to ultrasonic frequencies above 20 kHz, which are respectively below and above the human hearing threshold frequencies, known as the audible range- where most human hearing occurs. Different sources generate waves with different frequency characteristics and acoustic power. These include extremely destructive seismic waves produced by tectonic plates movements or volcanic explosions, to non-destructive acoustic microscopy imaging that provides detailed insights into the internal structure and integrity of materials and components across various industries, enhancing quality control, research, and development processes. Adapted from [144]

The dynamic wave equation in its various forms has been contrived and mathematically elaborated by numerous mathematicians and physicists throughout history. Following I. Newton's laws of motion, J. R d'Alembert [1717-1783] penned the uniaxial dynamics while contributions from L. Euler [1707-1783], J. Fourier [1768-1830] and A.L Cauchy [1789-1857] led to the generalised wave equation, which elucidates the interplay between time and space distribution of acoustic pressure p, density ρ and acoustic velocity V_{AW}[1], for a compressible material medium. These generalised parameters can be either scalar or vector components and results in:

$$\frac{\partial^2 p(\mathbf{r},t)}{\partial t^2} - {V_{\mathrm{AW}}}^2 \Delta p(\mathbf{r},t) = 0 \quad \Leftrightarrow \quad \frac{\partial^2 \mathbf{u}(\mathbf{r},t)}{\partial t^2} - {V_{\mathrm{AW}}}^2 \Delta \mathbf{u}(\mathbf{r},t) = 0 \tag{4.1}$$

where $\mathbf{u}(\mathbf{r},t)$ is the displacement vector field. From continuum mechanics and in the linear approximation, a solid body, under the action of external forces, experiences a deformation its point vector $\mathbf{r}$ undergoes a transformation to $\mathbf{r}'$. The displacement vector field is thus given as :

$$\mathbf{u}(\mathbf{r},t) = \mathbf{r}'(\mathbf{r},t) - \mathbf{r}(\mathbf{r},t) \tag{4.2}$$

In the case of an acoustic wave propagating in a medium, the alternating regions of compression and expansion lead to displacement of the material media defined by the displacement vector fields. Figure [4.2], is a representation of the collective longitudinal and shear oscillations of the material media.

Historically Bulk Acoustic Waves (BAWs), which propagate through the volume of a material, have played a crucial role in condensed matter physics both for destructive and non-destructive applications. In destructive applications, known as fracture mechanics, they have been used to understand

[1] The acoustic velocity is given by $V_{\mathrm{AW}} = \sqrt{\partial p(\mathbf{r},t)/\partial \rho}$

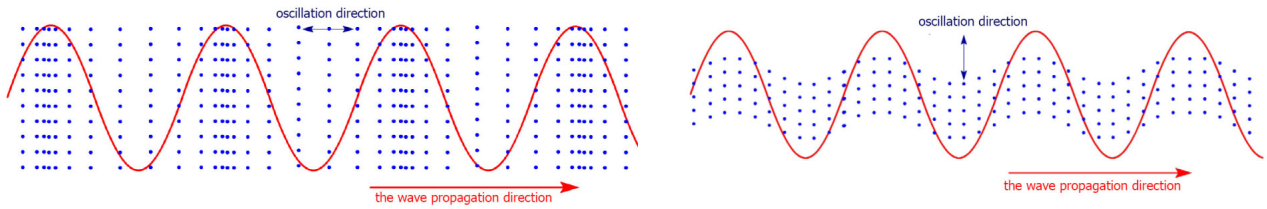

Figure 4.2: Diagram showing the propagation of an elastic wave and the associated particle displacements. **(a)**: For a longitudinal wave, the particles oscillate parallel to the direction of propagation. **(b)**: In the case of a shear or transverse wave, the particles are in a perpendicular motion with respect to the wave vector. Adapted from [145].

stress distribution, deformation and failure modes by observing the materials' response to high-stress conditions [146]. This has provided valuable insights into material strength and durability, guiding the development of more resilient materials. Conversely, in non-destructive applications, bulk waves have been pivotal in techniques such as ultrasonic testing and acoustic microscopy, where they enable the inspection and characterisation of materials without causing any harm. These methods have been employed to detect internal flaws, assess material properties such as elastic constants, and ensure structural integrity in critical components across industries such as aerospace, automotive, and construction [147], [148]. Transitioning from the study of bulk waves, the exploration of Surface Acoustic Waves (SAWs) has opened new avenues. Unlike bulk waves, which travel through the volume of a material, surface waves propagate along the material's surface. These waves, such as Rayleigh and Love waves, are particularly sensitive to surface and near-surface phenomena, making them invaluable for applications requiring detailed surface analysis. Moreover, standing at a pivotal moment where the application of sensors across various fields is at its peak and will undeniably keep on increasing, a shift towards more compact and integrated systems is needed [149]. SAW-based devices represent a perfect example enabling miniaturisation while maintaining both sensing and actuation under a single platform.

1.1 Surface Acoustic Waves

Surface acoustic waves (SAWs) are elastic waves first described by Lord Rayleigh [1842-1919]. The elastic energy generated by the wave propagation is typically confined close to the surface, $\approx$ 1-1.5 λ_{SAW}, and decreases exponentially in the depth of the material medium, making SAWs excellent representation of guided evanescent waves [150]. Harnessing these characteristics, SAWs are extremely suitable for sensing and detection applications due to their ability to interact with surface-bound phenomena, such as defects, coatings or biological molecules. This interaction leads to changes in the wave properties, such as amplitude and phase that can be analysed to deduce information about the environment or the surface [151]. Furthermore, SAW-based devices are implemented in a range of signal processing applications, such as resonators, filters among others, due to their long distance and low-loss propagation, frequency response and device integration [149], [152]. Several SAW modes exist and are apparent by their accompanied particle motion and potential applications. The most common types of SAWs include: Rayleigh, Sezawa and Love waves among others.

1.1.1 Rayleigh Waves

The Rayleigh elastic wave is characterised by the elliptical motion, in the vertical plane, of the elastic displacements. Figure [4.3]**(a)**: is a representation of a propagating Rayleigh wave. In this configuration, the particle motion is confined to the xz plane, with a two-dimensional wave solution. Indeed, as the Rayleigh wave mode involves a combination of both the longitudinal, $\mathbf{u}_L$, and transverse, $\mathbf{u}_T$, displacement vectors, the dual-mode motion results in the surface particles moving in an undulating elliptical motion, similar to ocean waves. In this type of wave, the velocity depends exclusively on the properties of the substrate and the crystalline structure [149]. The effective penetration of the Rayleigh waves decreases exponentially within the substrate thickness and is usually less than a wavelength. Examples of media commonly used for the Rayleigh wave mode excitation include: 128°

and 41° YX Lithium Niobate (LNO), ST-Quartz, Gallium Arsenide (GaAs), Zinc-Oxide (ZnO) among others [149], [153].

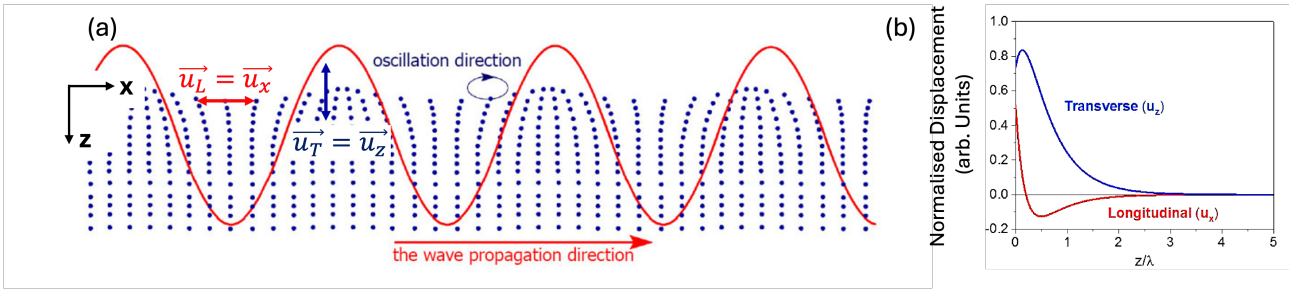

Figure 4.3: (a): Diagram showing the propagation of a Rayleigh-type SAW. As the Rayleigh wave travels along the surface, the material media move in an elliptical path, in the plane vertical and parallel to the direction of propagation. The motion of particles decreases exponentially with depth from the surface, making Rayleigh waves predominantly surface waves. Adapted from [145]. **(b):** Normalised displacement for the transverse and longitudinal components. Note that both components decrease exponentially with depth, and that the longitudinal component changes sign in the layer. Adapted from [154].

Sezawa Waves

Sezawa waves, named after Y. Sezawa [1895-1944], are the higher order modes of the fundamental Rayleigh waves. They are only present in a layered medium of different acoustic impedance[2], more specifically where a thin, slower (lower velocity) layer is deposited on a faster (higher velocity) substrate. Compared to Rayleigh mode, Sezawa modes penetrate less deeper in the substrate layer and can thus collect more information about sub-surface and interface structures. Moreover, these modes have higher phase velocity and consequently higher SAW frequencies [153].

1.1.2 Shear horizontal Waves

Shear Horizontal, also known as Transverse waves, are a special type of SAWs whereby the particle motion is exclusively perpendicular to the direction of propagation and parallel to the surface. In the absence of longitudinal deformations, the consecutive top surface layers slide over one another leading to shear deformation across the material medium. This type of deformation does not interact with fluid media. Moreover, one advantage of shear horizontal SAWs is that they do not decay exponentially with depth, but can travel several wavelength or permeate the entire thickness of the substrate. Consequently, they are excellent to probe highly attenuating environments, underwater inspection or for monitoring pipeline. Shear horizontal waves are commonly used in materials such as: 36° YX $LiTaO_3$, 36° YX LNO, Quartz, $KNbO_3$ [149].

Love Waves

Love waves, named after A.E Love [1863-1940], are SAWs that involve purely transverse particle motion but in the horizontal plane, and accompanied by an exponential amplitude decay in depth. These are waves that propagate through a thin deposited layer on top of a substrate. Love waves are guided only if their transverse velocities are higher in the substrate than in the layer, and result in very high acoustic energies concentrated in the thin guiding layer [155]. As such, Love waves are extremely sensitive to mass loading[3]. These waves are also important in seismology as they are usually the first waves detected following an earthquake. Illustrations of standard media used to generate Love waves are SiO_2, ZnO, TiO_2 [149].

[2] Acoustic impedance is a measure of a medium's opposition to sound waves being propagated inside it. The acoustic impedance is given as: $Z_0 = \sqrt{\rho V_{AW}}$

[3] Mass loading refers to the addition of a secondary layer, particles or external electromagnetic or strain field on a well-known substrate under study

2 Linear Elasticity

Building upon the displacement vector field, equation [4.2], this section provides the fundamental concepts of elasticity, essential for understanding the generation, propagation and interaction of SAWs. It is worth noting that this manuscript solely addresses linear elasticity, and the point of view being considered here is that of continuum mechanics, meaning that matter is taken at a macroscopic scale with physical properties varying continuously from one point to another, except along certain surfaces of discontinuity[4].

2.1 Introduction to Strain, Stress and Hooke's Law

Strain

A solid material's response under applied forces results in a relative displacement. The point vector $\mathbf{r}(\mathbf{r},t)$ can undergo not only a change in length, but also a local rotation. This relative displacement vector is thus given as:

$$\mathbf{du}(\mathbf{r},t) = \mathbf{dr}'(\mathbf{r},t) - \mathbf{dr}(\mathbf{r},t) = \sum_{\mathrm{i,j}} \underbrace{\frac{\partial u_\mathrm{i}}{\partial x_\mathrm{j}}}_{\nabla_\mathrm{x}\mathbf{u}} dx_\mathrm{j}\,\mathbf{x}_\mathrm{i} = \sum_{\mathrm{i,j}} \left(\varepsilon_\mathrm{ij} + \Omega_\mathrm{ij}\right) dx_\mathrm{j}\,\mathbf{x}_\mathrm{i} \tag{4.3}$$

where geometric compatibility imposes the existence of symmetric (ε_ij), and anti-symmetric (Ω_ij), tensors respectively:

$$\nabla_\mathrm{x}\mathbf{u} = \underline{\underline{\varepsilon}} + \underline{\underline{\Omega}}$$

The concept of strain quantifies the local deformation or relative displacement of material points relative to a rigid body displacement [156]. The Eulerian-Almansi finite strain tensor, $\underline{\underline{\varepsilon}}$, and the local rotational strain tensor, $\underline{\underline{\Omega}}$, in the small-perturbation theory are respectively given as [155]:

$$\varepsilon_\mathrm{ij} = \frac{1}{2}\left(\frac{\partial u_\mathrm{i}}{\partial x_\mathrm{j}} + \frac{\partial u_\mathrm{j}}{\partial x_\mathrm{i}}\right) \qquad \& \qquad \Omega_\mathrm{ij} = \frac{1}{2}\left(\frac{\partial u_\mathrm{i}}{\partial x_\mathrm{j}} - \frac{\partial u_\mathrm{j}}{\partial x_\mathrm{i}}\right) \tag{4.4}$$

It is useful to note that the diagonal terms of the strain tensor correspond to relative elongations, while the trace denotes a local volume variation. The non-diagonal terms, on the other hand, give the shear strain components. Furthermore, it has been demonstrated that in a bulk infinite material, the local rotations do not contribute to the equations of motion as they lack inertial effects [155]. Typical values of strain components for propagating SAWs range from 10^{-6} to 10^{-3}.

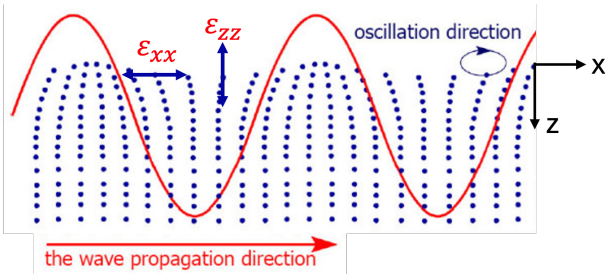

Figure 4.4: Representation of the ε_{xx} and ε_{zz} oscillating strain components for a propagating Rayleigh wave. Adapted from [145].

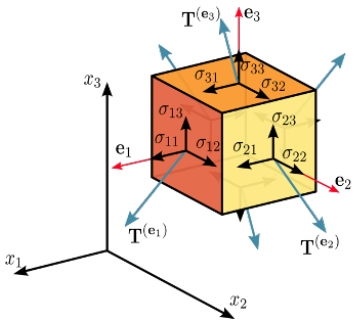

Figure 4.5: Components of stress tensor in three dimensions. Adapted from [157].

Stress

The external forces inducing deformations in the solid material are either through mechanical contact at one surface, σ_ij, or from applied fields within its volume, f_i. These forces- mechanical traction and field-induced forces like gravity or electric fields- facilitate mechanical equilibrium by acting between

[4] A more precise definition of continuum mechanics refers to the fluctuations in measurements through their spatial and temporal averages. These fluctuations are considered independent of the number of molecules within the volume during measurement. It is this statistical homogeneity that somewhat justifies the concept of a continuous medium.

neighbouring particles, which transmit them across surfaces within the solid, ensuring stability and enabling material response to the external stimuli [155]. The resultant force for a solid material in mechanical equilibrium is thus given by:

$$T_{\mathrm{i}} = \int_S \sigma_{\mathrm{ij}}\, ds + \int_V f_{\mathrm{i}}\, dV = \int_V \left(\frac{\partial \sigma_{\mathrm{ij}}}{\partial x_{\mathrm{j}}} + f_{\mathrm{i}} \right) dV$$

and the elasto-dynamical equation of motion governing the local displacement through the medium is written, in terms of the stress tensor, σ_{ij}, and displacement u_{i}, as:

$$\frac{\partial \sigma_{\mathrm{ij}}}{\partial x_{\mathrm{j}}} + f_{\mathrm{i}} = \rho \frac{\partial^2 u_{\mathrm{i}}}{\partial t^2} \tag{4.5}$$

Hooke's Law

A Taylor expansion series of the stress tensor for an elastic material solid gives [158]:

$$\sigma_{\mathrm{ij}}\left(\varepsilon_{\mathrm{kl}}\right) = \underbrace{\sigma_{\mathrm{ij}}\left(0\right)}_{\to 0} + \left(\frac{\partial \sigma_{\mathrm{ij}}\left(\varepsilon_{\mathrm{kl}}\right)}{\partial \varepsilon_{\mathrm{kl}}} \right)_{\varepsilon_{\mathrm{kl}}=0} \varepsilon_{\mathrm{kl}} + \frac{1}{2} \left(\frac{\partial^2 \sigma_{\mathrm{ij}}\left(\varepsilon_{\mathrm{kl}}\right)}{\partial \varepsilon_{\mathrm{kl}}\, \partial \varepsilon_{\mathrm{mn}}} \right)_{\varepsilon_{\mathrm{kl}},\varepsilon_{\mathrm{mn}}=0} \varepsilon_{\mathrm{kl}}\, \varepsilon_{\mathrm{mn}} + \ldots$$

In the approximation of small deformations the second-order term and above can be neglected, leading to the generalised Hooke's law and a bijection between stress and strain components via the stiffness tensor: $\underline{\underline{C}}$. The stiffness or elasticity tensor, is a rank-4 tensor and possesses 81 components (3^4).

$$\sigma_{\mathrm{ij}} = C_{\mathrm{ijkl}}\, \varepsilon_{\mathrm{kl}} \tag{4.6}$$

2.2 Elasto-dynamical wave equation

Using equation [4.4], the stress can be related to the displacement vector components by:

$$\sigma_{\mathrm{ij}} = \frac{1}{2} \sum_{\mathrm{kl}} C_{\mathrm{ijkl}} \left(\frac{\partial u_{\mathrm{k}}}{\partial x_{\mathrm{l}}} + \frac{\partial u_{\mathrm{l}}}{\partial x_{\mathrm{k}}} \right) = \sum_{\mathrm{kl}} C_{\mathrm{ijkl}} \frac{\partial u_{\mathrm{k}}}{\partial x_{\mathrm{l}}} \tag{4.7}$$

Neglecting gravitational effects, equation [4.5] thus gives the elasto-dynamical wave equation for an anisotropic crystal:

$$\rho \frac{\partial^2 u_{\mathrm{i}}}{\partial t^2} = \sum_{\mathrm{jkl}} C_{\mathrm{ijkl}} \frac{\partial^2 u_{\mathrm{l}}}{\partial x_{\mathrm{j}}\, \partial x_{\mathrm{k}}} \tag{4.8}$$

As $\varepsilon_{\mathrm{ij}}$ and σ_{ij} tensors are symmetric, permutations of pair indices of the elasticity tensor ($C_{\mathrm{ijkl}} = C_{\mathrm{jikl}}$ and $C_{\mathrm{ijkl}} = C_{\mathrm{ijlk}}$), do not affect equation [4.8]. This reduces the number of independent elastic components to 36. Using Voigt contraction[5] ($\mathrm{C}_{\underbrace{ij}_{\mathrm{x}}\underbrace{kl}_{\mathrm{y}}} \leftrightarrow \mathrm{C}_{\mathrm{xy}}$), these can thus be written in a 6×6 Tensor.

Furthermore, the differential of the Gibbs free energy (c.f. equation [1.2]) can be written using $\mathrm{dU} = \delta\mathrm{Q} + \delta\mathrm{W} = \mathrm{T\ dS} + \sigma_{\mathrm{ij}}\, \mathrm{d}\varepsilon_{\mathrm{ij}}$. This implies the following thermodynamic Maxwell relation:

$$C_{\mathrm{ijkl}} = \frac{\partial^2 G}{\partial \varepsilon_{\mathrm{ij}} \partial \varepsilon_{\mathrm{kl}}} = C_{\mathrm{klij}}$$

This property reduces the number of independent elastic components to 21, with C_{ij} being symmetric on both sides of the diagonal. Equation [4.9]-**Left** gives the elasticity tensor for a triclinic crystal system, i.e the system representing the most general crystallographic structure. Equation [4.9]-**Right**

[5] $\sigma = \begin{bmatrix} \sigma_{xx} & \sigma_{xy} & \sigma_{xz} \\ & \sigma_{yy} & \sigma_{yz} \\ & & \sigma_{zz} \end{bmatrix}$ (1, 6, 5, 4, 2, 3) The Voigt notation condenses the representation of tensor components and is typically used for symmetric tensors in solid mechanics. An unordered (i,j) pair indices can be arranged into a single vector of length 6, or a row vector of length 6.

gives the elasticity tensor for FeRh, which has a cubic symmetry. Additional symmetric invariances lead to only three independent elastic components: C_{11}, C_{12} and C_{44} [159].

$$C_{ij} = \underbrace{\begin{pmatrix} C_{11} & C_{12} & C_{13} & C_{14} & C_{15} & C_{16} \\ C_{12} & C_{22} & C_{23} & C_{24} & C_{25} & C_{26} \\ C_{13} & C_{23} & C_{33} & C_{34} & C_{35} & C_{36} \\ C_{14} & C_{24} & C_{34} & C_{44} & C_{45} & C_{46} \\ C_{15} & C_{25} & C_{35} & C_{45} & C_{55} & C_{56} \\ C_{16} & C_{26} & C_{36} & C_{46} & C_{56} & C_{66} \end{pmatrix}}_{\text{Triclinic case: maximum 21 independent } C_{ij}}; \quad C_{ij}^{\text{FeRh}} = \underbrace{\begin{pmatrix} C_{11} & C_{12} & C_{12} & 0 & 0 & 0 \\ C_{12} & C_{11} & C_{12} & 0 & 0 & 0 \\ C_{12} & C_{12} & C_{11} & 0 & 0 & 0 \\ 0 & 0 & 0 & C_{44} & 0 & 0 \\ 0 & 0 & 0 & 0 & C_{44} & 0 \\ 0 & 0 & 0 & 0 & 0 & C_{44} \end{pmatrix}}_{\text{FeRh (Cubic symmetry)} \rightarrow \text{ 3 independent } C_{ij}} \quad (4.9)$$

3 Acoustic wave velocities and acoustic modes

In this section, the solutions for acoustic wave modes and their corresponding velocities are determined. Three compressible media are considered. The first case deals with an infinite medium or the bulk medium and corresponds to the most commonly known wave equation as written in equations [4.1]. Then is considered the semi-infinite case, i.e. for a finite medium which corresponds to the situation where Rayleigh acoustic modes propagate. Thirdly is considered a layered medium which is closer to the Rayleigh wave propagation modes in this manuscript.

3.1 Bulk acoustic wave velocities

In this section, the solutions for acoustic wave modes and their corresponding velocities are determined. The displacement of the particles u_i, is given by an arbitrary function F, propagating to the right:

$$u_i = {u_i}^0 F\left(t - \frac{n_j\, x_j}{V_{AW}}\right)$$

with n_j a unit vector. The second derivatives with respect to time and space of equation [4.8] yield the Christofell equation:

$$\rho\, {V_{AW}}^2\, u_i^0 = \underbrace{C_{ijkl}\, n_j\, n_k}_{\Lambda_{il}}\, u_l^0 \quad (4.10)$$

The acoustic phase velocities and the acoustic wave modes of an acoustic wave propagating along the $\vec{n}$ direction, in a crystal of elastic stiffness C_{ijkl} are the eigen-values and eigen-vectors of Λ_{il}. For a given direction, there exists three phase velocities roots of the secular equation:

$$\mid \Lambda_{il} - \rho\, {V_{AW}}^2\, \delta_{il} \mid = 0 \quad (4.11)$$

3.1.1 Case of cubic crystal (e.g. FeRh)

Considering the form of the elasticity tensor for FeRh, equation [4.9] and the definition of Λ_{il}, plane wave solutions are given as:

$$\Lambda = \begin{pmatrix} C_{11}{n_1}^2 + C_{44}\,({n_2}^2 + {n_3}^2) & (C_{12} + C_{44})\, n_1 n_2 & (C_{12} + C_{44})\, n_1 n_3 \\ (C_{12} + C_{44})\, n_1 n_2 & C_{11}{n_2}^2 + C_{44}\,({n_1}^2 + {n_3}^2) & (C_{12} + C_{44})\, n_2 n_3 \\ (C_{12} + C_{44})\, n_1 n_3 & (C_{12} + C_{44})\, n_2 n_3 & C_{11}{n_3}^2 + C_{44}\,({n_1}^2 + {n_2}^2) \end{pmatrix} \quad (4.12)$$

Wave propagating along <100> direction

In this case, $n_1 = 1$ and $n_2 = n_3 = 0$. The three eigen-values, solutions of equation [4.11] are thus:
- a Longitudinal wave mode: $V_{AW,1} = V_L = \sqrt{\frac{C_{11}}{\rho}}$,
- two shear wave modes: $V_{AW,2,3} = V_T = \sqrt{\frac{C_{44}}{\rho}}$

Wave propagating along <110> direction

In this case, $n_1 = n_2 = 1$ and $n_3 = 0$. Solutions of equation [4.11] give three distinct wave velocities:
- One Pure shear wave: $V_{AW,1} = V_T = \sqrt{\frac{C_{44}}{\rho}}$ polarised parallel to x_3,
- One Quasi-shear waves: $V_{AW,2} = V_T = \sqrt{\frac{(C_{11}-C_{12})}{2\rho}}$ and,
- One Quasi-Longitudinal waves: $V_{AW,3} = V_L = \sqrt{\frac{(C_{11}+C_{12}+2C_{44})}{2\rho}}$.

3.2 Acoustic wave velocities for a semi-infinite medium

The volume acoustic wave propagation considered so far has been derived for an infinite medium, specifically for a propagating wave encountering no boundary conditions. However, these solutions are no longer valid when the medium is limited, for e.g. a semi-infinite medium[6]. In such cases, boundary conditions must be taken into account, and this significantly alters the behaviour of the wave mode and propagation. For instance, Rayleigh SAW modes propagate along the boundary with amplitudes that decay exponentially with depth. Additionally, the presence of boundaries can lead to the reflection, refraction, and mode conversion of waves, resulting in more complex wave interactions. In the semi-infinite medium, in order to determine the different acoustic propagation modes both the equations governing the propagation and the boundary constraints must be considered, with any acoustic solutions satisfying both sets of equations.

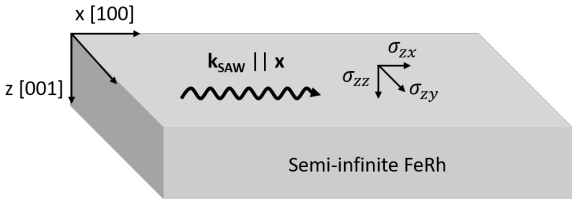

Figure 4.6: Schematics of a semi-infinite FeRh layer with cubic symmetry. The Rayleigh wave propagates along the x-axis and is evanescent along the z-axis. Note the stress tensors normal to the FeRh surface.

The Rayleigh wave velocity is investigated on a cubic FeRh layer. The Rayleigh wave is considered to propagate along the x-axis which is parallel to the crystallographic [100] direction. Recall, the elasticity tensor of this cubic FeRh layer is defined in equation [4.9].

Partial waves solutions

For a Rayleigh wave propagating in the semi-infinite layer, the particle displacements are in an elliptical motion in the {x,z} plane. The partial wave solutions are written as evanescent plane waves, with the attenuation coefficient $\zeta > 0$:

$$\begin{cases} u_x = U\, e^{(-\zeta z)}\, e^{i(\omega t - kx)} \\ u_y = 0 \\ u_z = W\, e^{(-\zeta z)}\, e^{i(\omega t - kx)} \end{cases} \tag{4.13}$$

The corresponding solutions of the elasto-dynamical wave equation [4.8] are thus:

$$\begin{cases} \rho_{FeRh}\dfrac{\partial^2 u_x}{\partial t^2} = C_{11}\dfrac{\partial^2 u_x}{\partial x^2} + C_{12}\dfrac{\partial^2 u_z}{\partial x \partial z} + C_{44}\left(\dfrac{\partial^2 u_z}{\partial x \partial z} + \dfrac{\partial^2 u_x}{\partial z^2}\right) \\ \rho_{FeRh}\dfrac{\partial^2 u_z}{\partial t^2} = C_{44}\left(\dfrac{\partial^2 u_z}{\partial x^2} + \dfrac{\partial^2 u_x}{\partial x \partial z}\right) + C_{12}\dfrac{\partial^2 u_x}{\partial x \partial z} + C_{11}\dfrac{\partial^2 u_z}{\partial z^2} \end{cases} \tag{4.14}$$

$$\Rightarrow \begin{cases} -\rho_{FeRh}\omega^2\, U = (-k^2 C_{11} + \zeta^2 C_{44})\, U + i\zeta k\,(C_{12} + C_{44})\, W \\ -\rho_{FeRh}\omega^2\, W = i\zeta k\,(C_{12} + C_{44})\, U + (-k^2 C_{44} + \zeta^2 C_{11})\, W \end{cases} \tag{4.15}$$

[6] A semi-infinite medium extends infinitely in two directions and is bounded in the third direction.

A non-trivial solution, given as (U,W), different than $(0,0)$, is possible if and only if the following determinant is zero, i.e:

$$\begin{vmatrix} -k^2 C_{11} + \zeta^2 C_{44} + \rho_{\mathrm{FeRh}}\,\omega^2 & i\zeta k\,(C_{12}+C_{44}) \\ i\zeta k\,(C_{12}+C_{44}) & -k^2 C_{44} + \zeta^2 C_{11} + \rho_{\mathrm{FeRh}}\,\omega^2 \end{vmatrix} = 0 \tag{4.16}$$

Using the definition of the phase velocity, $\omega = \mathrm{V_R}\ \mathrm{k}$,

$$\left(\frac{\zeta}{k}\right)^4 + \frac{-C_{11}^2 - C_{44}^2 + (C_{12}+C_{44})^2 + \rho_{\mathrm{FeRh}} V_{\mathrm{R}}^2\,(C_{11}+C_{44})}{C_{11}C_{44}} \left(\frac{\zeta}{k}\right)^2 + \frac{(C_{44} - \rho_{\mathrm{FeRh}} V_{\mathrm{R}}^2)(C_{11} - \rho_{\mathrm{FeRh}} V_{\mathrm{R}}^2)}{C_{11}C_{44}} = 0 \tag{4.17}$$

Solving this equation results in two solutions: q_1^2 and q_2^2 for $\mathrm{q} = \frac{\zeta}{k}$:

$$q^4 + \underbrace{\frac{-C_{11}^2 - C_{44}^2 + (C_{12}+C_{44})^2 + \rho_{\mathrm{FeRh}} V_{\mathrm{R}}^2\,(C_{11}+C_{44})}{C_{11}\,C_{44}}}_{\mathbf{A}}\, q^2 + \underbrace{\frac{(C_{44} - \rho_{\mathrm{FeRh}} V_{\mathrm{R}}^2)(C_{11} - \rho_{\mathrm{FeRh}} V_{\mathrm{R}}^2)}{C_{11}\,C_{44}}}_{\mathbf{B}} = 0 \tag{4.18}$$

The two solutions verify: $\mathrm{q}_1^2 + \mathrm{q}_2^2 = \mathbf{A}$ and $\mathrm{q}_1^2 \times \mathrm{q}_2^2 = \mathbf{B}$, with

$$r_{\mathrm{j}} = \frac{W_{\mathrm{j}}}{U_{\mathrm{j}}} = \frac{k^2 C_{11} - {\zeta_{\mathrm{j}}}^2 C_{44} - \rho\omega^2}{i\zeta_{\mathrm{j}} k\,(C_{12}+C_{44})} \qquad \mathrm{j} \in 1{,}2 \tag{4.19}$$

However, these solutions do not satisfy the boundary conditions. In order respect the latter, a combination of the above partial waves are necessary:

$$\begin{cases} u_{\mathrm{x}} = \left[\, U_1\ e^{(-\zeta_1 z)} + U_2\ e^{(-\zeta_2 z)} \,\right] e^{i(\omega t - kx)} \\ u_{\mathrm{y}} = 0 \\ u_{\mathrm{z}} = \left[\, W_1\ e^{(-\zeta_1 z)} + W_2\ e^{(-\zeta_2 z)} \,\right] e^{i(\omega t - kx)} \end{cases} \tag{4.20}$$

Boundary conditions

In the semi-infinite medium, the only boundary condition is the free top surface layer. Here, the stress components are zero:

$$\text{at } \mathrm{z} = 0: \qquad \Rightarrow \qquad \sigma_{\mathrm{iz}} = \sigma_{\mathrm{xz}} = \sigma_{\mathrm{yz}} = \sigma_{\mathrm{zz}} = 0 \tag{4.21}$$

$$\begin{cases} \sigma_{\mathrm{xz}} = C_{44}\left(\dfrac{\partial u_{\mathrm{z}}}{\partial x} + \dfrac{\partial u_{\mathrm{x}}}{\partial z}\right) = ik(W_1 + W_2) + \zeta_1 U_1 + \zeta_2 U_2 = 0 \\ \sigma_{\mathrm{yz}} = C_{44}\dfrac{\partial u_{\mathrm{y}}}{\partial z} = 0 \\ \sigma_{\mathrm{zz}} = C_{12}\dfrac{\partial u_{\mathrm{x}}}{\partial x} + C_{11}\dfrac{\partial u_{\mathrm{z}}}{\partial z} = ikC_{12}(U_1 + U_2) + C_{11}(\zeta_1 W_1 + \zeta_2 W_2) = 0 \end{cases} \tag{4.22}$$

using the relationship between W and U first, and then the definition of $\mathrm{r_j}$, from equation [4.19], the boundary conditions lead to:

$$\begin{pmatrix} \zeta_1 + ikr_1 & \zeta_2 + ikr_2 \\ ikC_{12} + \zeta_1 r_1 C_{11} & ikC_{12} + \zeta_2 r_2 C_{11} \end{pmatrix} \begin{pmatrix} U_1 \\ U_2 \end{pmatrix} = 0 \tag{4.23}$$

$$\begin{vmatrix} {q_1}^3\,C_{11} + q_1\left(C_{12} + \rho_{\mathrm{FeRh}}\,{V_{\mathrm{R}}}^2\right) & {q_2}^3\,C_{11} + q_2\left(C_{12} + \rho_{\mathrm{FeRh}}\,{V_{\mathrm{R}}}^2\right) \\ {q_1}^2\,C_{11}C_{44} + C_{12}\left(C_{44} - \rho_{\mathrm{FeRh}}\,{V_{\mathrm{R}}}^2\right) & {q_2}^2\,C_{11}C_{44} + C_{12}\left(C_{44} - \rho_{\mathrm{FeRh}}\,{V_{\mathrm{R}}}^2\right) \end{vmatrix} = 0 \tag{4.24}$$

Similarly, a non-trivial solution exists if and only if the following determinant is zero, i.e:

$$\begin{aligned} q_1^2\,q_2^2\,C_{11}^2\,C_{44} + \left(q_1^2 + q_2^2\right) C_{11}C_{12}\left(C_{44} - \rho_{\mathrm{FeRh}}{V_{\mathrm{R}}}^2\right) - q_1 q_2 C_{11}(C_{12}+C_{44})\rho_{\mathrm{FeRh}}{V_{\mathrm{R}}}^2 \\ + C_{12}\left(C_{12} + \rho_{\mathrm{FeRh}}{V_{\mathrm{R}}}^2\right)\left(C_{44} - \rho_{\mathrm{FeRh}}{V_{\mathrm{R}}}^2\right) = 0 \end{aligned}$$

Using the definition of **A** and **B**, it can be factorised to:

$$\begin{aligned} \left(C_{44} - \rho_{\mathrm{FeRh}}{V_{\mathrm{R}}}^2\right)^2 \left[C_{11}\left(C_{11} - \rho_{\mathrm{FeRh}}{V_{\mathrm{R}}}^2\right) + C_{12}\frac{C_{44}^2 + C_{11}^2 - (C_{12}+C_{44})^2 - \rho_{\mathrm{FeRh}}{V_{\mathrm{R}}}^2\,(C_{11}+C_{44}) + C_{12}(C_{12} + \rho_{\mathrm{FeRh}}{V_{\mathrm{R}}}^2)}{C_{44}} \right]^2 \\ = \frac{C_{11}(C_{12}+C_{44})^2\,(\rho_{\mathrm{FeRh}}{V_{\mathrm{R}}}^2)^2}{C_{44}}(C_{11} - \rho_{\mathrm{FeRh}}{V_{\mathrm{R}}}^2)(\rho_{\mathrm{FeRh}}{V_{\mathrm{R}}}^2) \end{aligned}$$

Rayleigh wave solution for [100]

The generalised Rayleigh wave velocity equation for a [100] propagation is thus given as:

$$\left(C_{44}-\rho_{\mathrm{FeRh}}{V_{\mathrm{R}}}^2\right)\left[C_{11}^2-C_{12}^2-C_{11}\,\rho_{\mathrm{FeRh}}{V_{\mathrm{R}}}^2\right]^2=C_{11}C_{44}\left(C_{11}-\rho_{\mathrm{FeRh}}{V_{\mathrm{R}}}^2\right)\left(\rho_{\mathrm{FeRh}}{V_{\mathrm{R}}}^2\right)^2 \tag{4.25}$$

with the acoustic displacements of the form:

$$u=\left[\begin{pmatrix}U_1\\0\\W_1\end{pmatrix}e^{(-q_1 z')}+\begin{pmatrix}U_2\\0\\W_2\end{pmatrix}e^{(-q_2 z')}\right]e^{i(\omega t-k x)} \tag{4.26}$$

3.3 Farnell-Adler model of layer-on-substrate

In this section, the reader is introduced to the Farnell-Adler model, which is a theoretical framework developed to describe the propagation of acoustic waves in thin films[7] [160]. It is an extension of the semi-infinite model presented in the previous section, to layered medium. Figure [4.7] is a schematic representation of the two layered samples studied in this manuscript. The complete stack can be found on figure [2.9]. Note for simplicity and in order a too avoid long mathematical developments, only two layers are presented on each sample. However, for the mathematical implementation, and the data presented in section [5], we have implemented tri-layer systems. These stacks and the resultant Farnell-Adler tri-layer matrix are given in appendix [A].

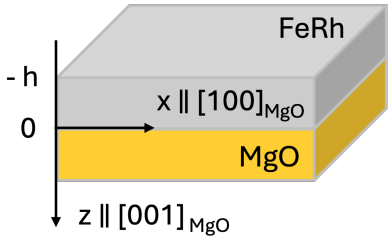

Crystalline Sample A: FeRh grown on MgO. The FeRh layer is rotated by 45° so as to reduce the lattice parameter mis-match between the FeRh layer and MgO substrate (c.f. chapter [1]), such that k_{SAW}|| $[110]_{\mathrm{FeRh}}$ || $[100]_{\mathrm{MgO}}$

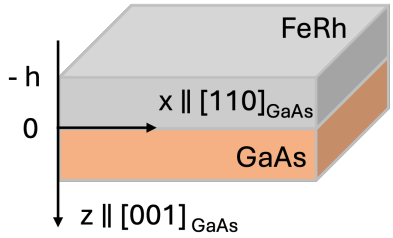

Polycristalline Sample B: FeRh grown on GaAs. The polycrystalline nature of the FeRh layer is taken into consideration by looking for effective elastic constants. Moreover, here the SAW propagate with k_{SAW}|| $[110]_{\mathrm{GaAs}}$

Figure 4.7: Schematic representation of the two FeRh samples and the direction of SAW propagation.

One of the key aspects of this model is deriving the dispersion relations, which establish the relationship between the SAW wave-vector and frequency. In layered media, where elasticity tensors differ between layers, these dispersion relations reflect the acoustic impedance, essentially illustrating how each layer influences the acoustic propagation through the adjacent layers. Solving the Farnell-Adler model implies searching for acoustic wave solutions respecting a set of boundary conditions at the layer-substrate, layer-layer and free-layer interfaces. Solving the dispersion relations predicts the existence of the allowed acoustic wave modes and the modes velocities.
In order to simplify the complexity of the model, several hypotheses are employed in this manuscript:

1. The layered medium is taken to be a semi-infinite medium; i.e. is considered to extend infinitely in the {x,y} plane and bounded along the z direction;

2. The magnetic properties of the FeRh layer are neglected and no magneto-acoustic interaction is considered;
The inclusion of the magnetic properties of FeRh will be studied in chapter [5]. However, it is also

[7] By thin films, the authors implied films with thickness much smaller than the wavelength of the propagating wave

possible to include the former, and this modifies the elasticity tensor components by including magneto-strictive coupling terms- hardening of the elasticity tensor. The magnetisation/acoustic dynamics are then solution of the generalised elasto-dynamical wave equation [4.8]. This solution is studied in [20].

3. The piezoelectric nature of the substrate layers[8] are neglected; i.e. only the difference in acoustic impedance is important in this study;
The presence of piezoelectricity introduces electromechanical[9] coupling coefficients into the wave equations. The SAWs now carry both mechanical and electrical time- and space-varying components. The acoustic impedance of the layers will now include the latter, and this results in the additional boundary conditions [155]. Taking into account the piezoelectricity harden the elastic constants. However, as GaAs is only weakly piezoelectric, this approximation remains valid.

4. Growth-related strains are not taken into consideration in the elastic constants.
This hypothesis is true for our 50 nm-thick FeRh grown on MgO film. Indeed, Arregi *et al.* measured the evolution of strain on the FeRh phase transition for crystalline films and showed that films above 40 nm showed enough strain relief, that no growth-related strain shift are discernible in the phase transition [49]. Note that this is not true for film less than 40 nm, in particular below 20 nm. On the other hand, as the FeRh on GaAs is not epitaxial and is a 270 nm-thick layer, the hypothesis holds. Hence, the elastic constants are taken to be constant within the layers.

The Farnell-Adler model is first explained on the reduced crystalline sample A: FeRh/MgO, and then applied to the reduced polycrystalline sample B: FeRh/GaAs. Again, note that in both cases only the solution of a bi-layer of FeRh and its substrate is written here to alleviate the notations, although the acoustic modes were then calculated for the complete systems. Nevertheless, the resultant Farnell-Adler determinant for 3-layered system is given in appendix [A].

3.3.1 Crystalline FeRh on MgO

In the case of the 50 nm-thick FeRh grown on MgO, the FeRh grows with its in-plane lattice rotated by 45° in order to be matched to the MgO substrate. Consequently, a SAW propagating along the crystallographic [100] of MgO, propagates along the [110] crystallographic direction of the FeRh layer.

i Elasticity Tensors

Both MgO and FeRh have a crystallographic cubic symmetry, i.e. they have only 3 independent elastic coefficients as seen in equation [4.9]. The elasticity tensors for the two layers are given in the standard referential base as:

$$C_{ij}^{MgO} = \begin{pmatrix} C_{11} & C_{12} & C_{12} & 0 & 0 & 0 \\ C_{12} & C_{11} & C_{12} & 0 & 0 & 0 \\ C_{12} & C_{12} & C_{11} & 0 & 0 & 0 \\ 0 & 0 & 0 & C_{44} & 0 & 0 \\ 0 & 0 & 0 & 0 & C_{44} & 0 \\ 0 & 0 & 0 & 0 & 0 & C_{44} \end{pmatrix} \quad \& \quad \widehat{C_{ij}^{FeRh}} = \begin{pmatrix} \widehat{C}_{11}^* & \widehat{C}_{12}^* & \widehat{C}_{13}^* & 0 & 0 & 0 \\ \widehat{C}_{12}^* & \widehat{C}_{22}^* & \widehat{C}_{23}^* & 0 & 0 & 0 \\ \widehat{C}_{13}^* & \widehat{C}_{23}^* & \widehat{C}_{33}^* & 0 & 0 & 0 \\ 0 & 0 & 0 & \widehat{C}_{44}^* & 0 & 0 \\ 0 & 0 & 0 & 0 & \widehat{C}_{55}^* & 0 \\ 0 & 0 & 0 & 0 & 0 & \widehat{C}_{66}^* \end{pmatrix} \tag{4.27}$$

with the elastic components of FeRh written in the {[110]} reference to respect the 45° lattice rotation.

$$\widehat{C_{ij}^{FeRh}}: \begin{cases} \widehat{C}_{11}^* = \widehat{C}_{22}^* = \widehat{C}_{44} + \frac{1}{2}\left(\widehat{C}_{11} + \widehat{C}_{12}\right) \\ \widehat{C}_{13}^* = \widehat{C}_{23}^* = \widehat{C}_{12} \\ \widehat{C}_{44}^* = \widehat{C}_{55}^* = \widehat{C}_{44} \end{cases} \quad \text{and:} \quad \begin{cases} \widehat{C}_{12}^* = -\widehat{C}_{44} + \frac{1}{2}\left(\widehat{C}_{11} + \widehat{C}_{12}\right) \\ \widehat{C}_{33}^* = \widehat{C}_{11} \\ \widehat{C}_{66}^* = \frac{1}{2}\left(\widehat{C}_{11} - \widehat{C}_{12}\right) \end{cases}$$

In the rest of the manuscript, C_{ij} denotes elastic coefficient of the substrate, while $\widehat{C}_{ij}$ that of the FeRh layer and C_{ij}^* any rotated layer, i.e. in the [110] basis.

[8] In reality for Sample A: The Piezoelectric material is the Zinc Oxide layer, not included in our model here.
[9] These coefficients describe the strength of the interaction between mechanical strains and electric fields.

The bulk Rayleigh velocity, similar to the calculation leading to equation [4.25], gives for a Rayleigh wave propagation along the [110] direction:

$$\left(\widehat{C}^*_{44} - \rho_{\mathrm{FeRh}} V_{\mathrm{R}}^2\right)\left[\widehat{C}^*_{11}\widehat{C}^*_{33} - \widehat{C}^{*\,2}_{13} - \widehat{C}^*_{33}\rho_{\mathrm{FeRh}} V_{\mathrm{R}}^2\right]^2 = \widehat{C}^*_{33}\widehat{C}^*_{44}\left(\widehat{C}^*_{11} - \rho_{\mathrm{FeRh}} V_{\mathrm{R}}^2\right)\left(\rho_{\mathrm{FeRh}} V_{\mathrm{R}}^2\right)^2 \tag{4.28}$$

ii Partial waves solutions

Using the reference described in figure [4.7], the SAW has a wave-vector parallel to the **x**-direction: $k_{\mathrm{SAW}} \parallel [100]_{\mathrm{MgO}} \parallel [110]_{\mathrm{FeRh}}$. Partial wave solutions are sought similarly to equation [4.13], and the same procedure as equations [4.14-4.17] lead to:

- **MgO substrate**

$$q_{\mathrm{s}}{}^4 + \left[\frac{-C_{44}^2 - C_{11}^2 + (C_{12}+C_{44})^2 + \rho_{\mathrm{MgO}} V_{\mathrm{R}}^2 (C_{11}+C_{44})}{C_{11}\,C_{44}}\right] q_{\mathrm{s}}{}^2 + \frac{(\rho_{\mathrm{MgO}} V_{\mathrm{R}}^2 - C_{11})(\rho_{\mathrm{MgO}} V_{\mathrm{R}}^2 - C_{44})}{C_{11}\,C_{44}} = 0 \tag{4.29}$$

The equation (4.29) has 4 different roots. The strain amplitude in the MgO substrate must vanish when z $\to \infty$. Only two roots give a decreasing amplitude with z: q_+ et q_-. The amplitudes (U,W) for the given q_+ et q_- verify the following relationships, with r_{s} the ratio of the out-of-plane to in-plane amplitude displacements:

$$r_{\mathrm{s}} = \frac{W_{\mathrm{s}}}{U_{\mathrm{s}}} = \frac{k^2\,C_{11} - \zeta_{\mathrm{s}}^2\,C_{44} - \rho_{\mathrm{MgO}}\,\omega^2}{i\,\zeta_{\mathrm{s}}\,k\,(C_{12}+C_{44})} = \frac{C_{11} - q_{\mathrm{s}}^2\,C_{44} - \rho_{\mathrm{MgO}}\,V_{\mathrm{R}}^2}{i\,q_{\mathrm{s}}\,(C_{12}+C_{44})} \qquad \underbrace{\mathrm{s} \in 1,2}_{\mathrm{s} \equiv \text{substrate}} \tag{4.30}$$

- **FeRh Layer**

$$\widehat{q}_l{}^4 + \left[\frac{-\widehat{C^*}^{\,2}_{44} - \widehat{C}^*_{11}\,\widehat{C}^*_{33} + (\widehat{C}^*_{13}+\widehat{C}^*_{44})^2 + \rho_{\mathrm{FeRh}} V_{\mathrm{R}}^2 (\widehat{C}^*_{33}+\widehat{C}^*_{44})}{\widehat{C}^*_{33}\,\widehat{C}^*_{44}}\right] \widehat{q}_l{}^2 + \frac{(\rho_{\mathrm{FeRh}}\,V_{\mathrm{R}}^2 - \widehat{C}^*_{11})(\rho_{\mathrm{FeRh}}\,V_{\mathrm{R}}^2 - \widehat{C}^*_{44})}{\widehat{C}^*_{33}\,\widehat{C}^*_{44}} = 0 \tag{4.31}$$

The equation (4.31) has 4 roots. Similarly, $\widehat{r}_l$ the ratio of the out-of-plane to in-plane amplitude displacements: $\frac{\widehat{W}_1}{\widehat{U}_1} = \widehat{r}_1$; $\frac{\widehat{W}_2}{\widehat{U}_2} = \widehat{r}_2$ ... give:

$$\widehat{r}_l = \frac{\widehat{C}^*_{11} - q_l^2\,\widehat{C}^*_{44} - \rho_{\mathrm{FeRh}}\,V_{\mathrm{R}}^2}{i\,q_l\,(\widehat{C}^*_{13}+\widehat{C}^*_{44})} \qquad \underbrace{l \in 1,4}_{\mathrm{l} \equiv \text{layer}} \tag{4.32}$$

iii Linear combination of partial waves

Similar to equation [4.20], the partial waves solutions need to be written as linear combination in order to satisfy the boundary conditions.

- **MgO substrate**
$$u = \left[\sum_{\mathrm{i}=1,2} \begin{pmatrix} U_{\mathrm{i}} \\ 0 \\ W_{\mathrm{i}} \end{pmatrix} \exp^{(-q_{\mathrm{i}} k z)}\right] \exp^{i(\omega t - kx)} \tag{4.33}$$

- **FeRh layer**
$$\widehat{u} = \left[\sum_{\mathrm{i}=1,2,3,4} \begin{pmatrix} \widehat{U}_{\mathrm{i}} \\ 0 \\ \widehat{W}_{\mathrm{i}} \end{pmatrix} \exp^{(-\widehat{q}_{\mathrm{i}} k z)}\right] \exp^{i(\omega t - kx)} \tag{4.34}$$

iv Boundary conditions

1. Continuity of the longitudinal and transverse displacement at the interface ($z = 0$)

The intimate contact between the layer and substrate at their interface, implies that the displacement of the material media is continuous. In other words, there is a continuity in the transverse and longitudinal displacements at the interface. Using $W_{\rm s} = r_{\rm s}\, U_{\rm s}$ and $\widehat{W}_l = \hat{r}_l\, \widehat{U}_l$.

$$\begin{cases} \sum_{\rm i=1}^{2} U_{\rm i} - \sum_{\rm i=1}^{4} \widehat{U}_{\rm i} = 0 \\ \sum_{\rm i=1}^{2} W_{\rm i} - \sum_{\rm i=1}^{4} \widehat{W}_{\rm i} = 0 \end{cases} \longrightarrow \begin{pmatrix} 1 & 1 & -1 & -1 & -1 & -1 \\ r_1 & r_2 & -\hat{r}_1 & -\hat{r}_2 & -\hat{r}_3 & -\hat{r}_4 \end{pmatrix} \begin{pmatrix} U_1 \\ U_2 \\ \widehat{U}_1 \\ \widehat{U}_2 \\ \widehat{U}_3 \\ \widehat{U}_4 \end{pmatrix} = \begin{pmatrix} 0 \\ 0 \end{pmatrix} \tag{4.35}$$

2. Continuity of the normal stress at the interface (z=0)

Similarly, components of stress σ_{i3} must be continuous across the interface.

$$\sigma_{33}^{\rm s}\,(z=0) = \sigma_{33}^{l}\,(z=0) \qquad \Longleftrightarrow \qquad C_{12}\,\varepsilon_{11} + C_{11}\,\varepsilon_{33} = \widehat{C}_{13}^{*}\,\widehat{\varepsilon_{11}} + \widehat{C}_{33}^{*}\,\widehat{\varepsilon_{33}} \tag{4.36}$$

For z=0, the equation (4.36) implies that:

$$\begin{cases} -k\left[i\,C_{12}\,(U_1+U_2) + C_{11}\,(q_1\,W_1 + q_2\,W_2)\right]\exp^{i(\omega t - kx)} = \\ k\left[i\,\widehat{C}_{13}^{*}\left(\widehat{U}_1+\widehat{U}_2+\widehat{U}_3+\widehat{U}_4\right) + \widehat{C}_{33}^{*}(\hat{q}_1\,\widehat{W}_1 + \hat{q}_2\,\widehat{W}_2 + \hat{q}_3\,\widehat{W}_3 + \hat{q}_4\,\widehat{W}_4)\right]\exp^{i(\omega t - kx)} \end{cases} \tag{4.37}$$

3. Continuity of the sagittal shear stress at the interface (z=0)

$$\sigma_{13}^{\rm s}\,(z=0) = \sigma_{13}^{l}\,(z=0) \qquad \Longleftrightarrow \qquad 2\,C_{44}\,\varepsilon_{13} = 2\,\widehat{C}_{44}^{*}\,\widehat{\varepsilon_{13}} \tag{4.38}$$

$$\begin{cases} -k\,C_{44}\left[(U_1\,q_1 + U_2\,q_2) + i(W_1+W_2)\right]\exp^{i(\omega t - kx)} = \\ -k\,\widehat{C}_{44}^{*}\left[\left(\widehat{U}_1\,\hat{q}_1 + \widehat{U}_2\,\hat{q}_2 + \widehat{U}_3\,\hat{q}_3 + \widehat{U}_4\,\hat{q}_4\right) + i(\widehat{W}_1 + \widehat{W}_2 + \widehat{W}_3 + \widehat{W}_4)\right]\exp^{i(\omega t - kx)} \end{cases} \tag{4.39}$$

The top FeRh layer, in contact with air, is assumed to be mechanically stress free. Thereon vanishing stress components.

4. Vanishing of the sagittal shear stress at the free surface (z = −h)

$$\sigma_{13}^{l}(z=-h) = 0 \iff 2\,\widehat{C}_{44}^{*}\,\widehat{\varepsilon_{13}} = -k\,\widehat{C}_{44}^{*}\left[\sum_{m=1}^{4}(\widehat{U}_{\rm m}\,\hat{q}_{\rm m} + i\,\widehat{W}_{\rm m})\exp^{\hat{q}_{\rm m}kh}\right]\exp^{i(\omega t - kx)} = 0 \tag{4.40}$$

5. Vanishing of the vertical stress at the free surface (z = −h)

$$\sigma_{33}^{l}(z=-h) = 0 \;\leftrightarrow\; \widehat{C}_{13}^{*}\,\widehat{\varepsilon_{11}} + \widehat{C}_{33}^{*}\,\widehat{\varepsilon_{33}} = -k\left[\sum_{m=1}^{4}(i\,\widehat{C}_{13}^{*}\,\widehat{U}_{\rm m} + \hat{q}_{\rm m}\,\widehat{W}_{\rm m}\,\widehat{C}_{33}^{*})\exp^{\hat{q}_{\rm m}kh}\right]\exp^{i(\omega t - kx)} = 0 \tag{4.41}$$

v Summary of the boundary conditions

Using the definition of the ratio of out-of-plane to in-plane displacements [4.30,4.32], the equation governing the continuity in the displacements [4.35] and stress components [4.36,4.39,4.40,4.41] at the interface and free layer respectively, the boundary conditions are grouped into a single matrix.
Recall: $\widehat{\cdot}$ represents the FeRh layer -l and s is the substrate. And $r_{\rm i} = \frac{W_{\rm i}}{U_{\rm i}}$
To simplify the notation:

$$\begin{cases} a_{\rm s} = & C_{44}\,(q_{\rm s} + i\,r_{\rm s}) \\ \hat{a}_l = & \widehat{C}_{44}^{*}\,(\hat{q}_l + i\,\hat{r}_l) \end{cases} \qquad \& \qquad \begin{cases} b_{\rm s} = & i\,C_{12} + C_{11}\,q_{\rm s}\,r_{\rm s} \\ \hat{b}_l = & i\,\widehat{C}_{13}^{*} + \widehat{C}_{33}^{*}\,\hat{q}_l\,\hat{r}_l \end{cases} \tag{4.42}$$

$$\begin{pmatrix} 1 & 1 & -1 & -1 & -1 & -1 \\ r_1 & r_2 & -\widehat{r}_1 & -\widehat{r}_2 & -\widehat{r}_3 & -\widehat{r}_4 \\ a_1 & a_2 & -\widehat{a}_1 & -\widehat{a}_2 & -\widehat{a}_3 & -\widehat{a}_4 \\ b_1 & b_2 & -\widehat{b}_1 & -\widehat{b}_2 & -\widehat{b}_3 & -\widehat{b}_4 \\ 0 & 0 & \widehat{a}_1 \exp^{\widehat{q}_1 kh} & \widehat{a}_2 \exp^{\widehat{q}_2 kh} & \widehat{a}_3 \exp^{\widehat{q}_3 kh} & \widehat{a}_4 \exp^{\widehat{q}_4 kh} \\ 0 & 0 & \widehat{b}_1 \exp^{\widehat{q}_1 kh} & \widehat{b}_2 \exp^{\widehat{q}_2 kh} & \widehat{b}_3 \exp^{\widehat{q}_3 kh} & \widehat{b}_4 \exp^{\widehat{q}_4 kh} \end{pmatrix} \begin{pmatrix} U_1 \\ U_2 \\ \widehat{U}_1 \\ \widehat{U}_2 \\ \widehat{U}_3 \\ \widehat{U}_4 \end{pmatrix} = \begin{pmatrix} 0 \\ 0 \\ 0 \\ 0 \\ 0 \\ 0 \end{pmatrix} \tag{4.43}$$

A non-trivial solution exists, if and only if the determinant of (4.43) is zero, i.e

$$\begin{vmatrix} 1 & 1 & -1 & -1 & -1 & -1 \\ r_1 & r_2 & -\widehat{r}_1 & -\widehat{r}_2 & -\widehat{r}_3 & -\widehat{r}_4 \\ a_1 & a_2 & -\widehat{a}_1 & -\widehat{a}_2 & -\widehat{a}_3 & -\widehat{a}_4 \\ b_1 & b_2 & -\widehat{b}_1 & -\widehat{b}_2 & -\widehat{b}_3 & -\widehat{b}_4 \\ 0 & 0 & \widehat{a}_1 \exp^{\widehat{q}_1 kh} & \widehat{a}_2 \exp^{\widehat{q}_2 kh} & \widehat{a}_3 \exp^{\widehat{q}_3 kh} & \widehat{a}_4 \exp^{\widehat{q}_4 kh} \\ 0 & 0 & \widehat{b}_1 \exp^{\widehat{q}_1 kh} & \widehat{b}_2 \exp^{\widehat{q}_2 kh} & \widehat{b}_3 \exp^{\widehat{q}_3 kh} & \widehat{b}_4 \exp^{\widehat{q}_4 kh} \end{vmatrix} = 0 \tag{4.44}$$

The solution given by equation [4.44] gives the velocity (here the Rayleigh Velocity V_R) if k (k_{SAW}) is fixed or the k value if the velocity is fixed. For us, we fix the k_{SAW} value and we calculate the corresponding Rayleigh velocity. An iteration is then performed to calculate $k_{SAW} = 0$ (where the $V_R = V_{layer}$) to $k_{SAW} >> \frac{1}{d}$, where d is the thickness of the FeRh film. Here, $V_R = V_{substrate}$. Solutions of the Rayleigh velocity with respect to temperature and the dispersion relationship is given in section [5], for a SiO_2/FeRh/MgO stack. As Sample B is polycrystalline, we cannot just replace the corresponding elastic constants and resolve equation [4.44]. A discussion is necessary.

3.3.2 FeRh on GaAs

In order to evaluate the Rayleigh velocity for the polycrystalline FeRh/Ta/GaAs system, the same procedure as the previous section is repeated. However, two remarks are necessary. The SAWs now propagate along the [110] crystallographic direction of GaAs as it is piezoelectric along this direction [161], [162]. Hence, similar to the crystalline FeRh on MgO, the elasticity tensor of GaAs is written in the [110] reference frame, c.f equation [4.27]. Secondly, the polycrystalline nature of the FeRh layer needs to be taken into consideration.

Based on works from Voigt *et al.* [163] and Reuss *et al.* [164], Hill *et al.* examined the relationship between crystalline aggregates and single crystals [165]. The investigation showed that the actual elastic modulus of an aggregate typically fall between the Voigt and Reuss values. Noting that Voigt proposed averaging the stress-strain relations over all possible lattice orientations, with uniform strain throughout the aggregate, and that Reuss assumed uniform stress, Hill proposed a mathematical framework leading to the following expressions for the elastic constants in a polycristalline material.
Using the same notation as before namely $\widehat{\cdot}$ represents the FeRh layer and $\cdot^{\text{eff}}$ represents a polycrystalline layer :

$$\widehat{C_{ij}^{\text{FeRh}}} = \begin{pmatrix} \widehat{C_{11}}^{\text{eff}} & \widehat{C_{12}}^{\text{eff}} & \widehat{C_{12}}^{\text{eff}} & 0 & 0 & 0 \\ \widehat{C_{12}}^{\text{eff}} & \widehat{C_{11}}^{\text{eff}} & \widehat{C_{12}}^{\text{eff}} & 0 & 0 & 0 \\ \widehat{C_{12}}^{\text{eff}} & \widehat{C_{12}}^{\text{eff}} & \widehat{C_{11}}^{\text{eff}} & 0 & 0 & 0 \\ 0 & 0 & 0 & \widehat{C_{44}}^{\text{eff}} & 0 & 0 \\ 0 & 0 & 0 & 0 & \widehat{C_{44}}^{\text{eff}} & 0 \\ 0 & 0 & 0 & 0 & 0 & \widehat{C_{44}}^{\text{eff}} \end{pmatrix} \tag{4.45}$$

with

$$\widehat{C_{11}}^{\text{eff}} = \frac{7\widehat{C_{11}}^2 - 4\left(2\widehat{C_{12}} - \widehat{C_{44}}\right)\left(\widehat{C_{12}} + 2\widehat{C_{44}}\right) + \widehat{C_{11}}\left(\widehat{C_{12}} + 32\widehat{C_{44}}\right)}{5\left(3\widehat{C_{11}} - 3\widehat{C_{12}} + 4\widehat{C_{44}}\right)} \tag{4.46}$$

$$\widehat{C_{12}^{\text{eff}}} = \frac{4\,\widehat{C_{11}}^2 + 7\,\widehat{C_{11}}\,\widehat{C_{12}} - 11\,\widehat{C_{12}}^2 - 6\,\widehat{C_{11}}\,\widehat{C_{44}} + 26\widehat{C_{12}}\,\widehat{C_{44}} - 4\,\widehat{C_{44}}^2}{5\left(3\,\widehat{C_{11}} - 3\,\widehat{C_{12}} + 4\,\widehat{C_{44}}\right)} \tag{4.47}$$

$$\widehat{C_{44}^{\text{eff}}} = \frac{\widehat{C_{11}^{\text{eff}}} - \widehat{C_{12}^{\text{eff}}}}{2} \tag{4.48}$$

- **FeRh Layer**

$$\widehat{q_l}^4 + \widehat{q_l}^2\left(-2 + \frac{\widehat{C_{11}^{\text{eff}}} + \widehat{C_{44}^{\text{eff}}}}{\widehat{C_{11}^{\text{eff}}}\,\widehat{C_{44}^{\text{eff}}}}V_{\text{R}}^2\rho_{\text{FeRh}}\right) + \frac{(\widehat{C_{11}^{\text{eff}}} - V_{\text{R}}^2\rho_{\text{FeRh}})(\widehat{C_{44}^{\text{eff}}} - V_{\text{R}}^2\rho_{\text{FeRh}})}{\widehat{C_{11}^{\text{eff}}}\,\widehat{C_{44}^{\text{eff}}}} = 0 \tag{4.49}$$

$$\hat{r}_l = \frac{\widehat{W_l}}{\widehat{W_l}} = \frac{\widehat{C_{11}^{\text{eff}}} - \widehat{C_{44}^{\text{eff}}}\,\widehat{q_l}^2 - \rho_{\text{FeRh}}V_{\text{R}}^2}{i\hat{q}_l(\widehat{C_{13}^{\text{eff}}} + \widehat{C_{44}^{\text{eff}}})} \qquad \underbrace{l \in 1,4}_{\text{l} \equiv \text{layer}} \tag{4.50}$$

- **GaAs substrate**

$${q_{s'}}^4 + \frac{(C_{13'}^2 - C_{11'}C_{33'} + 2C_{13'}C_{44'} + (C_{33'} + C_{44'})V_{\text{R}}^2\rho_{\text{GaAs}})}{C_{33'}C_{44'}}{q_{s'}}^2 + \frac{(C_{11'} - V_{\text{R}}^2\rho_{\text{GaAs}})(C_{44'} - V_{\text{R}}^2\rho_{\text{GaAs}})}{C_{33'}C_{44'}} = 0 \tag{4.51}$$

$$r_{s'} = \frac{W_{s'}}{U_{s'}} = \frac{C_{11'} - q_{s'}^2C_{44'} - \rho_{\text{GaAs}}V_{\text{R}}^2}{iq_{s'}(C_{13'} + C_{44'})} \qquad \underbrace{s \in 1,2}_{\text{s} \equiv \text{substrate}} \tag{4.52}$$

To simplify the notation:

$$\begin{cases} a_{s'} = & C_{44'}\,(q_{s'} + i\,r_{s'}) \\ \hat{a}_l = & \widehat{C_{44}^{\text{eff}}}(\hat{q}_l + i\hat{r}_l) \end{cases} \quad \& \quad \begin{cases} b_{s'} = & i\,C_{13'} + C_{33'}\,q_{s'}\,r_{s'} \\ \hat{b}_l = & i\widehat{C_{13}^{\text{eff}}} + \hat{q}_l\hat{r}_l\widehat{C_{33}^{\text{eff}}} \end{cases} \tag{4.53}$$

$$\begin{pmatrix} 1 & 1 & -1 & -1 & -1 & -1 \\ r_{1'} & r_{2'} & -\hat{r}_1 & -\hat{r}_2 & -\hat{r}_3 & -\hat{r}_4 \\ {a_{s'}}_1 & {a_{s'}}_2 & -\hat{a}_1 & -\hat{a}_2 & -\hat{a}_3 & -\hat{a}_4 \\ {b_{s'}}_1 & {b_{s'}}_2 & -\hat{b}_1 & -\hat{b}_2 & -\hat{b}_3 & -\hat{b}_4 \\ 0 & 0 & e^{hk\hat{q}_1}\hat{a}_1 & e^{hk\hat{q}_2}\hat{a}_2 & e^{hk\hat{q}_3}\hat{a}_3 & e^{hk\hat{q}_4}\hat{a}_4 \\ 0 & 0 & e^{hk\hat{q}_1}\hat{b}_1 & e^{hk\hat{q}_2}\hat{b}_2 & e^{hk\hat{q}_3}\hat{b}_3 & e^{hk\hat{q}_4}\hat{b}_4 \end{pmatrix} \begin{pmatrix} U_{1'} \\ U_{2'} \\ \widehat{U_1} \\ \widehat{U_2} \\ \widehat{U_3} \\ \widehat{U_4} \end{pmatrix} = 0$$

Similar to the previous calculation on MgO, we started the calculation based on the Farnell-Adler model for the FeRh/GaAs bi-layer. However, following the experimental generation of SAWs and the accumulation of sufficient acoustic data, we realised that the Tantalum layer, which has a lower Rayleigh velocity with respect to both FeRh and GaAs (c.f. section [5]) needs to be taken into account. This tri-layer model, was implemented numerically, with the additional boundary conditions between the FeRh and Ta layers. As this tri-layer model leads to too lengthy calculations, and is difficult to be reproduced here, we made the choice to explain the step-by-step resolution of the Farnell-Adler model only on the bi-layer model on both samples. However, in appendix [A], we have given the full (10×10) matrix equivalent to equation [4.44]. Resolving this matrix gives either solutions of k_{SAW} or V_R, as explained before. The dispersion relationship can thus be calculated.

4 Determination of Elastic constants on FeRh

Even though FeRh was discovered more than eighty years ago, there is no complete record of determination of its three independent elastic constants across the magneto-structural phase transition. First principles calculations of AFM and FM phononic band structures at absolute zero indicated an average; increase of $\approx$ 19% in the C_{11} component, decrease of $\approx$ 8% in the C_{12} and $\approx$ 9% in the C_{44} components across the AFM-to-FM transition [166], [167]. Using ultrasonic picosecond measurements, Cooke *et al.* measured the longitudinal and transverse velocities on two 200 nm-thick FeRh, of different Rh and Fe concentration, grown on MgO samples exhibiting respectively AFM and FM phases at room temperature [63]. Using equations from section [3.1], a difference of $\approx$ 9% between the C_{11} components is estimated. In order to have a much more robust determination of the elastic components to compute the Rayleigh velocities with respect to temperature, (c.f. Section [3.3]), their experimental determination were investigated [168]. This work was led half-way through the thesis by our group's post-doc D. Ourdani, L. Thevenard and B. Perrin at the INSP.
Two complementary experimental techniques were used: Brillouin Light Scattering (BLS) and picosecond acoustic measurements. Firstly, we measured the back-scattered light beam coming from a d = 200 nm-thick epitaxial FeRh grown on MgO, using a BLS setup operating at a wavelength of λ = 532 nm and a 150 mW power. This crystalline equi-atomic sample exhibited an AFM phase at room temperature with the transition occuring between 83°C and 110°C. Figure [4.8] shows the anti-Stokes Brillouin shift for three different SAW wave-vectors at room temperature, i.e. in the AFM phase. The wave-vectors are directed parallel to the [100] (resp. [110]) crystallographic direction of MgO (resp. FeRh). Three SAW modes can be observed on the spectra, with the lowest frequency representing the Rayleigh mode accompanied by the first two measurable Sezawa modes, which are higher order SAW modes. By varying the angle of the incident light beam, we can vary the corresponding SAW wave-vector as: $k_{SAW} = 4\pi \sin(\theta_{inc})/\lambda$. Three k_{SAW} are represented here. We can observe that by increasing the latter, the BLS shift increases. From that, are extracted the dispersion relationships for the three SAW modes. Using the Farnell-Adler model of thin-film on substrate (as explained in the next section), we can recover the three elastic constants in the semi-infinite FeRh layer. However, no unique set of solution for the elastic constants (C_{11}, C_{12} and C_{44}) exists when they are all left as free parameters. However, BLS measurements only do not allow the distinction between the different sets of solutions.

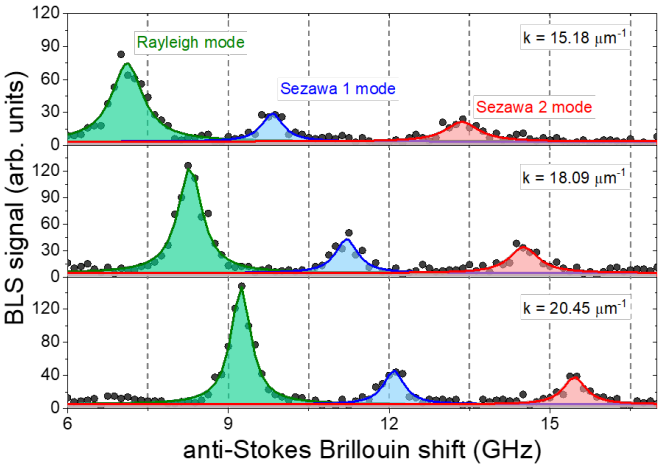

Figure 4.8: BLS spectra for three different k_{SAW} in the AFM phase at room temperature. Three different acoustic modes (Rayleigh, Sezawa 1 and Sezawa 2) can be observed. Increasing the wave-vector shifts the modes frequencies. Reproduced from [168].

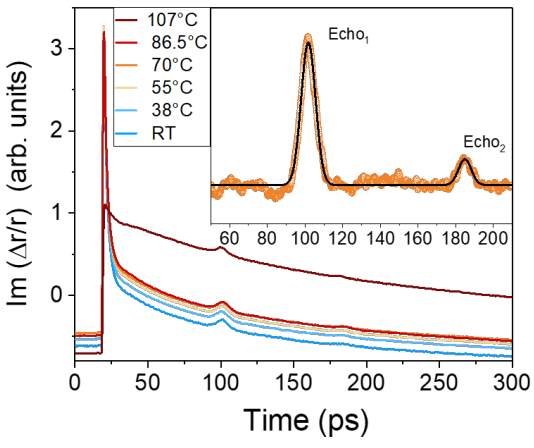

Figure 4.9: Typical acoustic picosecond interferometry measurement. The first peaks correspond to a signal of electronic origin, followed by a slower decay of thermal origin. The inset shows more conveniently the acoustic echoes obtained by removing the thermal background and used to deduce the longitudinal wave travel time. Reproduced from [168].

For that matter we use a pump-probe picosecond acoustic setup based on interferometric detection

[169]. Figure [4.9] represents a typical temporal scan of the probe beam, with r representing the amplitude of the light electric field reflection coefficient. Im(Δr/r) is the phase variation of the light electric field induced by the vertical displacement of the FeRh surface A picosecond-pulse sent to the surface generates a propagating volume longitudinal wave through the FeRh layer and is reflected off the FeRh/MgO interface. These reflections, upon reaching the surface, are observed as acoustic echoes seen at $\approx$ 100 ps and $\approx$ 190 ps time-stamps. Knowing that Δt = 2 d V_L, the equations of section [3.1.1] and ρ_{FM}[10] = 9957.7 kg m^{-3}, ρ_{AFM} = 9888.49 kg m^{-3}, the value of the C_{11} elastic component can be calculated. Both the BLS and picosecond acoustic measurements are repeated for a discrete range of temperature covering the AFM and FM phases. Using these values of C_{11}, we can recover a unique set of solutions for the elastic constants from the BLS-measured dispersion relationships.

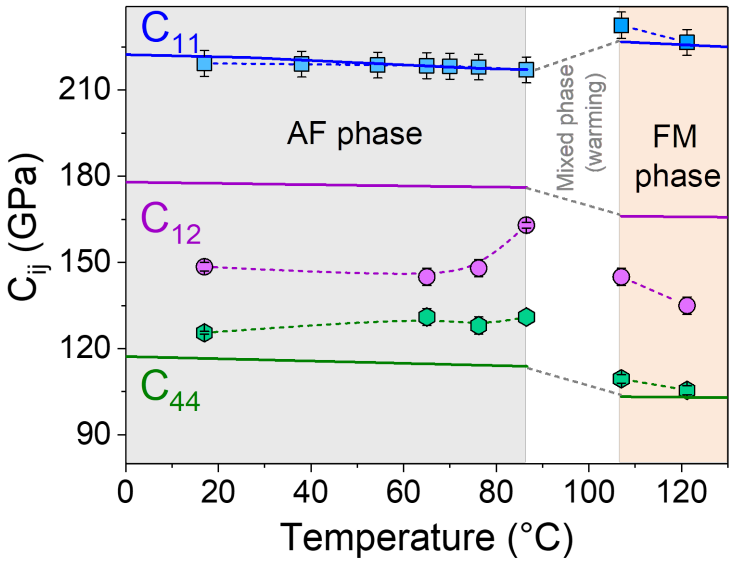

Figure 4.10: Temperature-dependence of elastic constants of FeRh: determined by the analysis of the BLS and picosecond acoustics data (symbols with dashed lines, at more temperatures for the latter), or calculated by TDEP anharmonic lattice dynamics (full lines). Adapted from [168].

To complement the experimental measurements, the study also included first-principles calculations to estimate the elastic constants theoretically. These calculations were based on density functional theory (DFT)- with a temperature-dependent effective potential (TDEP) method [170]. Figure [4.10] represents the corresponding experimental (symbols and dotted lines) and numerical (full lines) determination of the elastic constants with respect to temperature across the AFM-to-FM phase transition. A steep jump of $\approx$ 6% is observed for the C_{11} component, which aligns with Cooke *et al.* [63]. Moreover, we observe that C_{44} exhibits a relatively stable behaviour in the AFM phase, followed by a decrease from 130 to 110 GPa at the transition. This decline is akin to what Cooke et al. reported, though their values (77 to 57 GPa) were obtained indirectly from specific heat measurements. Additionally, we identify a non-monotonic trend in C_{12} within the AFM phase, with a sharp increase (approximately 20 GPa) as the FM phase is approached. The numerical estimates obtained from DFT calculations showed good temperature agreement with the experimental results, in particular across the transition. A maximum discrepancy of 2.4% is obtained for C_{11}, 13% for C_{44} and 23% for C_{12}. This concordance between theory and experiment enhances the credibility of the findings, validates the measurement techniques and the theoretical models, and provides a comprehensive understanding of the temperature dependency of the elastic properties of FeRh.

[10]These values were calculated from the XRD measurements courtesy of J. Arregi and V. Uhlir

5 Determining the V_R and dispersion relations

The aim of this section is to use the measured elastic constants of FeRh obtained to have a quantitative evolution of the Rayleigh velocity, V_R, with respect to temperature and the dispersion relations (V_R versus k_{SAW}). The Crystalline Sample A- FeRh/MgO is considered first, followed by the polycrystalline Sample B-FeRh/GaAs. Recall, the full stack of the two samples can be found on figure [2.9].

5.1 SiO_2/FeRh/MgO

Using the two previous sections, and the literature values of the MgO and SiO_2 layers, the Rayleigh velocity with respect to temperature is calculated. Note that here, the Rayleigh propagation is along the [100] crystallographic direction on MgO and [110] on the FeRh. Two observations of Table [4.1] are the order of magnitude difference between the MgO and SiO_2 values, and the fairly slow decrease for a temperature change of 100°C. On Figure [4.11] is given the calculated bulk Rayleigh velocities

SiO_2(100 nm)/FeRh (50 nm)/MgO			
Layer	Elastic constant	T = 0°C (Fully AFM)	T = 100°C (Fully FM)
MgO [171]	C_{11}(GPa)	298.3	292.2
	C_{12}(GPa)	95.8	96.2
	C_{44}(GPa)	156.5	155.3
	ρ (kg m^{-3})	3590.0	3578.3
SiO_2 [172]	C_{11}	77.5	79.6
	C_{44}	30.7	31.3
	C_{12}	16.1	17.0
	ρ (kg m^{-3})	2200	-

Table 4.1: Literature values of the elastic constants and mass density for Sample A. The elastic constants of FeRh is taken from Figure [4.10]

on each of the three different material layers. In Black is represented the MgO with a bulk Rayleigh velocity of $\approx$ 5500 ms^{-1}, in Grey the SiO_2 with a Bulk Rayleigh velocity of 3400 ms^{-1} and the FM and AFM bulk Rayleigh velocity. In the AFM phase it is 2762 ms^{-1}, while in the FM phase 2752 ms^{-1}. The velocity decreases with increasing temperature. Note here, the difference in value between the AFM and FM phases is small ($\approx$ 0.36 % only).

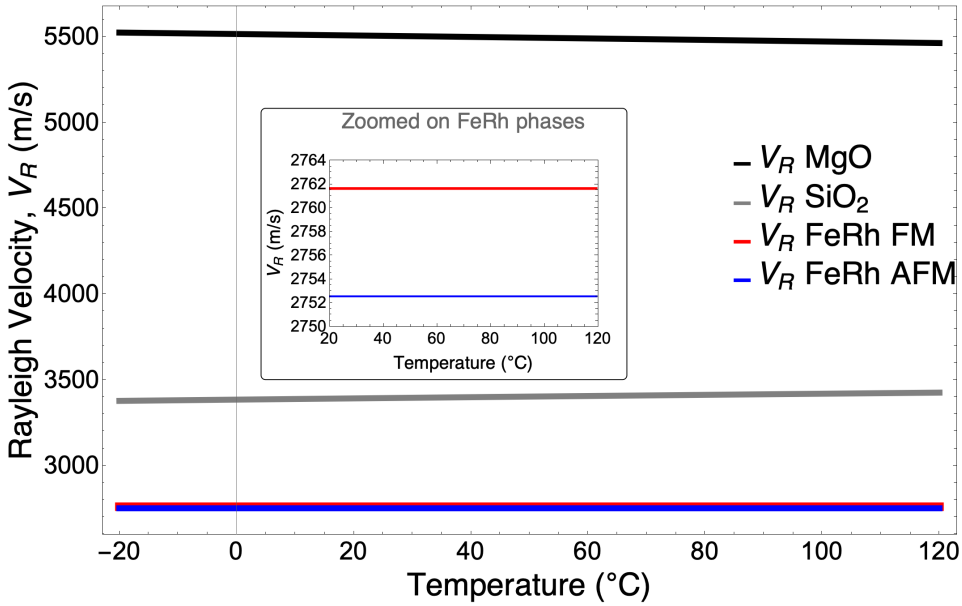

Figure 4.11: Illustration of the Bulk Rayleigh wave velocity (V_R) as a function of temperature for the different layers separately: MgO, SiO_2, and FeRh in both its ferromagnetic (FM) and antiferromagnetic (AFM) phases. MgO exhibits the highest Rayleigh velocity, indicating its strong elastic properties.

Using the Farnell-Adler model developed above, the Rayleigh velocity is now calculated for the three-layers and represented on figure [4.12]. In dotted lines are represented the separated bulk velocities on each layer, given to aid the comprehension. In the three layer system, the FeRh Rayleigh velocity decreases from the bulk MgO value at $k_{SAW} = 0$, with respect to the wave-vector. This illustrates the dispersive nature of a wave propagation in a layered system. Indeed, as seen in Table [4.1], as the elastic constants between the layers are different, the acoustic waves experiences different acoustic impedance in each of the layer. As k_{SAW} is increased, the penetration depth is reduced and the waves are more and more influenced by the top layers, in this case the SiO_2 and FeRh layers. Thus the rapid decrease in the Rayleigh velocities towards values closer to the top two layers for larger k_{SAW}. At $k_{SAW} = 40\ \mu m^{-1}$, corresponding to a SAW penetration depth of ≈ 25 nm, the SAW experiences only the SiO_2 top-most layer. This is indeed what is seen. The layered Rayleigh velocity calculated corresponds to the Rayleigh velocity on bulk SiO_2. The inset is a zoom for the AFM (blue coloured) and FM (red coloured) phases. For the wave-vectors being studied on this material (c.f. Table [6.1], the major contribution thus comes from the MgO layer.

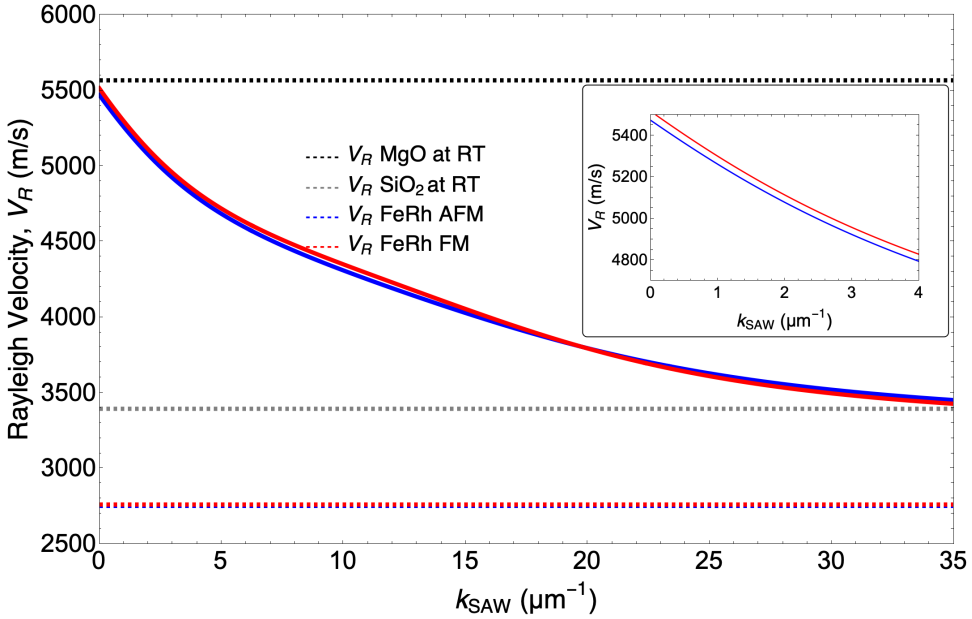

Figure 4.12: Dispersion relation calculated on the three layers system: SiO_2/FeRh/MgO. At low k_{SAW} and large SAW penetration, the major contribution to the SAW velocity comes from the MgO substrate. For higher k_{SAW} values, the penetration depth decreases and the SAW is more and more confined to the top layers. The Rayleigh velocity decreases correspondingly to match the lower bulk velocities of SiO_2 and FeRh.

Although the calculated Rayleigh velocities led to insightful results, the lack of crystalline samples hindered the project. Building on the the polycrystalline Sample B, the same procedure is applied on the FeRh/Ta/GaAs tri-layer system.

5.2 FeRh/Ta/GaAs

As develop in section [3.3.2], the polycrystalline nature of FeRh was taken into consideration. Similarly, in order to calculate the correct Bulk and layered Rayleigh velocity, the isotropic nature of the Tantalum layer is implemented in the calculation. In Table [4.2], are given the elastic constants and mass densities for the Ta, GaAs and FeRh layers at two different temperatures. Note the mass density of Tantalum is almost three times that of GaAs.

FeRh(270 nm)/Ta (100 nm)/GaAs			
Layer	Elastic constant	T = 0°C (Fully AFM)	T = 100°C (Fully FM)
Ta (Isotropic) [173]	C_{11}(GPa)	265.6	263.0
	C_{12}(GPa)	158.6	168.7
	C_{44}(GPa)	82.5	80.3
	ρ (kg m^{-3})	16600	-
GaAs [110] [174], [175]	C_{11}(GPa)	145.5	144.0
	C_{12}(GPa)	27.1	26.8
	C_{44}(GPa)	59.2	58.6
	ρ (kg m^{-3})	5316.9	-
	C_{ij}^{eff}	T = 86.5°C AFM	T = 107°C FM
FeRh [168]	C_{11}(GPa)	275.0	275.3
	C_{12}(GPa)	134.0	123.6
	C_{44}(GPa)	70.5	75.8
	ρ (kg m^{-3})	9889	9820

Table 4.2: Literature values of the elastic constants and mass densities for Sample B. The elastic constants of FeRh are taken from Figure [4.10].

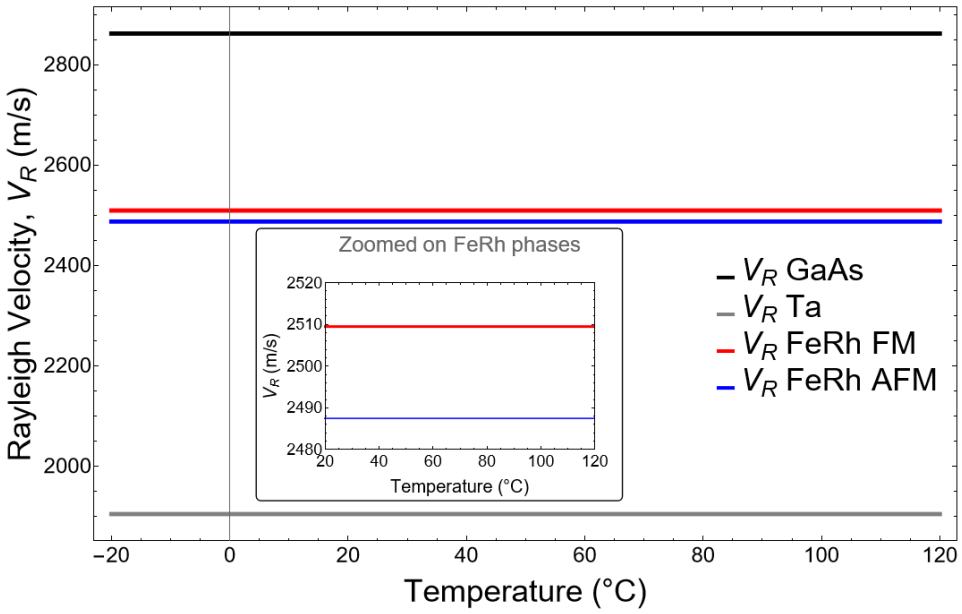

Figure 4.13: Illustration of the Bulk Rayleigh wave velocity (V_R) as a function of temperature for the different layers separately: GaAs, Ta, and FeRh in both its ferromagnetic (FM) and antiferromagnetic (AFM) phases. Note here, the Rayleigh velocity on tantalum is $\approx$ 1970 ms^{-1}.

On Figure [4.13] are represented the bulk Rayleigh velocities of each of the three separated materials. For the GaAs layer, represented in black, the Rayleigh velocity is 2850 ms^{-1}, for the Tantalum layer it is 1900 ms^{-1}. In the FeRh FM phase it is 2564 ms^{-1}, while in the AFM phase 2488 ms^{-1}. The difference between the two phases here is $\approx$ 3 % only.

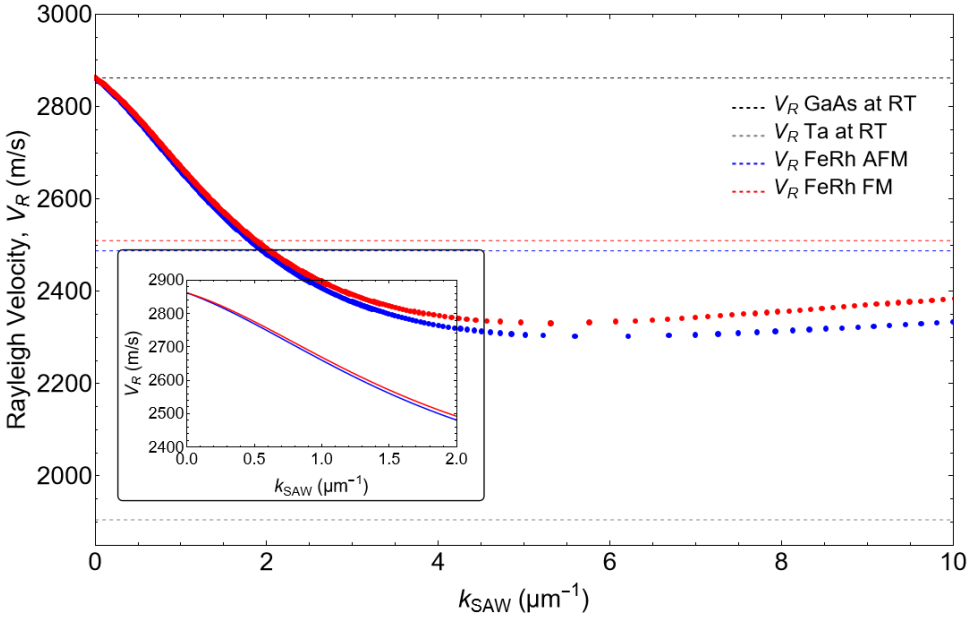

Figure 4.14: Dispersion relation calculated on the three layers system: FeRh/Ta/GaAs. At low k_{SAW} and large SAW penetration, the major contribution to the SAW velocity comes from the GaAs substrate. Immediately, for non-zero k_{SAW} values, there is a rapid decrease in the Rayleigh velocity. This is explained by the large mass density difference of Tantalum, making the layered system extremely dispersive.

6 Generating SAWs

There are two primary methods for exciting Surface Acoustic Waves (SAWs). The first method involves optical excitation via the thermo-elastic effect as seen in section [4]. It consists of sending a pulsed laser light either on the back of a substrate or the surface layer itself. The absorption of the former leads to rapid localised heating and subsequent expansion, which generates a pressure wave that propagates either as longitudinal bulk or surface acoustic waves [26]. The second method uses electrical excitation via Inter-Digitated Transducers (IDTs) through the piezoelectric effect. SAW-IDT devices typically consist of a piezoelectric material that serves as the substrate or as a thin layer on top of a non-piezoelectric substrate. In the case of Polycrystalline Sample B: FeRh/Ta/GaAs, Gallium Arsenide (GaAs) is used as a piezoelectric substrate, while for Crystalline Sample A: the SiO_2/FeRh/MgO layer, an additional Zinc Oxide (ZnO) layer is deposited as the piezoelectric layer on the non-piezoelectric Magnesium Oxide (MgO) substrate (c.f. figure [2.9].)

Both methods offer distinct advantages and limitations. Laser excitation provides a non-contact approach with precise spatial control and the capability to generate high-frequency SAWs, making it versatile for various materials, applications or in environments where physical contact might disturb the system [176]. However, laser excitation introduces thermal effects and requires a complex setup for detection (e.g using an interferometer [169]). On the other hand, piezoelectric methods directly convert an electric field into mechanical vibrations, ensuring high efficiency, frequency control, and long-term stability. Yet, piezoelectric SAW generation is limited to materials with piezoelectric properties, involves contact with the sample and may have lithographic limitations on the SAW frequency generated. The maximum typical SAW frequencies are thus limited to a few gigahertz. However, several groups have tried pushing this limit using unconventional approach. First, using nano-imprint lithography, Büyükköse *et al.* were able generated SAWs at a maximum of 16.1 GHz on ZnO/SiO_2/Si [177]. Similarly, Zheng *et al.* fabricated Interdigited Transducers (IDTs) using an advanced electron beam lithography (EBL) process combined with ion beam milling, reducing the IDT period to 160 nm, enabling excitation of SAWs at a maximum frequency of approximately 30 GHz [178]. However, such techniques are costly and rarely available.

In this work, the SAWs are generated by piezoelectricity, and the focus is turned to the latter. Choosing

the right materials for both the piezoelectric components and the IDTs is crucial to the device's performance and efficiency. This section explains the fundamentals of piezoelectricity and how these principles are applied to the design of SAW devices discussed in this manuscript.

6.1 Piezo-electricity

At their core, IDT devices leverage the piezoelectric effect exhibited by certain crystals. Piezoelectric crystals possess fixed dipoles that are electrically polarised, in a fixed direction, upon the application of an external mechanical strain (direct effect), or are deformed under the influence of an electric field (inverse effect). The discovery of the direct piezoelectric effect in 1880 by Pierre and Jacques Curie [179], stemmed directly from the exploration of principles connecting the symmetry and asymmetry of causes and effects. Given that the piezoelectric effect operates exclusively within an anisotropic crystal lattice, careful consideration is given to the crystal's cut and orientation during the material's design and manufacturing process. One fundamental indicator of the quality of a material intended for SAW generation, is the electro-mechanical coupling coefficient κ_{EM}, which signifies the material's ability to convert mechanical energy into electrical signals and inversely.

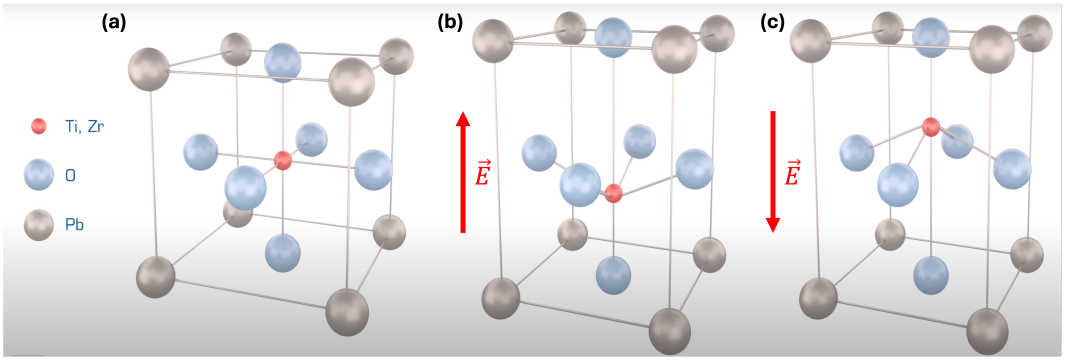

Figure 4.15: Schematic representation of a PZT (lead zirconate titanate) crystal in an electric field. The spheres represent the different atoms: Red (Ti:4^{4+} or Zr^{4+}), Blue (O:$^{2-}$) and Grey (Pb:$^{2+}$). **(b):** Application of an electric field shifts the negative ions downwards, and changes the lattice structure. **(c):** When the electric field changes direction, The net polarisation is now reversed, aligning with the new direction of the electric field, and recreating the same lattice deformation. Adapted from [180].

In a piezoelectric material, the application of an electric field creates a strain and vice-versa. The electric field causes the centre of mass of the positive and negative ions to shift. However, as the crystal is anisotropic, these dipoles do not cancel each other. Figure [4.15] is a schematic representation of a common piezoelectric ceramic, the perovskite Lead zirconate titanate (PZT). Under the application of an electric field, the displacement of the central atom relative to the surrounding oxygen atoms generates a net dipole moment. This results in a strained unit cell. The direction of this dipole aligns with the applied field, reversing when the field direction is reversed.

Piezoelectricity arises from the coupling between mechanical strain and electric polarisation. It is thus possible to write[11] the electric displacement, **D**, in terms of the dielectric constant, ϵ , the strain, ε , and the piezoelectric coefficient, e_{ijk} , as well as the mechanical stress, σ , in terms of strain, elastic coefficient, C_{ijkl} , and the electric field, **E**.

$$\begin{cases} D_{\mathrm{i}} &= e_{\mathrm{ijk}}\,\varepsilon_{\mathrm{jk}} + \epsilon_{\mathrm{ij}}\,E_{\mathrm{j}} \\ \sigma_{\mathrm{ij}} &= C_{\mathrm{ijkl}}\,\varepsilon_{\mathrm{kl}} - e_{\mathrm{kij}}\,E_{\mathrm{k}} \end{cases} \tag{4.54}$$

As such,

- For a material under zero stress ($\sigma = 0$): $\varepsilon = \frac{eE}{C}$; An electric field effectively creates a strain.
- For a material under zero strain ($\varepsilon = 0$): σ = - eE ; An electric field generates a stress.

[11] A full step-by-step demonstration of the following equations can be found in [155].

6.2 Inter-digitated Transducers

As said above, generating SAWs with piezoelectricity involves using Interdigitated Transducers (IDTs). IDTs are fabricated using lithographic techniques (optical or electronic), and are generally placed on top of the piezoelectric surface or embedded beneath the surface [153], [181].

6.2.1 Operation of the IDT

An IDT consists of electrodes or fingers, typically made of aluminum or gold, arranged in a comb-like pattern with interleaved spaces or as a specific array, deposited on a piezoelectric substrate. These fingers are subjected to an alternating potential difference, as schematically represented in the figure [4.16]. This alternating potential difference generates an alternating electric field that induces compression and dilation in the vicinity of the surface, giving rise to an elastic wave via piezoelectricity. Each pair of electrodes emits an elastic wave, that constructively interferes most efficiently when the mechanical period is half of the SAW wavelength. The corresponding SAW velocity is then related to the excitation frequency by the relationship: $f_{SAW,n} = V_R/\lambda_{SAW,n}$, where n gives the higher order harmonics. The SAW wavelength and resonant frequency are determined by the geometric configuration of the IDTs while the Rayleigh velocity, V_R , is dependent on the piezoelectric substrate. The electrode spacing is d, and N gives the number of electrode pairs (here N = 3).

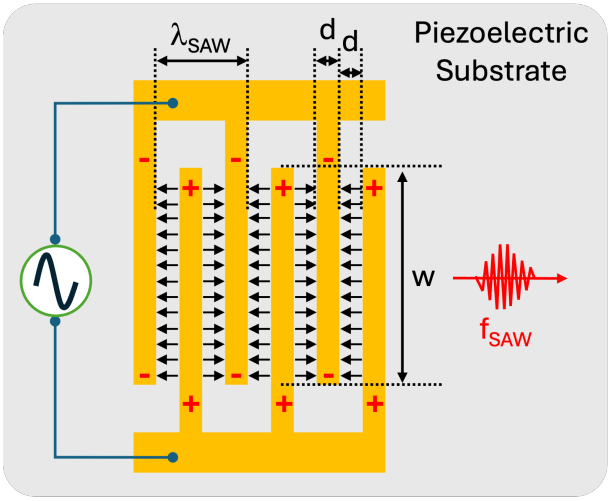

Figure 4.16: Operation of the IDT

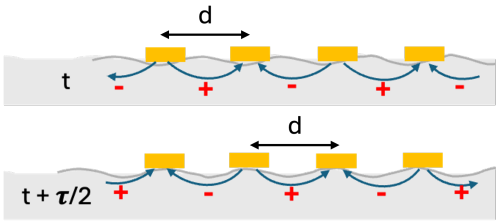

Figure 4.17: Mechanical strains associated with the IDTs at two different time stamps with an interval of $\tau/2$. Note that, the electric fields between neighbouring fingers are reversed and coincide at the exact moment the opposite region of pressure reaches the fingers, thereby amplifying the acoustic wave cumulatively.

The cumulative effect of each electrode is as follows [155]. Figure [4.17], shows schematically the influence of each electrode in the comb-like pattern. At a given polarity and time t, a Rayleigh wave is generated by mechanical stress, and travels at a speed, V_R, over a distance, d , during half the period. At t + $\tau/2$, where τ is $1/f_{SAW}$, the said stress reaches the neighbouring pair of electrode, which coincides to the moment the electrical voltage switches polarity. An in-phase stress is generated, which adds up to that generated by the first electrode pair. This cumulative effect is called synchronisation frequency or simply the resonance frequency of the IDT. If the frequency deviates from this value, the interference between the elastic signals emitted by the different pairs of fingers is no longer completely constructive and the resulting signal is reduced. The more electrodes pairs N in the design, the narrower the frequency bandwidth. For a Rayleigh SAW on GaAs with velocity ≈ 2800 ms^{-1} and λ_{SAW} = 10 μm, the centre frequency[12] is given by: $f_{SAW,0} = V_R/\lambda_{SAW,0} = 280$ MHz, and the frequency bandwidth of the IDT is given by $\Delta f_{SAW} = f_{SAW,0}$ / N. For 10 electrodes pairs, Δf_{SAW} is equal to 28 MHz, while for 100 electrodes pairs it is down to 2.8 MHz.

Figure [4.18] is an example of a IDT resonance for $\lambda_{SAW,2} = 17.3$ μm, $f_{SAW,2} \approx 298$ MHz and N = 10. On average, $\Delta f_{SAW,2}$ is ≈ 13 MHz. Moreover, Figure [4.18] shows the temperature dependency of

[12] More specifically, the frequency response of a simple IDT at resonance can thus be written as: $\text{Response}(f_{SAW}) \propto \text{sinc}\left(\frac{N\pi(f_{SAW}-f_{SAW,0})}{f_{SAW,0}}\right)$

the centre frequency at 298 MHz on the FeRh/MgO sample and frequency bandwidth. Three remarks are necessary here. First that the efficiency of SAW generation is not constant with temperature. Secondly, it is seen that as the temperature increases, the centre frequency decreases. This is true, as for a fixed λ_{SAW}, $f_{SAW,0} \propto V_R$. Indeed, from figure [4.12] it is seen that at the SAW wave-vector generated on this sample ($k_{SAW} < 3\ \mu m^{-1}$), the biggest contribution to the SAW velocity comes from the MgO layer. Consequently, as the Rayleigh velocity decreases with increasing temperature, the centre frequency shifts to lower frequencies. Finally the frequency bandwidth does not change much with temperature: Δf_{SAW} min = 11 MHz, max = 13 MHz.

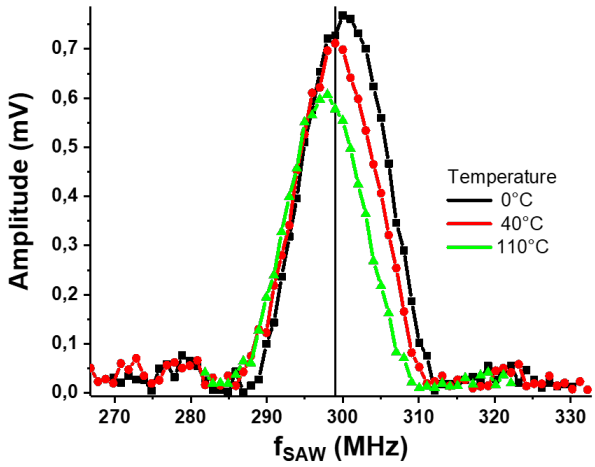

Figure 4.18: Temperature dependence of the centre frequency at $f_{SAW,2} = 298$ MHz on ZnO/SiO_2/FeRh/MgO sample (c.f. fig. [2.9]). Note the sinus-cardinal shape of the SAW resonance around its centre frequency. Different amplitudes are measured at different temperature, meaning that the efficiency of the IDT changes with temperature. A shift to lower frequencies is observed and matches with the Rayleigh temperature dependency in MgO.

6.2.2 Configuration of InterDigitated Tranducers

Several configurations of the electrodes are possible when designing the InterDigitated Tranducers. Aforementioned before, is the simplest geometry possible for the generation of SAWs, with the oppositely deposited electrodes connected alternatively to opposing electrical potential. In this manuscript, two alternative configurations were used namely the Split 4-4 and the Split 5-2 respectively [182].

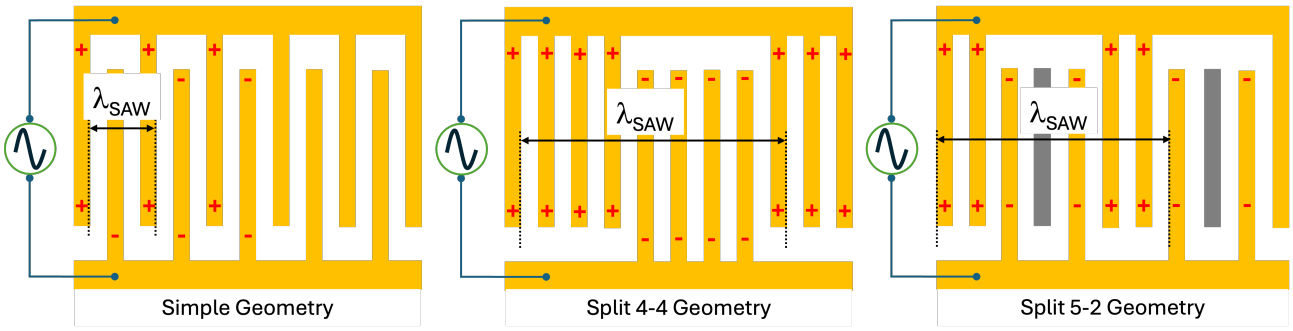

Figure 4.19: Three possible geometries for the IDT design. The Simple Geometry, the Split 4:4

Figure [4.19] gives a schematic representation of three possible IDT geometries. The simple geometry allows the generation of the fundamental frequency, and very low amplitude subsequent odd-harmonics. On the other hand, the two split designs allow the generation of several harmonics. In the split 4-4 geometry, the electrodes are divided into two sets, with each set containing four fingers. The fingers of each set are interleaved with the fingers of the other set, resulting in a total of eight fingers in one period. Odd harmonics of the fundamental are generated with this configuration: $f_1, f_3, f_5, f_7, ...$ In the 5-2 configuration, on the other hand, the electrodes are divided into two sets with one set containing 2 fingers and the other set containing 3 fingers, where one is left unconnected to either polarity. This unconnected finger is defined as a dummy finger. There is a total of five fingers and 10 spacings per

period. The asymmetrical arrangement of the fingers allows the generation of all possible harmonics: $f_0, f_2, f_3, f_4, ...$

6.2.3 Different Layers and IDT Fabrication

Here is recalled the complete stack of the two samples. For Sample A: FeRh/MgO, the IDTs are deposited on the piezoelectric ZnO, as neither MgO nor SiO_2 are piezoelectric. Moreover, in no case one could deposit the IDTs on FeRh as there would be an electrical short-circuiting. For the Sample B, it is recall that the fabrication process is simple. Here the IDTs are deposited directly on the piezoelectric GaAs.

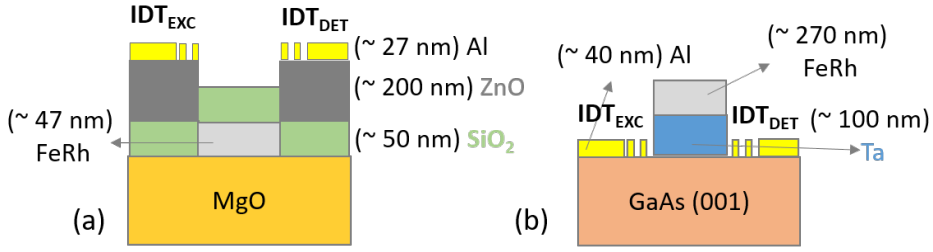

Figure 4.20: Schematic representations of the two stacks for Crystalline Sample A and Polycrystalline Sample B. Not to scale. The layer thickness was measured using a Dektak Profilometer by L. Becerra.

7 Schematic representation of the two samples

7.1 Crystalline Sample A: FeRh/MgO

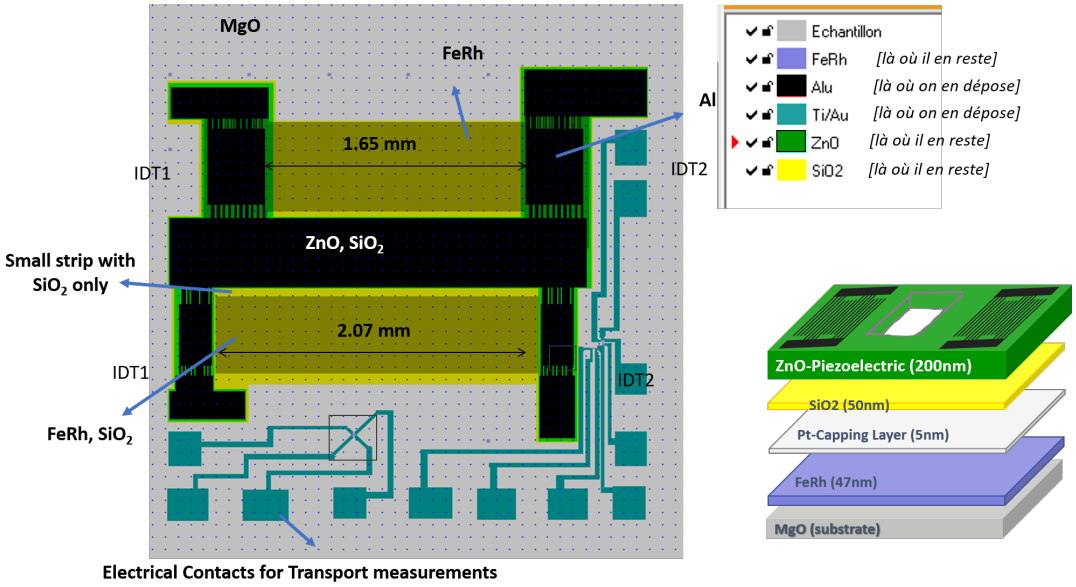

Figure 4.21: Crystalline Sample A complete .cif Stack. This is not in the same colour scheme as before, as they it is fairly difficult to distinguish the respective layers. The yellow coloured layer here represents the SiO_2, and the green layer the ZnO. The ZnO is present only under the IDTs (represented in black). In purple is the FeRh layer. However since this layer is further below, on the .cif image, the FeRh delay lines are represented as maroon-ish rectangles. There are two of length L = 1.65 mm (delay line 4:4) and L = 2.07 mm (delay line 5:2). Very important for chapter [6], note although the SiO_2 layer is present over the FeRh, there is fine region whereby there is only the SiO_2. This is useful to isolate the reflectivity contribution of the FeRh layer only. Note the presence of a second delay line for split 4:4 where we were not able to generate any SAWs. This is the top delay line with a length of L = 1.65 mm. Note also the electrical contact made for transport measurement (resistivity vs Temperature in the presence/absence of SAW), also rendered useless by no emission of SAWs, and subsequent destruction of the FeRh strips due to too high current injected.

7.2 Polycrystalline Sample B: FeRh/GaAs

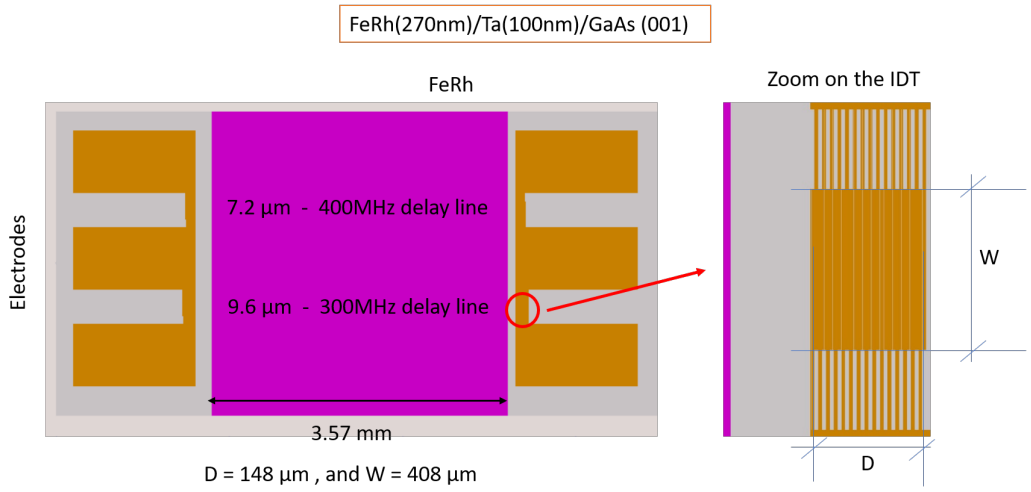

Figure 4.22: Polycrystalline Sample B complete .cif image. Note the central FeRh strip line bordered on either side by the IDT deposited on the GaAs directly. These 2 regions bordering the FeRh central strips were covered by Kapton scotch during the sputtering process (c.f. [2]). Note the two delay lines: 300 MHz and 400 MHz which are fundamental to understand chapter [7]. Courtesy E. Dandeu and G. Olivetti

.

The table below gives a summary of the IDT geometries on the two samples, with their corresponding SAW wave-length, fundamental frequencies and subsequent harmonics.

Excitable Frequencies in (MHz) on MgO		
Harmonics	Split 4:4 (λ_0= 20μm)	Split 5:2 (λ_0= 35.6μm)
f_0	268	152
f_2	-	300
f_3	761	442
f_4	-	581
f_5	1216	711
f_6	-	840
f_7	1650	963

Excitable Frequencies in (MHz) on GaAs		
Harmonics	Split 4:4 (λ_0= 9.6μm)	Split 4:4 (λ_0= 7.2μm)
f_0	299	398
f_3	899	1192
f_5	1543	-

Table 4.3: Excitable frequencies for our 2 multi-frequency IDTs on either MgO or GaAs

8 Experimental setup: SAW generation and detection

As developed in Chapter [2] section [3.1], the sample is placed inside a cryostat, connected to a series of electrical cables (2 RF ports and 21 DC cables[13]) and probed using a laser or LED source. Indeed, the series of electrical cables consists of DC contacts for electrical transport measurements and RF cables that feed the IDT. Figure [4.23], is a schematic representation of the electrical excitation coupled with the electrical or optical SAW detection. The sample is placed inside the cryostat, and a zoom on the latter shows the substrate, connected to a pair of IDT deposited on a piezoelectric layer: IDT_{EXC} and

[13]These were designed for transport measurements on Sample A. However, the transport bars were dysfunctional. Since no subsequent sample with transport bars, were available, no transport measurements were undertaken during the thesis.

IDT_{DET}, an RF port, an oscilloscope and the laser spot coming from a probing laser. A continuous sinusoidal signal at frequency f_{SAW} ($\approx$ 200 MHz - 1GHz), is modulated into a squared-pulse train function, with pulses typically $\approx$ 200 - 300 ns by a Vector-Signal-Generator. This signal is sent to the RF port of the exciting IDT, IDT_{EXC}. By piezoelectric effect, the electrodes that made up the IDT vibrate, and a surface acoustic wave is generated at k_{SAW} perpendicular to the IDT.

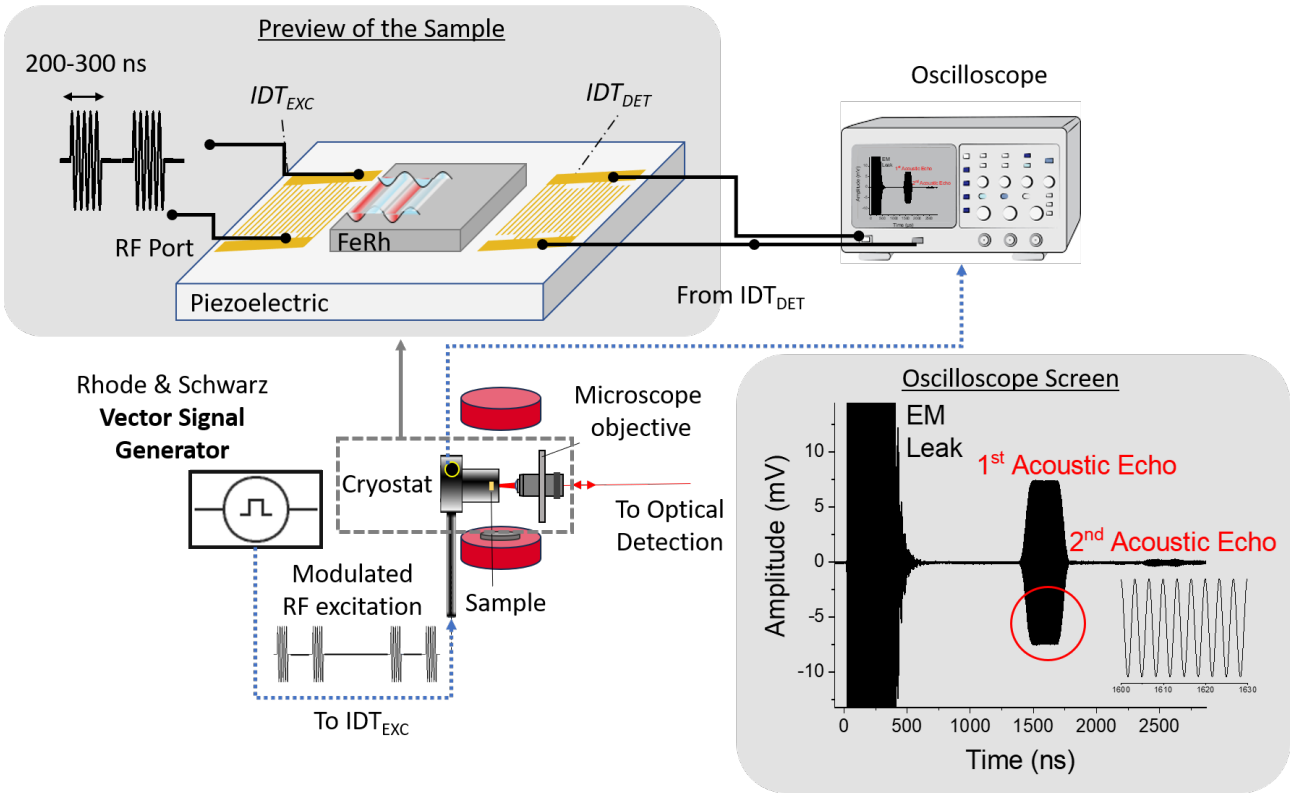

Figure 4.23: Schematic representation of the sample with a pair of IDTs, one for the generation of SAW and a second one for the detection of the latter. The modulated pulses are fed to the former, and an the signal received by the latter is sent to an oscilloscope. On the oscilloscope screen, the EM leak and the slower acoustic echos are observed. A zoom on the echo signal shows the sinusoidal signal at f_{SAW}.

Once the SAWs are generated, propagate and interfere with the metallic FeRh layer, it is possible to detect them either optically or all-electrically. The optical detection will be presented briefly in Chapter [9]. Yet, all the data presented in this manuscript stem from the all-electrical SAW generation and detection method, as illustrated here. Once the excitation IDTs have generated the SAWs, they travel over the whole FeRh mesa or delay line and reaches IDT_{DET}, placed a few millimetres away (Sample A: the delay line = 2.07 mm or 1.65 mm- we were not able to generate SAWs on the latter; while on Sample B, the delay line is 3.57 mm). This converts the incoming dynamic strains into an electronic signal, which is then fed into an oscilloscope for analysis. The inset of fig. [4.23] exemplified a typical signal on the oscilloscope screen. Two types of signal with respect to time are depicted. An electromagnetic leak due to inductive effect that travels at the speed of light, and a much slower acoustic signal or echo travelling at the Rayleigh velocity (typically 5400 ms^{-1} on MgO and 2800 ms^{-1} on GaAs). A second acoustic echo is represented on the oscilloscope. This originates from the reflection of the SAW and has twice the time stamp. For a signal with twice the time-stamp, this means that it was generated by the EM leak impinging on IDT_{DET}, that first travelled towards IDT_{EXC}, reflected and then detected back by IDT_{DET}. Note, this separation between the EM leak and the echos is visible only due to the square modulation of the RF excitation. The first acoustic echo, as described in Chapters [5], [6] and [7], is monitored with respect to temperature and/or magnetic field.

Chapter Summary

1. The chapter begins with an introduction to fundamental concepts of elasticity, focusing specifically on linear and rotational strains, and the wave equations. This is essential for the next chapter.

2. Determined experimentally using BLS and pico-second acoustic measurements the complete set of elastic constants on FeRh, in the AFM and FM phases.

3. Acoustic wave velocities and modes were calculated for various systems, including bulk materials and semi-infinite media, with propagation directions considered along either the [100] or [110] crystallographic directions.

4. The Farnell-Adler model, which describes thin film propagation on layered media, was introduced. We then used the aforementioned elastic constants to calculate the Rayleigh velocities on our layered systems. Then we focus on the dispersion relations.

5. The chapter concludes with a discussion on the generation of SAWs using IDTs, and the associated SAW frequencies on the two samples. The electrical setup for SAW generation and detection is introduced ans described schematically.

Chapter 5

SAW-FMR

Objectives

In this chapter, the concepts of magneto-elasticity and magnetostriction are introduced and thoroughly examined. The interaction between a propagating surface acoustic wave (SAW) and a magnetic system is demonstrated, with a focus on deriving the magneto-elastic coupling field induced by the SAW. Subsequently, a detailed mathematical model is developed to describe the interaction between the surface acoustic wave and ferromagnetic resonance (SAW-FMR). This model provides a theoretical framework for understanding the dynamics of SAW-induced magnetic phenomena and offers insights into how these interactions can be quantified and manipulated. The chapter aims to elucidate the underlying principles governing magneto-elastic effects and their implications for advanced material science applications. By integrating theoretical derivations with practical considerations, this work contributes to the broader understanding of magneto-acoustic interactions and their potential applications in emerging technologies.

Contents

1 Introduction to SAW-FMR

As established in the previous chapters, controlling magnetic states or magnetism in general, typically involves employing various techniques. The easiest prevalent approach, at the beginning, consisted in applying magnetic or electric fields [183], or temperature, alongside doping [184], [185] or alloying [186] to match for possible applications. Then came the advent of spintronics and techniques such as spin injection [187], [188], spin-transfer or spin-orbit torques [189]–[191] and current-driven domain wall motion [192] among others. This manuscript, primarily focuses on dynamic strain-controlled magnetism via magneto-acoustics. This interaction of phonons with magnetic states, or more specifically to coherent magnetic excitation, magnons, has been formulated by Kittel in the late 50s [16], who demonstrated that the magneto-elastic free energy contribution to the total magnetic free energy led to an equivalent effective field, driving magnetisation dynamics. In the following years, the existence of FMR driven by acoustic waves was demonstrated [193]–[195], and subsequent studies involving Nickel or Yttrium Iron Garnets (YIG), were undertaken for non-resonant and resonant coupling [196], [197]. The first fifteen years of the 21st century have witnessed numerous studies investigating the coupling mechanisms of static strains [198] with magnetisation and their resultant effects on magnetic anisotropy and ferromagnetic resonance (FMR) across a broad spectrum of multi-ferroic structures [199], both theoretically and experimentally [200]. As significant advancements were made, interests have surged in using dynamic strains to act on magnetisation remotely. Surface Acoustic Waves (SAWs) emerge as an ideal candidate due to their inherent advantages, including low attenuation and long distance propagation, adjustable frequency and wave-vector, high-energy efficiency, low-cost, and ease of device integration with microwave electronics [201]. Today, the study of SAW-Spin Wave (SW) interaction via Interdigitated Transducers (IDTs)-generated SAWs is now a full-fledged branch of spintronics.

2 Magneto-elasticity

Bridging the gap between the propagating SAWs, i.e. temporal and spatial dynamical strains, and magnetisation is the phenomenon of magneto-elasticity. Magneto-elasticity is equally relevant for dynamical or static strains. Magneto-elastic effects arise due to the interplay between the exchange interaction and magnetic anisotropy, and distortions of the crystal lattice, or more particularly the atomic orbitals [202]. When an external magnetic field is applied, the orientation of the individual magnetic moments changes, which disturb the equilibrium state of the crystal lattice, resulting in strain or deformation. Conversely, mechanical stress influences the magnetic state of the material. One of the most commonly known magnetoelastic effects is magnetostriction, where the shape and size of a magnetic material is altered in response to an externally applied magnetic field. Magneto-elastic effects play a crucial role in various technological applications, such as acoustic actuators [203] and resonators [204], magnetic sensors [205], and energy conversion, among many others. In this section, the reader is introduced to the theoretical concepts governing magneto-elasticity.

2.1 Elastic Contribution

Crystal lattices can be deformed by a series of forces both of internal or external origins. A solid is said to be elastic if it returns to its initial state of rest after the removal of the force. Similar to the model developed in the previous chapter [4], the elastic or potential energy density can be written in terms of the elasticity tensor C_{ijkl}, and the strain components ε_{ij}. In the harmonic approximation it is given as:

$$f_{EL} = \frac{1}{2} C_{ijkl}\, \varepsilon_{ij}\, \varepsilon_{kl} \tag{5.1}$$

For an elastic material with cubic symmetry, using the elasticity tensor from equation [5.2], equation [5.1] can be written as:

$$f_{EL} = \frac{1}{2} C_{11} \left(\varepsilon_{xx}^2 + \varepsilon_{xx}^2 + \varepsilon_{zz}^2\right) + 2\, C_{44} \left(\varepsilon_{xy}^2 + \varepsilon_{xz}^2 + \varepsilon_{yz}^2\right) + C_{12} \left(\varepsilon_{xx}\varepsilon_{yy} + \varepsilon_{xx}\varepsilon_{zz} + \varepsilon_{yy}\varepsilon_{zz}\right) \tag{5.2}$$

2.2 Magnetostrictive Contribution

Isotropic changes in the volume under the influence of a magnetic field are called volume magnetostriction or forced magnetostriction. Alternatively, if the resultant linear strains are different along different directions, the magnetic material is said to follow anisotropic magnetostriction or Joule magnetostriction. Discovered in 1842 by J. Joule [1818-1889], the linear saturation magnetostriction λ_S , is defined as the change in length per unit length for a material being magnetised to saturation, where λ_S denotes magnetostrictive constants.

$$\lambda_S = \frac{\Delta l}{l_0} \tag{5.3}$$

Magnetostriction can be manifested as either parallel or perpendicular to the applied magnetic field, depending on which direction the strain is being measured. Figure [5.1], shows schematically the magnetostrictive coefficients respectively parallel or perpendicular to the direction of the applied magnetic field for a non-zero field. Given that a magnetostrictive material can either expand or contract under a field value, the same is true for the constant as seen in figure [5.2]. The inverse effect, commonly known as the Villari effect, is also true, whereby straining a magnetic material can influence the preferential axis of magnetisation. The Villari effect is the one used to act on FeRh, in this work.

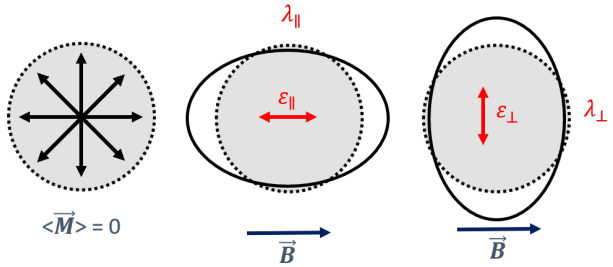

Figure 5.1: Representation of a fully demagnetised magnetic sample. Upon the application of the magnetic field, the magnetic moments in the sample aligns parallel to the field and the magnetic sphere is deformed. The strains ε_i, and magnetostrictive constants λ_i, respectively parallel and perpendicular to the magnetic field are respectively illustrated in red.

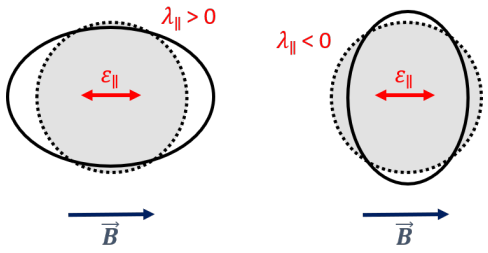

Figure 5.2: For strain measurement parallel to field, the magnetostrictive constant can either be positive: it is thus easier to magnetised a sample in the Tensile stress direction, ie the direction of application of the field; or negative: it is more difficult.

Magnetostriction arises due to magneto-crystalline anisotropy (c.f. Chapter [3]), or more particularly due to spin-orbit interaction and crystal fields. As the material solid is deformed by the magnetic field, the crystalline structure is altered and so are the crystal fields, which in turn influences on the crystallographic anisotropy. Several direct or indirect alternative magnetostrictive effects exist, for example the Wiedemann effect [1862] [206], which causes a mechanical torsion under the action of a helical magnetic field, or the magneto-volume [207] or surface magnetostriction [208] and so forth. Cobalt displays the largest room-temperature magnetostriction of any pure element. For alloys, Terfenol-D[1] presents the highest known magnetostriction, while commonly used engineering materials include Galfenol, AlFer, MetGlas, Cobalt-Ferrites and Nickel. [209].

For a magnetic cubic anisotropy

The magnetostrictive contribution to the total magnetic energy, for a cubic anisotropy, can be written in terms of the strain components and magnetisation direction cosines as:

$$\begin{aligned} f_{ME}^{C} &= B_1 \sum_i \alpha_i^2 \, \varepsilon_{ii} + 2\, B_2 \sum_{i \neq j} \alpha_i \alpha_j \, \varepsilon_{ij} \\ &= B_1 \left[\varepsilon_{xx} \, \alpha_x^2 + \varepsilon_{yy} \, \alpha_y^2 + \varepsilon_{zz} \, \alpha_z^2 \right] + 2\, B_2 \left[\varepsilon_{xy} \, \alpha_x \alpha_y + \varepsilon_{xz} \, \alpha_x \alpha_z + \varepsilon_{yz} \, \alpha_y \alpha_z \right] \end{aligned} \tag{5.4}$$

[1] Terbium-Iron-Dysprosium

where B_i, are the magnetoelastic constants which describes the degree to which the applied magnetic field induces the magnetostrictive strain and conversely.

In the case of a Rayleigh wave propagating along the **x** direction, the continuum displacements are u_x and u_z. Consequently, the magneto-elastic contribution can be simplified as:

$$\begin{aligned} f^{C}_{ME,R} &= B_1 \left[\varepsilon_{xx}\,\alpha_x^2 + \varepsilon_{zz}\,\alpha_z^2\right] + 2\,B_2\,\varepsilon_{xz}\,\alpha_x\alpha_z \\ &= B_1 \left[\cos^2(\phi_M)\,\sin^2(\theta_M)\,\varepsilon_{xx} + \cos^2(\theta_M)\,\varepsilon_{zz}\right] + B_2\,\cos(\phi_M)\,\sin(2\,\theta_M)\,\varepsilon_{xz} \end{aligned} \tag{5.5}$$

For a magnetic isotropy

The magnetostrictive contribution to the total magnetic energy, is then given by: $B_1 = B_2 = B_{ISO}$

$$f^{I}_{ME} = B_{ISO}\left(\varepsilon_{xx}\,\alpha_x^2 + \varepsilon_{yy}\,\alpha_y^2 + \varepsilon_{zz}\,\alpha_z^2 + 2\varepsilon_{xy}\,\alpha_x\alpha_y + 2\varepsilon_{xz}\,\alpha_x\alpha_z + 2\varepsilon_{yz}\,\alpha_y\alpha_z\right) \tag{5.6}$$

which in the case of a Rayleigh wave propagating along the **x** direction becomes:

$$f^{I}_{ME,R} = B_{ISO}\left(\varepsilon_{xx}\,\alpha_x^2 + \varepsilon_{zz}\,\alpha_z^2 + 2\varepsilon_{xz}\,\alpha_x\alpha_z\right) \tag{5.7}$$

2.2.1 Linking magnetostriction constants λ_i and magnetoelastic constants B_i

Consider a cubic anisotropy. The total elastic energy is:

$$f_{EL\text{-}TOT} = f_{EL} + f_{ME}$$

The equilibrium strain configurations are given by [114]:

$$\begin{cases} \frac{\partial f_{EL\text{-}TOT}}{\partial \varepsilon_{ii}} & = C_{11}\,\varepsilon_{ii} + C_{12}\,(\varepsilon_{jj} + \varepsilon_{kk}) + B_1\,\left(\alpha_i{}^2\right) = 0 \\ \frac{\partial f_{EL\text{-}TOT}}{\partial \varepsilon_{ij}} & = 2\,C_{44}\,\varepsilon_{ij} + B_2\,\alpha_i\,\alpha_j = 0 \qquad i{\neq}j \end{cases} \tag{5.8}$$

Using equation [4.2], the strain components can be generalised in terms of its direction cosines: $|\mathbf{du}(\mathbf{r},t)| = |\mathbf{dr}(\mathbf{r},t)|\;\varepsilon_{ij}\;\beta_i\;\beta_j$ where: $\lambda = \Delta l/l_0 = |\mathbf{du}(\mathbf{r},t)|/\;|\mathbf{dr}(\mathbf{r},t)|$. For crystalline samples with cubic symmetry, the magnetostrictive constants for saturation magnetisation in the [100], [111] and [110] directions and deformation measured in the direction of magnetisation, are respectively:

$$\lambda_{[100]} = -\frac{2}{3}\frac{B_1}{C_{11}-C_{12}};\quad \lambda_{[111]} = -\frac{1}{3}\frac{B_2}{C_{44}};\quad \lambda_{[110]} = -\frac{1}{6}\frac{B_1}{C_{11}-C_{12}} - \frac{1}{4}\frac{B_2}{C_{44}} = \frac{1}{4}\lambda_{[100]} + \frac{3}{4}\lambda_{[111]} \tag{5.9}$$

For isotropic samples, it is expected that $\lambda_{[100]} = \lambda_{[111]} = \lambda_s$ [114], while for untextured polycrystal and amorphous alloys, $\lambda_s = \frac{2}{5}\,\lambda_{[100]} + \frac{3}{5}\,\lambda_{[111]}$ [210], [211].

2.2.2 Typical magneto-strictive constants found in the literature

Iron Alloy	B_1 (MPa)	λ_{100} ($\times 10^{-6}$)	Ref
Fe (Polycrystalline)	1.72	- 6.8	[212]
$Fe_{1-x}Ga_x$ (x = 0.15–0.3)	-12 to 16	200 to 400	[213]
Fe	7		[21]

Table 5.1: Common magneto-strictive values for Fe alloys. The B_2 values are generally not available.

As no recorded values of B_1 and B_2 on FeRh are present in the literature, a discussion is needed on what to choose for FeRh. It is generally assumed that $B_1 = B_2$ in SAW-FMR papers. Duquesne *et al.* supposed $B_1 = B_2 = 7$ MPa for epitaxial Fe thin films [21], while Kuß *et al.* supposed $B_1 = B_2 =$ - 19.5 MPa on CoFeB [19]. However, this approximation is generally made in the case of an isotropic sample, which is not the case here, even for the Polycrystalline Sample B: FeRh/Ta/GaAs. A simplistic approximation of equating isotropic to polycrystalline does not stand here. Du Tremolet *et al.* argued

that in the case whereby $\lambda_{\parallel}$ and $\lambda_{\perp}$ are of different magnitude and sign, polycrystalline $\neq$ isotropic [206]. For Fe, at 300 kA/m, $\lambda_{\parallel} = \approx -27 \times 10^{-6}$ and $\lambda_{\perp} = \approx 25 \times 10^{-6}$. Moreover, note that the signs are different on Fe. Moreover, Du Tremolet *et al.* discussed the existence of another contribution to the total magneto-elastic energy dependent on the elastic displacements: magneto-rotation [206]. However, there exists no linear contribution to the magneto-elastic energy for an isotropic sample. Subsequently, the approximation $B_1 = B_2$ is erroneous. Thus, we take instead $B_2 = -2\ B_1 = 7$ MPa, to match our collaborators value [21].

2.3 Magneto-rotation

Over the last couple years, in addition to the influence of the compressional ε_{ii}, and shear strains ε_{ij}, components of the rotational strain tensor are being investigated. Recall, Eulerian-Almansi finite strain and the local rotational strain tensors are defined as (c.f. Chapter [4]):

$$\varepsilon_{ij} = \frac{1}{2}\left(\frac{\partial u_i}{\partial x_j} + \frac{\partial u_j}{\partial x_i}\right) \qquad \& \qquad \Omega_{ij} = \frac{1}{2}\left(\frac{\partial u_i}{\partial x_j} - \frac{\partial u_j}{\partial x_i}\right) \tag{5.10}$$

Maekawa *et al.* [214] showed that the interaction between the rotational lattice motion and magnetic spins results in a Hamiltonian equivalent to the magneto-elastic contribution, which persists even in the thin film limit. Moreover, rotational strains do not vanish at the free surface limit but even contribute one-to-two times more than the linear magneto-elastic counterpart [19]. Figure [5.3] is a schematic representation of the magneto-rotation coupling. As the SAW propagates, the lattice rotates and the shape anisotropy varies accordingly, modifying the total magnetic energy. Following the direction of the SAW ($\pm k_{SAW}$), the lattice motion is reversed. Hence, depending on the coupling terms involved, the magneto-rotation effect is either amplified or damped [215].

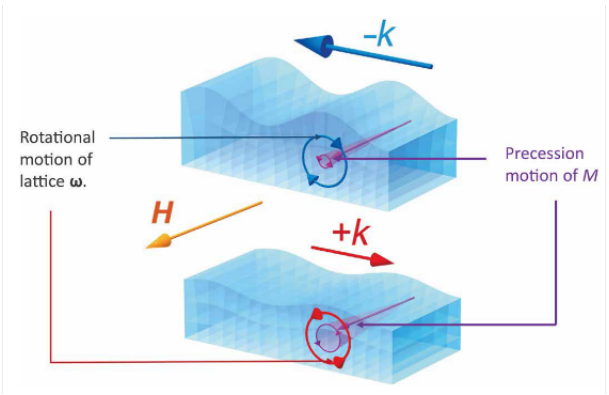

Figure 5.3: Schematic representation of the lattice rotational motion for SAW propagating along two opposite directions. This rotational motion has the same frequency as the SAW, i.e the lattice motion undergoes a full 360° rotation for λ_{SAW}. Note that, depending on the SAW propagation direction, the motion of the lattice is reversed. This chiral nature of magneto-rotation allows for enhanced non-reciprocal SAW-SW interactions. The lattice motion amplifies or hampers the magnetisation dynamics. This is represented by the larger red cone depicting larger precessional magnetic motion. Adapted from [215]

In the case of a Rayleigh wave propagating along the **x** direction (strain $\rightarrow u_x$ and u_z)[2]. The magneto-rotation contribution for FeRh is:

$$\begin{aligned} f_{MR}^{C} &= \mu_0\, M_s^2\, \Omega_{xz}\, \alpha_x\, \alpha_z \\ &= \frac{\mu_0\, M_s^2}{2}\, \cos(\phi_M)\, \sin(2\,\theta_M)\, \Omega_{xz} \end{aligned} \tag{5.11}$$

Similar to the competition of various free energy densities affecting the Landau-Lifshitz-Gilbert (LLG) equation [3.6], both the magneto-elastic and magneto-rotative terms can contribute to the dynamics. Indeed, for a propagating SAW, the dynamical contributions due to time- and space-varying linear ε_{ij}, and rotational strain ω_{ij} components modify both crystalline and demagnetising contribution to the magnetic anisotropy of the layer. This in turns generate internal magneto-elastic tickle field contributions that drive magnetisation dynamics.

[2] $\varepsilon_{yz} = \omega_{yz} = 0$

2.4 Magneto-elastic tickle fields

The tickle fields acting on the magnetic moments, driving magnetisation dynamics are given as the functional derivatives of the total magnetic energies. Similarly, magneto-elastic energies induce magneto-elastic tickle fields which can be calculated as:

$$b_\theta(\vec{r},t) = -\frac{1}{M_s}\frac{\partial\left(f_{ME}+f_{MR}\right)}{\partial\theta} \qquad \& \qquad b_\phi(\vec{r},t) = -\frac{1}{\sin\theta_0\, M_s}\frac{\partial\left(f_{ME}+f_{MR}\right)}{\partial\phi} \tag{5.12}$$

Using equations [5.5] and [5.11], the angular dependency of the magneto-elastic tickle field driving precession can thus be written for an in-plane magnetised sample ($\theta = \pi/2$), as:

$$b_\theta = \left(\frac{2B_2}{M_s}\,\varepsilon_{xz} + \mu_0\, M_s\, \Omega_{xz}\right)\cos(\phi_M) \tag{5.13}$$

$$b_\phi = \frac{2B_1}{M_s}\,\sin(\phi_M)\cos(\phi_M)\,\varepsilon_{xx} \tag{5.14}$$

A maximum coupling between the Surface acoustic wave and the Spin wave is expected for frequency ($f_{SAW} = f_{SW}$) and wave-vector ($\mathbf{k}_{SAW} = \mathbf{k}_{SW}$) matching, while respecting the angular distribution of magneto-elastic tickle fields. Consider the case of an in-plane magnetised sample with the magnetic equilibrium angle ϕ_M, taken with respect to the direction of propagation of the SAW, i.e ($\phi_M = 0° \parallel \mathbf{k}_{SAW}$). In that case, if the magnetisation is parallel to $\mathbf{k}_{SAW}$ ($\phi_M = 0°$), the only contribution is from the out-of-plane components ε_{xz} and Ω_{xz}. On the other hand, if the magnetisation is perpendicular to $\mathbf{k}_{SAW}$ ($\phi_M = 90°$), the magneto-elastic tickle field is zero. Remember, no SAW-FMR coupling is expected for this geometry, provided the magnetisation follows the magnetic field.

To assess the relative influence of the magneto-elastic tickle fields in equations [5.13] and [5.14], the mean relative values of the linear and rotational strains calculated in Chapter [4] are recalled here for the 299 MHz SAW: $<\varepsilon_{xx}> = 3.4\times10^{-5}$; $<\varepsilon_{xz}> = 5.7\times10^{-6}$; $<\Omega_{xz}> = 1.14\times10^{-4}$. Thus, assuming $B_2 = -2\,B_1 = 7.9\times10^6$ J/m^3, each term contributes to:

$$b_\theta = \left(\underbrace{\frac{2B_2}{M_s}\,<\varepsilon_{xz}>}_{\approx 6\times10^{-5}} + \underbrace{\mu_0\, M_s\, <\Omega_{xz}>}_{\approx 2\times10^{-4}}\right)\cos(\phi_M)$$

$$b_\phi = \underbrace{\frac{2B_1}{M_s}\,<\varepsilon_{xx}>}_{\approx 8\times10^{-5}}\sin(\phi_M)\cos(\phi_M)$$

The major contribution comes from the magneto-rotational term.

Note: an important point to remember here is that b_ϕ and b_θ are in phase quadrature.

3 SAW-driven Ferromagnetic Resonance

3.1 State of the art: SAW-FMR

Acoustic wave (or more particularly Surface Acoustic wave) interaction with the magnetic layer owing to magneto-elastic coupling has recently inspired several interdisciplinary research ranging from fundamental condensed matter physics, to energy-efficient applications passing by on-chip circuit implementation. In this section, an up-to-date review of SAW-mediated magnetic resonance is presented.

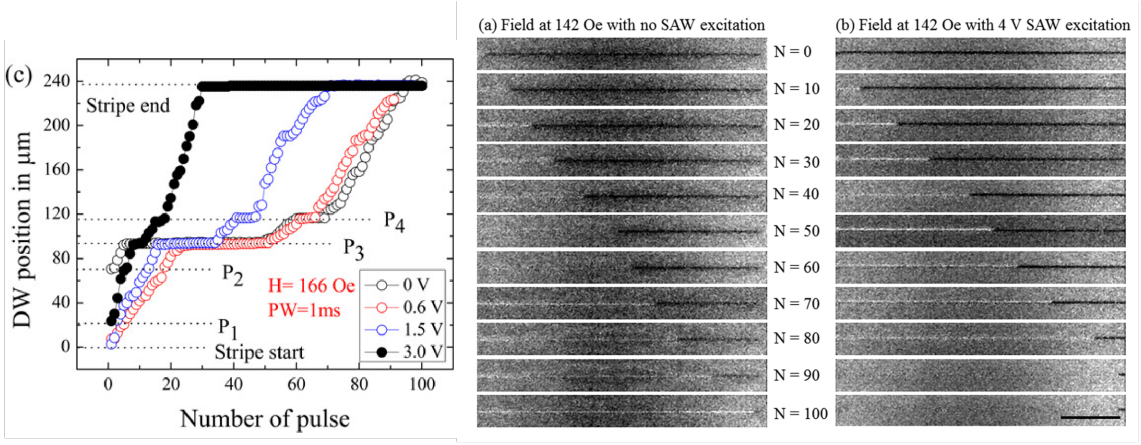

Figure 5.4: Left: Domain wall position as a function of the number of pulses for a 3 μm wide CoPt stripe, with put-of-plane anisotropy, at a fixed magnetic field of 166 Oe and a pulse width of 1 ms for different SAW voltage. At higher SAW voltages, domain walls depin more readily, evidenced by the reduced number of pulses required to move the DWs across the pinning sites. The horizontal plateaus in the graph correspond to pinning sites where the DW motion is temporarily halted. As SAW voltage increases, these plateaus shorten, indicating easier depinning. [216] **Right**: shows MOKE signal without and with SAW, on the same 3 μm wide CoPt stripe. Not that for all voltages, the SAW promote DW motion represented by the Grey-line. Adapted from [217].

Resonant and Non-Resonant coupling

Non-resonant coupling typically refers to the interaction of Surface Acoustic Waves with a magnetic layer far from the conditions of resonant excitation of spin waves. SAW-assisted magnetic domain nucleation and the substantial reduction in coercivity ($\approx$ 60% reduction) have been demonstrated on out-of-plane diluted semiconductor P-doped GaMnAs layers when subjected to propagating SAWs [27], [218]. This was attributed to the transient reduction of the domain wall energy. These findings highlight the role of SAWs in modulating magnetic behaviour, offering insights into potential strategies for controlling magnetisation and magnetic domains and skyrmions, among many others, in thin-film systems. Hence, it has been demonstrated current-free domain wall (DW) motion up to 50 ms^{-1}[219] on FeGaB wires. Similarly, Adhikari *et al.* have used 114.8 MHz and 248.8 MHz SAWs to promote depinning of DW motion on magnetic perpendicular anisotropic CoPt multilayers [216], [217]. Figure [5.4-**Left:**] is the measurement data of the DW position with respect to the number of magnetic train pulses and for different SAW voltage fed to the IDTs. It can be seen that without SAW, there is already a DW motion mediated by the magnetic field. However, when considering the 0 V data set, this motion reaches a plateau. The effects of different SAW voltages, and thus SAW strains can be appreciated, and lead to faster and more efficient DW motion. **Right:** is the MOKE measurement of DW motion without and with standing SAW. Note the larger distances covered when the SAW is applied for every magnetic pulse train number. The DW velocity is increased on average 6-fold for a SAW voltage of 4 V.

More recently, Riveles *et al.* measured the DW motion without the simultaneous application of magnetic field, and up to 100 ms^{-1} on FeCo [220]. A uni-directional motion is obtained for a propagating Rayleigh SAW at a frequency of 1.3 GHz. Figure [5.5] is the probability measurement of detecting the SAW on the right side of the IDT without SAW (in black), for a SAW with wave-vector respectively to the right (red) and left (blue). H_{inj} is simply an injection field post-saturation. It can be seen that this probability is asymmetrical for the two directional waves, leading to unidirectional motion. Using micro-magnetic simulations, the authors studied this effect and proposed an asymmetrical transfer of linear-momentum, or a "DW springing", to the DW as origin of the lopsided motion.

On the other hand, one way to harness the full potential of Kittel formulation, consists in resonant coupling between SAWs and SWs leading to coherent magnons excitation. This magnon-phonon interaction can also lead to strong coupling and the promotion of hybrid magnon-phonon quasi-particles.

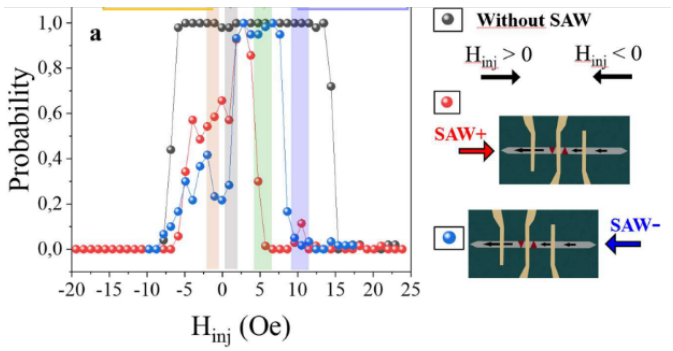

Figure 5.5: Probability plot of detecting a DW between two right contacts of the strip under three different conditions: without SAW (black dots), with SAW travelling from left to right (SAW+, red dots), and with SAW travelling from right to left (SAW-, blue dots). Here, the presence and direction of the SAW influence the likelihood of DW detection, with notable differences in detection probability depending on whether the SAW is propagating towards the right or left. The author proposed that this is due to the SAWs pushing the DWs in their propagation direction, aiding or hampering domain reversal processes. Adapted from [220].

One of the original papers on IDT-generated SAW resonance with magnetic layer was published in 2011 by Weiler *et al.* [17]. SAWs from 0.17-to-3.6 GHz were generated on a Ni/LNO substrate. Figure [5.6-**top:**] is the schematic illustration of the substrate, 50-nm thick Ni magnetic layer and IDTs separated by a 0.85 mm delay line. Following the SAW generation, it excites the SW in the Ni layer via magneto-elasticity. The SAW loses energy and this is represented on the figure **Bottom**. These are VNA measurements of the difference in SAW forward and backward transmissions for a magnetic field applied at 30° to k_{SAW}, and it can be seen the existence of symmetrical resonance at field values $\approx \pm$ 8 mT for a 2.24 GHz SAW. Note the presence of a hysteretic small field resonance around $\pm$ 2 mT. Angular SAW-FMR was studied and followed the magneto-elastic tickle field angular dependencies of equations [5.14,5.13], by having a maximum resonant effect at 45° to k_{SAW}. Using a similar geometry and replacing the Ni by a Co/Pt layer, the same authors also demonstrated the existence of SAW-generated spin-current [221]. Acoustic spin-pumping is the generation of spin-current from the Co ferromagnetic layer to the Pt layer by magnetisation precession. This can be seen as a fundamental building block of future spintronics and straintronics applications.

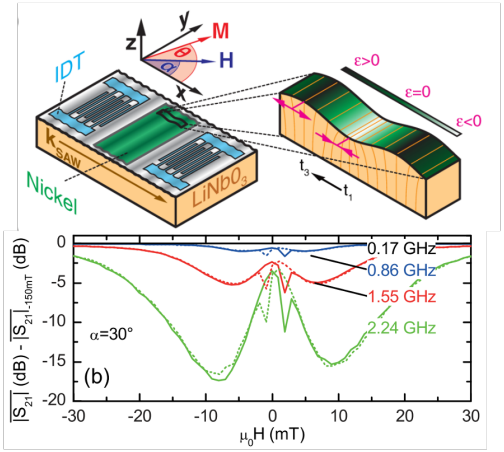

Figure 5.6: Top: Schematic representation of the Ni magnetic layer grown on the piezoelectric LNO and the IDT for SAW generation. The zoom on the Ni layer represents the SAW propagation and the corresponding changes in dynamical strains, ε_{ij}. **Bottom:** is the difference in SAW transmission with respect to the applied magnetic field. Note the two SAW transmission dips around $\pm$ 10 mT for 2.24 GHZ, and a decreasing resonance field value with decreasing SAW frequency. This is sign of SAW-FMR. Adapted from [17].

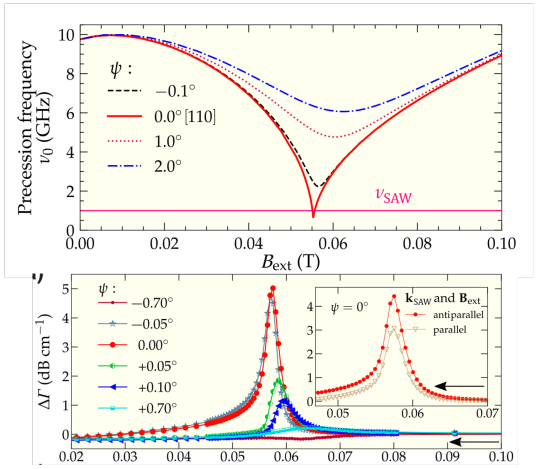

Figure 5.7: Top: Calculated Fe SW eigenfrequencies for the magnetic field applied parallel and thinly deviated from the [110]-Hard Axis of magnetisation. Note the sub-GHz SAW frequency. Similarly, SAW attenuation with respect to magnetic field for different field angles. In red the field is parallel to k_{SAW}, and a maximum attenuation (and consequently SAW-FMR) is measured. A slight deviation of 0.1° is enough to decrease by 5-fold this attenuation. Adapted from [21].

Recently, Duquesne *et al.* demonstrated the ON-OFF switching between SAW-FMR resonant interaction on a high-epitaxial quality Fe thin-film grown on GaAs [21]. The SAW propagates along the crystallographic [110] direction of GaAs represented in red (or denoted by 0.0°) on figure [5.7]. The figure **Top:** represents the calculated eigen-spinwave frequencies for the magnetic field applied along a hard-axis of magnetisation. This allows the softening of the SW frequencies to match the sub-GHz generated SAW. Due to the high-crystallinity, a simple tilt of 1° of the external applied magnetic field is enough to prevent phonon-magnon frequency matching. Similarly, on the figure **Bottom** is represented the SAW attenuation with respect to the magnetic field. A larger SAW attenuation implies that energy has been transferred to promote resonance and drive magnetisation dynamics. The highest SAW attenuation, and consequently the most efficient resonance, was measured for the magnetic field applied at 0.0°. In contrast, a dramatic decrease in the SAW-FMR resonance is observed when the magnetic field is tilted by only 0.1°, represented by the blue-coloured plot. The SAW attenuation is reduced 5-fold. Interest for highly directional SAW-FMR interaction conditions and the ability to abruptly switch between resonant and non-resonant states makes SAW-FMR an appealing foundation for sensing devices or magnetic-field monitoring. Furthermore, the inset represents the SAW attenuation for the SAW wave-vector parallel or opposite to the magnetic field in the 0.0° geometry. Here, a clear non-reciprocal SAW-FMR interaction is noted. Harnessing this effect is discussed below.

Strong Magnon-Phonon coupling

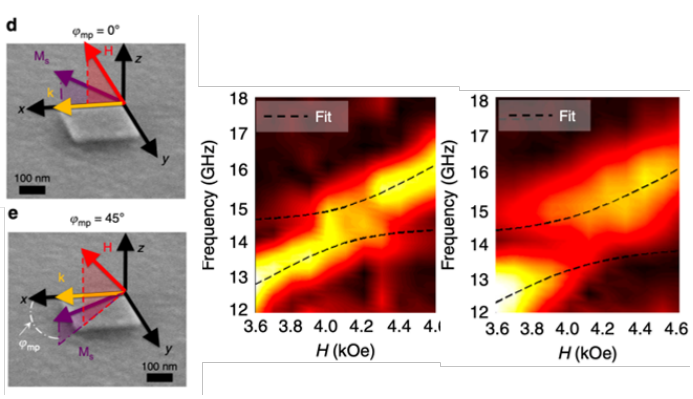

Figure 5.8: Left Panel: Geometry showing the Ni nanomagnet and the corresponding direction of the magnetic field. Top it is parallel to k_{SAW}, while bottom is makes a 45° angle. **Right Panel:** shows the Fourier Transform of a Time-resolved MOKE experiment showing the frequency spectrum in the two geometries. Note the presence of a gap in both cases, and this is maximised in the case where the magnetisation is at 45° to the SAW wave-vector. The dotted lines are present to aid visualisation. Adapted from [222].

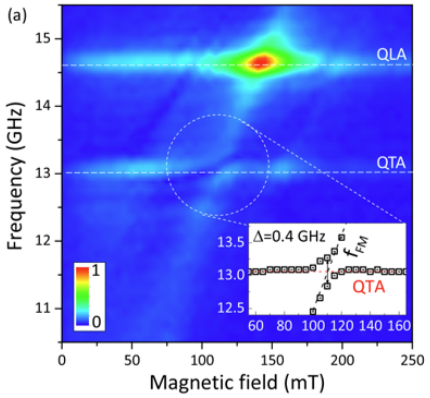

Figure 5.9: Color map showing the spectral density measured by Magneto-optical Kerr effect rotation as a function of magnetic field. The two horizontal lines represent the quasi-transverse and quasi-longitudinal phonon modes. Note the opening of a gap, and the signature of magnon-phonon hybridisation around 13 GHz. Inset represents numerical calculation of the cooperativity. Adapted from [223].

As discussed in the previous section, in order to observed magnon-phonon interaction, there needs to be frequency and wave-vector matching. Good material selections, for e.g. with small damping (YIG), and good lattice matching between the magnetic layer and substrate, result in small FMR line-width. Depending on the strength of this interaction, achieving strong magnon-phonon coupling regime is realisable. Generally, strong coupling is possible when the coupling strength is larger than the decay rates of the two individual particles, in this case the phonon and magnon. This interaction then leads to a hybrid magneto-acoustic mode, generally termed as magnon-polarons or magnon-phonon quasi-particles [224]. Here a digression is made from SAW to bulk-acoustic waves. Berk *et al.* studied the strong coupling interaction on a 330 x 330 x 30 nm single isolated Ni nano-structure [222] and represented on figure [5.8]. A laser pump irradiates the Ni sample and generate confined and quantised phononic modes in the x,y plane. Time-resolved MOKE measurements are then undertaken to measure the SW frequency response, and converted to the frequency domain using Fourier transform. **Left**

Panel: represents the geometric configuration showing the nanomagnet and the magnetisation. In the top layer the magnetisation is parallel to k_{SAW}, while in the bottom layer it makes a 45° angle. **Right Panel:** shows the FT measurements for the two geometries. A gap is clearly seen in both figures, with a maximum at ≈ 4 kOe. This frequency gap at the anti-crossing defines the strength of the strong coupling interaction and is generally defined as the cooperativity[3], C [225]. In the parallel configuration, the cooperativity is said to be, C = 0.74. By rotating the nanomagnet by 45°, the coupling strength is maximised and the cooperativity is increased by almost 66% to C = 1.65. Similarly Godejohann *et al.* investigated the conditions for hybrid excitation on galfenol ($Fe_{81}Ga_{19}$) [223]. The experimental setup involved optical pump-probe techniques, where a pump laser pulse excited a Rayleigh SAW and drove the magnetisation dynamics, and a probe pulse measured the resulting changes in temporal reflectivity and MOKE rotation which is indicative of phonon and magnon activities respectively. Figure [5.9] is the colour mapping of the MOKE signal with respect to a magnetic field applied in the direction maximising magnon-phonon interaction. Anti-crossing or gap is observed for a field close to 110 mT and a frequency of 13 GHz. To understand these interactions, the researchers developed a numerical model of three interacting oscillators, representing the magnon mode and two phonon modes (QTA-Quasi Transverse and QLA-Quasi Longitudinal), describing the complex amplitudes of these modes and their coupling strengths, with both methods giving the same gap splitting. The implications of strong coupling interaction can lead to new functionalities in data storage and processing. Collective transport properties and non-reciprocal propagation are essential building block for developing the next-generation of magnonic and phononic devices.

Non-reciprocal Magnon-Phonon interactions

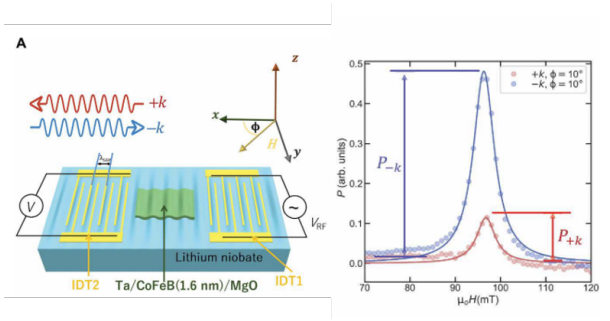

Figure 5.10: Left: Schematic representation of SAW generated on Ta/CoFeb/MgO with the two SAW propagation directions. **Right:** SAW attenuation near SW resonance for the two SAW wave-vector directions. Note the huge difference in the two non-reciprocal attenuation. Adapted from [215].

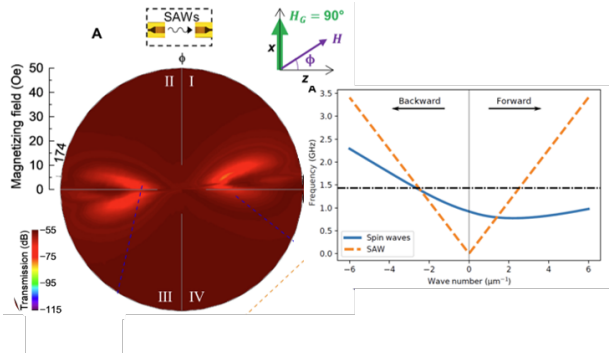

Figure 5.11: Left: Angular SAW-transmission measurement, for the forward and backward SAW propagation. Note the existence of non-reciprocal SAW absorption in the I quadrant. **Right:** Calculated dispersion relation for the SAW and the SW. Note the the SW dispersion relation and the asymmetric crossing points. The results of this crossing is a change of the acoustic dispersion law and the enhanced absorption of backward propagating SAW. Adapted from [226].

Non-reciprocal magnon-phonon interaction refers to a situation whereby the interaction between the magnons and phonons particles are dependent on their direction of propagation, or simply of their wave-vector directions. This non-reciprocity breaks the system's symmetry, where the interaction strength or dynamics are usually the same in both forward and backward directions (space-symmetry), and can lead to unique and intriguing physical effects such as uni-directional wave propagation, non-symmetric dissipation rates, and directional-dependent energy transfer. The non-reciprocal (NR) magnon-phonon interaction umbrella term can be classified into two broad sub-sections depending on their origin, giving NR resonant absorption or NR resonance field values. Xu *et al.* demonstrated both experimentally and theoretically the non-reciprocal acoustic wave attenuation in a perpendicularly anisotropic film

[3] $C \propto \frac{CouplingStrength}{\gamma_{magnon}\,\gamma_{phonon}}$ where γ defines the individual damping rates.

composed of Ta/CoFeB/MgO [215]. Figure [5.10] illustrates the magnetic system and the two SAW propagation directions. **Right:** is represented the SAW attenuation near SW-resonance for $\pm$ k_{SAW}. Note the huge difference in the normalised attenuation spectra. This non-reciprocal behaviour arises due to the shear wave component (c.f. equations [5.11]), induced by SAWs, interacts with the magnetic properties of the film. This interaction leads to an effective field that either enhances or suppresses magnetisation precession, depending on the direction of the SAW. The second effect is related to asymmetrical spin-wave dispersion relations for e.g. in synthetic antiferromagnet (SAF) or resultant of chiral interaction such as interfacial Dzyaloskinskii-Moriya interaction[4]. Shah *et al.* studied the NR SAW interaction for a 1.435 GHz SAW on a FeGaB/Al_2O_3/FeGaB multilayer grown on LNO. Figure [5.11] shows the SAW transmission versus magnetic field for different orientations, for SAWs propagating in opposite directions. Note the colour scheme, in particular the yellow colour depicting the maximum SAW absorption present in this experiment. The colour map shows a non-reciprocal SAW transmission of $\approx$ 10 dB ($\approx$ 70% reduction in SAW amplitude). Using a simple band model, the authors calculated and showed the asymmetric band diagram of the multi-layer structure. Indeed, on fig. **left:** it is observed that the SW has a very asymmetrical dispersion. This results in that the magnetoelastic coupling effectively attenuates acoustic waves in one direction while allowing them to propagate in the opposite direction.

SAW-FMR experiments have significantly advanced our understanding of magnetoelastic coupling in thin-film magnetic materials, and has shown potential for developing miniaturised, high-frequency devices for spintronic applications. The above sub-sections have highlighted the importance of coupling, material and resonance conditions in optimising the efficiency of SAW-driven FMR.

4 SAW-FMR modelling

Following the discussion on the state of the art of SAW-FMR, the purpose of this section is to mathematical implement this interaction. Two distinct theoretical frameworks exist to describe this coupling, namely the **back-action approach** or the **power transfer method** respectively. Although both methods aim to illustrate the interaction between the mechanical strains of a propagating SAW and the magnetisation dynamics, they rely on different perspectives and so, different aspects of the phenomenon are emphasised. The back-action framework focuses on a feedback mechanism between the mechanical strain and the magnetisation dynamics and the mutual affect on one another [20], [228]. As the SAWs propagate, the action of the elastic displacements modify the local magnetic anisotropy and act as a perturbation on the magnetisation dynamics. As precession is launched, the magnetisation, in turns, influences and alters the elastic constants. This results in a change of the SAW wave-vector and consequently the SAW propagation, which then feeds back into the magnetisation dynamics, leading to further modifications of the magnetic behaviour. This back-action results in an intricate self-sustaining dependency between the SAW and the magnetic resonance.

On the other hand, the power transfer approach consists in equating the acoustic power to the magnetic power, assuming the SAWs act as effective magneto-elastic driving field [18], [229]. Indeed, this method derives the acoustic power flow from the Poynting vector and amounts it to the magnetic power needed to drive and sustain magnetisation dynamics. It allows an analysis of the magneto-elastic coupling, and the resultant effects on the magnetic susceptibility of the magnetic layer. In this manuscript, the power transfer approach is implemented to study the SAW-FMR interaction.

4.1 Power transfer approach

Developed by Dreher *et al.* [18], while taking into consideration a purely longitudinal acoustic wave, the general framework of the power transfer approach consists in calculating separately the acoustic power

[4]The Dzyaloshinskii-Moriya interaction (DMI) is an anti-symmetric exchange interaction between neighbouring spins, caused by strong spin-orbit coupling and symmetry breaking (lack of inversion symmetry). This interaction favours a canted or twisted spin arrangement, leading to non-collinear spin structures such as spin spirals and skyrmions [227].

of the propagating wave related to the displacement components and the variations of magnetic power available in the magnetic layer. The acoustic power is the power necessary to sustain the magnetisation dynamics and to oppose damping phenomenon. By using the power transfer method, the SAW-FMR can be studied. In this section, the reader is introduced to the step-by-step methodology to solve the SAW-FMR and to link the experimentally observed quantities, namely the amplitude variations $\Delta\Gamma$ and the relative velocity variations $\frac{\Delta V}{V}$ respectively.

4.1.1 Magnetic and Acoustic Powers

Magnetic Power

The power transfer approach is strictly equivalent to an FMR experiment. Hence the change in FMR power at absorption can be written, in terms of a radio-frequency driving field $\mathbf{h_{RF}}$, as:

$$\Delta P_{\mathrm{FMR}} = -\frac{\mu_0}{2}\frac{d\mathbf{M}}{dt}\cdot\mathbf{h_{RF}} \tag{5.15}$$

where $\mathbf{h_{RF}} = \mathbf{h_{RF}}\, \mathrm{e}^{-i(\omega t - k\cdot x)}$ and $\frac{d\mathbf{M}}{dt} = \mathrm{M_S}\, \mathrm{e}^{-i((\omega t+\psi)-k\cdot x)}\, \frac{\delta\mathbf{m}}{dt}$. Using the magnetic susceptibility, χ: $\delta\mathbf{m} = [\bar{\chi}]\cdot\mathbf{h_{RF}}$, the FMR power can be separated in terms of its real and imaginary terms as:

$$\begin{aligned}\Delta P_{\mathrm{FMR}} &= \Re\left[-\frac{\mu_0}{2}\frac{d\mathbf{M}}{dt}\cdot\mathbf{h_{RF}^*}\right] + i\,\Im\left[-\frac{\mu_0}{2}\frac{d\mathbf{M}}{dt}\cdot\mathbf{h_{RF}^*}\right] \\ &= \underbrace{\Re\left[\frac{i\omega\mu_0 M_S}{2}[\bar{\chi}]\,\mathbf{h_{RF}}\cdot\mathbf{h_{RF}^*}\right]}_{\text{FMR Absorption term}} + \underbrace{i\,\Im\left[\frac{i\omega\mu_0 M_S}{2}[\bar{\chi}]\,\mathbf{h_{RF}}\cdot\mathbf{h_{RF}^*}\right]}_{\text{FMR dispersion term}}\end{aligned} \tag{5.16}$$

The above formula is equivalent in the case of a SAW-FMR phenomenon, where the RF fields originate from the SAW magneto-elastic driving fields. The change in magnetic power of the FeRh magnetic layer is thus written as:

$$\Delta P_{\mathrm{FMR}} = \left[\frac{i\,\omega_{\mathrm{SAW}}\; M_{\mathrm{s}}}{2}\int_{V_0}(b_\theta, b_\phi)^*\,[\bar{\chi}]\begin{pmatrix}b_\theta\\ b_\phi\end{pmatrix}dV\right] \tag{5.17}$$

where, $\mathbf{b_i}$, are the effective magneto-elastic driving fields, as seen in equations [5.13] and [5.14]. The Polder susceptibility tensor $[\bar{\chi}]$ is the magnetic response of a material to the RF field, and characterises the absorption and dispersion of its RF energy. ω_{SAW} is the Rayleigh wave frequency and V_0 is the magnetic volume encountered by the SAW as it propagates over the magnetic layer.
The integrand can be expanded to:

$$(b_\theta, b_\phi)^*\begin{bmatrix}\chi_{11} & \chi_{12}\\ \chi_{21} & \chi_{22}\end{bmatrix}\begin{pmatrix}b_\theta\\ b_\phi\end{pmatrix} = b_\theta^* b_\theta\chi_{11} + b_\phi^* b_\phi\chi_{22} + b_\theta^* b_\phi\chi_{12} + b_\phi^* b_\theta\chi_{21} \tag{5.18}$$

Note, b_θ and b_ϕ are in quadrature (c.f. equations [5.13] and [5.14]); Hence, equation [5.17] can be written, in terms of the magnetic volume experienced by the SAW $\mathrm{V_0}$, as:

$$\Delta P_{\mathrm{FMR}} = \frac{i\,\omega_{\mathrm{SAW}}\; M_{\mathrm{s}}\, V_0}{2}\left(|b_\theta|^2\chi_{11} + |b_\phi|^2\chi_{22} + b_\theta^* b_\phi\chi_{12} + b_\phi^* b_\theta\chi_{21}\right) \tag{5.19}$$

The Polder matrix is given by :

$$\bar{\chi} = \begin{bmatrix}\chi_{11} & \chi_{12}\\ \chi_{21} & \chi_{22}\end{bmatrix} = \frac{\gamma}{D}\begin{bmatrix}\gamma\frac{E_{\phi\phi}}{M_{\mathrm{s}}}(\mathbf{k_{SW}}) - i\alpha\,\omega_{\mathrm{SAW}} & -i\omega_{\mathrm{SAW}}\\ i\omega_{\mathrm{SAW}} & \gamma\frac{E_{\theta\theta}}{M_{\mathrm{s}}}(\mathbf{k_{SW}}) - i\alpha\,\omega_{\mathrm{SAW}}\end{bmatrix} \tag{5.20}$$

where $E_{\phi\phi}$ and $E_{\theta\theta}$ are the second derivatives of the total magnetic free energy with respect to ϕ_{M} and θ_{M} respectively, and

$$\begin{cases} D = -(1+\alpha^2)\left(\omega_{\mathrm{SAW}}^2 - \omega_0^2 + i\kappa\,\omega_{\mathrm{SAW}}\right)\\ \omega_0^2(\mathbf{k_{SW}}) = \dfrac{1}{{M_{\mathrm{s}}}^2}\dfrac{\gamma^2}{\alpha^2+1}\left[E_{\theta\theta}(\mathbf{k_{SW}})\times E_{\phi\phi}(\mathbf{k_{SW}})\right]\\ \kappa = \dfrac{\gamma}{M_{\mathrm{s}}}\dfrac{\alpha}{\alpha^2+1}\left[E_{\theta\theta}(\mathbf{k_{SW}}) + E_{\phi\phi}(\mathbf{k_{SW}})\right]\end{cases} \tag{5.21}$$

Note: $b_\phi \in \Re$ as it depends on ε_{xx} only, leading to $b_\phi^* = b_\phi$ and consequently, $b_\theta \in \Im$. The cross magnetic susceptibility term, $\chi_{12} = -\chi_{21}$.

Applying equation [5.19] into equation [5.16] results in:

$$\Delta P_{\mathrm{ABS}} = \Re\left[\frac{1}{2}\, i\, \omega_{\mathrm{SAW}}\; M_{\mathrm{s}}\, V_0 \left(|b_\theta|^2 \chi_{11} + |b_\phi|^2 \chi_{22} + \chi_{12}(b_\theta^* b_\phi - b_\phi^* b_\theta)\right)\right] \tag{5.22}$$

$$\Delta P_{\mathrm{DIS}} = \Im\left[\frac{1}{2}\, i\, \omega_{\mathrm{SAW}}\; M_{\mathrm{s}}\, V_0 \left(|b_\theta|^2 \chi_{11} + |b_\phi|^2 \chi_{22} + \chi_{12}(b_\theta^* b_\phi - b_\phi^* b_\theta)\right)\right] \tag{5.23}$$

Considering only the ε_{xx} component gives:

$$\Delta P_{\mathrm{ABS}} = -\frac{1}{2}\, \omega_{\mathrm{SAW}}\; M_{\mathrm{s}}\, V_0\, \Im(\chi_{22})\, |b_\phi|^2 \tag{5.24}$$

$$\Delta P_{\mathrm{DIS}} = \frac{i}{2}\, \omega_{\mathrm{SAW}}\; M_{\mathrm{s}}\, V_0\, \Re(\chi_{22})\, |b_\phi|^2 \tag{5.25}$$

Conclusion: Using this simple example, it is shown that the SAW-FMR absorption is related to the imaginary part of the Polder tensor, while the SAW-FMR dispersion to the real part of the Polder tensor.

Acoustic Power

For a Rayleigh-type acoustic wave propagating along the **x** direction, of acoustic beam width t, the mean density of acoustic power transported over the film thickness d, can be written as:

$$P_{\mathrm{SAW}} = \frac{1}{2}\rho\, t\, V_{\mathrm{R}}\, {\omega_{\mathrm{SAW}}}^2 \int_0^d \left[|u_{\mathrm{x}}|^2 + \cancel{|u_{\mathrm{y}}|^2} + |u_{\mathrm{z}}|^2\right] dz \tag{5.26}$$

where the elastic mechanical displacement is written as: $u_{\mathrm{i}}\,(\vec{r}, t) = u_{\mathrm{i},0}\, e^{[-i(\omega t - k\cdot x)]}\, e^{-\zeta z}$.

The complete spatial dependency of the elastic displacement components in terms of SAW wave-vector and the longitudinal and transverse velocities has been calculated by Maekawa *et al.* [214]. V. Laude[5] did the numerical calculation of the thickness dependence of the u_{i} components with respect to the thickness of the FeRh/Ta/GaAs trilayer of Sample B. Numerically, we consider only the average values over the FeRh layer, i.e. the top 270 nm of the tri-layer.
For a SAW propagating along the **x** direction over a length L, the acoustic wave interacts with the magnetic layer. This interaction, as stated previously, is the source of the magneto-elastic tickle field driving precession, and is manifested as a change in the SAW wave-vector, with $\Im[\Delta k_{\mathrm{SAW}}] > 0$ and $\zeta > 0$:

$$\begin{aligned} u_{\mathrm{x=L}} &= u_{\mathrm{x=0}} \cdot e^{[i(k_0 + i\,\Im\Delta k_{\mathrm{SAW}} + \Re\Delta k_{\mathrm{SAW}})\, L]} \cdot e^{[-\zeta z]} \\ &= u_{\mathrm{x},0} \cdot e^{[-\Im\Delta k_{\mathrm{SAW}} L]} \cdot e^{[-i\,\Re\Delta k_{\mathrm{SAW}} L]} \cdot e^{[-\zeta z]} \\ \text{and so,} \qquad |u_{\mathrm{x=L}}|^2 &= |u_{\mathrm{x},0}|^2 \underbrace{e^{[-2\Im\,\Delta k_{\mathrm{SAW}} L]}}_{\text{Attenuation FMR}} \cdot \underbrace{e^{[-2\zeta z]}}_{\text{Attenuation}} \end{aligned} \tag{5.27}$$

Considering small interactions between the acoustic displacements and magnetic layer, a first order series expansion of $e^{[-2\Im\Delta k_{\mathrm{SAW}} L]}$, simplifies equation [5.26] to:

$$P_{\mathrm{SAW,\,x=L}} = \frac{1}{2}\rho\, t\, V_{\mathrm{R}}\, \omega_{\mathrm{SAW}}^2\, |u_{\mathrm{x},0}|^2\, [1 - 2\Im\Delta k_{\mathrm{SAW}} L] \tag{5.28}$$

The variation in density of acoustic power transported by the Rayleigh wave across the delay line is thus given as:

$$\begin{aligned} \Delta P_{\mathrm{SAW}} &= P_{\mathrm{SAW,\,x=L}} - P_{\mathrm{SAW,\,x=0}} \\ &= P_{\mathrm{SAW}}^0 \times [-2L\,\Im\Delta k_{\mathrm{SAW}}] \end{aligned} \tag{5.29}$$

[5] Institut FEMTO-ST, - Université de Bourgogne Franche-Comté et CNRS, Besançon, France

Equating Magnetic and Acoustic Powers

Following the Ansatz proposed by [18], [20], [229], where the acoustic and RF powers are equal to each other, i.e. the lost acoustic power is converted to drive magnetisation dynamics, the following expressions are obtained:

$$\Re[\Delta P_{\mathrm{FMR}}(B,T)] = \Im[\Delta k_{\mathrm{SAW}}(B,T)] \times -2\,L\,P^0_{\mathrm{SAW}} \tag{5.30}$$
$$\Im[\Delta P_{\mathrm{FMR}}(B,T)] = \Re[\Delta k_{\mathrm{SAW}}(B,T)] \times -2\,L\,P^0_{\mathrm{SAW}} \tag{5.31}$$

These are the most important equations, in this manuscript, for the modelling of the SAW-FMR interaction. In practice, all the acoustic power is not converted into magnetic power in the layer, but depends on a filling factor $0 < \eta < 1$. The filling factor determines the amount of acoustic energy transferred to the ferromagnetic layer. A higher filling factor means more of the acoustic energy is interacting with the ferromagnetic material, leading to a stronger magneto-elastic coupling. The filling factor can be represented mathematically as the ratio of the volume of ferromagnetic material interacting with the SAWs to the total volume seen by the SAWs as they propagate. If V_{FM} is the ferromagnetic volume and V_{TOT} the total volume seen by the SAW, then the filling factor is given as: $\eta = V_{\mathrm{FM}} \,/\, V_{\mathrm{TOT}}$.

The SAW acoustic power can be related to the magnetic power of the FeRh layer by:

$$\Delta P_{\mathrm{FMR}}(B,T) = \eta \Delta P_{\mathrm{SAW}}(B,T) \tag{5.32}$$

4.2 Expressions of the Amplitude and Velocity variations

4.2.1 Amplitude Variations

The SAW amplitude variation is taken as the logarithm of the fraction from the reference point, i.e. far from SAW-FMR resonance field or temperature values.

$$\begin{aligned}\Delta\Gamma = 20\log\left(\frac{A}{A_0}\right) &= 20\log\left(\frac{u_{\mathrm{x=L}}(B,T)}{u_{\mathrm{x=L}}(B_0,T_0)}\right) \\ &= 20\log\left(\frac{u_{\mathrm{x=0}}(B,T)\,e^{[-\Im\Delta k_{\mathrm{SAW}}(B,T)L]}}{u_{\mathrm{x=0}}(B_0,T_0)\,e^{[-\Im\Delta k_{\mathrm{SAW}}(B_0,T_0)L]}}\right)\end{aligned} \tag{5.33}$$

Using the assumption that $u_{\mathrm{x=0}}(B,T) = u_{\mathrm{x=0}}(B_0,T_0)$, the SAW amplitude variation is given by:

$$\begin{aligned}\Delta\Gamma &= 20\log e^{[[-\Im\Delta k_{\mathrm{SAW}}(B,T)L]-[-\Im\Delta k_{\mathrm{SAW}}(B_0,T_0)L]]} \\ &= 20\log e^{[\frac{\Re[\Delta P_{\mathrm{FMR}}(B,T)]-\Re[\Delta P_{\mathrm{FMR}}(B_0,T_0)]}{2\,P^0_{\mathrm{SAW}}}]}\end{aligned} \tag{5.34}$$

Experimentally, the above assumption implies that the IDT-generated SAWs are independent of the magnetic field and temperature. For the magnetic field variations, the assumption is true. For the temperature variations, this assumption cannot be satisfied. However, since most SAW-FMR experiments with respect to magnetic field are measured at constant temperatures, the approximation is nevertheless satisfied experimentally.

4.2.2 Relative Velocity Variations

Similarly the relative SAW velocity variations can be related to the real part of the SAW wave-vector as:

$$\frac{\Delta V}{V} = -\frac{\Delta\phi}{\phi_0} = -\frac{\Re\left[\Delta k_{\mathrm{SAW}}(B,T)\right] - \Re\left[\Delta k_{\mathrm{SAW}}(B_0,T_0)\right]}{k_{\mathrm{SAW}}} \tag{5.35}$$

$$\frac{\Delta V}{V} = -\frac{\Im[\Delta P_{\mathrm{FMR}}(B,T)] - \Im[\Delta P_{\mathrm{FMR}}(B_0,T_0)]}{2\,L\,P^0_{\mathrm{SAW}}\,k_{\mathrm{SAW}}} \tag{5.36}$$

5 SAW-FMR on FeRh

In this section, the total magnetic energy of the FeRh system is presented and applied to the Smit-Beljers formula that governs magnetisation dynamics (c.f. equation [3.9]). Eigen-frequencies and eigen-modes are calculated, and the conditions for matching with SAW frequencies are examined. Following this, and building on the above presented model of SAW-FMR, the generalised dependencies of the SAW amplitude and the relative velocity variations, are derived. These will provide insights into the coupled dynamics when compared with the experimental data collected (c.f. Chapters [7 to 8]).

5.1 General Case: FMR on FeRh

5.1.1 Magnetic energy terms

It is commonly known that bulk FeRh exhibits cubic magneto-crystalline anisotropy. In chapter [2], it has been demonstrated for Crystalline Sample A: FeRh/MgO, that the magnetic bi-axial anisotropy is conserved (c.f. section [3.3]). The same cannot be said about Sample B: FeRh/GaAs. As such, in the following, the magnetic crystalline anisotropy is considered to be made up of an uniaxial- due to growth or varying vertical Rhodium concentration, and a cubic anisotropy respectively denoted by anisotropy constants K_u and K_c. The magnetic field is applied in the plane of the sample, and makes an angle ϕ_H with the **x**-direction. Similarly, the magnetic anisotropies are defined with ϕ_u and ϕ_c being the anisotropy axes. The total magnetic free energy is then given as:

$$\begin{aligned} E_{TOT} &= E_{MCA} + E_{ZEE} + E_{DEMAG} + E_{DIP} + E_{EX} \\ &= \frac{K_c}{4}\left[\sin^4(\theta_M)\sin^2(2\,(\phi_M - \phi_c)) + \sin^2(2\theta_M)\right] + K_u\left[\sin^2(\theta_M)\cos^2((\phi_M - \phi_u))\right] \\ &- \mu_0 H M_s \sin(\theta_M)\cos(\phi_M - \phi_H) + \frac{1}{2}\mu_0 {M_s}^2\cos^2(\theta_M) - \frac{1}{2}\mu_0 \mathbf{M}\cdot\mathbf{H}_{DIP} + \mu_0 M_s \mathbf{H}_{EX}\cdot\mathbf{m} \end{aligned} \tag{5.37}$$

5.1.2 Smit-Beljers Formula

Using the Kittel formula derived in Chapter [3], equation [3.9], the eigen-spinwave frequencies are given for the FeRh sample, in the absence of damping as:

$$f_{prec} = \frac{\gamma}{2\pi\, M_s}\sqrt{E_{\theta\theta} \times E_{\phi\phi}} \tag{5.38}$$

The damping can be neglected here, since the focus is on the SW eigen-frequencies and SW modes, which are solutions of the Smit-Beljers formula. The damping term will not be ignored in the complete resolution of the SAW-FMR interaction, c.f. the Expressions of the Amplitude and Velocity variations in section [6]. $E_{\theta\theta}$ and $E_{\phi\phi}$ are respectively the second derivatives of the total energy density with respect to θ_M and ϕ_M and are given by:

$$\begin{cases} E_{\theta\theta} = \mu_0 H M_s \cos(\phi_H\text{-}\phi_M) + K_c\left(2 - \sin^2(2\,(\phi_c - \phi_M))\right) + 2K_u\cos^2((\phi_M - \phi_u)) \\ \qquad + \mu_0 M_s H_{EX}(k_{SW} a_{FeRh})^2 + \mu_0 {M_s}^2\,(1 - P_{00}) \\ E_{\phi\phi} = \mu_0 H M_s \cos(\phi_H\text{-}\phi_M) + 2K_c\cos(4\,(\phi_c - \phi_M)) + 2K_u\cos(2(\phi_M - \phi_u)) \\ \qquad + \mu_0 M_s H_{EX}(k_{SW} a_{FeRh})^2 + \mu_0 {M_s}^2\sin^2(\phi_M)\,(P_{00}) \\ E_{\theta\phi} = 0 \end{cases} \tag{5.39}$$

where P_{00} is the dimensionless dipolar factor defined as: P_{00} = 1 - $[(1 - e^{-k_{SW}d})/k_{SW}d]$ [230], and d being the thickness of the FeRh layer.

Since the SAW wave-vector considered here are small, a series expansion is performed on the dipolar contribution. This approximation is true for the $k_{SAW} = k_{SW}$ values considered here, as represented on figure [5.12]. P_{00} is plotted (in red) for k_{SW} = 0 to 2.5 μm^{-1}. Note the excitable wave-vectors represented here (grey dotted lines) are those corresponding to the excited SAWs on Polycrystalline

Sample B: FeRh/GaAs. In blue is plotted the series expansion of P_{00} up to the second order. Hence, it can be seen that the approximation is reasonable even for $k_{SW} = k_{SAW} = 1.963\ \mu m^{-1}$.

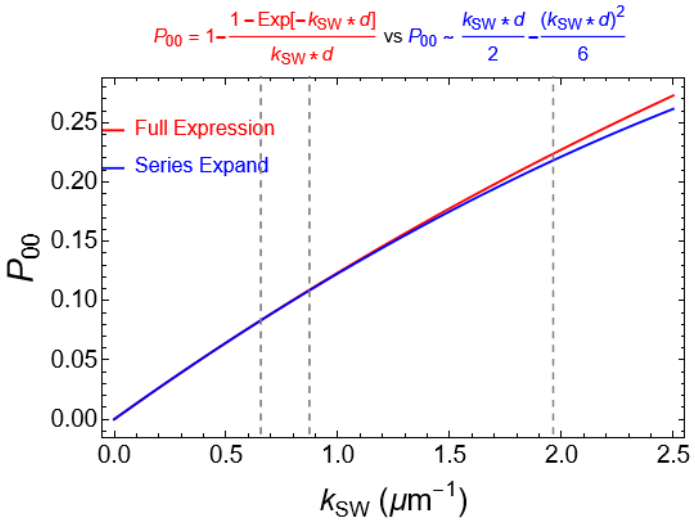

Figure 5.12: Evolution of the P_{00} function governing the dipolar spin wave contribution to the total magnetic energy. In Red is plotted the full exponential function: $P_{00} = 1 - [(1 - e^{-k_{SW}d})/k_{SW}d$, and in blue is plotted the series expansion for low k_{SW} up to the second order: $P_{00} \sim (k_{SW}d)/2 - (k_{SW}d)^2/6$. The vertical dotted lines represents the k_{SAW} values of the excited SAW: 0.654 μm^{-1}; 0.873 μm^{-1} and 1.963 μm^{-1} respectively. As seen, the approximation remains justified for the wave-vectors considered.

The dipolar contribution can thus be approximated to the $k_{SW} << 1$, approximation in a series expansion of the form:

$$\mu_0 \mathbf{H}_{DIP} = \mu_0 M_s \left[1 - \frac{dk_{SW}}{2!} + \frac{(dk_{SW})^2}{3!} + 0[k_{SW}^3]\right] \tag{5.40}$$

5.1.3 Simplest solution

In chapter [2], it was demonstrated that for the Crystalline Sample A: FeRh/MgO, the FeRh layer has a cubic magnetic anisotropy. The cubic anisotropy constant was thus found to be $K_C = 6.4$ kJm^{-3}. This geometry is considered here, i.e; a cubic magnetic anisotropy aligned with x $\parallel$ k_{SAW}. The Spin-Waves eigen-frequencies are calculated using the Smit-Beljers formula of equation [5.38] and the second derivatives defined by equations [5.39]. The first calculation of the eigen-frequencies is undertaken in the simplest possible case. The uniaxial anisotropy is ignored $K_u = 0$ kJm^{-3}. The easy-axis of anisotropy is taken to be along **x**, i.e. $\phi_c = 0°$, and the magnetisation is in-plane:

$$f_{prec} = \frac{\gamma}{2\pi}\sqrt{E_{\theta\theta} \times E_{\phi\phi}} \tag{5.41}$$

Using the VSM data, $M_s = 1.45 \times 10^6$ Am^{-1}; the SW frequency is plotted for the field applied parallel to **x** (Easy-Axis of Anisotropy), or at 45° to **x** (Hard Axis of Anisotropy), and represented on figure [5.13], and for the uniform spin-wave mode, i.e. $k_{SW} = 0\ \mu m^{-1}$. For the field along the easy axis, the SW frequency increases monotonously from a minimum value at zero-field related to the MCA term. On the other hand, for the field applied along the hard axis, a softening of the SW frequency is observed. This corresponds to the rotation of the magnetisation from the easy axis, until it aligns with the hard axis at $B_{SAT} = \frac{2K_c}{M_s}$. Then the frequency can only increase. The shaded region represents the frequency domain where surface acoustic waves can be excited in the setup presented in Chapter [4], Section [8]. The important point to note here, is that the frequency matching between the spin-wave and the SAWs is possible only by applying the field along a hard axis of anisotropy, in this geometry.

Consider $k_{SW} \neq 0\ \mu m^{-1}$, and calculate the SW dispersion relationship. This is represented on figure [5.14] for a magnetic field value of 15 mT, high enough for the sample to be fully saturated. Similarly, the field is applied along the Easy and Hard axes of magnetic anisotropy. Two magnon modes are seen. A backward-volume magneto-static surface wave (BVMSSW) for the field applied along the easy-axis (in pink), and a Damon-Eshbach (MSSW) mode[6] for the field parallel to the hard-axis (in

[6] In reality, this is not a pure Damon-Eshbach mode, since the geometry considered implies that k_{SW} and ϕ_M are not orthogonal

grey). The SAW wave-vectors present in our experiment are given in table **5.2**, and represented here by the vertical shaded region (the horizontal shaded region is the excitable SAW frequencies). Two important points to note here. First, coupling with Damon-Eshbach modes are difficult with the SAWs on this setup, and secondly, increasing f_{SAW} might enhance coupling with the MSSW mode.

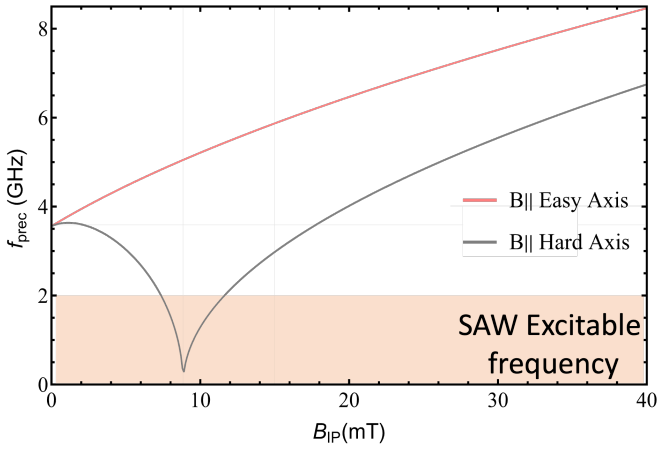

Figure 5.13: Evolution of the SW frequencies versus field applied respectively along an easy axis and a hard axis, for uniform spin-waves, $k_{\mathrm{SW}} = 0\ \mu\mathrm{m}^{-1}$. The shaded region corresponds to the frequency domain of possible SAW excitation on the Polycrystalline Sample B. Recall, in reality only discrete f_{SAW} are generated and given in table [**5.2**].

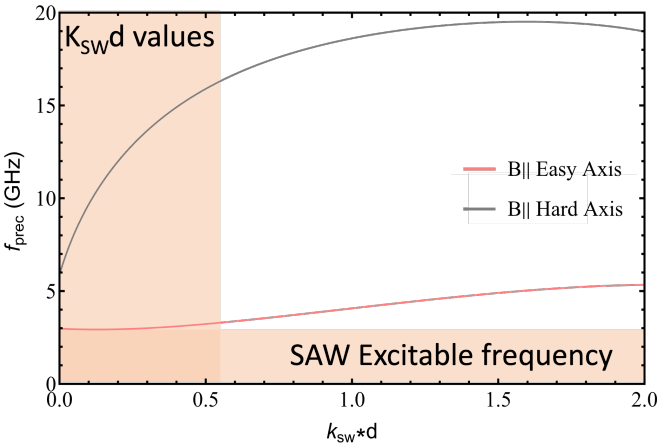

Figure 5.14: Dispersion relationship for an in-plane field of value 15 mT. At this field value, the magnetisation is saturated along the given axis, i.e. along either the easy or hard axis of anisotropy. Note the existence of a Backward Volume-MSSW mode parallel to the Easy Axis of magnetic anisotropy, and the existence of a pseudo-MSSW mode along the hard-axis.

Conclusion: To achieve resonant SAW-FMR interaction, the frequency and wave-vector of the SAW must match those of the Spin-Wave [7]. In conventional SAW-FMR experiments, the first two conditions are met by: (i) using a hard axis of magnetic anisotropy and applying an external magnetic field to soften the SW eigen-frequencies (c.f. fig. [5.13]), or (ii) generating high-frequency SAWs in magnetically isotropic samples. However, in certain scenarios such as in the absence of a magnetic hard-axis and/or lithographic limitations in achieving high SAW frequencies, these conditions cannot be fulfilled. Both of these constraints are present on the polycrystalline Sample B: FeRh/Ta/GaAs. Hence, in the next sub-section, the reader is introduced to an alternative method to soften the SW eigen-frequencies by using the magnetic coercivity.

5.2 Modelling FMR with magnetic hysteresis in the simple case- cubic anisotropy only

5.2.1 Conundrum

In the previous section, an implicit assumption has been used while calculating the eigen SW frequencies. While compiling equation [5.38] with equations [5.39], it has been considered that the two magnetic equilibrium angles $\phi_{\mathrm{M}} = \Psi$ or $\phi_{\mathrm{M}} = \Psi + \pi$, led to the same equi-energetic magnetic states leading to the same precessional frequency. However, although rarely acknowledged in SAW-FMR papers, this assumption is not true at all field values, but is valid only for high field values. The term high-field typically refers to FMR experiments with the applied magnetic field far above the coercive field values. Indeed, if hysteresis is considered, the contribution of the Zeeman energy term differs greatly for $\phi_{\mathrm{M}} = \Psi$ or $\phi_{\mathrm{M}} = \Psi + \pi$. This is demonstrated using the Smit-Beljers formula. For a given value of the applied magnetic field which is less than the coercivity of the sample, the magnetic equilibrium angle ϕ_{M}, depends on the magnetic history. Indeed, coming from positive high-field or negative high-field values lead to different magnetic equilibrium angle. Note that the macrospin model is considered here, i.e. the magnetisation switching from Ψ to $\Psi \pm \pi$ is considered coherent. For

[7] the frequency and wave-vector of the SAW must match those of the Spin-Wave, and there must be a non-zero magneto-elastic effective field acting on the magnetic moments

simplification only the cubic anisotropy is considered. The precession frequency is thus given by: (to alleviate notation $a_{\mathrm{FeRh}} \rightarrow$ a)

$$\omega = \frac{\gamma}{M_s}\sqrt{E_{\theta\theta} \times E_{\phi\phi}}$$
$$= \frac{\gamma}{M_s}\sqrt{\mu_0 H M_s \cos(\phi_H\text{-}\phi_M) + K_c\left(2\text{-}\sin^2(2\,(\phi_c\text{-}\phi_M))\right) + \mu_0 M_s H_{EX}(k_{SW}a)^2 + \mu_0 {M_s}^2\left(1\text{ - }\frac{dk_{SW}}{2} + \frac{d^2k_{SW}^2}{6}\right)}$$
$$\times\sqrt{\mu_0 H M_s \cos(\phi_H\text{-}\phi_M) + 2K_c\cos(4\,(\phi_c\text{-}\phi_M)) + \mu_0 M_s H_{EX}(k_{SW}a)^2 + \mu_0 {M_s}^2\sin^2(\phi_M)\left(\frac{dk_{SW}}{2}\text{ - }\frac{d^2k_{SW}^2}{6}\right)} \tag{5.42}$$

An analysis of this solution is necessary for three limiting cases: High-positive field ($\phi_{M_{eq}} = \phi_H = 0$ rad), High-negative field ($\phi_{M_{eq}} = \phi_H + \pi = \pi$) and at the coercivity field value ($B = \pm B_c$); c.f. figure [5.15].

f_{SAW} (MHz) →	299	398	889
λ_{SAW} (μm)	9.61	7.20	3.20
k_{SAW} (μm^{-1})	0.654	0.873	1.963
k d	0.177	0.236	0.53

Table 5.2 Parameters governing the three different SAW frequencies generated on the FeRh/Ta/GaAs sample.

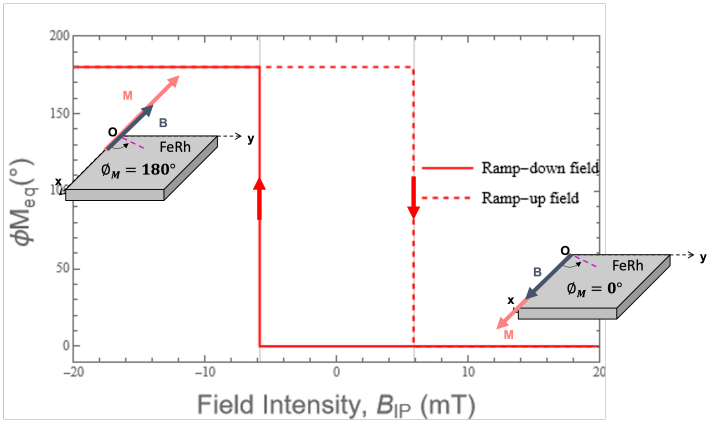

Figure 5.15: Illustration of a square hysteresis cycle for the magnetic field applied along $\phi_H = 0°$, and for a cubic magnetic anisotropy along x. If the field is applied along $\phi_H = 90°$, the equilibrium values goes from 90° to 270°.

5.2.2 Limiting Cases

i **If** $\phi_{M_{eq}} = \phi_H$

$$\omega = \frac{\gamma}{M_s}\sqrt{\mu_0 H M_s + K_c\left(2 - \sin^2(2\,(\phi_c - \phi_M))\right) + \mu_0 M_s H_{EX}(k_{SW}a)^2 + \mu_0 {M_s}^2\left(1\text{ - }\frac{dk_{SW}}{2} + \frac{d^2k_{SW}^2}{6}\right)}$$
$$\sqrt{\mu_0 H M_s + 2K_c\cos(4\,(\phi_c - \phi_M)) + \mu_0 M_s H_{EX}(k_{SW}a)^2 + \mu_0 {M_s}^2\left(\frac{dk_{SW}}{2}\text{- }\frac{d^2k_{SW}^2}{6}\right)\sin^2(\phi_H)}$$

The exchange term: $\mu_0 M_s H_{EX}(k_{SW}a)^2$ is very small and neglected. Recall, it is assumed that $\phi_c = \phi_H = 0$:

$$\omega = \frac{\gamma}{M_s}\sqrt{\left(\mu_0 H M_s + 2K_c + \mu_0 {M_s}^2\left(1\text{ - }\frac{dk_{SW}}{2} + \frac{d^2k_{SW}^2}{6}\right)\right)(\mu_0 H M_s + 2K_c)} \tag{5.43}$$

ii **If** $\phi_{M_{eq}} = \phi_H + \pi$

$$\omega = \frac{\gamma}{M_s}\sqrt{-\mu_0 H M_s + K_c\left(2 - \sin^2(2\,(\phi_c - \phi_M))\right) + \mu_0 M_s H_{EX}(k_{SW}a)^2 + \mu_0 {M_s}^2\left(1\text{ - }\frac{dk_{SW}}{2} + \frac{d^2k_{SW}^2}{6}\right)}$$
$$\sqrt{-\mu_0 H M_s + 2K_c\cos(4\,(\phi_c - \phi_M)) + \mu_0 M_s H_{EX}(k_{SW}a)^2 + \mu_0 {M_s}^2\sin^2(\phi_H)\left(\frac{dk_{SW}}{2}\text{- }\frac{d^2k_{SW}^2}{6}\right)}$$

The exchange term: $\mu_0 M_s H_{EX}(k_{SW}a)^2$ is very small and neglected. Recall, it is assumed that $\phi_c = \phi_H = 0$:

$$\omega = \frac{\gamma}{M_s}\sqrt{\left(-\mu_0 H M_s + 2K_c + \mu_0 {M_s}^2 \left(1 - \frac{dk_{SW}}{2} + \frac{d^2 k_{SW}^2}{6}\right)\right)(-\mu_0 H M_s + 2K_c)} \tag{5.44}$$

A first conclusion here, is to observe that the solutions of equations [5.43] and [5.44] indeed differ.

iii At coercivity: B = ± B_c

In a macrospin model, by definition of the coercivity, the switching field is given by: $\mu_0 H_c = B_c = \frac{2K_c}{M_s}$, equivalent to the overcoming of the effective magnetic anisotropy (here only the cubic anisotropy). Hence, the frequency at the switching field or coercivity is given as:

$$\omega(B_c) = \frac{\gamma}{M_s}\sqrt{\left(-B_c + \frac{2K_c}{M_s} + \mu_0 M_s\left(1 - \frac{dk_{SW}}{2}\right)\right)\underbrace{\left(-B_c + \frac{2K_c}{M_s}\right)}_{\to 0}} \tag{5.45}$$

Using the parameters of **Table 5.2**, the corresponding field value in order to cancel the first bracket corresponding to the second derivative $f_{\theta\theta}$ is quite huge ≈ 1.2 T to 1.7 T. This is not the case for the $f_{\phi\phi}$ term. At the coercivity, the second derivative of the total magnetic energy with respect to ϕ is zero. This implies that the eigen-SW frequency goes to zero. Hence, we can see that:

$$\omega \propto \underbrace{\sqrt{E_{\theta\theta}E_{\phi\phi}}}_{B\to\pm B_c} \to 0$$

Recap

On figure [5.16] is represented the calculated SW eigen-frequencies for two cases: (i) The case where no magnetic hysteresis is considered, in grey. As the field is applied at $\phi_B = 0°$, i.e. along the easy-axis, the SW eigen-frequency can only increase from a minimum (here the effective anisotropy at zero-field value). (ii) In the case where the magnetic hysteresis is considered, (in red), the SW eigen-frequency can go to arbitrarily low values, close to the coercivity of the sample, and zero at the coercivity (in the low k_{SW} approximation.

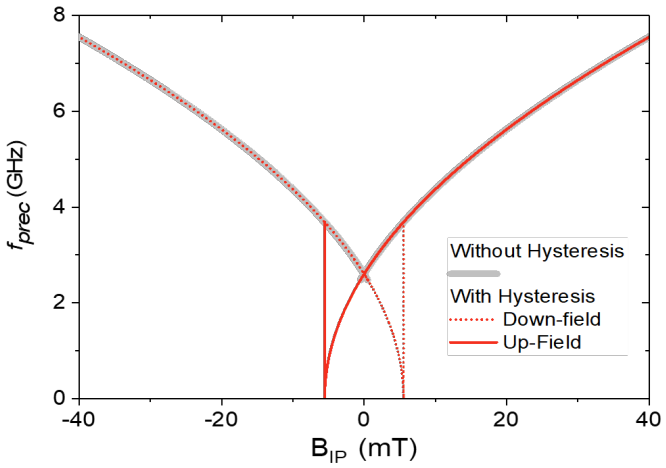

Figure 5.16: Evolution of the Spin-Wave eigen-frequencies when not considering the magnetic hysteresis (in grey), and while considering the magnetic hysteresis (in red), for a cubic anisotropy with the field applied along the easy-axis, here $\phi_B = 0°$. For no hysteresis, the minimum frequency corresponds to the effective anisotropy present in sample at zero-field value. Then this frequency can only increase monotonously with increasing field values. When the magnetic hysteresis is considered, the SW eigen-frequencies are softened close to the coercivity and are zero at the coercive fields, in the small SW approximation.

5.2.3 SW frequencies and modes

Using this hysteretic nature of the magnetic equilibrium angles, the SW eigen-frequencies are calculated for the uniform and largest SAW wave-vectors (c.f. Table **[5.2]**- $k_{SW} = 1.963\ \mu m^{-1}$.), and represented

on figure [5.17]. Here, is considered the case: $\phi_M = \phi_H = 0$. Higher SW wave-vectors imply larger exchange contribution and dipolar contributions in equation [5.42]. The exchange contribution is $\approx 10^{-5}$-10^{-4} T, and the dipolar contribution is $\approx$ 0.1-0.6 T, the major contribution to the SW frequency is due to the dipolar energy terms. Increasing the wave-vector reduces the frequency in this geometry. The shaded region represents the excitable SAW frequencies on our samples. Now the frequency matching with the SAW is possible.

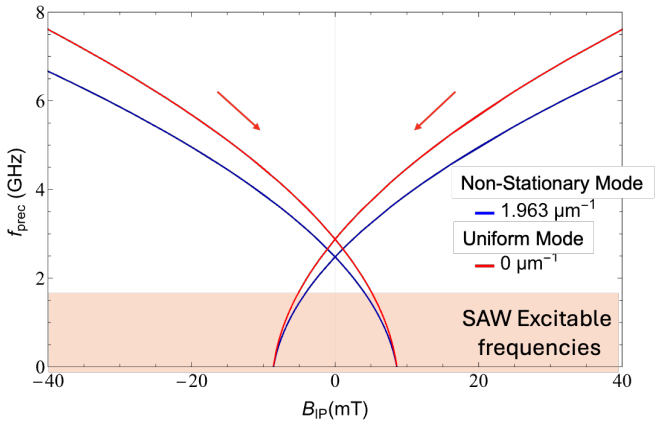

Figure 5.17: SW eigen-frequencies in the case of the magnetic field applied parallel to k_{SAW}. The uniform mode and the highest k_{SW} values are represented. Here the hysteresis on the magnetic equilibrium angle is allowed and this implies that the SW frequencies can be softened to arbitrarily low frequencies close to the coercivity. The shaded region represents the range where the three discrete SAW values can be generated. SAW and SW frequency matching is now possible.

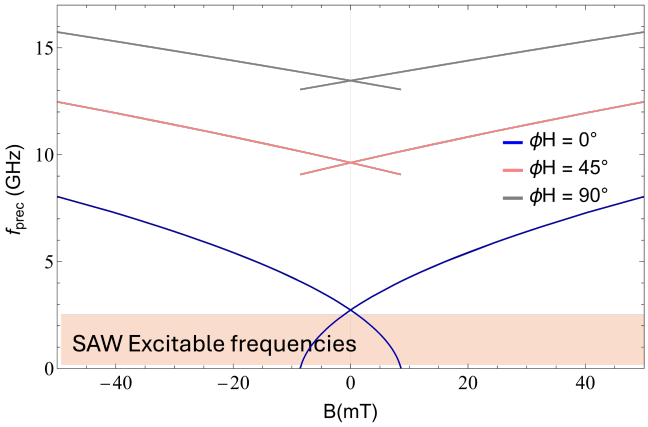

Figure 5.18: SW eigen-frequencies in the case of $k_{SAW} = k_{SW} = 0.654\ \mu m^{-1}$ for the magnetic field applied along three different angles, for a cubic magnetic anisotopy. The observation here, is that for this macrospin model, only a magnetic field applied parallel to the SAW wave-vector allows a softening for frequency matching to occur. This SW mode is the Backward Volume MSSW as described before. Note, for larger values of ϕ_H, the hysteresis jump is smaller and smaller.

Similarly, on figure [5.18] is represented the SW eigen-frequency at 0.654 μm^{-1} for the magnetic field applied parallel (blue)- Backward Volume SW mode, at 45° (red) and perpendicular 90° (grey)- Damon Eschbach mode, to k_{SAW}. For SAWs generated by our IDTs, the only achievable coupling, assuming the given form of magnetic anisotropy, is possible when the field is parallel to the SAW propagation direction. It is to be noted also, that the hysteresis in the frequency becomes less and less pronounced as the magnetisation is further away from the easy-axis, i.e. from the SAW wave-vector propagation direction.

6 Expressions of the Amplitude and Velocity variations

In this section the generalised expression of the SAW amplitude and relative velocity variations are derived from the general form of the total magnetic energy given in the previous section.

The starting point is the expression of the RF power given by equation [5.17], with the Polder susceptibility given by equation [5.20] .

$$\begin{aligned}\Delta P_{\mathrm{FMR}} &= \left[\frac{i\,\omega_{\mathrm{SAW}}\;M_{\mathrm{s}}}{2}\int_{V_0}(b_\theta,b_\phi)^*\,[\bar{\chi}]\begin{pmatrix}b_\theta\\ b_\phi\end{pmatrix}\,dV\right]\\ &= \frac{i\,\omega_{\mathrm{SAW}}\;M_{\mathrm{s}}\,V_0}{2}\left(|b_\theta|^2\chi_{11}+|b_\phi|^2\chi_{22}+\chi_{12}(b_\theta^* b_\phi - b_\phi^* b_\theta)\right)\end{aligned} \tag{5.46}$$

To simplify the notation: $f_{\mathrm{ii}}(\mathbf{k}_{\mathrm{SW}}) \rightarrow f_{\mathrm{ii}}$ and $\omega_{\mathrm{SAW}} \rightarrow \omega$

$$\begin{aligned}&\Delta P_{\mathrm{FMR}} = \frac{\omega M_{\mathrm{s}} V_0}{2(1+\alpha^2)(i\kappa\omega+\omega^2-\omega_0^2)}\times\\ &\left(|b_\theta|^2\left(\gamma\mu_0\left(\frac{E_{\phi\phi}\gamma}{M_{\mathrm{s}}}-i\alpha\omega\right)\right)+|b_\phi|^2\left(\gamma\mu_0\left(\frac{E_{\theta\theta}\gamma}{M_{\mathrm{s}}}-i\alpha\omega\right)\right)+(b_\theta^* b_\phi - b_\phi^* b_\theta)\,(i\gamma\mu_0\omega)\right)\end{aligned} \tag{5.47}$$

The complete mathematical demonstration can be found in Appendix [B].

The κ term of equation [5.21], is replaced and the FMR power is separated into its real and imaginary terms as: $\Delta P_{\mathrm{FMR}} = \Re\,\Delta P_{\mathrm{FMR}} + i\,\Im\Delta P_{\mathrm{FMR}}$

$$\Re\Delta P_{\mathrm{FMR}} = \frac{2\left[-\alpha\omega(|b_\theta|^2+|b_\phi|^2)(\alpha^2+1)(\omega^2-\omega_0^2)+\omega(b_\theta^* b_\phi - b_\phi^* b_\theta)(\alpha^2+1)(\omega^2-\omega_0^2)\right]}{4\left[\left((\alpha^2+1)(\omega^2-\omega_0^2)\right)^2+(\gamma\alpha\omega(E_{\theta\theta}+E_{\phi\phi}))^2\right]} \tag{5.48}$$

$$\Im\Delta P_{\mathrm{FMR}} = \frac{2\left[\frac{\gamma}{M_{\mathrm{s}}}(E_{\phi\phi}|b_\theta|^2+E_{\theta\theta}|b_\phi|^2)(\alpha^2+1)(\omega^2-\omega_0^2)-\gamma\alpha\omega(E_{\theta\theta}+E_{\phi\phi})(\alpha^2+1)(\omega^2-\omega_0^2)\right]}{4\left[\left((\alpha^2+1)(\omega^2-\omega_0^2)\right)^2+(\gamma\alpha\omega(E_{\theta\theta}+E_{\phi\phi}))^2\right]} \tag{5.49}$$

with the SAW amplitude attenuation $\Delta\Gamma$, and the SAW relative velocity variations $\frac{\Delta V}{V}$, defined as seen before:

$$\Delta\Gamma = 20\log e^{\left[\frac{\Re[\Delta P_{\mathrm{FMR}}(B,T)]-\Re[\Delta P_{\mathrm{FMR}}(B_0,T_0)]}{2\,P^0_{\mathrm{SAW}}}\right]} \tag{5.50}$$

$$\frac{\Delta V}{V} = -\frac{\Im[\Delta P_{\mathrm{FMR}}(B,T)]-\Im[\Delta P_{\mathrm{FMR}}(B_0,T_0)]}{2\,L\,P^0_{\mathrm{SAW}}\,k_{\mathrm{SAW}}} \tag{5.51}$$

6.1 Limiting Cases

The second derivatives are recalled here:

$$\begin{cases}E_{\theta\theta} = \mu_0 H M_{\mathrm{s}}\cos(\phi_{\mathrm{H}}\text{-}\phi_{\mathrm{M}})+K_{\mathrm{c}}\left(2-\sin^2(2\,(\phi_{\mathrm{c}}-\phi_{\mathrm{M}}))\right)+\mu_0 M_{\mathrm{s}} H_{\mathrm{EX}}(k_{\mathrm{SW}}a)^2+\mu_0 {M_{\mathrm{s}}}^2\left(1\text{ - }\frac{dk_{\mathrm{SW}}}{2}+\frac{d^2k_{\mathrm{SW}}^2}{6}\right)\\ E_{\phi\phi} = \mu_0 H M_{\mathrm{s}}\cos(\phi_{\mathrm{H}}\text{-}\phi_{\mathrm{M}})+2K_{\mathrm{c}}\cos(4\,(\phi_{\mathrm{c}}-\phi_{\mathrm{M}}))+\mu_0 M_{\mathrm{s}} H_{\mathrm{EX}}(k_{\mathrm{SW}}a)^2+\mu_0 {M_{\mathrm{s}}}^2\sin^2(\phi_{\mathrm{M}})\left(\frac{dk_{\mathrm{SW}}}{2}\text{ - }\frac{d^2k_{\mathrm{SW}}^2}{6}\right)\end{cases} \tag{5.52}$$

and the magneto-elastic tickles fields given in equations [5.13-5.14] as:

$$b_\theta = i\left(\frac{2B_2}{M_{\mathrm{s}}}\,\varepsilon_{\mathrm{xz}}+\mu_0\,M_{\mathrm{s}}\,\omega_{\mathrm{xz}}\right)\cos(\phi_{\mathrm{M}}) = iB_{\varepsilon\omega}\cos(\phi_{\mathrm{M}}) \tag{5.53}$$

$$b_\phi = \frac{2B_1}{M_{\mathrm{s}}}\,\sin(\phi_{\mathrm{M}})\cos(\phi_{\mathrm{M}})\,\varepsilon_{\mathrm{xx}} \tag{5.54}$$

6.1.1 Field parallel to SAW propagation- cubic anisotropy only

In order to simplify the calculations, only the cubic anisotropy is considered. Moreover, here: $\phi_{\mathrm{H}} = 0°$ and the cubic anisotropy is assumed to be aligned with $\mathrm{k_{SAW}}$, $\phi_{\mathrm{c}} = 0°$

i At saturation

$\phi_{\mathrm{M}} = \phi_{\mathrm{H}} = 0°$. Here: $\mu_0 H = B_{\mathrm{SAT}} > \frac{2K_{\mathrm{c}}}{M_{\mathrm{s}}}$ and $\omega_{\mathrm{SAW}} << \omega_0$, $\alpha = 0$[1]
The delay line volume is defined as: $V_{DL} = \mathrm{L\ t\ d}$, and the magnetic fraction in the system as: $\mathrm{x_{FM}} = V_0/V_{DL}$.

$$\left.\frac{\Delta V}{V}\right|_{\mathrm{B_{SAT}}} \propto \quad x_{\mathrm{FM}} \frac{M_{\mathrm{s}}}{{V_{\mathrm{SAW}}}^2 B_{\mathrm{SAT}}} \tag{5.55}$$

Note the dependence on $1/{V_{\mathrm{SAW}}}^2$ and $1/B_{\mathrm{SAT}}$.

$$\Delta\Gamma|_{\mathrm{B_{SAT}}} \propto \quad \frac{x_{\mathrm{FM}}\, \alpha\, {\omega_{\mathrm{SAW}}}^2}{{V_{\mathrm{SAW}}}^3\, {B_{\mathrm{SAT}}}^2} \tag{5.56}$$

Note the dependence of $1/{V_{\mathrm{SAW}}}^3$ and B_{SAT}. Again, higher B_{SAT}, i.e. if the field is further and further from the resonance, the SAW attenuation goes rapidly to zero, i.e. no resonance. Moreover, here $\Gamma|_{\mathrm{B_{SAT}}}$ depends on ${\omega_{\mathrm{SAW}}}^2$. Higher SAW frequency, implies a larger value of SAW amplitude attenuation.

ii At Coercivity

$\phi_{\mathrm{M}} = \phi_{\mathrm{H}} + \pi$. Here: $\mu_0 H = \frac{2K_{\mathrm{c}}}{M_{\mathrm{s}}}$ and $\alpha = 0$[1]

$$\left.\frac{\Delta V}{V}\right|_{\mathrm{B_c}} = 0 \tag{5.57}$$

and

$$\Delta\Gamma|_{\mathrm{B_c}} \quad \propto \quad \frac{\alpha\, \gamma^2\, V_0}{{V_{\mathrm{SAW}}}^3} \tag{5.58}$$

6.1.2 Final solution for field applied parallel to $\mathrm{k_{SAW}}$

Experimentally, as explained in Chapter [4], and as will be measured experimentally in the next chapter [6], the relative velocity measurement and the amplitude attenuation are both measured with respect to field. Furthermore, at the resonance, it has been defined that; the maximum variation of SAW velocity at resonance is $\Delta\Xi$, where

$$\Delta\Xi = \left.\frac{\Delta V}{V}\right|_{\mathrm{B_{SAT}}} - \left.\frac{\Delta V}{V}\right|_{\mathrm{B_c}} \tag{5.59}$$

similarly, the maximum SAW attenuation at resonance is measured as:

$$\Delta\Gamma = \Delta\Gamma|_{\mathrm{B_{SAT}}} - \Delta\Gamma|_{\mathrm{B_c}} \tag{5.60}$$

So, using the above demonstration, the mathematical expressions of $\Delta\Xi$ and $\Delta\Gamma$, at the resonance, are given as:

i Relative velocity variations

$$\Delta\Xi \quad \propto \quad x_{\mathrm{FM}} \frac{M_{\mathrm{s}}}{{V_{\mathrm{SAW}}}^2 B_{\mathrm{SAT}}} \tag{5.61}$$

ii Amplitude variations

$$\Delta\Gamma \quad \propto \quad \frac{\alpha V_0}{{V_{\mathrm{SAW}}}^3} \left(\frac{{\omega_{\mathrm{SAW}}}^2}{{B_{\mathrm{SAT}}}^2} - \gamma^2 \right) \tag{5.62}$$

The change in the relative velocity variation with respect to the SAW frequency lies in the SAW velocity V_{SAW}, i.e. the Rayleigh Velocity. This is in contrast to $\Delta\Gamma$ which varies proportionally to ${\omega_{\mathrm{SAW}}}^2$. This is in accordance to the experimental data shown in Chapter [8]. Note also, that the dispersive nature of the tri-layer systems will appear in the variation of $\mathrm{V_{SAW}}$ with frequency (in the denominator). The proportionality to α relates to the SAW attenuation.

In the next chapters, the relative SAW velocity variations and the SAW amplitude variations are measured with respect to temperature Chapter [6], with respect to magnetic field Chapter [7] and with respect to temperature coupled with magnetic field Chapter [8].

Chapter Summary

1. The chapter begins by exploring methods for controlling magnetism via magneto-elastic effects, which is the interplay between magnetic anisotropy and lattice distortions. This is the foundation for SAW-FMR interactions.

2. A state-of-the-art of SAW-FMR research including SAW-driven depinning of domain walls, current-free motion in FM wires, and spin current generation in Co/Pt layers are given. These advances showcase SAW's potential for miniaturised, energy-efficient magnetic devices.

3. The power transfer approach for mathematical modelling of the SAW-FMR, linking acoustic power loss to magnetic power absorption is presented. In this framework, the Polder susceptibility tensor and the magneto-elastic tickle fields predict the resonance conditions.

4. A mathematical explanation of SAW-FMR resonance at magnetic coercivity is given. This is the most important point of this manuscript. Here, it is shown, that the SW eigenfrequencies are softened close to the coercivity, and this allows the frequency matching with sub-GHz SAWs.

5. The chapter concludes with the calculation of the expressions for the SAW amplitude and relative velocity variations at the resonance fields.

Part III

Data Analysis SAW Transmission versus Temperature and/or Magnetic field

Chapter 6

SAW-T

Objectives

In this chapter, the interaction between Surface Acoustic Waves (SAWs) and the FeRh magnetic layer is studied by varying the temperature across the antiferromagnetic-ferromagnetic (AFM-FM) phase transition. Reflectivity measurements are employed to determine whether the dynamic strains result in a shift of the transition temperatures or an alteration of the thermal hysteresis. Subsequently, acoustic measurements are made to investigate the influence of different SAW frequencies on the velocity and amplitude measurements, examining whether signs of SAW interaction with the FeRh layer are evident across the phase transition. Through these investigations, insights into the behaviour of SAWs in relation to the FeRh magnetic layer during phase transitions are sought.

Contents

Introduction to SAW-Interaction with Temperature

Beginning with this chapter and continuing into the next two chapters, the reader is introduced to the experimental data taken on the FeRh samples. In this chapter, the focus is on the SAWs' amplitude attenuation and the SAW relative velocity variations, with respect to temperature (SAW-T). It is recalled here that FeRh exhibits a first-order phase transition going from a low-temperature AFM phase to a high-temperature FM phase. In the first section, the methodology to treat the experimental data is given. Then, SAW interaction with the FeRh layer is studied on Crystalline Sample A using reflectivity measurements, followed by a comprehensive review of probing phase transition using SAW. Following that, are introduced SAW-T measurements on the Polycrystalline Sample B, whereby the SAW velocity and SAW attenuation are measured, analysed and discussed.

1 Acquiring acoustic data

As seen in Chapter [4] section [8], the SAWs are generated by the excitation IDTs, via the piezoelectric effect, and travel across the FeRh delay lines of length L, in a time τ. Schematic representations of the two FeRh samples and their corresponding delay lines can be seen on figures [4.21] and [4.22]. Following the SAW propagation and interaction with the magnetic layer, the second IDTs (detection IDTs) pick up the incoming SAWs. If the SAWs interact with the magnetic layer in any way, a change in its amplitude and phase is expected with respect to either temperature and/or magnetic field. For the former, only a thermal hysteretic behaviour similar to the FeRh magnetic layer can hint towards SAW-FeRh interaction. In order to extract such interactions[1], the acoustic signal is fitted by a sinusoidal function:

$$A(t) = A(B,T)\cos\left[\omega t + \phi(B,T)\right]$$

with A being the SAW amplitude measured experimentally by the oscilloscope, ω the RF frequency at which the SAWs are generated and ϕ the phase at detection. These detected changes in amplitude and phase form the basis of our measurements.

The SAW amplitude attenuation is measured in decibels/cm (dB/cm) and given as:

$$\Delta\Gamma = \frac{20}{L}\log\left(\frac{A}{A_0}\right) \tag{6.1}$$

with A_0, the amplitude at reference (typically the starting temperature/field value).

As the phase variation, as it varies over more than 2π over a complete field and/or temperature scan, a phase unwrapping is performed to avoid 2π jumps in the recorded data. Figure [6.1] gives a step-by-step explanation of how to recover the velocity variation from the collected raw phase variation data. As seen, for a complete ramp, here shown with respect to temperature from T = 130°C to - 20°C and back to the initial temperature. phase jumps are recorded. As the phase difference is measured [mod]2π, a small code is used to unwrap the phase difference, and to obtain a linear variation as represented on fig. **(b)**. This phase variation unwrapped corresponds to the change in the SAW wave-vector as it propagates and interacts with the magnetic FeRh layer. This can be written as:

$$\Delta\phi = -\Re\left(\Delta k_{\mathrm{SAW}}\right) L = \frac{\omega_{\mathrm{SAW}}\,\Delta V_{\mathrm{R}}}{{V_{\mathrm{R}}}^2} L \tag{6.2}$$

$$\frac{\Delta\phi}{\omega_{\mathrm{SAW}}\,\tau} = \frac{\Delta V_{\mathrm{R}}}{V_{\mathrm{R}}} = \frac{V_{\mathrm{R}} - V_{\mathrm{R,REF}}}{V_{\mathrm{R,REF}}} \tag{6.3}$$

[1] The signal is processed using LabView and Origin.

A relative phase variation is thus equal to a relative velocity variation $\frac{\Delta V}{V}$:

$$\frac{\Delta\phi}{\phi} = \frac{\phi - \phi_{\mathrm{REF}}}{\phi_{\mathrm{REF}}} = \frac{V_{\mathrm{R}} - V_{\mathrm{R,REF}}}{V_{\mathrm{R}}} = \frac{\Delta V}{V} \tag{6.4}$$

This is illustrated by Fig. **(c)**. Now, this relative velocity variation corresponds to the full stack, i.e. all the layers encountered by the propagating SAWs. In order to isolate the FeRh layer contribution, a slope corresponding to the velocity variation due to the change of the elastic coefficients of the substrate (C_{ij}) with temperature is removed. This is allowed because the layer is quite thin. The final relative velocity variation with respect to temperature is given in fig. **(d)**. Hence a thermal hysteresis is observed, and will be studied in more details in this chapter. Note, if ever, after removing the temperature-dependent slope, there is still a presence of a drift (be it electronic or of other origin), the cycle is corrected such that the beginning and the end overlap each other, and the hysteresis is closed.

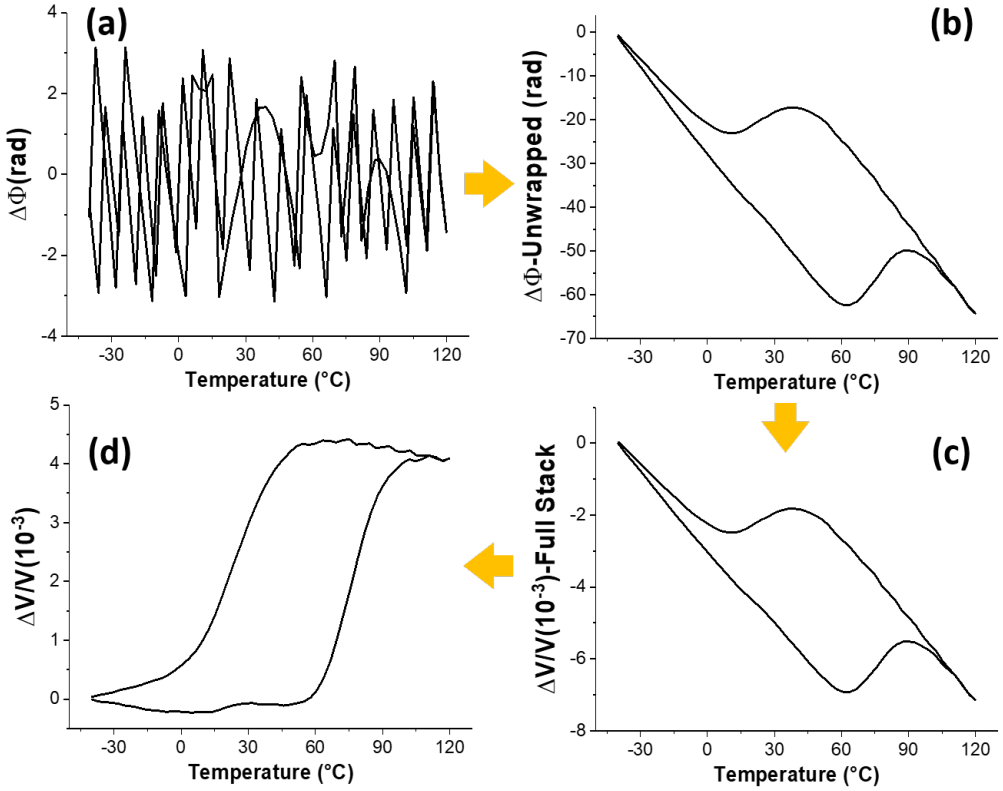

Figure 6.1: Step-by-step explanation of the retrieval of the relative velocity variation from the SAW phase variation data. This is taken on the delay line 2 of Sample B at 398 MHz. **(a)** represents the raw phase variation data with respect to temperature. As the phase is measured for $\in$ [- π,π], the data need to be unwrapped with respect to temperature as exemplified by **(b)**. Now only two phase jumps are observed close to the phase transition. However, there is still a need to remove the temperature dependence of the substrate layer so as to keep only the FeRh contribution across its magnetic phase transition. Hence, a slope of $\approx$ - 60 rad/°C needs to be removed. More details on this in appendix [C]. **(d)**: is a typical illustration of the SAW relative velocity variation with respect to temperature on Polycrystalline Sample B.

The final relative velocity variation is thus given as:

$$\frac{\Delta V}{V}_{|\mathrm{FeRh}} \sim \frac{\Delta V}{V}_{|\mathrm{Stack}} - \frac{\Delta V}{V}_{|\mathrm{Ta/GaAs}} \tag{6.5}$$

From fig. **(c)**, the slope removed is $\approx$ - 60 rad/°C, which corresponds to the $\approx$ - 0.2 $\mathrm{ms^{-1}K^{-1}}$ temperature variation of the Rayleigh velocity on GaAs. (c.f. Appendix [C])[2]. The typical precision

[2]Note that here i have considered only the temperature dependence of GaAs. This was done as my Mathematica

of our amplitude variation is ≈ 100 μV, measured on the oscilloscope. For the $\Delta V/V$, this can go down to 1×10^{-5} (generally at low frequency, which imply less noise). It is to be noted here that other groups typically measure SAW-FMR interactions using a Vector Network Analyser (VNA) (c.f. fig. [5.6]). In this manuscript, by measuring the SAW interaction using the oscilloscope, a real time and visual analysis of the SAW is possible. Moreover, the RF signal directed towards the exciting IDTs, from the signal generator (c.f. figure [4.23]) can be amplified externally. It is less common to place an amplifier in parallel to a VNA, due to isolation and linearity factors. In addition, as the interaction can be observed on the oscilloscope, it is much more straightforward to differentiate between different acoustic modes and velocities (c.f. the inset of figure [4.23]). Finally, on a VNA it is difficult to measure the response at other frequencies. Moreover, in our setup, by coupling the electrical SAW generation with an optical SAW detection, as will be discussed in Chapter [9], local SAW interaction can be investigated, using photo-elastic effect for example.

2 Searching for SAW-assisted magnetic phase transition

Sample A-Crystalline FeRh/MgO

In this section, the non-resonant coupling effect of SAW with the magnetic FeRh layer is investigated. The magnetic phase of a material is related to the electronic configuration. For this reason, magnetic phase transitions which strongly modify the electronic band structure as in the case of FeRh, can be monitored through reflectivity measurements. Moreover, as developed in chapter [1], FeRh has a magneto-structural phase transition going from the AFM-to-FM phase, with a 1% increase in the unit cell volume. In chapter [5], it was shown that static and dynamic strains also influence the magnetic free energies. Hence, the aim here, is to investigate the potential of SAWs to induce a modification of the AFM-FM transition temperatures. The experimental methodology used in this section, consists in varying the temperature from the fully AFM phase, to the fully FM phase and back to the original temperature, while concomitantly performing reflectivity measurements to monitor the phase transition (c.f. chapter [2]). Two sets of reflectivity measurements are taken on the same area: with and without SAWs being generated on the FeRh layer. By analysing a difference in the transition temperatures between the two curves, any influence of the dynamical strains on the phase transition is revealed and can be quantitatively assessed. The experiments are performed in zero-magnetic field and for 6 different SAW frequencies up to 958 MHz.

Figure [6.2] is an image of part of the delay line obtained by reflectivity measurement on Crystalline Sample A. The full stacked can be found in figure. [2.9] and the layering on figure [4.21]. Here, the excitation IDT can be observed (on the right), with part of the FeRh delay line. The yellow-boxed area is the region taken as reference to calculate the mean reflectivity with respect to temperature, with and without SAW, and for different SAW frequencies. Please refer to figure [4.21]. Note the region where there is the SiO_2 layer only. This SiO_2 is present over the FeRh delay line as well. Hence, the choice of visualising not only the FeRh delay line but a region where the SiO_2 only is present. By removing this weighted contribution in the reflectivity ramp, only the FeRh contribution is obtained. The correction of the reflectivity intensity I, is given as:

$$I_{\mathrm{FeRh}}[i] = I_{\mathrm{FeRh/Si0_2}}[i] - I_{\mathrm{Si0_2}}[i] \times \frac{I_{\mathrm{FeRh/Si0_2}}[1]}{I_{\mathrm{Si0_2}}[1]} \tag{6.6}$$

where i denotes the data points index taken over the course of the whole temperature ramp. Figure [6.3] is a typical RAW reflectivity measurement (i.e. without correction from SiO_2 layer) obtained from averaging over the whole yellow area with respect to temperature. This temperature ramp here, is performed without SAW propagation and over the FeRh magnetic phase transition. As seen in chapter [2], there is a reduction of ≈ 9.3%, higher than what is measured by Saidl *et al.* at 633 nm, which is ≈

code was not working properly, and i did not have enough time to implement the temperature dependence of Tantalum. Hence, I was not able to have the velocity variation of the Ta/GaAs bi-layer. Nevertheless, the removal of the temperature dependence due to the GaAs layer is enough.

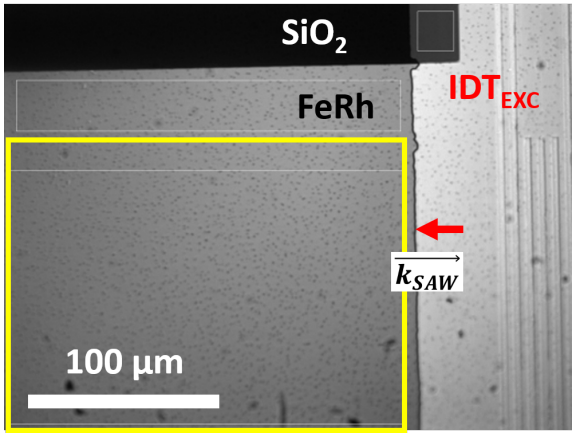

Figure 6.2: Image of the top surface of Sample A-crystalline obtained by reflectivity measurement. Note the FeRh layer (dark grey), the region with the IDT (vertical line bars) and the SAW wave-vector (the SAW propagates from right-to-left here). The yellow box represents part of the delay line onto which the SAWs propagate and interact with the magnetic FeRh layer, whenever the IDT is being used.

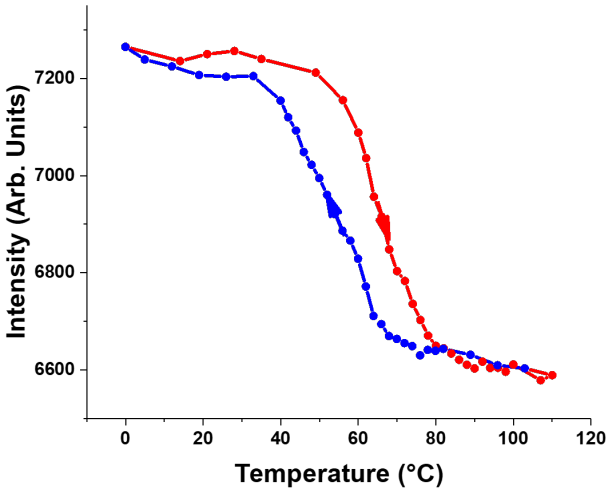

Figure 6.3: Raw intensity measurement data with respect to temperature obtained by reflectivity measurement on the FeRh delay line, for Sample A-Crystalline FeRh/MgO. The heating (red) and cooling (blue) branches are separated to aid visualisation. Note the reduction of reflectivity when going from the AFM-to-FM phase and the presence of the thermal hysteresis.

2.5% [100]. This might thus be due to the SiO_2 coating. Note also the presence of a hysteresis, similar to what is observed on the VSM measurements.

As the SAW propagates, it creates dynamical strain fields. These strains can alter the local magnetic anisotropy [231], modify the energetic landscape and reduce the local coercivity [27] (c.f. State of the art in Chapter [5]). In so doing, the SAW can potentially shift the temperatures at which the magnetic phase transition occurs. Likewise, under certain conditions, the strain fields can stabilise or destabilise a specific magnetic phase, AFM or FM (similar to the discussion on substrate/layer lattice matching c.f. Chapter [1]), leading to earlier or delayed magnetic phase transitions. It is believed here, that the SAW interaction with the FeRh can reduce the AFM-to-FM transition temperature[3] and reduce the domain of the thermal hysteresis [232], [233]. This will be discuss at the end of this section.

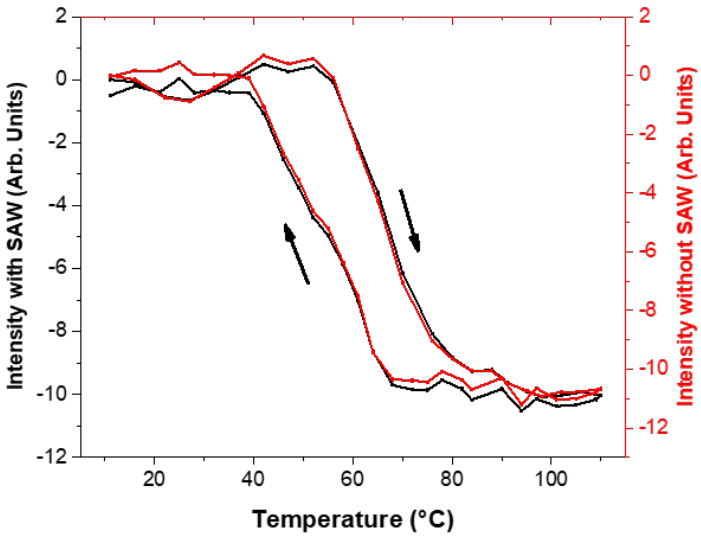

Figure 6.4: Left Axis- Black: Evolution of the reflectivity across the phase transition performed on the yellow boxed area of the delay line. All the reflectivity data have been corrected to remove the temperature influence of SiO_2 layer, i.e. only the reflectivity of the FeRh layer with respect to temperature is being probed here. Here SAW pulse trains of width 200 ns and period 10 μs, at a frequency of 150 MHz are generated. **Right axis- Red:** Reflectivity measurement performed on the same area, and without a SAW. Visually, no noticeable difference is observed on the reflectivity data in the presence/absence of a propagating SAW.

Figure [6.4] is an illustration of the reflectivity measurements with respect to temperature, in the yellow-boxed area, with (in black) and without a propagating SAW (red). Here the SAW is excited at

[3] Wu *et al.* actually showed that this depends on the SAW pulse width and RF power [232].

a frequency of 150 MHz and a RF power of 20 dBm, which corresponds to ≈ 100 mW[4]. Note also that the generator has been characterised with a power loss of - 0.28 dBm/GHz. Feeding 20 dBm to the IDT to generate SAWs at 150 or 958 MHz, correspond to different real electrical power (in this case only 48 mW at 958 MHz). However, at the time of the experiment (Beginning of the PhD, a constant 20 dBm was applied for all the 6 SAW frequencies), since i was not familiar yet with the concept of dBm/Impedance. No further measurements were possible afterwards as the electrical contacts feeding the IDTs were damaged, and no further SAW signal was measured. Coming back to the 150 MHz data, the reflectivity curves were corrected so as to remove the reflectivity temperature-dependence of the underlying SiO_2 layer (c.f. equation [6.6]. No noticeable differences in the reflectivity curves are observed visually here, either for the heating or cooling ramps.

f_{SAW} (MHz) →	152.5	297	437	575	767	833	958
λ_{SAW} (μm)	35.6	17.8	11.9	8.9	7.1	5.9	5.1

Table 6.1: SAW frequencies, wave-length and penetration depth ($\delta = \lambda_{SAW}$) for the split 5:2 IDT of the Crystalline Sample A: FeRh/MgO

The experiment is repeated for all the possible harmonics generated by the IDT, i.e. for f_{SAW} going from 150 to 958 MHz. As the effective thickness or penetration depth[5] of a SAW is inversely proportional to its wave vector magnitude, higher frequency SAWs penetrate less deeply into the material and are more confined to the surface layer. A 152.5 MHz SAW has a penetration depth of $\delta = 35.6$ μm, while a 958 MHz SAW penetrates over $\delta = 5.1$ μm. The FeRh layer is 50 nm-thick here. Although it would be expected that a higher SAW frequency would interact more with the FeRh layer, this was not observed in the experiments, as shown in Figure [6.5]. In order to have a more precise recording of the transition temperatures, the heating and cooling ramps were separated, and the transition temperatures determined by taking the derivative of either branch. For the heating ramp (red zone), experiments with SAW ON and SAW OFF (absence of SAW) have transition temperatures similar to each other. Likewise, for the cooling branch, although there seems to be a slight difference between SAW ON and SAW OFF data, it is within the margin of error to be able to conclude on the SAW influencing the transition.

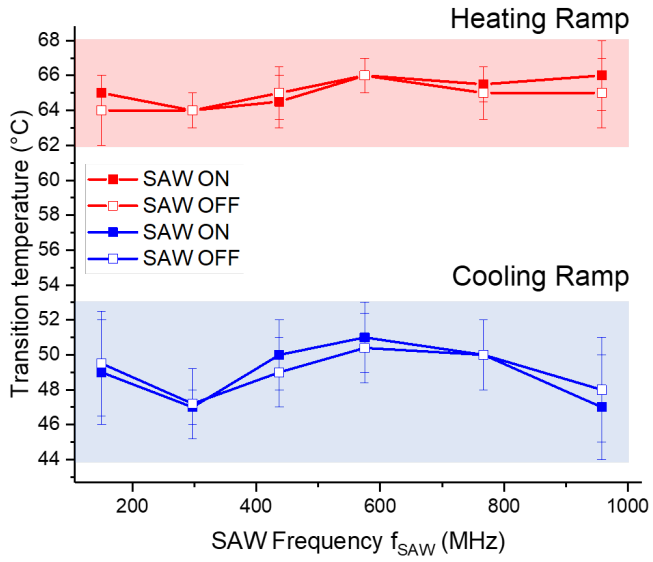

Figure 6.5: Evolution of the transition temperatures for the heating and cooling ramps, obtained by derivating the reflectivity curves, for the 6 excitable SAW frequencies. In red is represented the heating ramp and in blue the cooling ramp. No change is seen in the transition temperatures for the former. In the case of the cooling ramp, although there seems to be a slight difference in the transition temperature (≈ 2°C), the lack of complementary data does not allow to have a definite picture on the influence of the SAW.

One possible explanation for the lack of influence of the SAW on the transition temperatures, is the FeRh fraction seen by the SAW is small. Indeed, for the 6^{th} harmonics, the SAW wavelength is ≈ 5.9 μm. As the film thickness is only 50 nm-thick, it is still only 0.9% of the total penetration depth of the SAW. Three possible ways to establish the influence of SAW propagation on FeRh, in the future,

[4]To convert dBm to mW: P (mW) = $10^{\frac{P(dBm)}{10}}$
[5]Effective penetration depth, $\delta = \lambda_{SAW}$

is to consider either:

-(i) a thicker crystalline FeRh layer, in this way the SAWs interact with a larger fraction of FeRh.
-(ii) using the same 50 nm-thick FeRh layer and applying an external magnetic field (since it is known that an external magnetic field influences the transition temperatures). Unfortunately, these experiments were not possible since the electrical contacts to the IDTs were damaged and no subsequent SAW excitation were possible on the sample (c.f. fig. [4.21]).
-(ii) using the 270 nm-thick Sample B and measure reflectivity measurements. This was actually performed for the three different frequencies. Unfortunately, the reflectivity was either dominated by ice crystals/organic matter (c.f. discussion in chapter [2]), or too noisy to measure any SAW effect on the phase transition.
-(iv) devising an improvement of the experiment setup such that the generation of the SAW is modulated and the reflectivity measurement are phased synchronised and the reflectivity detection is performed using a lock-in detection method, at the SAW modulation frequency, (similar to the improvement in the SAW generation and detection implemented in Chapter [9]).

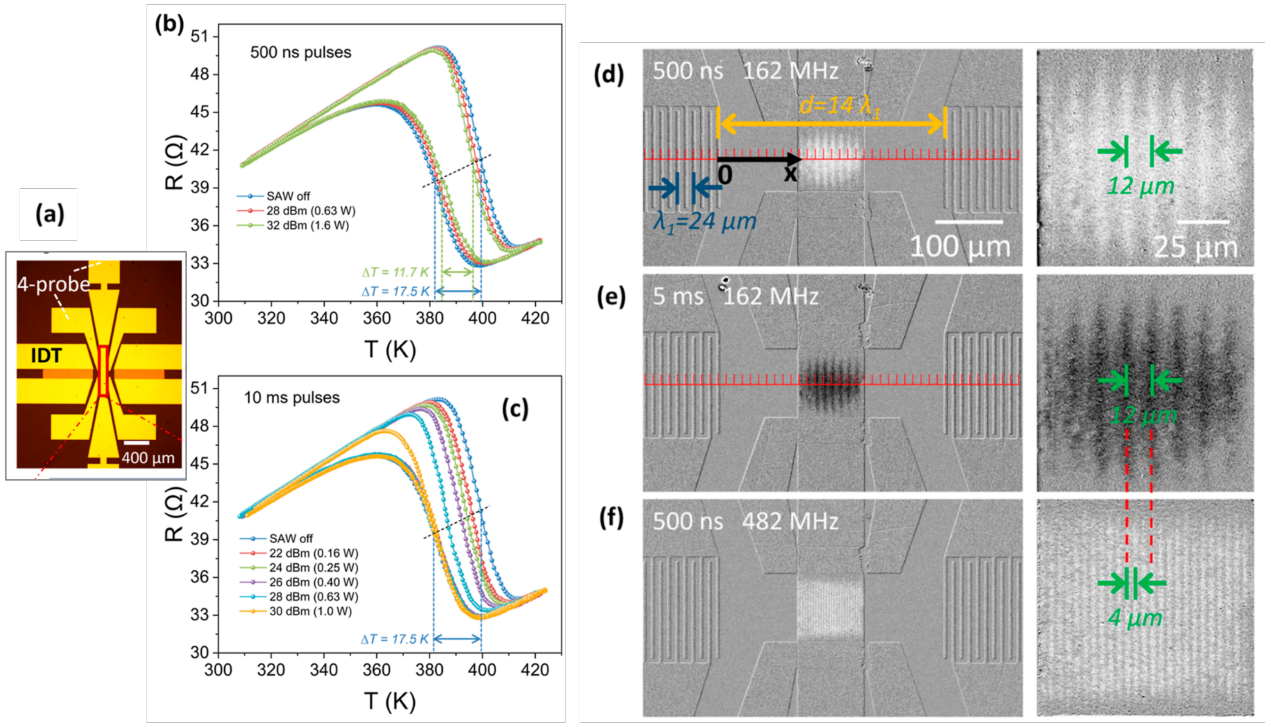

Figure 6.6: **(a)**:Photo-micrograph of the SAW device with the horizontal IDTs. Note the red rectangle in the centre is the region of interest here. **(b)-(c)**: Resistivity versus temperature for SAW on or SAW off. For **(b)**, for a SAW pulse of 500 ns, it can be seen that the thermal hysteresis is reduced, as the transition temperature of the heating branch is reduced while the transition temperature of the cooling branch is increased. For 10 ms pulses as illustrated in **(c)**, the heating and cooling branches have different behaviour. Here, only the transition temperature of the heating branch is affected. This is due to the dynamic strain field modulating the energy differently depending on whether the SAW pulse is short or long. **(d)-(f):** Reflectivity measurements showing the modification of magnetic domains with a stationary SAW in between the IDTs at 162 MHz.**(d):** The system is prepared in the mixed phase and a stationary 500 ns SAW is generated. The magnetic domains have comb-like stripes structures, with separation length corresponding to the SAW wave-length. The white regions represent the AFM domains. If a long pulse is applied, 5 ms, the domains are reversed as seen in **(e)**. Now the dark stripes correspond to FM domains. This magnetic domain writing technique is possible at hihgher harmonics. In fig. **(f)** is represented a 500 ns pulse at 482 MHz. Note the separation length of the comb-like stripes structures has been reduced to match the SAW wave-length. Adapted from [232].

Although we were able to act neither on the magnetic phase transition nor on the transition temperatures, another team published recently (April 2024), very interesting and conclusive results for polycrystalline FeRh grown on LNO using SAWs [232]. Using a 50 nm-thick FeRh layer, they were able to modulate the magnetic phase transition and to study the effect of SAW pulses on the magnetic thermal hysteresis, and on the magnetic domain structures. These results are represented on figure

[6.6]. **(a)** Shows a Photo-micrograph image of the IDTs, which generate SAWs horizontal onto the red rectangular region made up of FeRh. Two different measurements are taken: 4-points resistivity versus temperature as represented on figures **(b)-(c)**; and reflectivity measurements as given on figures **(d)-(f)**. On the resistivity measurements, it was shown that the application of SAW pulses with varying pulse widths and powers significantly impacted the FeRh phase transition. SAW pulses with a pulse width of 500 ns were found to reduce the thermal hysteresis as seen on fig. **(b)**. This affect both the heating and cooling branches, with the former shifting to lower temperatures while the latter shifting to higher temperatures. On the other hand, longer SAW pulses (10 ms) had different effects, as given on **(c)**. Here, only the heating branch shifted to lower temperatures while the cooling branch remained unaffected. The mechanisms underlying the SAW-induced magnetic phase transition modulation were then explored using a COMSOL simulation based on a Preisach model. This model provides a theoretical framework for understanding the energy modulation induced by SAWs, and it was proved that SAWs can dynamically modulate the transition temperatures. The short SAW pulses were responsible for inducing iso-thermal magnetic phase transition, by assisting both the AFM and FM energy barrier cross-over, and promoting both the AFM-to-FM and FM-to-AFM phase transitions. On the other hand, it was suggested that acousto-thermal effects governed the long SAW pulse interaction. In other words, a conversion of strain to heat, only affect the heating branch. For the reflectivity measurements, Wu *et al.* demonstrated the ability of standing SAWs to create comb-like phase domains within the FeRh strip, with domain separation length corresponding to half the SAW wave-lengths. As these domains were observed only in regions where the SAWs are transmitted, they suggested a strong correlation between the SAW strain field and domain formation. A full cycle of SAW-induced writing and erasing of the comb-like patterns was achieved, showing their precise control FeRh magnetic domains by SAWs.

In the rest of this chapter, instead of using the SAWs as means to assist or influence the phase transition, the SAWs serve as probing tool. Indeed, using acoustic waves to study phase transition is a well known technique, and has been used since the early 1950s.

3 Probing phase transition with acoustic waves

During a phase transition, a continuum medium undergoes significant changes in its lattice, magnetic, or electronic structures at specific transition temperatures. In chapter [1], it has been demonstrated that for an equi-atomic FeRh, these changes are concomitant, occurring simultaneously at the antiferromagnetic-to-ferromagnetic phase transition. This type of magneto-structural change impacts several key properties, including the elasticity tensor, density, electron-pairing dynamics, and magnetic order among others. As sound waves propagate through a medium by inducing vibrations in the medium atomic lattice, these altered properties at the transition significantly influence sound propagation. Specifically, acoustic velocities depend on the stiffness and density of the material, while acoustic attenuation is affected by non-resonant scattering and resonant absorption processes, which are in turn, influenced by defects and magnetic fluctuations near phase transition points. In this way, these effects have laid the groundwork for probing phase transition with acoustic waves.

3.1 State of the art: Probing Phase transition using acoustic waves

Through the validation of superconductivity theory via the propagation of shear waves in bulk Indium [234] and the investigation of first-order temperature-induced semiconductor-to-metal transitions using surface acoustic waves (SAWs) [235], acoustic investigation of phase transition has significantly advanced our understanding of phase dynamics in condensed matter physics. In the early 1970s, Rehwald *et al.* developed a theoretical framework based on the Landau theory of phase transition, emphasising the crucial role of coupling mechanisms between strain and order parameter [236]. Their observations indicated that the measured elastic constants varied precisely in accordance with the order parameter. The authors further underscored how measurements of sound velocity and attenuation can effectively identify both continuous (second-order) and discontinuous (first-order) phase transitions, providing a versatile tool for studying various materials and phase transitions, including magnetic

[237], structural [238] and ionic [236] transitions.

Using these properties, Worgull *et al.* investigated the temperature dependence of the relative change and attenuation of ultrasonic (5 and 10 MHz) longitudinal and transverse waves across the martensitic first-order phase transition of Ni_2MnGa, revealing anomalies in the elastic modulus correlated with the martensitic transformation at the phase transition [239]. These anomalies were attributed to the coupling between the acoustic waves and the structural order parameter. Similarly, M. Rosen reported analogous couplings during the antiferromagnetic-to-ferromagnetic (AFM-to-FM) transition in Terbium [240], aligning with the framework established by Rehwald *et al.* earlier. He stated that since the elastic constants are second derivatives of the thermodynamic potential with respect to strain, a magnetic contribution to the velocity variations should be expected in the vicinity of any magnetic ordering transition. K. Fossheim explored the behaviour of this phase transition on Perovskites using an acoustic reflector [238]. On figure [6.7] is represented the velocity and attenuation with respect to temperature of a Bulk longitudinal acoustic wave on $KMnF_3$. $KMnF_3$ has a crystallographic tetragonal to monoclinic phase transition around 91.5 K and a cubic to tetragonal phase transition around 187.5 K. As these phase transitions occur, the acoustic wave interacts with a fluctuation of the order-parameter, which in this case is the change in elastic constants. The dip observed in the velocity measurements and an increased attenuation at the transitions are indicative of the dip in the elastic constants near the structural phase transitions, and by domain attenuation as mentioned by the author. Similarly, R. Hemphill studied how a thin film of vanadium dioxide (VO_2) influences the propagation of surface acoustic waves (SAWs)[235]. VO_2 exhibits a sharp change in electrical conductivity near 68°C, transitioning from an insulator to a metal. Figure [6.8] shows the SAW attenuation measurement at a frequency of 40 MHz across varying temperatures. There is a rapid increase in attenuation starting below 60°C, reaching a maximum ($\approx$ 55 dB/cm) at around 40°C. This sharp rise corresponds to the phase transition of VO_2 from its insulating to metallic state. Likewise, the hysteresis of VO_2, typical of first-order phase transition, was detected by the SAW.

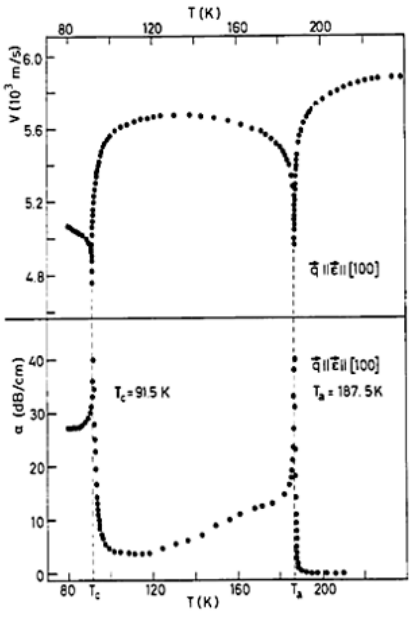

Figure 6.7: Bulk longitudinal velocity and attenuation measurements on $KMnF_3$ Perovskites. Two structural phase transitions are observed and detected on both the velocity **(top)** and the attenuation **(bottom)**, in the form of dips or peak of absorption. This represents the critical behaviour of the $KMnF_3$, confirming theoretical predictions about how elastic constants should behave near phase transitions. Adapted from [238].

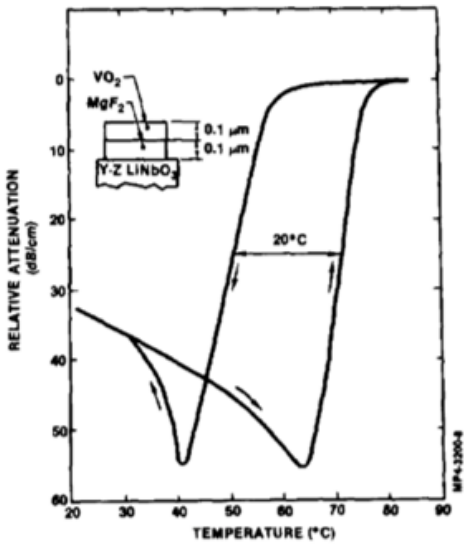

Figure 6.8: SAW attenuation with respect to temperature on Vanadium Oxide. Below 60°C, SAW attenuation increased sharply, peaking at 55 dB/cm around 40°C for the cooling ramp and peaks around 65°C for the heating ramp. This corresponds to the hysteretic insulator-to-metal phase transition critical temperatures. Adapted from [235].

To sum up, the pertinent points of the extensive literature on acoustic probing of phase transitions, relevant to this manuscript study can be summarised as follows. In a first-order phase transition, the sound velocity exhibits a finite discontinuity [241]. This discontinuity is generally independent or less dependent on the frequency of the acoustic wave and originates from the static variations in the elastic constants [238], referring to the real part of these constants. In contrast, acoustic attenuation typically involves relaxation processes and depends on changes in the imaginary part of the elastic constants, which exhibit a higher-order frequency dependency. Luthi *et al.* predicted that sound wave attenuation possesses a quadratic frequency dependence [237].

Using this, we now look at the interaction of the SAWs across the AFM-FM magnetic phase transition of FeRh.

4 SAW relative velocity variations vs Temperature

4.1 Introduction

Starting from this section, the majority of the data presented involves the Polycrystalline Sample B: FeRh/GaAs (c.f. fig. [2.9]). Here, the reader is introduced to SAW velocity or amplitude attenuation measurements, as described in Chapter [2]. A typical SAW interaction with FeRh measurement consists in exciting a SAW at a frequency f_{SAW}, and to vary either the temperature, magnetic field or both and to look for any interaction, be it resonant or non-resonant. By collecting simultaneously the amplitude or velocity variations, the SAW interaction with the FeRh magnetic layer can be analysed. The former is related to the change in SAW amplitude, while the latter is related to a change in its phase, i.e. a temporal delay. In this section, the focus is aimed towards the relative SAW velocity variation, denoted as $\frac{\Delta V}{V}$. Then SAW attenuation measurements are studied in the following section. Note that all the data presented here are measured in zero magnetic field.

4.2 Relative velocity variations at 398 MHz

On Figure [6.9] is represented a standard relative velocity measurement data, following the data acquisition, and conversion from SAW phase variation to relative velocity variation and the removal of the elastic contribution of the substrate layer to the measurements (c.f. section [1]) . Starting from, either a pure FM phase at high temperature ($\approx$ 130°C), or the AFM phase at low temperature ($\approx$ - 40°C), a heating or cooling ramp is performed and back to the starting temperature. In the example here, the reference is at - 40°C, and all subsequent measurements are taken from this reference temperature. The heating ramp- represented in red is considered first. No variation in velocity is observed until $\approx$ 50°C, which actually corresponds to the temperature whereby the phase transition going from AFM-to-FM phase begins. A rapid increase in the $\Delta V/V$ value is then observed, and a cap is reached when reaching the fully FM phase, $\approx$ 102°C, denoted as FM-phase. When the sample is cooled- represented in blue, the relative velocity variation is seen to be hysteretic and the decrease in value starts around ($\approx$ 52°C). The hysteresis closes at the starting temperature. The opening at the transition, or simply between the FM-phase and AFM-phase temperatures, is denoted as $\Delta\Xi$. In the rest of the manuscript, $\Delta\Xi$ is studied with respect to frequency, temperature and/or magnetic field. At 398 MHz, $\Delta\Xi = 3.52 \times 10^{-3}$. This opening at the transition is significant.

Figure [6.10] shows the superposition of the relative velocity variation at 398 MHz, and the magnetometry measurement- in grey, with respect to temperature. Both curves shows similar temperature dependencies, with transition temperatures and hysteresis occurring around the same temperature range. This means that a measurement of the SAW phase variation is sensitive to the entire FeRh layer, and across the phase transition. Recall, for a SAW with frequency 398 MHz, the corresponding wavelength and SAW effective penetration depth is 7.2 μm. As the FeRh layer is only 270 nm thick, this corresponds to the FeRh layer being $\approx$ 3.8% of the total medium seen by the SAW. The SAW velocity measurement is thus very sensitive to probe the thin film, and a good evaluation of the FeRh magnetic phase transition. This percentage goes further down for the 299 MHz frequency, where it is

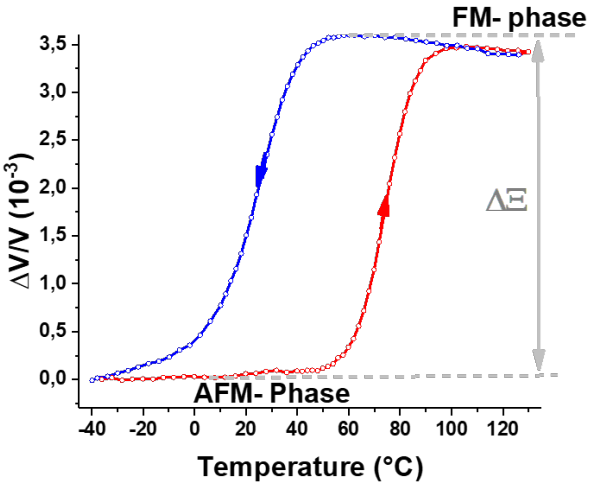

Figure 6.9: Typical relative velocity variation measurement with respect to temperature. Here f_{SAW} = 398 MHz. The measurement is usually taken by ramping across the transition and back to the starting temperature. In this case, the starting temperature is -40°C, and the cycle is divided into two ramps: the heating ramp- red coloured, and the cooling ramp- blue coloured. An opening is measured across the phase transition and denoted as $\Delta\Xi = 3.52\times 10^{-3}$.

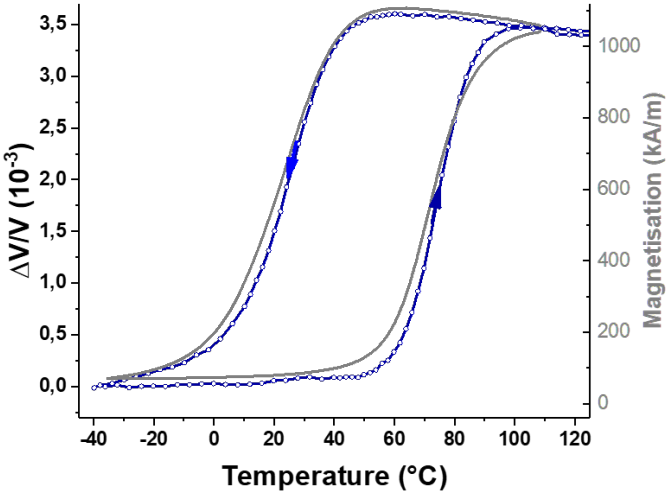

Figure 6.10: Superposition of the ΔV/V measurement for 398 MHz, and the magnetometry measurement represented in black. The phase variation shows similar temperature dependency to the magnetometry measurement. This confirms that a measurement of the SAW relative velocity variation is sensitive to the FeRh, and probes the entire magnetic layer, contrary to the reflectivity measurements.

correlated to only 2.8%. This percentage of FeRh seen by the SAW stands for the Filling ratio, η, seen in the FMR model of Chapter [5]. In order to understand this point, a slight digression is made, and the only usable SAW-T measurement on Crystalline Sample A is given on figure [6.11]. This is for a 437 MHz SAW travelling on the SiO_2/FeRh/MgO (c.f. figure [2.9]). Although the signal is noisy, the relative velocity variation is an order less, and the opening at the transition taken as denoted from the graph, $\Delta\Xi = 2.1 \times 10^{-4}$. Here, the FeRh is only 47-nm thick and the effective SAW penetration depth around 11.9 μm, which makes the FeRh only 0.4% of the total depth seen by the SAW. This might explain the order of magnitude less in the recorded signal.

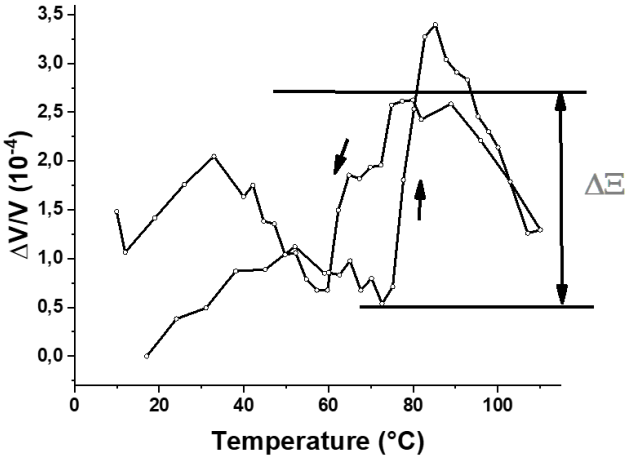

Figure 6.11: Relative velocity variation for the Crystalline Sample A: FeRh/MgO performed at 437 MHz. Compared to Sample B, the measured signal is an order of magnitude less, and noisy. If we try to close the signal in the AFM phase, no opening is recorded. The opening recorded is $\Delta\Xi = 2.1 \times 10^{-4}$.

4.3 Relative velocity variations for all SAW frequencies

The discussion is continued on the Polycrystalline Sample B, and the relative velocity variation is now represented for the three generated SAW frequencies on figure [6.12]. All three curves are measured by heating the sample from - 40°C (fully AFM), and across the transition up to 120°C (fully FM phase) and back to the initial temperature. The shapes are generally the same for the three frequencies, with two distinct levels corresponding to the AFM and FM phases and an increase in the relative velocity

variation, $\Delta\Xi$, accompanied by the thermal hysteresis. By following the heating branch, it is seen that the increase in the variation occurs around ($\approx$ 50°C) for all three frequencies. Likewise, for the cooling branch, the decrease starts around ($\approx$ 52°C). These correspond to the transition temperatures observed on the VSM data. Hence, these show that any SAW phase variation measurement is not only sensitive to the FeRh layer, but to its magneto-structural phase transition. Indeed, as discussed in the state of the art, the SAW velocity can be affected by a change in magnetic states or a change in structure, or more particularly a change in elastic constants.

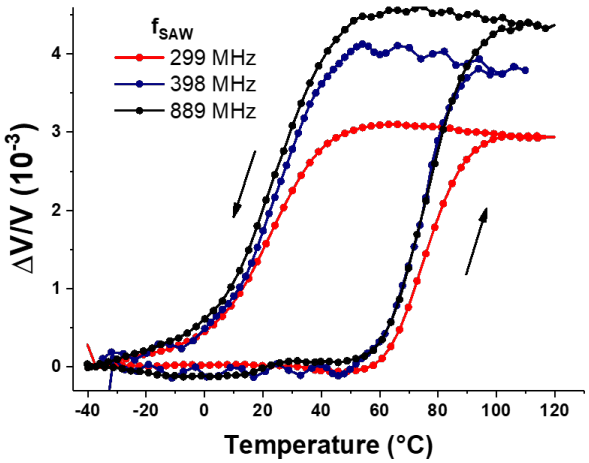

Figure 6.12: Relative velocity variations for the three excited SAW frequencies with respect to temperature, and across the phase transition. The three frequencies have similar thermal hysteresis.

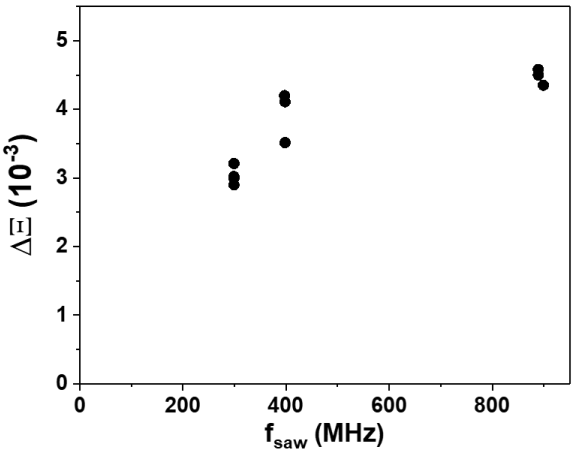

Figure 6.13: Evolution of $\Delta\Xi$ with respect to frequency in zero-field. The slight dispersion in values at a given frequency may be related to a slightly different experimental condition, since the SAWs are very sensitive to any surface contaminants (c.f. [2]

Likewise, the opening at the transition, $\Delta\Xi$, can be recorded from the measurements. The reference is taken at - 40°C for all data sets. It is observed that $\Delta\Xi$ increases with increasing SAW frequency. For f_{SAW} = 299 MHz, $\Delta\Xi = 3.1 \times 10^{-3}$, for f_{SAW} = 398 MHz, $\Delta\Xi = 4.1 \times 10^{-3}$, and for f_{SAW}= 889 MHz, $\Delta\Xi = 4.55 \times 10^{-3}$. The frequency dependency of $\Delta\Xi$ is represented on figure [6.13], for all recorded data sets. It can be seen that $\Delta\Xi$ increases monotonously with the frequency, and seems to reach a saturation value although measurements at higher frequencies would be necessary to confirm this tendency. Note that the difference between the smallest and largest values of $\Delta\Xi$ is 47%.

In Chapter [4], it has been demonstrated using Brillouin Light Scattering (BLS) and Picosecond Acoustic measurements that there is a difference in the elastic constants (C_{ij}), between the AFM and FM phases. The velocity is known to be dependent of these elastic constants. For that matter, the Farnell-Adler model developed in Chapter [4] is exploited, with the aim of determining the theoretical dependency of $\frac{\Delta V}{V}$ with temperature, the magnetic phase of FeRh and the SAW frequency.

4.3.1 Numerical versus Experimental data

In Chapter [4] the temperature dependence of the Rayleigh velocities for GaAs, Ta and FeRh was calculated and given for the AFM and FM phases, (c.f. Figure [4.13]). Then the evolution of the Rayleigh velocity for the three layer system was calculated using the Farnell-Adler model, and it was shown that the Rayleigh velocity goes from the substrate Rayleigh velocity at low k_{SAW}, and decreases below the Rayleigh velocity of the FeRh layer. Hence, using the calculated dispersion relationship for Polycrystalline Sample B: FeRh/Ta/GaAs, the contribution of the change in elastic constant to $\Delta\Xi$ is evaluated numerically. This numerical model was performed in collaboration with V. Laude (Femto-ST and UBFC[6]).

[6]Université de Bourgogne-Franche-Comté

Figure [6.14] is the experimental $\Delta\Xi$ variation with SAW frequency seen before. On these are superposed the numerical calculation of the $\Delta\Xi$ with respect to the SAW frequency (red-line). It is observed that the numerical calculation curve is quite similar to the experimentally recorded $\Delta\Xi$ sets. The numerical model and the data are in good agreement. At 299 MHz, the difference between the mean experimental data and the numerical model is 4.6%, for 398 it is 17%, while for the 889 MHz frequency it is - 11%. At 889 MHz, the model predict a larger contribution of the elastic constant. For the other two frequencies, this imply the existence of another contribution. This is investigated by applying a magnetic field, and measuring the relative SAW velocity variations (c.f. section [3.1.2]).

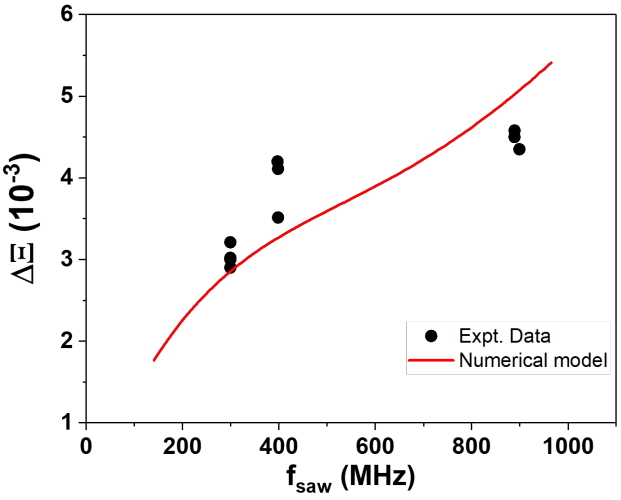

Figure 6.14: Evolution of the experimentally measured $\Delta\Xi$ with respect to f_{SAW} (black). The full line represents the numerically calculated $\Delta\Xi$ using the Farnell-Adler model. The numerical model, based on the change in elastic constants across the phase transition, is in agreement with the experimental measurements of the relative velocity variations.

Conclusion:

In this section, we have shown that it was possible to calculate numerically the opening at the AFM-FM phase transition, seen on the relative velocity variation, using only the elastic constants measured in chapter [4]. Moreover, the model is in good agreement with the experimental measurements. Hence, the $\Delta V/V$ measurements are good estimation of the effective elastic constants C_{ij} governing the tri-layer system, and follow well the magnetic state of the system.

5 SAW amplitude attenuation versus Temperature

As developed in Chapter [4], temperature variations of the SAW amplitude and velocity are measured simultaneously. A decrease in the SAW amplitude can can be the result of either:

1. SAWs interaction with the FeRh magnetic layer- either phonon-magnon coupling, or SAW interaction with magnetic domains and/or magnetic domain walls.
=> This typically depends on the frequency. At coupling or resonant conditions, higher frequency implies higher SAW amplitude attenuation;

2. A temperature variation can lead to being out-of-the IDT centre frequency
=> In designing the IDTs, the number of teeth was chosen so as to have a broad IDT resonance curve. The SAW frequency was then chosen so as to match the IDT centre frequency, over the whole temperature range studied (c.f. fig. [4.18] and subsequent discussion).

Hence, to sum up, one way to recognise SAW-FeRh interaction is to look for hysteresis features. Two types of interactions are possible: resonant and non-resonant. Resonant interactions involve the matching of SAW and SW frequencies by applying a magnetic field or a temperature variation, leading to significant energy transfer and an amplification of the SAW amplitude attenuation. In this section, the SAW amplitude attenuation is measured with respect to temperature across the phase

transition. Using the Polycrystalline Sample B: FeRh/GaAs, the experimental data of the 299 MHz SAW is considered first. Following this presentation, the influence of the frequency is considered by investigating the three excitable SAW frequencies. Then a comparison between the data obtained on Crystalline-Sample A is carried-out.

5.1 SAW amplitude attenuation at 299 MHz on FeRh/GaAs

Figure [6.15-**Top**:] shows the SAW amplitude attenuation measurement for a SAW at a frequency of 299 MHz. This is obtained by ramping the temperature from - 40 °C, in the fully AFM phase, to 120 °C, in the fully FM phase, and cooled back to the initial AFM phase. Here two amplitude attenuation temperatures or amplitude dips are observed, with each one occurring on either the heating or cooling ramp. The heating ramp is represented by open data points and the cooling ramp using filled data points respectively. In order to understand these temperatures, the magnetometry measurement is also included on the fig.-**below**, in grey. It can be seen that the two dips actually correspond to temperatures corresponding to midway along the phase transition. These temperatures (T_{up} = 71°C and T_{down} = 24°C), are approximately at the coexistence of 50-50% of FM and AFM phases.

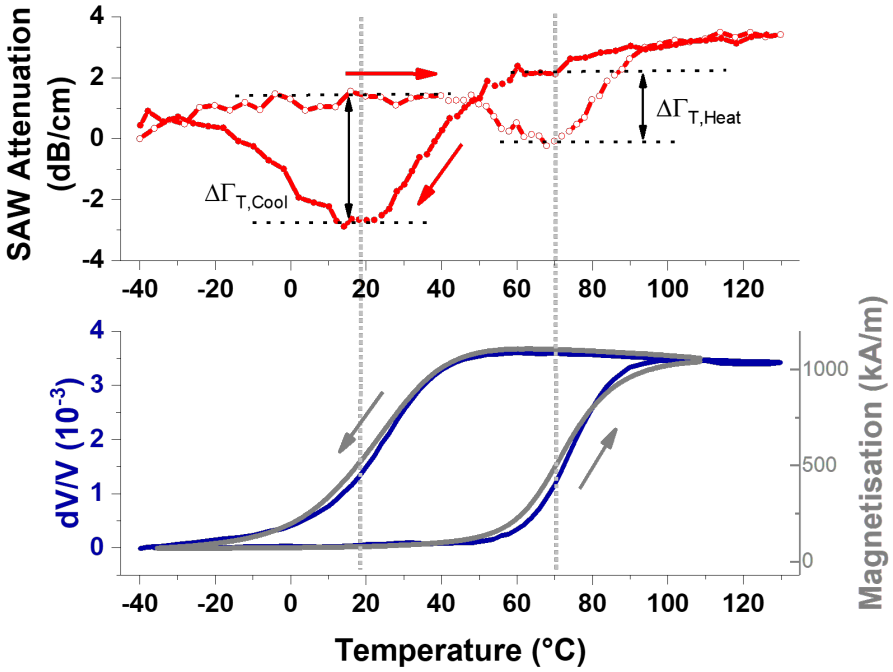

Figure 6.15: Top: SAW amplitude attenuation measurement with respect to temperature at f_{SAW} = 299 MHz. Two amplitude dips are observed, one on the heating and one on the cooling ramp respectively. Note that the two $\Delta\Gamma$ values are different with the dip in the cooling ramp being approximately twice that of the heating ramp. $\Delta\Gamma_{T,Heat}$ = - 2.2 dB/cm and $\Delta\Gamma_{T,Cool}$ = - 4.05 dB/cm **Bottom:** Relative velocity variations and Magnetisation versus temperature measurements- as seen above. It can be seen that the two resonant dips actually correspond to the temperatures midway in the transition, i.e. whereby there is approximately a 50-50% ratio between the AFM and FM phases.

Let the heating ramp be considered from - 40 °C. It is observed that the SAW amplitude variation is relatively constant up to ≈ 48°C, the temperature corresponding to the beginning of the AFM-to-FM phase transition on the VSM measurement. The maximum SAW attenuation is observed at ≈ 20°C (midway the transition on the VSM), and then joins with the cooling ramp at higher temperatures. The same is true for the cooling ramp, the beginning, maximum and ending of the SAW attenuation, match the beginning and ending of the phase transition from the FM-to-AFM phase. It is not understood why the SAW attenuation is less in the FM phase than at the reference starting temperature. There is not only a unique set of data at 299 MHz, but at least three usable set of data, with each showing similar temperature dependencies and SAW amplitude attenuation. The slope is measured to be 0.017 dB/°C. One possible reason might be the presence of invisible organic matter or ice-crystals, on the Polycrystalline Sample B surface, at low temperatures as discussed in Chapter [2]. The SAWs lose

energy by scattering, and as the sample is heated and the organic substances evaporate or the ice-crystals melt, this scattering is reduced. Nevertheless, SAW attenuation is measured from one branch with respect to the other and denoted as $\Delta\Gamma_{T,i}$. Both values are significant at 299 MHz. This is measured to be $\Delta\Gamma_{T,Heat} = 2.2$ dB/cm at 71°C (corresponding to the SAW losing 8% of its amplitude) and $\Delta\Gamma_{T,Cool} = 4.05$ dB/cm at 20°C (corresponding to 15 %). The shape of the SAW attenuation is quite similar to the measurement on Vanadium Oxide (c.f. figure [6.8]. Indeed, at the transition corresponding to a transition from an insulator to a metal, a sharp SAW attenuation was observed.

5.2 SAW amplitude attenuation at all SAW frequencies on FeRh/GaAs

In order to understand this interaction, the experiment is repeated for all three excitable SAW frequencies. On figure [6.16] is represented the SAW amplitude attenuation measurement for all three SAW frequencies and stacked for clarity. In red is recalled the frequency seen above, i.e. for 299 MHz. The black curve corresponds to the 899 MHz SAW. Here, no dip is observed, in contrast to the lowest frequency. There is a continuous decrease in the SAW amplitude attenuation with respect to the increasing temperature. In the fully FM phase, i.e. at 130°C, the recorded SAW amplitude attenuation is measured to be a stunning - 51 dB/cm for the 889 MHz SAW. This corresponds to the SAW losing 98% of its amplitude. One possible reason for this continuous amplitude attenuation is a resonant interaction with the FM fraction of the FeRh layer, with a maximum at the maximum of FM fraction. Note also the noise level, varying from 5 to 10 dB/cm at times. This is because the SAW amplitude of this particular frequency, is at the limit of what our oscilloscope can actually measure: the amplitude recorded here lie between 18-70 μV, which is close to our oscilloscope sensitivity 100 μV.

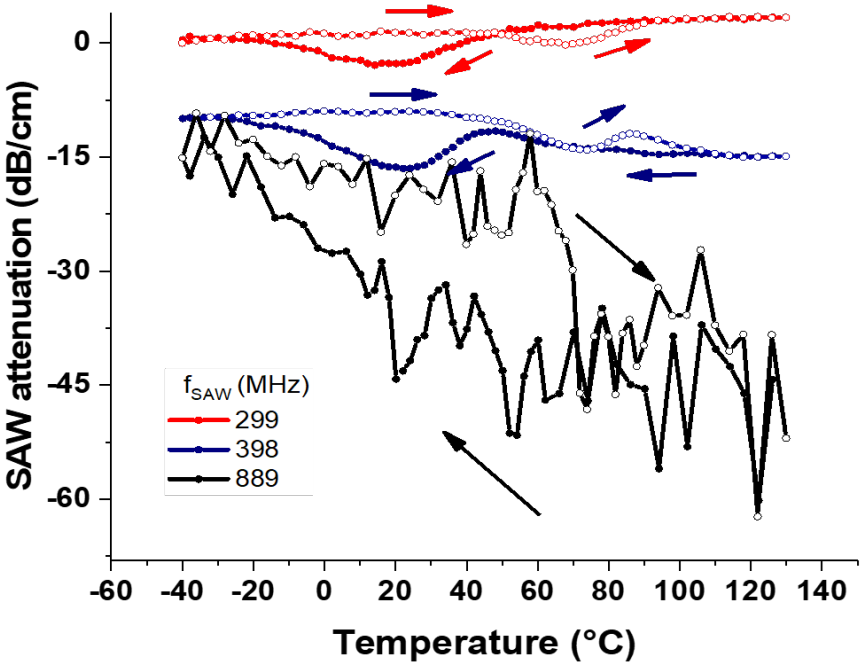

Figure 6.16: SAW amplitude variations with respect to temperature for the three excitable SAW frequencies. The data are stacked for clarity, and recorded from the fully AFM phase (-40°C to the fully FM phase (130°C). For the lowest frequency (299 MHz- represented in red), two dips at temperatures corresponding half-way in the transition is recorded. $\Delta\Gamma$ in the cooling ramp is larger than for the heating ramp. For the highest frequency (889 MHz- represented in black), a SAW attenuation possibly primarily influenced by the FM fraction is recorded. As the temperature is increased from the AFM phase, the FM fraction present increases, and is maximum at temperatures higher than $\approx$ 110°C. Similarly, the SAW attenuation is observed to increase continuously with temperature. On the other hand, for the 398 MHz SAW, the SAW attenuation seems to be a contribution of both the resonant dips and the non-resonant FM mediated attenuation.

Similarly is represented in blue the SAW attenuation for the 398 MHz SAW frequency. The recorded signal is different from either the two dips measured at 299 MHz or the continuous increase in amplitude attenuation of the 889 MHz SAW. Instead, the signal recorded seems to be a contribution of

both these measurements. The heating ramp and cooling ramps are respectively represented by open and filled points. For the heating ramp, the heating branch now lies above the cooling branch at T = 71°C. On the other hand, for the cooling ramp, at 20°C, $\Delta\Gamma_{T,Cool}$ = - 7.65 dB/cm. This corresponds to the SAW losing ≈ 21% of its amplitude. This can be compared to the 15% decrease recorded at 299 MHz.

An increase in SAW frequency results in a larger SAW amplitude attenuation, with respect to temperature. Let us now discuss the possible origin. The coincidence of the SAW amplitude attenuation dips with the temperatures corresponding to mid-way of the phase transition, suggests an influence of either FM/AFM domain walls or the FM/AFM fraction of the layer on the SAW transmission. Assuming that the number of AFM/FM domains present is maximum at 50-50% of the transition, several hypotheses can be proposed:

1. **Scattering of SAWs with domain walls**: This leads to a reduction of the amplitude of the detected waves with similar wave-vector as the excited ones. This scattering could be due to the structural in-homogeneity and variations in the magnetic properties at the domain walls.

2. **Multiple SAW Reflections**: Reflections of the SAWs at the numerous elastically mismatched AFM/FM interfaces could significantly reduce the transmitted SAWs. These reflections occur because the acoustic impedance mismatch at the domain boundaries, creating partial reflections and transmissions. This energy loss in SAW scattering by magnetic arrays was seen recently by Au *et al.* [242].

=> These two hypotheses would necessitate that the SAW wavelength be comparable to the size of the AFM/FM domains. However, this condition is not met, as the domain sizes are sub-micronic dimension. Hence, these hypotheses may be less plausible in explaining the observed amplitude dips.

3. **Resonant Interactions**: The SAWs could interact resonantly with the eigen-modes of the AFM/FM domain walls. This resonance would enhance the energy transfer from the SAWs to the domain walls, thereby reducing the SAW amplitude.

=> This hypothesis, in contrast, does not require the SAW wavelength to match the domain size. Instead, the longer wavelength SAWs could act as a uniform strain across a large number of domains, making this hypothesis more feasible. Although FM-FM domain walls are known to have typical eigen-frequencies in the range of a few hundred MHz [243], [244], AFM/FM domain walls resonance frequencies are not known.

In order to investigate the nature of the SAW-resonant and non-resonant interactions, the next two chapters are devoted to the study of SAW interaction in the presence of a magnetic field.

5.3 Comparison with SAW amplitude attenuation on FeRh/MgO

Fortunately, one usable SAW measurement was recorded on the crystalline-Sample A SiO_2/FeRh/MgO sample, before damaging the contacts. Recall, here the FeRh is 47 nm-thick (c.f. fig. [2.9]. The amplitude attenuation is represented on figure [6.17-**top**] is for a 438 MHz SAW. As the phase transition does not occur at the same temperatures, the SAW attenuation measurement starts at ≈ 0°C, but the same procedure is respected, i.e. the experiment is performed from the fully AFM to the fully FM phase and back to the initial temperature. The observations are as follows. Contrary to the measurement seen before, there are now two distinct plateaux, one at 0 dB/cm- the reference, and one at - 25.1 dB/cm, in the fully FM phase. The low-temperature plateau is relatively constant up to ≈ 60°C, which corresponds to the beginning of the phase transition as depicted by the magnetometry measurement on figure-**bottom**. Then there is a continuous decrease in the SAW attenuation up to 98°C, again corresponding to the temperature at which the VSM states that the layer is fully ferromagnetic. For the cooling ramp, the SAW attenuation decreases even before the appearance of the beginning of the

phase transition, and reaches the 0 dB/cm plateau at 57°C, before the sample is measured to be fully AFM. The SAW attenuation measurement is hysteretic, with a transition width similar to the VSM measurement. In the fully FM phase, $\Delta\Gamma$ = - 25.1 dB/cm, which corresponds to the SAW losing $\approx$ 37% of its amplitude.

This measurement is similar to what is observed on Sample B at the 889 MHz, although that here the SAW is generated at a lower frequency, 438 MHz, and even though the film is thinner (47 nm-thick FeRh/MgO vs 270 nm-thick FeRh/GaAs). One possible reason might be that the magnetic domain are bigger here, leading to less domain walls across the whole delay line.

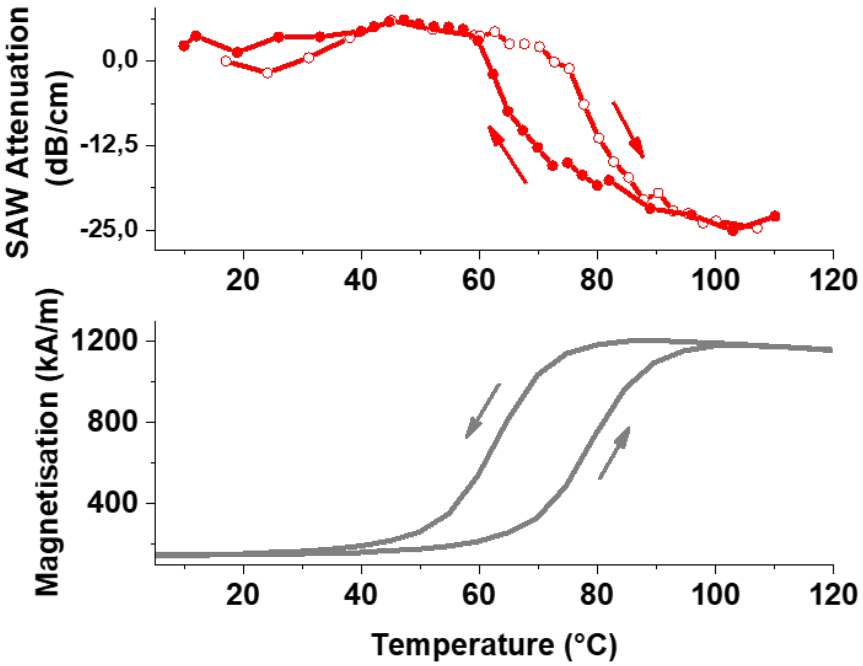

Figure 6.17: Top: SAW attenuation with respect to temperature for the SiO_2/FeRh/MgO sample. Two levels are seen far from the phase transition and the attenuation increases continuously when the sample is heated across the phase transition. Moreover, it is hysteretic. For the heating ramp, the SAW attenuation increases at temperature corresponding to the beginning of the AFM-to-FM phase transition ($\approx$ 57°C. The maximum SAW attenuation, $\Delta\Gamma$ = - 25.1 dB/cm, is found in the fully FM phase. When the sample is cooled down, the SAW attenuation however does not have the same temperature dependency as the VSM measurement represented by **bottom**.

By comparing both the relative SAW velocity variations and the SAW amplitude attenuation, a stronger dependency on the SAW frequency is observed for the latter. This is in line with the findings of the state of the art in section [3].

Chapter Summary

1. Reflectivity measurements were used to assess whether the dynamic strains induced by SAWs have any impact on the transition temperatures of FeRh or on the thermal hysteresis. These attempts were unsuccessful.

2. Relative velocity variation measurements revealed an increase at the AFM-FM phase transition, are very sensitive to the FeRh thin films and to be a good evaluation of the magnetic state of the FeRh layer.

3. The opening at the transition, on the relative velocity variations $\Delta\Xi$, increases with increasing f_{SAW}.

4. Numerical calculation of the Rayleigh velocities, using the elastic constants determined in Chapter [4], showed that increase in $\Delta\Xi$ corresponds mainly to a change in elastic constants across the AFM-FM phase.

5. SAW amplitude attenuation measurements showed signs of different contributions with respect to f_{SAW}.

Chapter 7

SAW-B

Objectives

In this chapter, the interaction between Surface Acoustic Waves (SAWs) and the FeRh magnetic layer under the influence of an external magnetic field is explored. The magnetic coercivity is investigated to identify the conditions that lead to SAW-Ferromagnetic Resonance (SAW-FMR) interaction. A comparison with the Power Transfer SAW-FMR model is conducted to validate our theoretical framework. Furthermore, angular SAW-FMR measurements are performed to provide a comprehensive analysis of the observed phenomena, and discussed with respect to the magneto-elastic driving fields. Through these studies, a deeper understanding of the dynamic behaviour of the FeRh layer in response to SAW excitation is sought, contributing to our advancements in the field of magneto-acoustic interactions.

Contents

1 Introduction

Following the previous Chapter, where SAW interaction with the magnetic FeRh layer was studied with respect to temperature, the focus of this Chapter is SAW-FMR interaction when applying a magnetic field: SAW-B. It is divided into two main categories: namely (i) SAW B-field measurements with k_{SAW} parallel to the direction of the externally applied field $\phi_B = 0°$[1] and, (ii) SAW B-field angular measurements, i.e. where $\phi_B \neq 0°$. In this chapter, only Polycrystalline Sample B: FeRh/GaAs is studied (c.f. figures [2.9] and [4.22]).

This chapter begins by introducing the necessary terms needed for the comprehension, followed by the SAW-B measurements of the amplitude and phase with $\phi_B = 0°$, i.e. for the field parallel to k_{SAW}, for the three SAW frequencies in the fully FM phase (at 130°C). Then the temperature dependency of the SAW-FMR interaction is studied. The experimental data are then analysed with the $\Delta\Gamma$ and $\Delta\Xi$ formulae derived in Chapter [5], for the SAW-FMR power transfer approach. The third section deals with the Angular SAW-FMR (a-SAW-FMR) measurements. A comparison with the angular dependency of the effective fields and the a-SAW-FMR data is carried out. Then, using the Magneto-Optical Kerr, MOKE experiment (c.f. Chapter [2]) and the SAW-FMR model (c.f. Chapter [5]) the a-SAW-FMR data are discussed in thorough details.

2 SAW-FMR for B parallel to k_{SAW}: FM phase T = 130°C

2.1 Introduction

In this first section, only the SAW measurements with the magnetic field parallel to the SAW propagation direction is considered. Recall, the SAW travels parallel to the [110] crystallographic direction of GaAs on Sample B. For magnetic field values larger than the effective magnetic anisotropy[2] of the FeRh sample, $B > \mu_0 H_{eff}$, the equilibrium magnetisation angle is assumed to lie along the direction of propagation of the SAW, i.e. $\phi_B = \phi_M = 0°$. In this geometry, the magneto-elastic tickle fields, seen in Chapter [5] become:

$$b_\theta = \left(\frac{2B_2}{M_s}\,\varepsilon_{xz} + \mu_0\, M_s\, \Omega_{xz}\right)\cos(\phi_M) = \frac{2B_2}{M_s}\,\varepsilon_{xz} + \mu_0\, M_s\, \Omega_{xz} \qquad \text{and} \tag{7.1}$$

$$b_\phi = \frac{2B_1}{M_s}\,\sin(\phi_M)\cos(\phi_M)\,\varepsilon_{xx} = 0 \tag{7.2}$$

The only contribution in driving the magnetisation dynamics thus results from the $\mu_0\, h_\theta$ tickle field.

2.2 SAW-FMR at 299 MHz at 130°C

In this section the SAW-FMR experiment is performed for a SAW at 299 MHz and at a constant temperature of 130°C, i.e. in the fully FM phase. Both the SAW relative velocity variations and the SAW amplitude attenuation measurements are discussed in concert, in this chapter.

Velocity

Figure [7.1] is an example of the typical signal obtained when performing SAW-FMR measurements with respect to magnetic field. First is represented the data set for the SAW relative velocity. The signals are obtained by starting at a high field value (generally ± 200 mT to ensure that the magnetisation is saturated parallel to the field, and that the sample is far from any resonant conditions/fields). The field is thus ramped to the corresponding ∓ saturation field and back to the initial field value. The fig. **left** shows the full range of the signal with measurements here going from 200 to - 200 mT. Note that the maximum SAW velocity variation, denoted by $\Delta\Xi$, is taken from the reference/starting field value. Here, and in the rest of the chapter, the grey area, close to zero-field values, is of interest.

[1] ϕ_B is defined as the angle between $\mathbf{k}_{SAW}$ and the direction of the magnetic field.
[2] Recall, the magnetic anisotropy of Sample B is not known at this point.

A gradual decrease in the measured signal is observed immediately after the start of the measurement, with a maximum change around the zero-field values. A typical zoom around the latter is shown on the fig. **right**. By varying the magnetic field from - 200 mT, it is thus observed that the relative velocity variation decreases gradually up to 0 mT. Then a small plateau is seen over a 2 mT range, followed by a sharp dip at 3 mT, that is interpreted as a resonance. This resonance field value is denoted as $B^V{}_{res+}$, corresponding to positive resonance field. A sharp reduction in $\Delta V/V$ is seen and the signal returns to its initial value, where no SAW phase change is measured when the field value is far away from the recorded SAW-FMR resonance. The same is true for the reverse ramp. For a complete SAW-B measurement, two hysteretic and opposite resonance field values are observed, with $\Delta\Xi$ at the two resonance field values being different. To begin, only the mean values of $\Delta\Xi$ and $B^V{}_{\text{res}}$ are considered. The difference in resonance fields or resonance dips between the positively-increasing or negatively-increasing field values, known as non-reciprocal interactions (c.f. Chapter [5]), is discussed at the end of this section. For a 299 MHz SAW, the resonant dips have a mean value of: $<\Delta\Xi> = -3.66\times10^{-4}$, with $\Delta\Xi_+ = -3.61\times10^{-4}$ and $\Delta\Xi_- = -3.71\times10^{-4}$. These values are an order of magnitude smaller than for the SAW-temperature measurements seen in the previous chapter, $\simeq 10^{-3}$; of the same order as measured previously on the ferromagnetic semiconductor GaMnAs $\simeq 10^{-4}$ [218], [245] and an order larger than phase measurements on Fe $\simeq 10^{-5}$[230]. The absolute value of the mean resonance field is $< B^V{}_{\text{res}} > = 3.2$ mT.

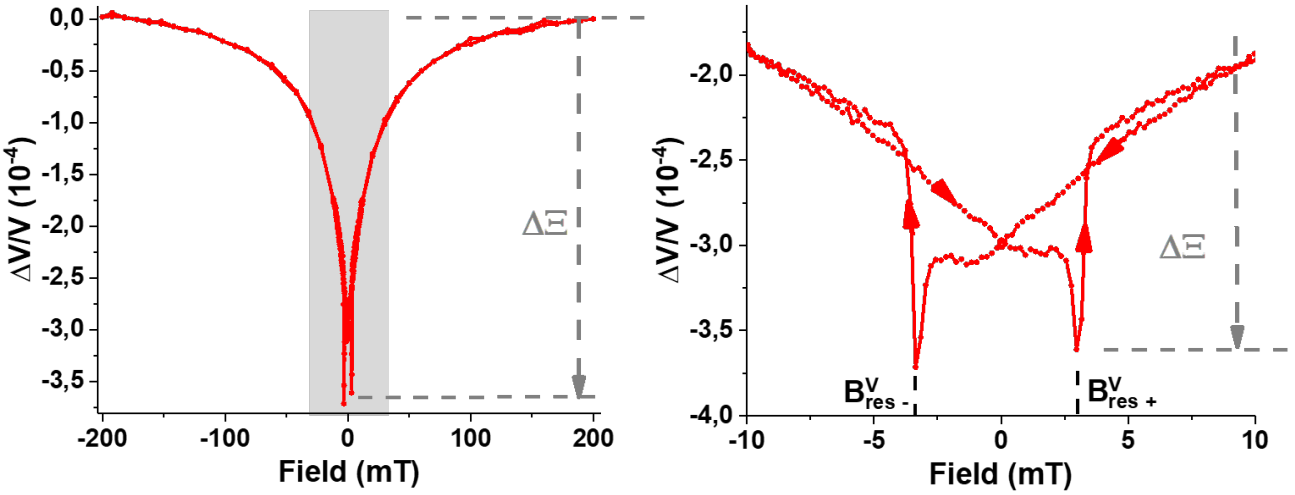

Figure 7.1: Left: SAW Relative velocity variation measurements at 299 MHz frequency. Here, the reference is taken at - 200 mT, the starting magnetic field value far from resonant condition, and large enough to ensure the whole layer has a uniform magnetisation. The measurement is taken by varying the magnetic field up to + 200 mT, and back to the initial field. A continuous decrease, or a variation in $\Delta V/V$ is observed with a minimum close to zero-field values. **Right:** Zoom around the resonance field values. The signal is symmetrical with respect to the field and two hysteretic resonance fields are measured and denoted by $B^V{}_{\text{res}\pm}$. The maximum velocity variation or $\Delta\Xi$ is always measured with respect to out-of-resonance field values. For the 299 MHz SAW, $<\Delta\Xi> = -3.66\times10^{-4}$.

Amplitude

Similarly, the SAW amplitude attenuation is represented on figure [7.2]. This data set is obtained simultaneously with the relative velocity measurement, and thus follows the same methodology (i.e. the field is ramped from - 200 mT → + 200 mT → - 200 mT.). By following positively increasing field values, the SAW attenuation has a shoulder-shaped variation, followed by a continuous decrease starting from - 3 mT as seen on the zoomed data on the **right**. The shoulder-shaped or positive amplitude attenuation is not fully understood, and will be discussed when studying angular SAW-FMR measurements. The maximum SAW amplitude attenuation is observed for $B^A{}_{res+}$. Again this attenuation is measured from the reference/starting field value and denoted as: $\Delta\Gamma$. Following the resonance, there is a sharp increase, over 1-2 mT, and the signal returns to out-of-resonance attenuation values. For a

complete ramp, two hysteretic resonance field values are recorded- similarly to the relative velocity variation measurements. The mean absolute resonance field is equal to 3.3 mT, which is very close to the value obtained on the phase measurements. Likewise, the mean value at resonance corresponds to an amplitude change of $\Delta\Gamma$ = - 1.3 dB/cm. This equates to a 299 MHz SAW losing $\approx$ 6% of its amplitude.

By comparing Figures [7.1] and [7.2], two important points can be identified. First, the complete ramps have different shapes for $\phi_B = 0°$. This difference is discussed in the penultimate section of the a-SAW-FMR measurements. Moreover, by comparing the amplitude and the velocity measurements, it is seen that for the latter, the relative velocity variation is monotonous from the starting field to the resonance field, while for the amplitude attenuation, it is non-monotonous with the presence of a shoulder-like shape. The resonance shape of $\Delta V/V$ and SAW attenuation will be discussed in the angular SAW-FMR section.

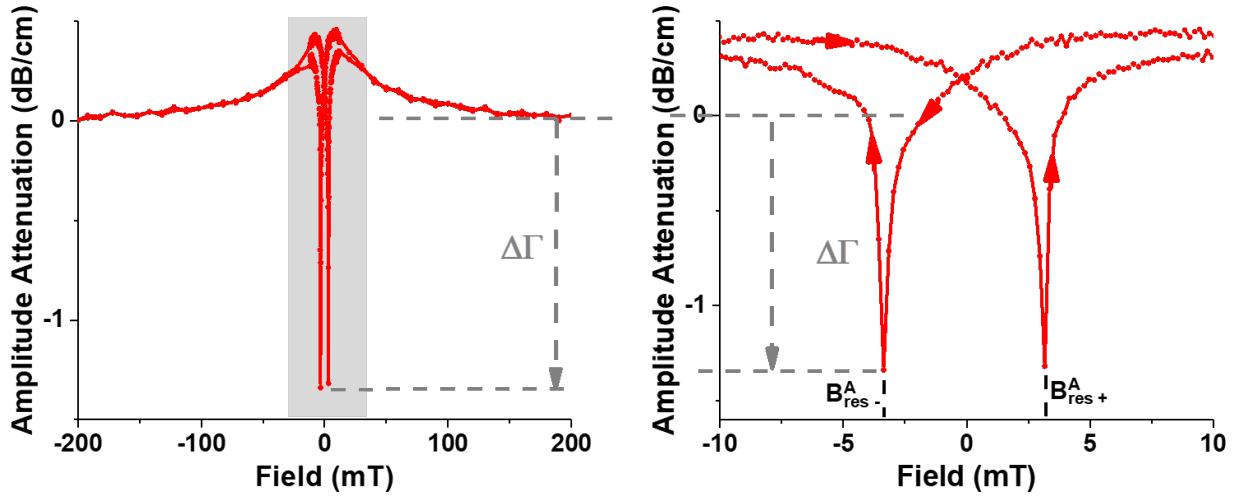

Figure 7.2: Left: SAW amplitude attenuation measurements for a 299 MHz SAW. The reference is taken at - 200 mT. This corresponds to the starting magnetic field value and the reference amplitude A_0. This field value is taken to be large enough to ensure the magnetisation is saturated parallel to the field. The measurement is taken by varying the magnetic field up to + 200 mT, and back to the initial field value. A shoulder-shape behaviour is observed close to the zero field values. The origin of this shape is not fully understood. **Right:** Zoom around the zero-field values. Coming from the initial field value, a gradual increase in SAW attenuation is observed at around - 3.3 mT, and then followed by a sharp reduction. Two hysteretic resonance fields are recorded again. The maximum amplitude attenuation, denoted as $\Delta\Gamma$ is recorded at the resonance field values $B^{A}{}_{res\pm}$. Here the mean SAW attenuation is $\Delta\Gamma$ = - 1.3 dB/cm.

2.3 SAW-FMR resonance fields coincide with the local coercivity at 130°C

In Chapter [5], it was demonstrated that an alternative way to obtain frequency and wave-vector matching (and consequently SAW-FMR interaction), between SAWs and SWs consisted in using the coercivity. Indeed, in the simple model studied, it was calculated that the spin-waves eigen-frequencies goes to zero (neglecting exchange interactions) for B parallel to k_{SAW} and the field along an easy axis, and is zero at the coercivity, in the low k_{SW} approximation. This opened a way to have arbitrarily low $f_{SW} = f_{SAW}$ matching, down to sub-GHz frequencies. In this section, this assertion is demonstrated experimentally. The SAW-FMR interaction and consequently SAW-FMR resonance, is shown to occur at the local coercivity field in the fully FM phase.

On figure [7.3-**(a)**] is represented a microscopic image of the Sample B showing the central FeRh strip, bordered on either side with the IDTs deposited directly on the GaAs substrate. The IDTs are the highly reflective rectangles on either sides of the delay line 1 or 2. Recall, on the delay line 1 are generated the 299 and 889 MHz SAW, while on delay line 2 is generated the 398 MHz SAW. The focus here is on the red-square close to the left IDT of delay line 1. This corresponds to the im-

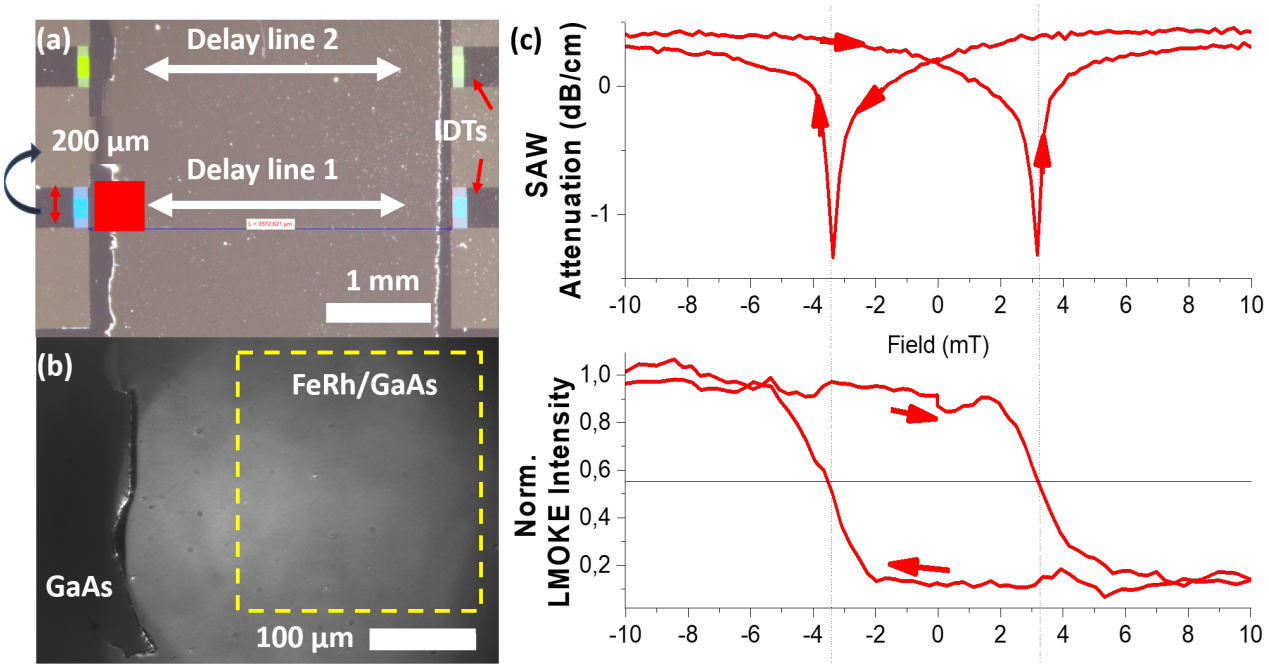

Figure 7.3: (a): Microscopic image of the Polycrystalline Sample B: FeRh/GaAs. Note the FeRh central rectangle (defined as stripes (c.f. chapter [2])), the two delay lines, and the two pairs of IDTs. Courtesy of G. Olivetti. **(b):** Imaging of the Sample B- here inside the cryostat by reflective microscopy. The yellow box corresponds to the zone where an averaging is performed on the LMOKE measurement. **(c):** Represents the SAW amplitude attenuation at 299 MHz and the local LMOKE measurement at 130°C. It can be observe that the resonance fields matches the local coercive fields measured by the LMOKE microscopy.

age labelled **(b)**, where the FeRh/GaAs part is seen to be more reflective than the GaAs layer only, since FeRh is metallic, and has a higher reflectivity than GaAs which is a semi-conductor. Using the Longitudinal-Magneto Optical Kerr Effect (LMOKE) measurements (c.f. Chapter [2] section [3.2]), the local LMOKE signal is determined by averaging over the yellow-box of approximately 220×240 μm^2. On the fig. **(c)** are represented the SAW amplitude attenuation seen in the previous section for a 299 MHz SAW, and the local LMOKE measurement at 130°C on the same delay line. The absolute value of the mean resonance field is 3.3 mT. On the LMOKE signal, the local coercive field is measured to be 3.5 mT. This coercive field obtained from LMOKE corresponds to the field at which half the area (ferromagnetic fraction) considered has switched to the opposite direction. This local designation of the coercivity can be understood by looking back at figures **(a) & (b)**. The volume over which the LMOKE signal was measured is only ≈ 220×240×0.01 μm^3, where 0.01 μm corresponds to the light penetration depth. This volume can be compared to the total ferromagnetic volume seen by the SAW which is the length of delay line × the acoustic beam width[3] × the thickness of the FeRh layer[4]: 3572×200×0.27 μm^3. Hence, as the LMOKE measurements probe only 0.3% of the total ferromagnetic FeRh seen by the SAW, the term local coercivity is justified.

Moreover, considering that the magnetic field step is δB = 0.2 mT, it can be affirmed that the 299 MHz SAW-FMR resonance field, measured on the amplitude measurements corresponds, within the given error bars, to the measured local coercivity at 130°C. This is a first step to prove, as per the mathematical demonstration of chapter [5], that the SAW-FMR resonances occur at the magnetic coercivity of the sample. Is this true for the other SAW frequencies?

[3]The acoustic beam width is the effective length of the IDT, which generate the SAWs. Here 200 μm, c.f. fig. [7.3**(a)**]

[4]The SAWs always see the whole thickness of the FeRh layer as their penetration depth, $\delta > d_{FeRh}$, even for the highest SAW frequency generated.

2.4 SAW-FMR for the 3 frequencies at 130°C

In this section, the SAW amplitude attenuation and the relative velocity variations with respect to the magnetic field is studied for the three excitable SAW frequencies. Even if the SAWs were not generated on the same delay lines[5] and interact with FeRh of different chemical composition (c.f. Chapter [4]), the three SAW frequencies are stacked on the same figures to aid the analysis. This difference in Rhodium originates from the graded composition growth technique, where a rhodium gradient is known to be present perpendicular to the delay lines. This gradient in composition is not known for the Sample B.

Velocity Variations

On Figure [7.4] is represented the stacked data for the 299 (red coloured), 889 (black coloured) and 398 (blue coloured) MHz SAWs. From figure [7.4], it can be measured that the mean resonance field absolute values are: 3.3 and 2.9 mT for the 299 MHz and 889 MHz SAWs respectively, while for the 398 MHz it is around 1.9 mT. Hence, for the same SAW delay line 1, it is observed that increasing the SAW frequency decreases the resonance field. Likewise, the $\Delta\Xi$ values for the different frequencies are: - 3.6×10^{-4} for the 299 MHz and - 3.7×10^{-4} for the 889 MHz, while it is - 4.7×10^{-4} for the 398 MHz. At $\phi_B = 0°$, by comparing the influence of the first harmonics, on $\Delta\Xi$ is thus more pronounced on delay line 2 than delay line 1. The maximum relative velocity variation was obtained mathematically in Chapter [5], eqn. [5.61] as:

$$\Delta\Xi \quad \propto \quad \frac{M_s}{{V_{SAW}}^2 B_{SAT}} \tag{7.3}$$

Yet, as calculated using the Farnell-Adler model in chapter [4] and illustrated on figure [4.14], as $f_{SAW} \nearrow$, $V_{SAW} \searrow$ due to dispersion in the tri-layer. Hence, $\Delta\Xi$ should increase $\propto 1/{V_{SAW}}^2$. On the Polycrystalline Sample B: FeRh/Ta/GaAs, this dispersion is quite substantial. This expected increase of $\Delta\Xi$ for the two frequencies of the same delay line is not observed experimentally. Although an increase ($\nearrow$ 31%), is observed when comparing $\Delta\Xi$ for the 299 MHz on delay line 1 to $\Delta\Xi$ for the 398 MHz on delay line 2 , this cannot be reasonable considered as obeying equation [7.3], since other parameters like M_s may also vary from one delay line to the other. The most important features though is the shape of the resonance. By starting far from the resonance (at - 200mT) and looking at the increasing field ramp, the presence of a plateau just before the resonance field is observed for the 398 and 299 MHz frequencies, and not on the 889 MHz SAW. Following the resonance field, there is a sharp increase in the signal for all three frequencies.

Returning to the resonance field values. For delay line 1, $< B_{res} > = 3.3$ mT at 299 MHz and $< B_{res} > = 2.9$ mT at 889 MHz. Higher frequency implies smaller resonance field value. The spin-wave dispersion is now added to the model presented on figure [5.17] to illustrate the frequency matching at coercivity and given on figure [7.5]. The spin-waves eigen-frequencies are calculated for the $k_{SW} = 0.654$ and 1.963 μm^{-1} wave-vectors, which correspond respectively to the 299 and 889 MHz SAW wave-vectors. Looking at figure [7.5], it is seen that the SAW-SW frequency matching occurs around 3.3 mT, for the red signal, while at the 889 MHz, the frequency matching occurs at lower resonance field, here at 1.8 mT. Thus, it can be seen that the higher frequency has indeed a lower resonance field value. Moreover, the calculated values for the 889 MHz is far from the recorded value (1.8 mT vs 2.9 mT) to the recorded resonance field. Here, an effective anisotropy of $K_{eff} = 2.7$ kJ/m^3 has been fed to the model. Note this effective anisotropy is less than recorded on crystalline FeRh: 6.4 kJ/m^3 by Mancini *et al.* [246] (here cubic anisotropy) and 7.4 kJ/m^3 from the MLD experiments (Crystalline Sample A with cubic anisotropy).

[5] Recall: the 299 MHz and 889 MHz are generated on the same delay line and are the first and third harmonics; the 398 MHz SAW was generated singly on another delay line. The two delay lines have the same length but slightly different FeRh chemical compositions. This was seen on the VSM measurements (c.f fig [2.5]), where the consecutive samples has different M(T) characteristics.

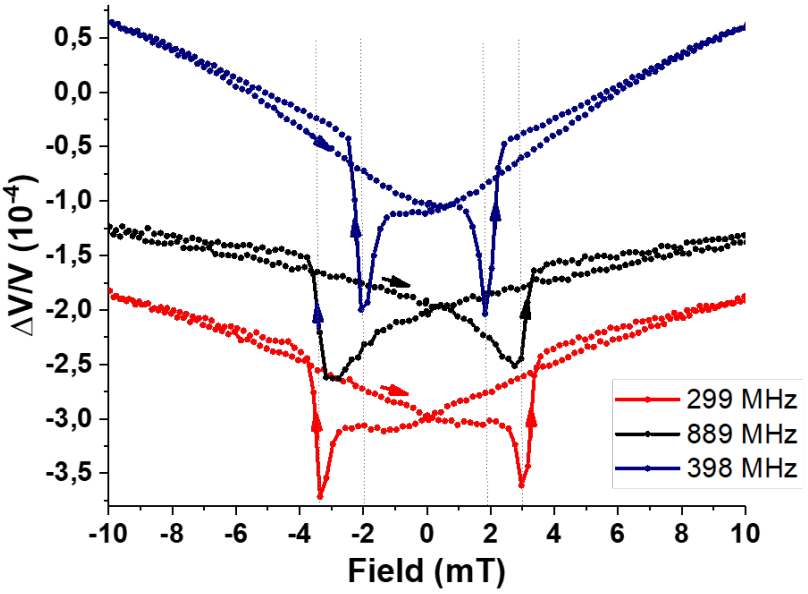

Figure 7.4: SAW relative velocity measurements with respect to the magnetic field, for the three excited SAW frequencies. The curves are up-shifted for clarity. The measurement are performed for a field parallel to k_{SAW} and in the fully FM phase (i.e. 130°C). For the same delay line, the resonance field is seen to decrease with increasing SAW frequency. This change is small for the $\Delta\Xi$. However, when comparing the 299 MHz SAW of delay line one to the 398 MHz SAW of delay line 2, $\Delta\Xi \nearrow 31\%$.

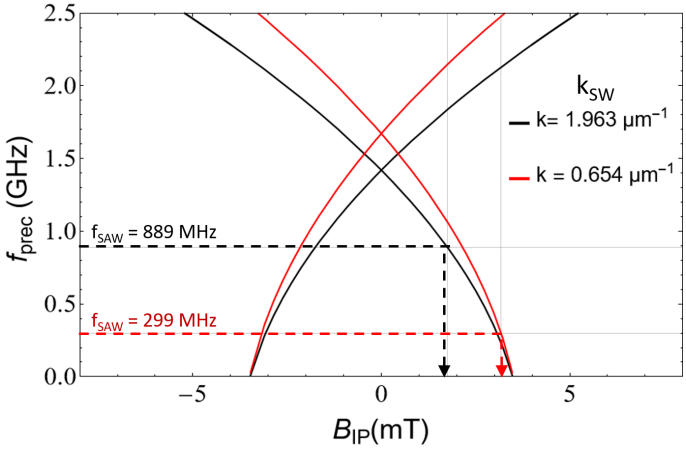

Figure 7.5: Calculation of the spin-wave eigen frequencies with respect to the magnetic field for $k_{SW} = k_{SAW} = 0.654$ and 1.963 μm^{-1} in full lines. In dotted lines are represented the 2 SAW frequencies generated on delay line 1: 299 and 889 MHz SAWs. In can be seen, that the field values at which the frequency matching occurs decreases with increasing frequencies. The calculated values align with the recorded resonance field. An effective anisotropy of $K_{eff} = 2.7$ kJ/m^3 was used in the model.

Amplitude attenuation

Similarly, the stacked SAW attenuation measurements for the three SAW frequencies is represented on figure [7.6]. Three important points are observed here: on the resonance fields $< B_{res} >$; the mean SAW attenuation value $\Delta\Gamma$; and the shape of the SAW attenuation. Firstly, the mean absolute resonance fields measured are: for the 299 MHz, $\approx$ 3.3 mT, for the 889 MHz $\approx$ 3.1 mT and for the 398 MHz $\approx$ 2.0 mT. Note those resonance field values match closely to those measured for the phase variations. Again, the significantly lower value of the 398 MHz resonance field comes form the fact that it was measured on the second delay line with another FeRh concentration. Likewise, the difference in resonance field values for different frequency on delay line 1 can be inferred from fig. [7.5]. In the following section [3], this frequency dependency will be discussed for different temperatures. Is the resonance-coercivity matching valid at all temperature?

Secondly, for the 299 MHz SAW, $\Delta\Gamma$ = - 1.25 dB/cm. This corresponds to the SAW losing $\approx$ 5% of its amplitude. For the 398 MHz SAW, $\Delta\Gamma$ = - 7 dB/cm, which corresponds to the SAW losing $\approx$ 25% of its amplitude. For the 889 MHz, the SAW attenuation goes to $\Delta\Gamma$ = - 29 dB/cm, which

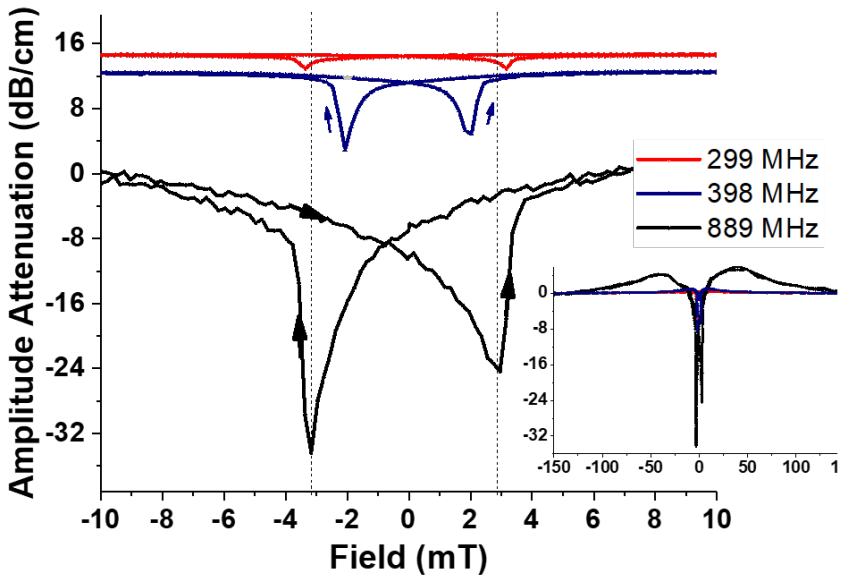

Figure 7.6: SAW amplitude attenuation with respect to magnetic field at a temperature of 130°C (i.e. in the fully FM phase) for the three excited SAW frequencies. The data sets are up-shifted for clarity. The three curves have similar field-dependency with a gradual decrease towards the resonance field value, followed by a sharp increase after the resonance. The maximum SAW attenuation or $\Delta\Gamma$ increases with increasing frequency, with the maximum at 889 MHz corresponding to - 29 dB/cm. **Inset:** Here the full magnetic field measurements are represented.

corresponds to the SAW losing a stunning $\approx 70\%$ of its amplitude. Note the two $\Delta\Gamma_{\pm}$ values have high non-reciprocity here: - 34.4 dB/cm vs - 24.3 dB/cm[6]. Here, clearly the SAW attenuation is higher for higher SAW frequencies. The evolution of $\Delta\Gamma$ from equation [B.44] of chapter [5] is recalled here:

$$\Delta\Gamma \quad \propto \quad \frac{\alpha V_0}{{V_{SAW}}^3}\left(\frac{{\omega_{SAW}}^2}{{B_{SAT}}^2} - \gamma^2\right) \tag{7.4}$$

it is seen here that $\Delta\Gamma$ is strongly dependent on the SAW frequency. Recall, the group velocities recorded for the three SAW frequencies are (299 MHz: 2617 m/s; 398 MHz: 2498 m/s and 889 MHz: 2252 m/s at 130°C). Hence using those values, the evolution of the maximum SAW amplitude attenuation is plotted versus ${\omega_{SAW}}^2/{V_{SAW}}^3$ as:

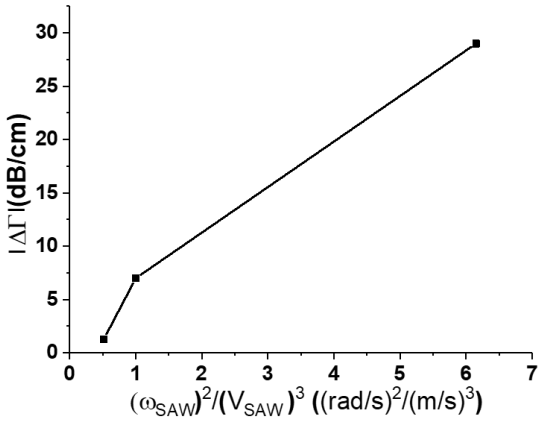

Figure 7.7: Evolution of $|\ \Delta\Gamma\ |$ vs ${\omega_{SAW}}^2/{V_{SAW}}^3$ for the three SAW frequencies. Two points to observe here. First, that the SAW attenuation increases sharply here. Secondly, This evolution is not linear. This dependency is studied in the next section.

Note also here, a non-reciprocity in the SAW attenuation measurements, with $\Delta\Gamma_- > \Delta\Gamma_+$, for all three frequencies. This non-reciprocity is more pronounced than for the relative velocity variation

[6] We know that the non-reciprocity is extremely dependent on the magnetisation alignment with k_{SAW}. So, this huge NR value might be the result of a small field mis-alignment favouring one B_c to its hysteretic value.

measurements. Finally, in the inset of fig. [7.6] is represented the SAW attenuation over the whole field ramp. Note the appearance of the shoulder-like shape, previously discussed at 299 MHz. For the field applied parallel to k_{SAW}, all three SAW attenuation measurements have the shoulder-like shapes, before the resonance. The shape becomes broader with increasing frequency.

3 SAW-FMR with B parallel to k_{SAW} versus temperature

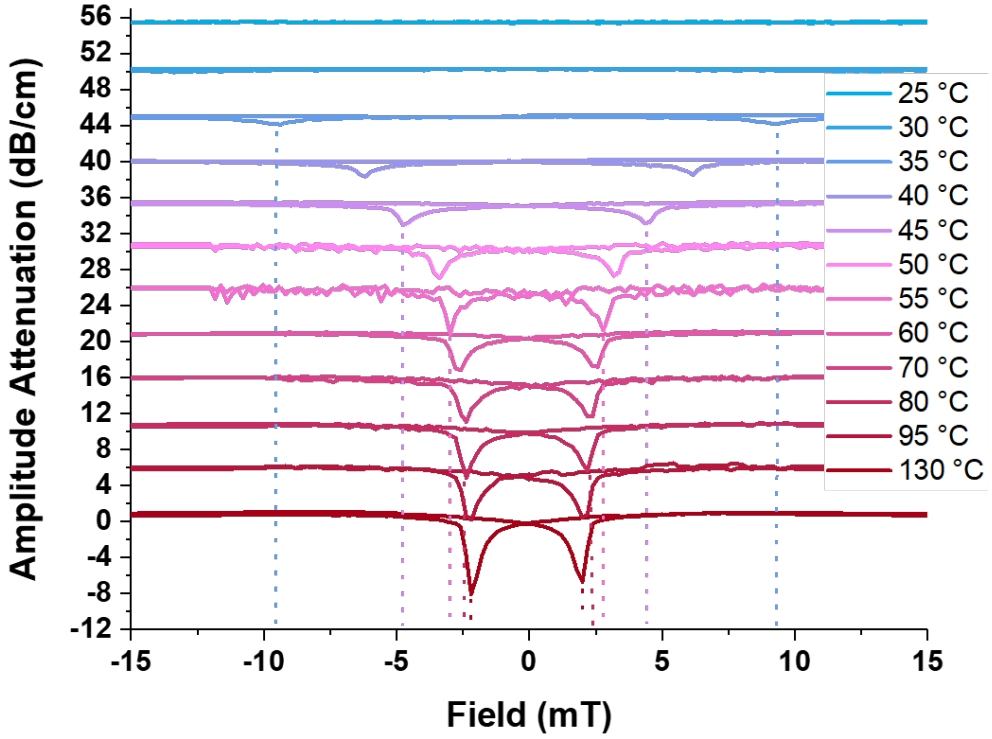

Figure 7.8: Evolution of the SAW amplitude attenuation with respect to the magnetic field, at 398 MHz, for different temperatures ranging from the fully FM phase (red) down to the AFM phase (light blue). The consecutive curves are up-shifted for clarity. Two important points to acknowledge here are: (i)- The resonance field values actually increases when the sample is cooled. (ii)- The SAW maximum attenuation $\Delta\Gamma$ decreases for decreasing temperatures.

It has been demonstrated previously (c.f. section [2.3]), that the SAW-FMR resonance fields coincided with the local coercivity, determined by LMOKE microscopy, for the fully FM phase. In this section, an investigation of this effect is undertaken with respect to temperature, and across the FM-to-AFM magnetic phase transition. First the SAW amplitude attenuation and the SAW relative velocity data are presented, while cooling the FeRh sample from 130°C down to 25°C. Then the LMOKE experiment is repeated for the corresponding temperature and a comparison between the resonance fields and coercivity is performed at all temperatures.

3.1 SAW-FMR parallel to k_{SAW} versus temperature at 398 MHz

By choice[7], here is presented the data for the 398 MHz SAW. Following the same procedure presented at 130°C, the SAW-FMR experiment is repeated from the fully FM phase (at 130°C) down to the AFM phase (at - 40°C). Each measurement is performed at a constant temperature, and following a unique cooling ramp, i.e. performed in a single day from a fully FM to a fully AFM phase. Hence there is no

[7]The choice to present the 398 MHz, although it is excited singly on the second delay line, stems from the fact that it still lies mid-way in the frequency range.

risk of being on a minor hysteresis loop. Note, the SAW frequency remains fixed for the whole temperature experiments, even though as T ↘, V_{SAW} ↘ and thus there is a risk of being out-of-resonance with the centre frequency of the IDTs. As explained in the previous chapter and on figure [4.18], the IDTs were designed with a number of electrodes (or fingers) such that the chosen SAW frequency lies within the resonance bandwidth over the whole temperature range chosen for our study.

The SAW attenuation measurements are given in figure [7.8], while the relative SAW velocity variations are in figure [7.9]. Two important effects are seen here. Firstly, when the sample is cooled, the resonance fields actually increase, going from 2.1 mT at 130°C to 13.1 mT at 30°C. The same dependency is observed for the SAW attenuation and SAW velocity measurements. On the velocity measurements, the resonance fields goes from 1.9 mT at 130°C to 12.4 mT at 30°C. The resonance fields on the velocity are slightly smaller. However, at these small field values, a convolution might exists with the magnetic field steps used when measuring the data. For all the SAW-B measurements, the step was $\delta B = 0.2$ mT.

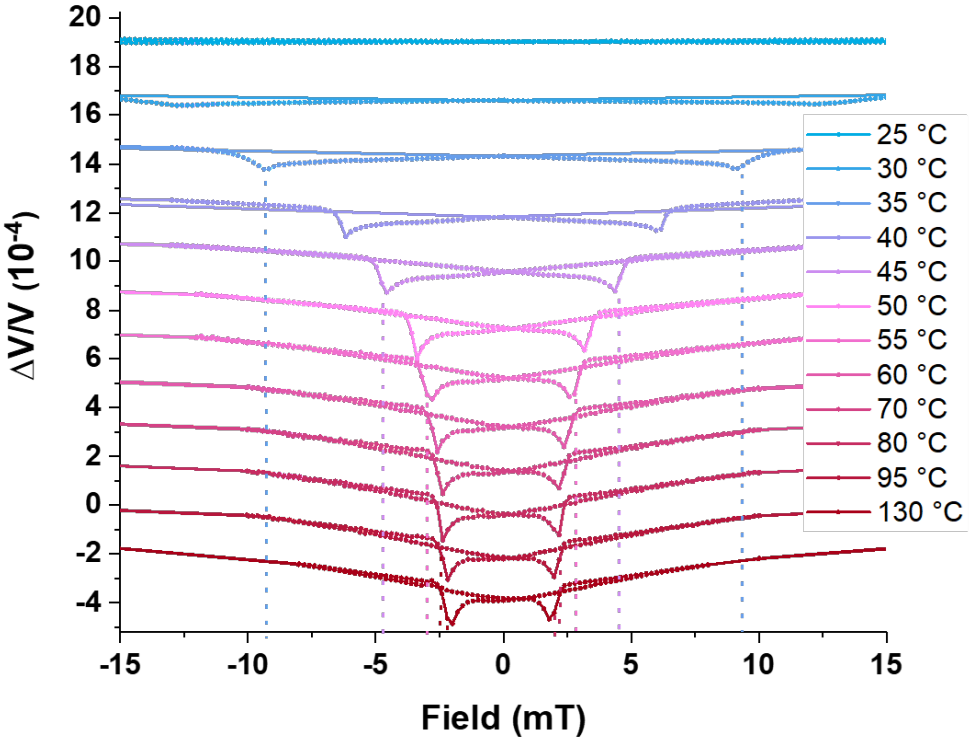

Figure 7.9: Evolution of the relative velocity variation with respect to the magnetic field for different temperatures, going from the fully FM phase (represented in red), to the fully AFM phase (represented in light blue). Similar to the SAW attenuation, the resonance filed increases with decreasing temperature, and the maximum velocity variation $\Delta\Xi$, decreases with decreasing temperature, and no phase variation is measured in the fully AFM phase, i.e. for all temperatures below 25°C.

Secondly, the maximum SAW attenuation $\Delta\Gamma$ and the maximum SAW relative velocity variations $\Delta\Xi$, are reduced when decreasing the temperature. This mean that, by decreasing the temperature there exists less and less SAW interaction with the magnetic FeRh, i.e. the x_{FM} fraction. Quantitatively, for $\Delta\Gamma$ this goes from - 7 dB/cm at 130°C to 0 dB/cm for all temperatures below 20°C, while for $\Delta\Xi$ this goes from - 4.7×10^{-4} at 130°C to - 0.99×10^{-4} at 25 °C. Note here, that an interaction was still noted on the velocity measurements at 25°C, while on the amplitude measurements, no attenuation were recorded. This might just be due to the limit in the recording precision of the oscilloscope (recall 100 μV for the amplitude). At lower temperature, no interaction was perceivable on either amplitude or velocity measurements, the FM-to-AFM transition being completed.

Shape-wise, for the SAW attenuation, coming from the initial -200 mT field, the attenuation decreases

gradually, has a dip at the resonance field and is followed by a sharp reduction in the SAW attenuation. The same is true for the relative velocity variations. However, contrary to the amplitude attenuation, whereby the dips are seen to be quite narrow near the resonance fields at all temperatures, in the case of the velocity measurement, the dips becomes broader and broader, for decreasing temperatures. The temperature dependency of $\Delta\Gamma$, $\Delta\Xi$ and mean absolute B_{res} are plotted and discussed in the following section.

3.2 SAW-FMR resonance fields coincide with the local coercivity at all temperature

Similar to the discussion in section [2.3], the resonance fields are compared with the local coercivity, measured using the LMOKE setup- now for different temperatures along the FM-to-AFM phase transition.

On figure [7.10-**Left:Top**] are represented the SAW amplitude attenuation measurement at 398 MHz for a constant temperature of 130°C in red. Using the Longitudinal-Magneto Optical Kerr Effect (L-MOKE) measurements (c.f. Chapter [2] section [3.2]), the local LMOKE signal is represented for the same delay line, on the fig. **Bottom**.The LMOKE signal is normalised, and both are represented on the same magnetic field range. Note that, the measurements are now performed on delay line 2. At 130°C, the mean absolute resonance field is measured to be 2.0 mT. On the LMOKE signal, the local coercivity is measured to be 2.2 mT. Considering that the magnetic field step is $\delta B = 0.2$ mT, it can be affirmed that the SAW-FMR resonance field measured on the amplitude measurements corresponds, within the given error bars, to the measured local coercivity. Likewise, on the fig. **Right** are represented the SAW attenuation and LMOKE signals at at 50°C in the mixed phase. The absolute resonance field is measured to be 3.3 mT, while the local coercivity is measured to be 3.2 mT. **This is the first experimental demonstration of the SAW magneto-acoustic resonance coinciding with the static local coercivity.** In other words, the resonant interactions between the SAWs and SWs occur at the coercivity of the sample, as per the mathematical demonstration shown in Chapter [5].

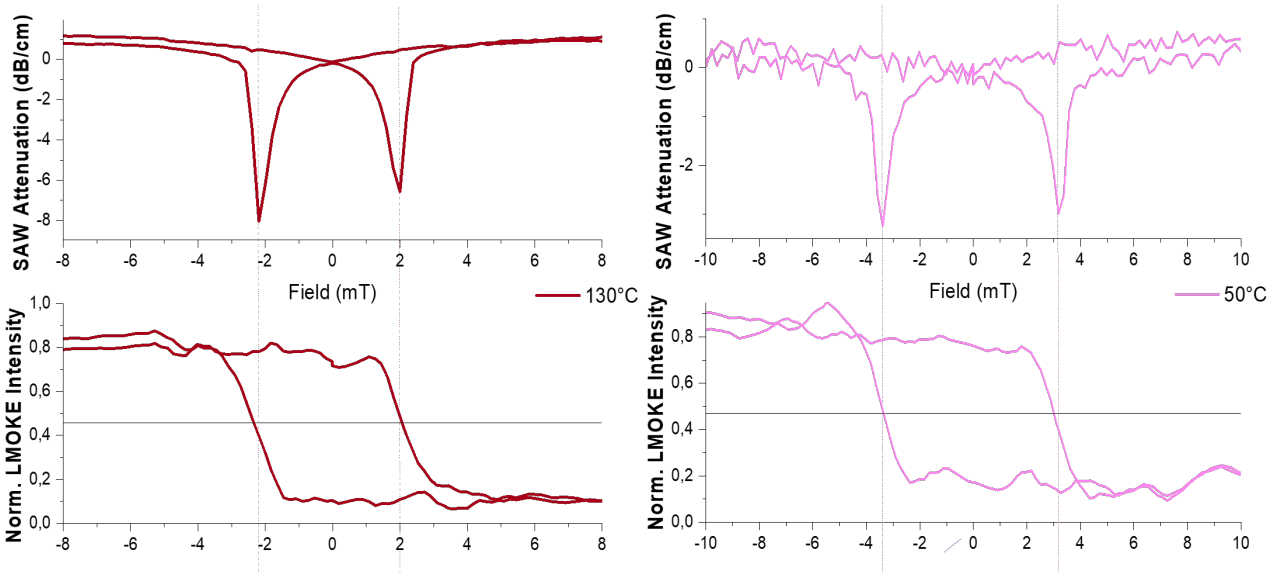

Figure 7.10: Top: SAW attenuation measurement at 398 MHz. **Bottom:**Normalised Longitudinal Magneto-Optical Kerr measurements on delay line 2. The two sets of measurements are performed at two constant temperatures: 130°C (in red- in the fully FM phase) and at 50°C (in pink). Note that at the two different temperatures, the SAW-FMR resonant magnetic fields coincide with the local coercivity.

The resonance field and coercive field are represented on figure [7.11], when cooling the sample from the fully FM phase (130 °C) down to 20 °C and for the three SAW frequencies. The two data sets are separated to represent the two delay lines, with delay line 1 representing the 299 and 889 MHz SAW, while delay line 2 represents the 398 MHz SAW. This is important as, although not demonstrated yet,

that they do not have the same Fe_xRh_{1-x} concentration, and thus not the same coercivity. Indeed, it is observed that the local coercivity between the two delay lines differ by approximately 1.4 mT, and that this difference is almost constant with respect to temperature.

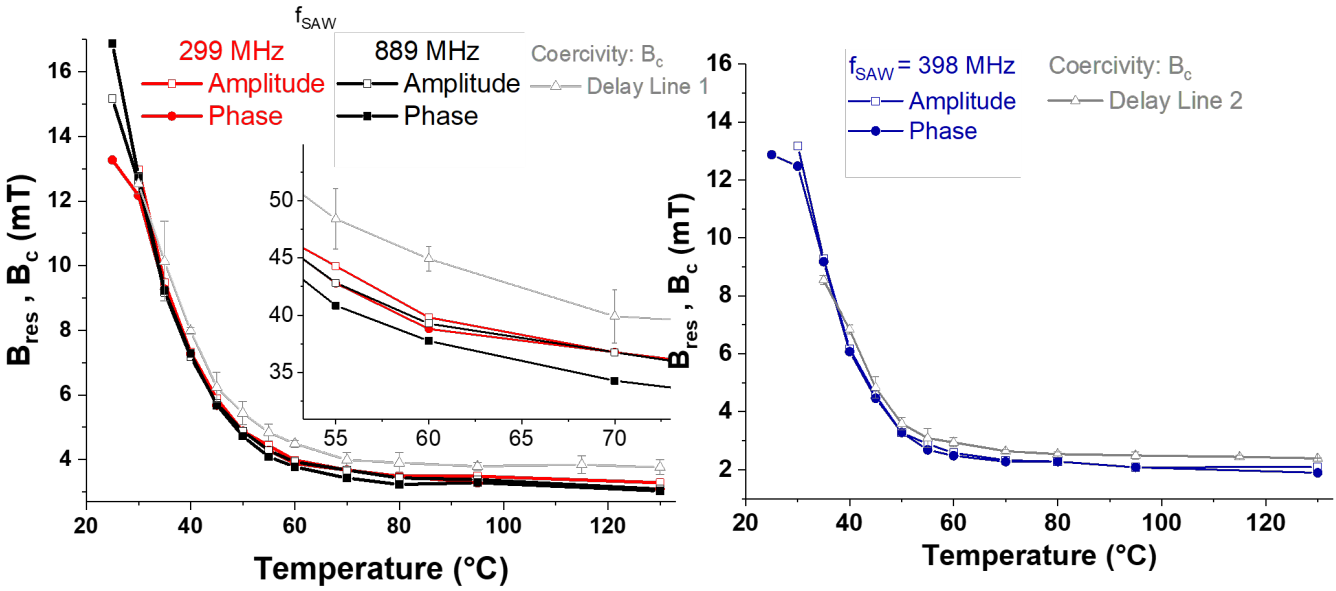

Figure 7.11: Temperature dependence of the coercivity (in grey), Amplitude attenuation resonance fields (open-symbols) and Phase variations resonance fields (closed-symbols) for the 398 MHz SAW (**right**), and the 299 and 889 MHz SAWs (**left**). The coercivity has the same temperature dependency on both delay lines, with the resonance fields closely matching this temperature dependence. On the inset are represented a zoom for the 299 and 889 MHz SAWs. Increasing the frequency implies lower resonance field at all temperatures.

Analysing the temperature dependencies of the resonance fields (amplitude-open points and velocity-full points), and the local coercivity show that they are similar. On the fig. **left-inset** it is observed that by increasing the frequency, (here are represented in black the 299 MHz and in black the 889 MHz SAWs), the resonance fields are smaller. By increasing f_{SAW}, the matching with the eigen-SW frequencies occur at lower and lower magnetic field values. This was already noted and discussed above using the numerical modelling (c.f. section [2.3]) at 130°C. If now, the resonance fields and coercive fields have same temperature dependencies, we can suppose this is true at all temperature. Nonetheless, a discussion of the temperature divergence of the coercivity with decreasing temperature is necessary.

3.2.1 Origin of the local coercivity temperature divergence

This temperature dependency of the coercivity is a known phenomenon [52], [247], as described on figure [7.11]. By cooling the sample from the fully FM phase down to 50°C, the ferromagnetic fraction decreases. The coercivity, as measured here corresponds to the magnetic field at which half the FM domains point to the right, and half point to the left, while ramping the field from right-to-left. The magnetisation switching here implies a nucleation-dominated reversal. If the FM fraction is less, the number of possible nucleation sites for magnetic switching is thus reduced. Hence, it is difficult for switching to occur, leading to an increase in the coercivity measured by Kerr-microscopy. For an AFM-dominated matrix, the switching becomes hardest and the coercivity diverges.

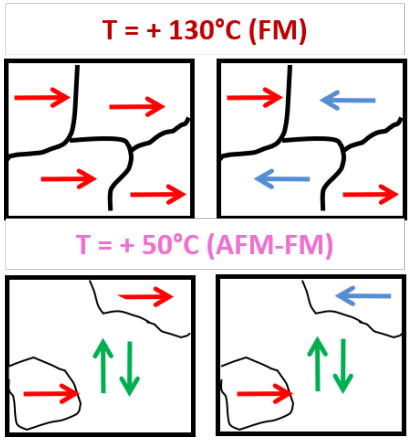

Figure 7.12: Schematic illustration of the domain reversal at the coercive field for the two temperatures seen above: T = 130°C (fully ferromagnetic phase-in red) and for T = 50°C (mixed phase- in pink). The single arrows represent FM magnetic moments, directed either to the right (red) or to the left (blue), while the double arrows represent AFM magnetic moments (green). In the fully FM phase, at saturation (B = + 200 mT), the sample is saturated, and all magnetic moments point to the right: **Top-Right**. Now the field is applied to the left. As the field reaches - 2.2 mT (c.f. fig [7.10]), half the magnetic moments (or here domains) are pointing to the initial right direction, while half are pointing to the left. This 50-50 right-left FM domains configuration corresponds to the coercive field measured by LMOKE. Now if the sample is cooled down to 50°C, AFM domains appear within the FM matrix, represented by green arrows. If the magnetic field is again ramped from right (+ 200 mT) to left (- 200 mT), at the corresponding coercivity, the ferromagnetic fraction present is less. Hence it is harder for the switching to occur. This reduction in the number of possible nucleation sites of magnetic switching leads to an increase in the coercivity measured by LMOKE. The coercive field thus increases with decreasing temperature. For T = 50°, the FM domains present are swamped within the AFM matrix, making the switching the hardest and the coercivity the largest.

Similar increase of coercivity has been recorded on FeRh patterns. Arregi *et al.* investigated the confinement effect and the magnetisation reversal on different FeRh structures. On figure [7.13] is represented the coercivity measured by LMOKE for different FeRh size and shape structures. Note that the coercive changes for the rectangular shape structures from $B_c = 11$ mT for 1 μm rectangle to $B_c = 18$ mT for 0.5 μm rectangle (64% ↗ for half the size), and $B_c = 27$ mT for ≈ 0.3 μm rectangle (145% ↗ for $\sim$ a quarter of the initial size). The same physical effect is at the origin of the increase in coercivity: reducing the size of the FeRh structures implies a decrease in the number of possible nucleation sites for the magnetisation reversal to occur.

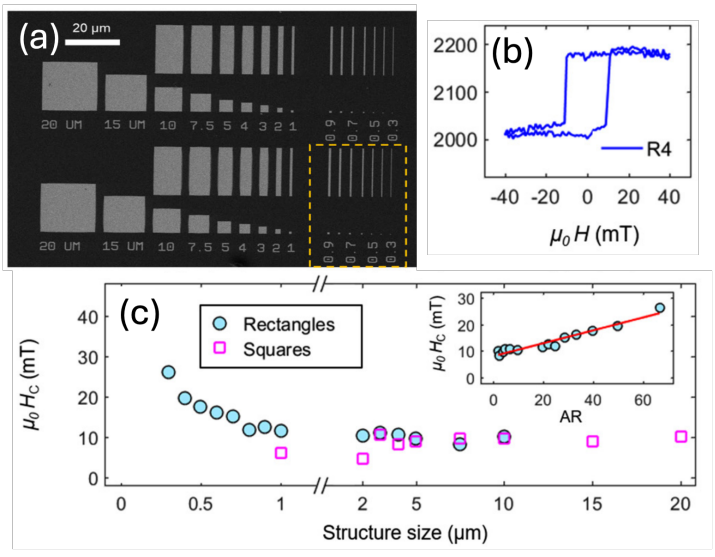

Figure 7.13: **(a):** Scanning electron micrograph of different FeRh structures (rectangles or squares shaped), with lateral dimensions between 0.3 and 20 μm. **(b)**: Longitudinal Kerr signal of the magnetisation reversal behaviour for a rectangle shape FeRh structure. Here for a width of 4 μm. **(c):** Evolution of the measured coercivity with the FeRh structure sizes. Note the measured increase of coercivity with decreasing FeRh structure sizes. For 1 μm rectangle, $B_c = 11$ mT; 0.5 μm rectangle, $B_c = 18$ mT; and ≈ 0.3 μm rectangle, $B_c = 27$ mT. Adapted from [52].

3.2.2 Comparison of the coercivity with the ferromagnetic fraction

In the previous chapter (c.f. fig. [6.10]), it has been demonstrated that a measurement of the relative SAW velocity variation is a very good estimate of the ferromagnetic fraction x_{FM}, present with respect to temperature. On figure [7.14] is represented the temperature dependency of the coercivity measured by LMOKE on delay line 1: 299 and 889 MHz SAWs, superposed to the relative SAW velocity variation measurements- scaled to represent the ferromagnetic fraction with respect to temperature (c.f. Chapter [6]). For the LMOKE measurements, the sample was cooled from T = 130°C. So, only the cooling ramp (denoted by the arrow) is under study here. At the beginning of the FM-to-AFM transition, ≈ 57°C, the coercivity is measured to be B_c = 4.5 mT. Here, it is seen that at 30°C, the last measurable coercivity signal by LMOKE signal, the FM fraction is ≈ 50%. The corresponding coercivity is recorded to be B_c = 12.5 mT. Thus, in our experiments, reducing the ferromagnetic fraction by half resulted in the coercivity to increase by 178%. Note, the LMOKE signal below 25°C were too noisy to obtain additional coercivity measurements.

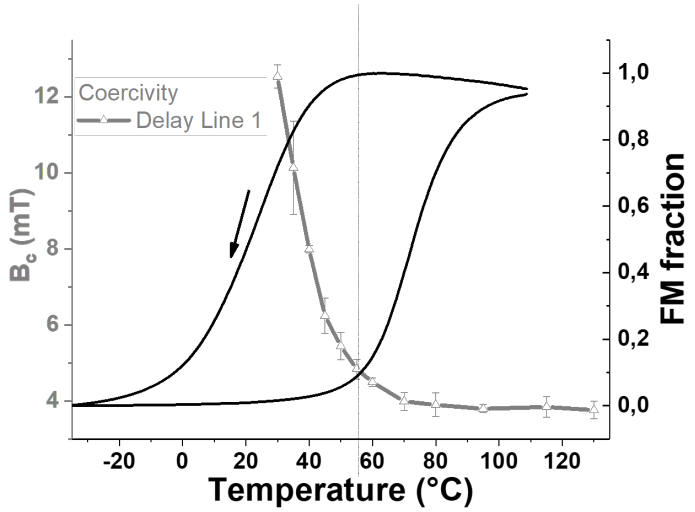

Figure 7.14: Left Axis: Coercive field measurement by LMOKE on the 299-889 MHz delay line with respect to temperature. **Right axis:** Ferromagnetic fraction obtained from the relative velocity measurements- here the 889 MHz SAW, with respect to temperature. For x_{FM} = 1, at the beginning of the FM-to-AFM transition, the coercivity is 4.5 mT. For T = 30°C, the coercivity is B_c = 12.5 mT. This temperature corresponds roughly where the is a 50-50 % of AFM and FM domains. Thus, reducing by half the available FM fraction, increased the coercivity by 178%.

Returning back to figure [7.11], the matching of the coercivity and resonance fields can now be understood by considering the ferromagnetic fraction present in the system. Thus, the increasing resonance values observed, correspond to a lesser fraction of ferromagnetic domains present within the FeRh delay line. This is validated by the smaller and smaller $\Delta\Gamma$ and $\Delta\Xi$ values seen on figures [7.8] and [7.9]. This is analysed in the next sub-section.

3.3 Temperature dependency of $\Delta\Gamma$ and $\Delta\Xi$ at resonance

On figure [7.15] are represented the temperature evolution of the maximum SAW velocity variation $\Delta\Xi$ (resp. **left**), and the maximum SAW amplitude attenuation $\Delta\Gamma$ (resp. **right**), at the resonance fields and for the three excited SAW frequencies. For both sets of data, it is observed that the three frequencies have similar temperature dependencies. On the velocity variations, there is a constant value, until ≈ 60°, which actually corresponds to the beginning of the FM-to-AFM phase transition. Then a rapid decrease in $\Delta\Xi$ values are observed. For the amplitude measurements, the SAW attenuation is observed to decrease right from the beginning of the cooling ramp.

From figure [7.14], it is seen that for the cooling branch, the FM-to-AFM phase transition begins at ≈ 60°C. So why on figure [7.15], a decrease in $\Delta\Gamma$ is observed even before the beginning of this transition? A discussion is necessary and here, a tentative explanation for the different behaviours of the amplitude attenuation and relative velocity variation is given. Figure [7.16] is a schematic illustration of SAWs scattering on FM-FM FeRh domains. The left IDT excites the SAW, which propagates, interacts and is scattered on the FM domains, and picked up by the second IDT on the right. In chapter [2], it has been shown that the sample is fully polycrystalline with no texture. So, at high temperature, even if the sample is fully ferromagnetic, for high magnetic field all the magnetic moments are aligned. However, once the magnitude of the field is reduced, and reaches the coercive field, domains with reverse

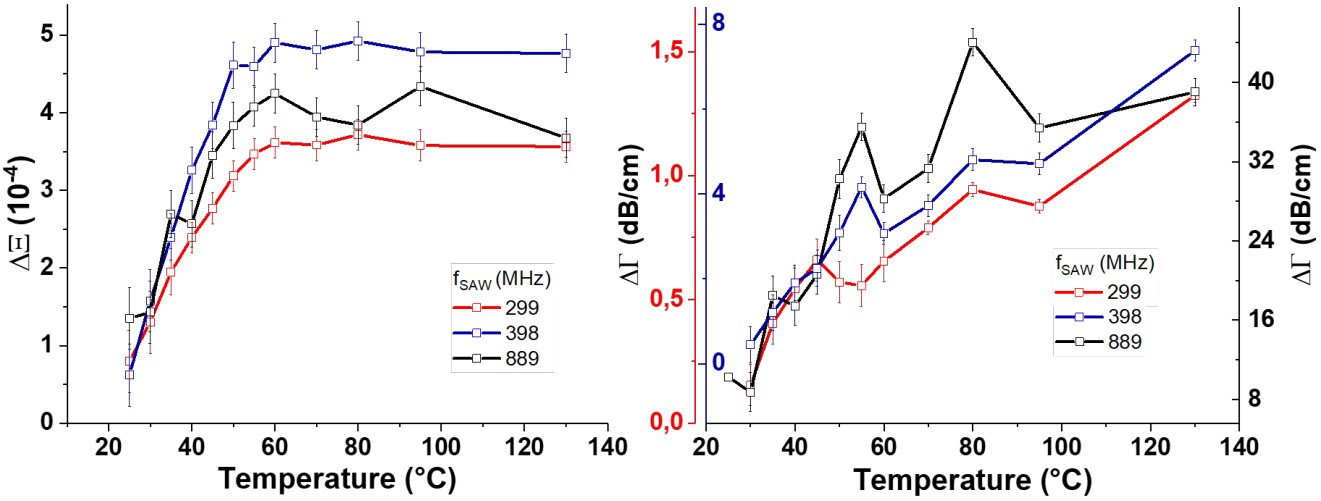

Figure 7.15: Evolution of the maximum velocity variation $\Delta\Xi$, and the maximum amplitude attenuation $\Delta\Gamma$, with respect to temperature and for the three excited SAW frequencies.

magnetisation appear. This could cause the SAWs to scatter on these FM-FM domains and FM-FM domain walls, and attenuate the SAW amplitudes. On the other hand, for the velocity measurements, the IDT geometry (parallel to each other across the delay line), forces the measured SAWs to have a similar wave-vector direction as the emitted k_{SAW}. Indeed, the parallel IDT geometry does not allow the measurement of the schematically represented wave-vector k''_{SAW} and k'''_{SAW}.

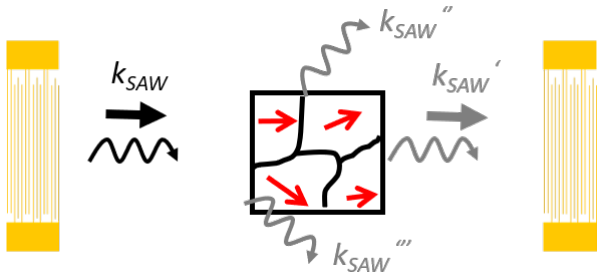

Figure 7.16: Schematics of a possible scattering of the SAWs on FM-FM domains and FM-FM domain walls, due to misalignment of each of the polycrystalline domains, with respect to the total magnetisation. This scattering affect only the SAW amplitude, as a measurement of the relative velocity variation is a measure of the signal SAW wave-vector, represented here by k'_{SAW}.

However, this is not the main explanation. The data of figure [7.15] are re-plotted on figures [7.17] and [7.18], with only the 299 and 889 MHz are considered. These are superposed to the evolution of the ferromagnetic fraction with respect to temperature seen before.

$$\Delta\Gamma \quad \propto \quad \frac{\alpha V_0}{{V_{SAW}}^3}\left(\frac{{\omega_{SAW}}^2}{{B_{SAT}}^2} - \gamma^2\right) \tag{7.5}$$

On figure [7.17] are represented the SAW attenuation maximum depth with respect to temperature, and eqn. [7.5] is the dependence of $\Delta\Gamma$ obtained previously. When the sample is cooled from the FM phase down to the AFM phase, T $\searrow \Leftrightarrow V_{SAW} \nearrow$. Here, the attenuation depth depends $\propto$ - $1/{V_{SAW}}^3$, and thus is seen to decrease extremely fast.

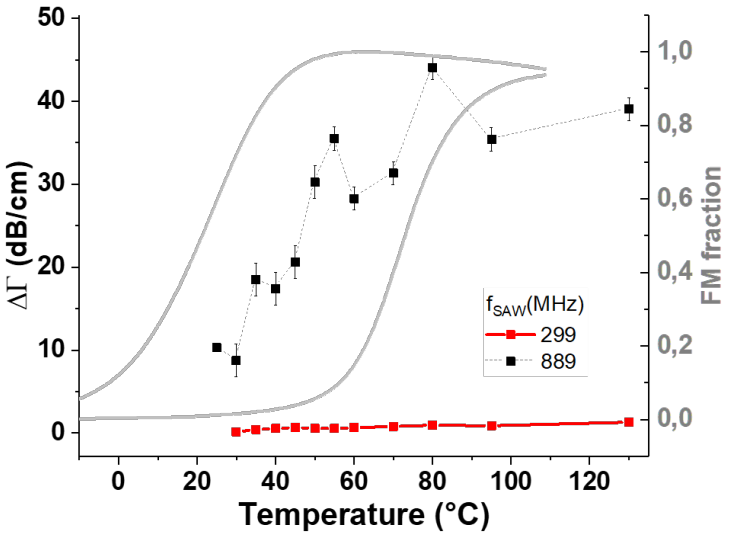

Figure 7.17: SAW amplitude resonance depth with respect to temperature for the 299 MHz and 889 MHz SAW frequencies: **left-**axis. The 889 MHz signal is huge compared to the lower frequency, i.e; the SAW has been greatly attenuated as seen before at 130°C. This evolution has been plotted with a dotted line, since it is not a monotonous decrease, but has rather a jigsaw-type evolution. On the **right-**axis is represented the ferromagnetic fraction measured from the velocity measurements (c.f. chapter [6]).

This decrease in V_{SAW} comes from the difference in elastic constants with respect to temperature (c.f. Chapter [4], section [5.2]) , and thus varies immediately when the sample is cooled. In other words, the change in elastic constants with respect to temperature, occurs even before the transition, although it has been demonstrated that a jump exists between the FM and AFM phases (c.f. chapter [4]).

Second point, the frequency dependency is also included in the ${\omega_{SAW}}^2$ term. Increasing the frequency for the same delay line results in significant increase in SAW-FMR and thus larger SAW attenuation resonance depth, $\Delta\Gamma$. This is a well-known effect of SAW-FMR experiments [17], [26], [229], [230].

Similarly, the $\Delta\Xi$ evolution of the relative velocity measurements are plotted with respect to the temperature for the two frequencies, as seen on fig. [7.18]. Here, two terms are important, the ferromagnetic fraction x_{FM} and the Rayleigh velocity V_{SAW}. Comparing the latter with the dependency of $\Delta\Gamma$, it can be observed that : $\frac{1}{V_{SAW}^3}$ decreases faster than $\frac{1}{V_{SAW}^2}$, for decreasing temperature. Coupling this dependency with SAW attenuation sensitivity to SAW scattering on FM-FM domains, AFM-FM domains and domain walls might explain the difference between the $\Delta\Gamma$ and $\Delta\Xi$ evolution.

$$\Delta\Xi \quad \propto \quad x_{FM}\frac{M_s}{{V_{SAW}}^2 B_{SAT}} \tag{7.6}$$

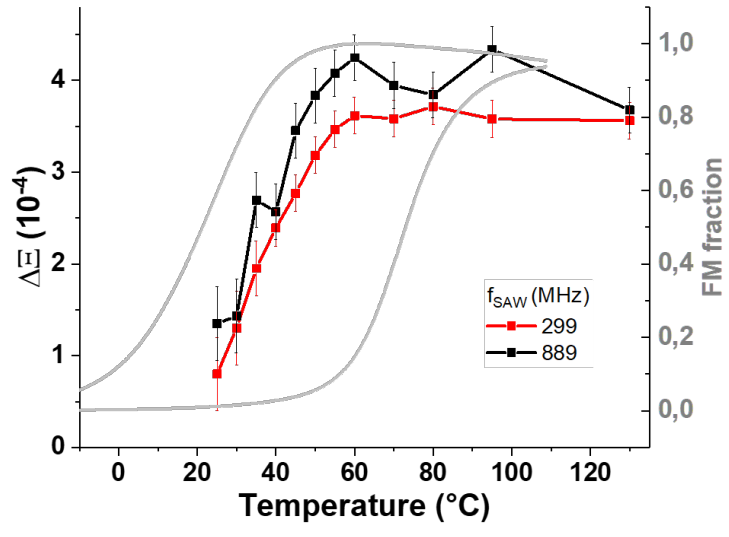

Figure 7.18: SAW relative velocity variation resonance depth with respect to temperature for the 299 MHz and 889 MHz SAW frequencies: **left-**axis. The frequency dependence is quite similar, with a change occurring around 60°C. On the **right-**axis is represented the ferromagnetic fraction measured form velocity measurements (c.f. chapter [6]).

The only dependency of $\Delta\Xi$ on the frequency is how V_{SAW} depends on the frequency. Remember, as seen in Chapter [4], section [5.2], the FeRh/Ta/GaAs tri-layer system is dispersive, as $f_{SAW} \nearrow \Leftrightarrow \frac{1}{V_{SAW}^2} \nearrow$, albeit less than the $\Delta\Gamma$ dependence. More importantly, it is observed that for the velocity, the resonance depths are constant down to $\approx 60°C$, which corresponds to the beginning of the FM-to-AFM phase transition, and thus a change in the ferromagnetic fraction x_{FM}. $\Delta\Xi$ being proportional to x_{FM}, this explains that the decrease of $\Delta\Xi$ with temperature starts only upon the beginning of the FM-to-AFM phase transition, in contrats to the behaviour of $\Delta\Gamma$.

4 Modelling SAW-FMR with B parallel to k_{SAW} in the FM phase

As developed in great details in chapter [5] section [4], the SAW-FMR interaction can be understood mathematically and modelled numerically. In this section, the reader is introduced to the results of the numerical modelling, in the case where the magnetic field is applied parallel to the direction of propagation of the SAWs, i.e. for $\phi_B = 0°$.

4.1 Modelling FMR with magnetic hysteresis

One of the conundrum arising from modelling a SAW-FMR model corresponding to our system is the evolution of the magnetic equilibrium angle $\phi_{M_{eq}}$ with respect to the magnetic field. For typical SAW-FMR model, i.e. where the magnetic hysteresis is not taken into consideration, $\phi_{M_{eq}}$ is obtained by minimising the total magnetic energy and looking for a global minimum. However, this approach does not yield the magnetic hysteresis. Instead, the magnetic equilibrium angle $\phi_{M_{eq,i}}$, should be calculated by iteration coming from the previous $\phi_{M_{eq,i-1}}$ and so on, when varying the magnetic field. While doing so, the nature of the coercivity needs to be discussed: is the 3.5 mm long FeRh delay line taken to be a single macro-spin, and thus the single magnetisation switching is observed or should the delay line be divided into weighted ferromagnetic domains each pointing either to the left or to the right. A discussion is necessary.

4.1.1 Approach 1: The Macro-spin Modelling

This is illustrated on figure [7.19]. In the macro-spin model or simply the Stoner-Wolfarth model, the sample is considered as a single magnetic domain (a macro-spin), with a single magnetisation vector, represented by the vector **M**. Varying the magnetic field from + 20 mT to - 20 mT, the magnetisation switching is modelled as a sharp jump at the coercivity: B_c = - $\frac{2K_{eff}}{M_s}$ here, where K_{eff} is the effective magnetic anisotropy considered present in the FeRh sample.

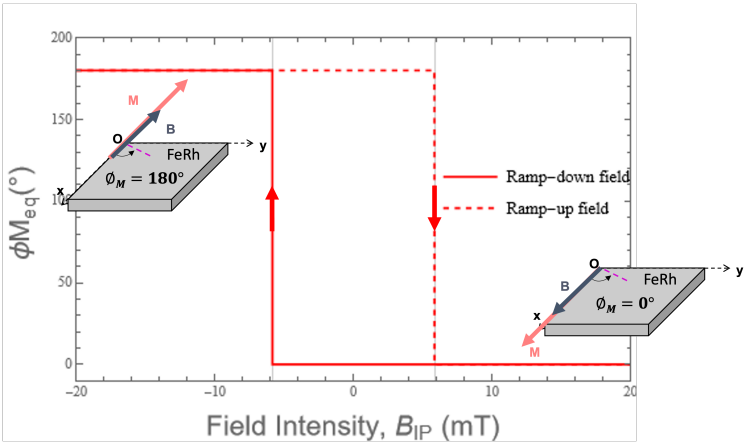

Figure 7.19: Illustration of a square hysteresis cycle for the magnetic field applied along $\phi_H = 0°$. For + 20 mT, the magnetic equilibrium angle lies along $\phi_M = 0°$. If the field is applied at 180°, and its magnitude varied, the magnetisation switches at $\approx$ - 6 mT, which represents the coercive field of the sample. In this macro-spin model, the switching is sharp.

Note, the sharp jumps at the coercivity, $\pm$ B_c. Recall, this magnetic equilibrium angle is fed into the second derivatives of the energy, $E_{\theta\theta}$ and $E_{\phi\phi}$. The FMR power is given by:

$$\Delta P_{FMR} = \frac{i\,\omega_{SAW}\,M_s\,V_0}{2}\left(|b_\theta|^2\chi_{11} + |b_\phi|^2\chi_{22} + (b_\phi b_\theta{}^* - b_\theta b_\phi{}^*)\chi_{12}\right) \tag{7.7}$$

where the Polder susceptibility terms are given by :

$$\bar{\chi} = \begin{bmatrix} \chi_{11} & \chi_{12} \\ \chi_{21} & \chi_{22} \end{bmatrix} = \frac{\gamma}{D} \begin{bmatrix} \gamma \frac{E_{\phi\phi}}{M_s} (\mathbf{k}_{SW}) - i\alpha\,\omega_{SAW} & -i\omega_{SAW} \\ i\omega_{SAW} & \gamma \frac{E_{\theta\theta}}{M_s} (\mathbf{k}_{SW}) - i\alpha\,\omega_{SAW} \end{bmatrix} \tag{7.8}$$

and with

$$\begin{cases} D = -(1+\alpha^2)\left(\omega_{SAW}^2 - \omega_0^2 + i\kappa\,\omega_{SAW}\right) \\ \omega_0^2 (\mathbf{k}_{SW}) = \dfrac{1}{{M_s}^2} \dfrac{\gamma^2}{\alpha^2+1} \left[E_{\theta\theta} (\mathbf{k}_{SW}) \times E_{\phi\phi} (\mathbf{k}_{SW})\right] \\ \kappa = \dfrac{\gamma}{M_s} \dfrac{\alpha}{\alpha^2+1} \left[E_{\theta\theta} (\mathbf{k}_{SW}) + E_{\phi\phi} (\mathbf{k}_{SW})\right] \end{cases} \tag{7.9}$$

This model works nicely to obtain $\Delta\Gamma$ and $\Delta\Xi$ numerically.

On figure [7.20] is represented the experimental data obtained previously for the 299 and 889 MHz SAWs. Now, these data are compared to the numerical modelling, seen in chapter [5] section [5.2], i.e. for a cubic anisotropy, with $\phi_u = \phi_B = 0°$. This means both the magnetic easy-axis and magnetic field are directed along the direction of propagation of the SAW. The numerically obtained SAW amplitude attenuation and relative velocity variations are represented on figure [7.23]. Table [7.1] summarise the relevant parameters for the numerical analysis. The strain components averaged over the 270 nm-thick FeRh layer, calculated by V. Laude are implemented here:

f_{SAW} (MHz)	k_{SAW} (μm^{-1})	$< \varepsilon_{xx} > (\times 10^{-4})$	$< \varepsilon_{xz} > (\times 10^{-4})$	$< \Omega_{xz} > (\times 10^{-4})$
299	0.654	0.34	0.06	1.14
398	0.873	0.44	0.11	1.55
889	1.963	0.74	0.66	3.68
$M_s = 1.447 \times 10^6$ A/m		$K_c = 3 \times 10^3$ J/m^3		$\gamma = 1.7 \times 10^{11}$ Hz/T

Table 7.1: Relevant parameters implemented in the SAW-FMR modelling seen below.

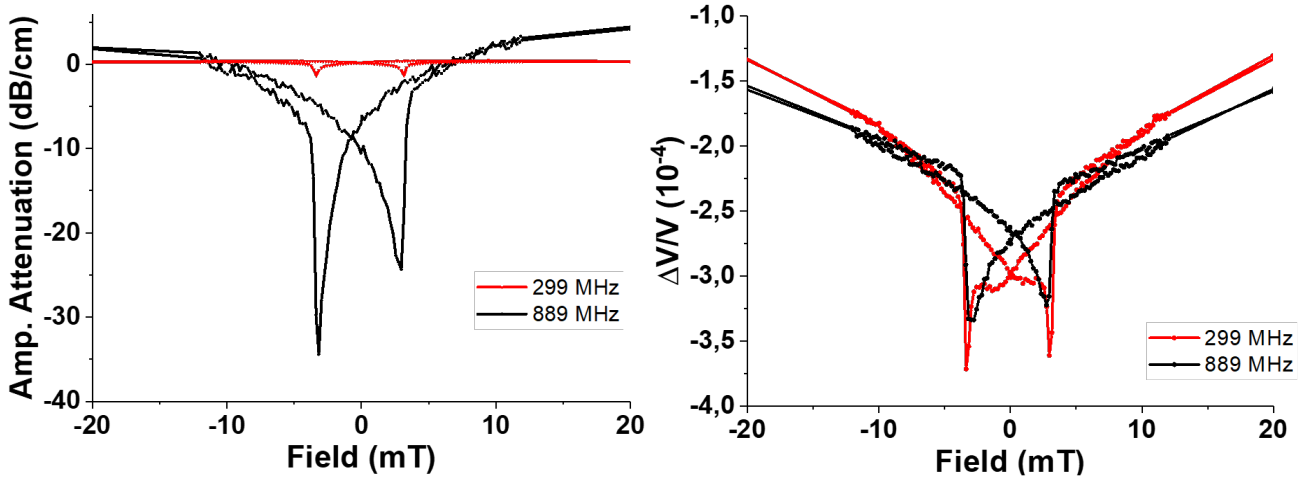

Figure 7.20: Experimental data for the SAW amplitude attenuation and the SAW relative velocity variations for the 299 and 889 MHz SAWs.

The model is seen to reproduce well the experimental data, with in particular a weak variation of $\Delta\Xi$ with the SAW frequency, and a much stronger variation with frequency for $\Delta\Gamma$. Note that on the phase variation, the increase in the variation observed previously, which starts way up from the resonance field is observed on the numerical model as well. Second point, coming from - B_{SAT} to + B_{SAT}, for all figures, the variations are gradual, followed by a jump towards the non-hysteretic part of the curve.

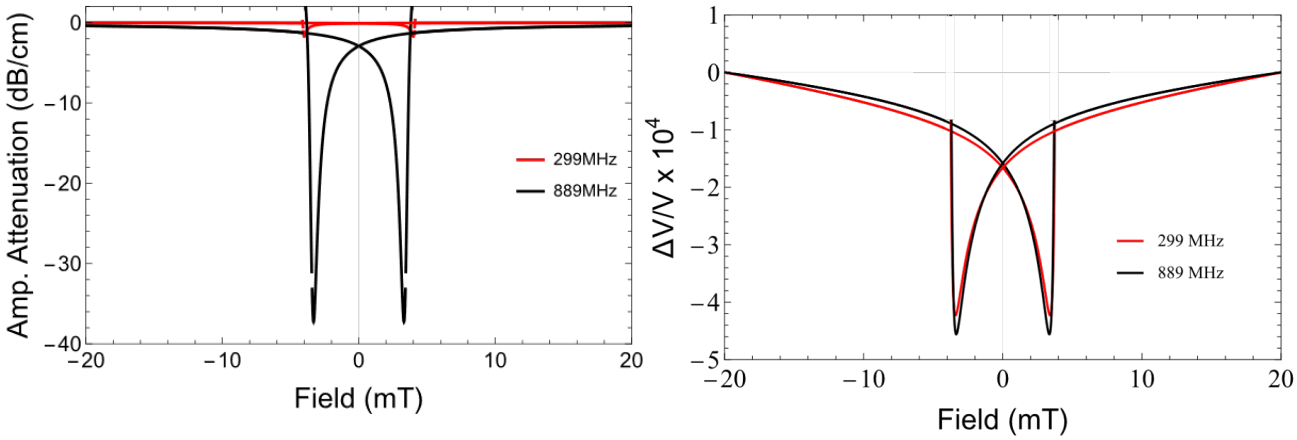

Figure 7.21: SAW amplitude attenuation and the relative velocity variations for the 299 MHz and 889 MHz SAW frequencies, calculated numerically.

One difference visible between the experimentally measured data, and the numerical model is that numerically there is no non-reciprocity in the depth $\Delta\Gamma$ and $\Delta\Xi$. However, although this is not represented here, this non-reciprocity can be included artificially, by including a small misalignment angle.

4.1.2 Approach 2: The multi-domain Modelling

In the second approach, the multi-domain nature of the FeRh delay line is taken into consideration. It is recalled, that the delay line is 3.57 mm long and the SAWs are excited by $\approx$ 200 μm wide IDTs. Hence, magnetically this is not a single macro-spin. Moreover, on LMOKE measurements (to be discussed in sub-sections [6.1.1] & [6.1.1], averaged over an area of 200 $\times$ 220 μm^2 with a light penetration depth of $\approx$ 10 nm), it is shown that the sample clearly does not behave as a macrospin, but exhibits filament-like domains of length $\approx$ 150-250 μm. Thus for SAWs propagating along the delay line, they encounter several magnetic domains with magnetisation directed differently. The coercivity of the sample cannot simply be taken as $B_c = \pm \frac{2K_{eff}}{M_s}$, where K_{eff} is the magnetic anisotropy of the whole 3.5 mm delay line.

Instead, at the coercivity, there is n% of domains pointed towards $\phi_B = 0°$, while (1-n)% domains pointed towards $\phi_B = 0° + 180°$. This hysteretic n% is then modelled using an error function centred on the experimentally observed 130°C coercive field (3.7 mT for delay line 1 and 2.4 mT for delay line 2). This is a much more physically correct approach towards the SAW interaction with the FeRh layer, and not usually taken into consideration in the literature, where authors take thin layers several mm^2 to behave like macro-spin system. An example of the multi-domain approach hysteresis is illustrated on figure [7.22] (note the error function is multiplied by the equilibrium angle here and is not $\in$ [0,1]). At 15 mT, a field value larger than coercivity, all the magnetic domains point towards $\phi_B = 0°$ here. Only two domains are considered for simplicity. if the field is applied at 180°, at the coercivity only half the domains have switched- as illustrated. The new coercive field value is less than $\pm \frac{2K_{eff}}{M_s}$.

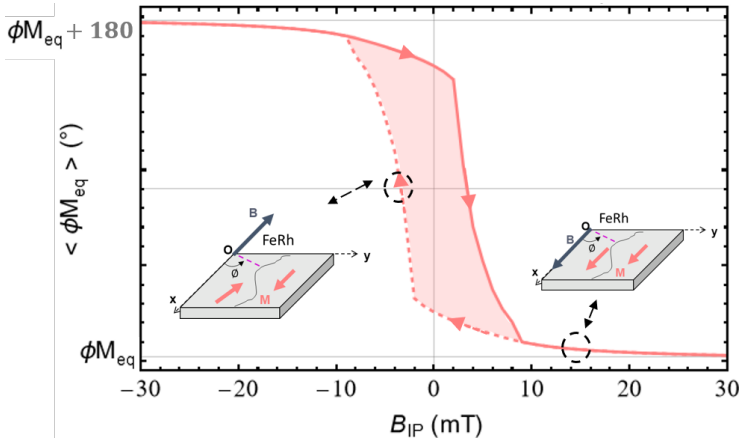

Figure 7.22: Illustration of a multi-domain approach to the magnetic hysteresis. For simplicity, only two domains have been represented. At high field, larger than coercivity, the two magnetic domains point to $\phi_B = 0°$. If the magnetic field is applied at 180°, at the coercivity, $B_c < \frac{2K_{eff}}{M_s}$, and only half of the domains have switched towards the magnetic field.

The multi-domain approach is applied to the numerical modelling of the SAW-FMR. The Relative velocity variation (c.f. equation [5.36] and the SAW amplitude attenuation (c.f. equation [5.34]) are now given by:

$$\Delta\Gamma \approx 20 \log \exp\left(\frac{n\,[\Im\Delta k_{SAW}(\phi_{M\rightarrow})L] - (1-n)\,[\Im\Delta k_{SAW}(\phi_{M\leftarrow})L]}{2\,L\,P^0_{SAW}}\right) \tag{7.10}$$

$$\frac{\Delta V}{V} \approx -\frac{n\,\Re\,[\Delta k_{SAW}(\phi_{M\rightarrow})] - (1-n)\,\Re\,[\Delta k_{SAW}(\phi_{M\leftarrow})]}{k_{SAW}} \tag{7.11}$$

where n defines the fraction of the domains as given before, and $\phi_{M\pm}$ the magnetisation equilibrium angles. Using the weighting contribution of the domains on the real and imaginary parts of the change of the SAW vector k_{SAW}, the amplitude attenuation and relative velocity variation can be calculated numerically and are given on figure [7.23]. This multi-domain numerical calculation was performed by L. Thevenard. As seen, the model works fairly well in the case of $\phi_B = 0°$. Moreover, the two approaches work, and the shape of the amplitude attenuation and $\Delta V/V$ are fairly well reproduced. Nevertheless, the second approach is physically a much more appropriate description of what the SAWs encounter during their propagation across the FeRh delay line.

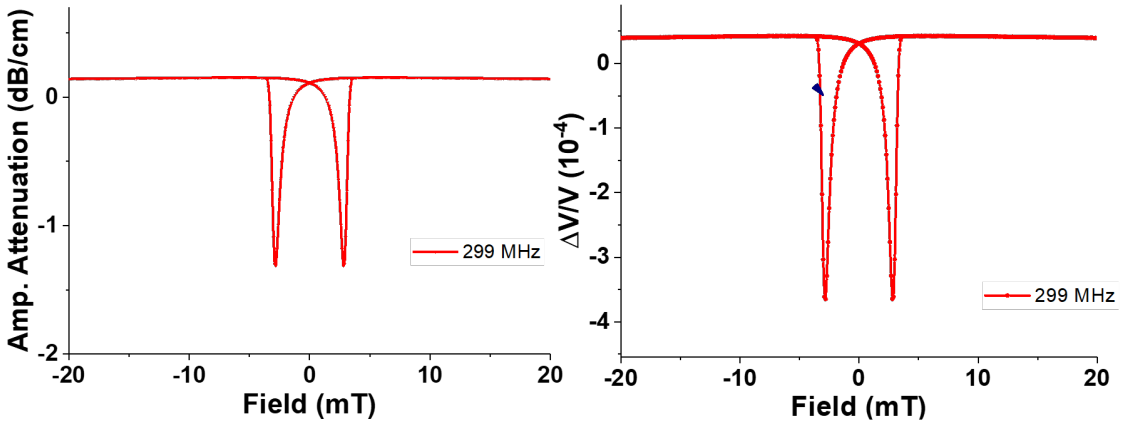

Figure 7.23: SAW amplitude attenuation and the relative velocity variations for the 299 MHz SAW frequencies, calculated numerically for the multi-domain approach. The multi-domain calculation was undertaken by L. Thevenard.

4.1.3 State of the art: Hysteretic SAW-FMR

As said in chapter [5], the hysteretic nature of samples are rarely taken into consideration when studying SAW-FMR. Although a hysteretic magnetisation switching with $\mu_0 H < \pm 3$ mT, was measured experimentally by Weiler *et al.* on Ni/LNO, it was not attributed to SAW-FMR interaction and was not considered [17].

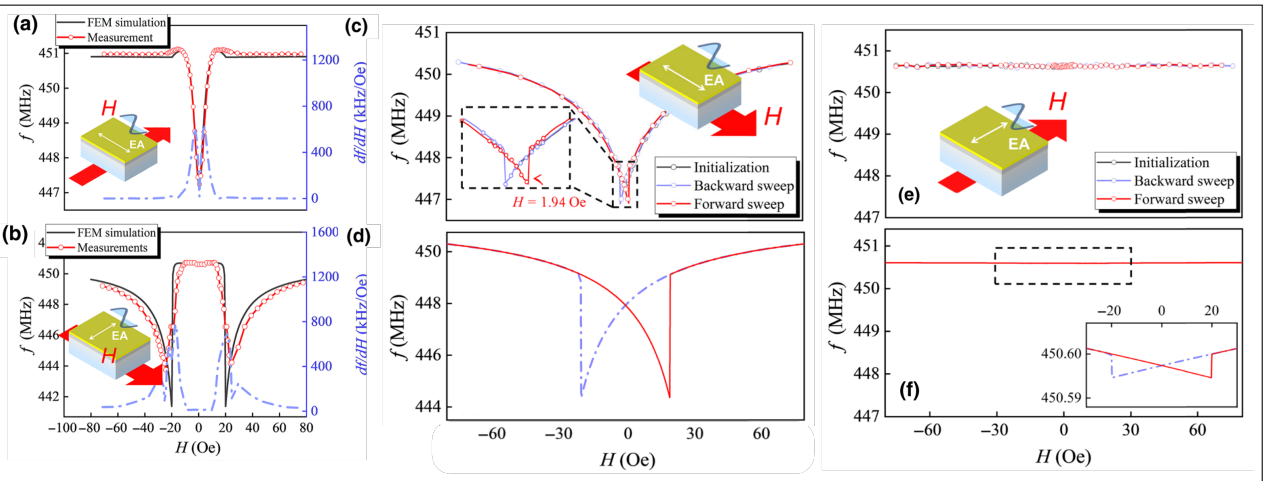

Figure 7.24: Fig. **(a),(c),(d)**-sample with uniaxial anisotropy along $\phi_u = 0°$, while for Fig. **(b),(e),(f)**-sample with uniaxial anisotropy along $\phi_u = 90°$. Fig **(a)-(b)**-Field applied along Hard-Axis leading to softening of SW eigen-frequency. Fig **(c)-(d)**-Field applied along Easy-Axis. Softening at the coercivity is due to the competition between the Zeeman and dipolar contribution. Adapted from [248]

While going through the literature, we nevertheless came across a fairly recent paper exploring magneto-acoustic coupling using Love-mode SAWs on Fe-Co-Si-B. These results are given on figure [7.24]. Note here, the ferromagnetic layer is deposited entirely on the IDT with reflector grating on either side, i.e. the SAW is confined and does not propagate over a FM delay line/mesa. The authors fabricated six samples with in-plane uniaxial anisotropy ϕ_u, directed along different angles between the easy-axis and k_{SAW}. We focus on $\phi_u = 0°$ (fig. **(a),(c),(d)**) and $\phi_u = 90°$ (fig. **(b),(e),(f)**). For the field applied along a Hard axis, (fig **(a)-(b)**), it is known that the SW eigen-frequencies can be softened. For $\phi_u = 0°$ the attenuation is at zero-field, while for $\phi_u = 90°$, there is a shift in the softening due to the in-plane dipolar contribution. Now, if the field is applied along the Easy-Axis (where the SW eigen-frequency can only increase) **(c) to (f)**, a frequency shift in the softening is seen to $\pm$ 1.94 Oe, for $\phi_u = 0°$. This softening is attributed to the Zeeman energy term in the dynamic magnetoelastic model, which is enhanced by a parallel applied field and reduced by an anti-parallel one, similar to our model. On the other hand, for $\phi_u = 90°$, almost no observable frequency response are seen, leading to a much weaker magneto-elastic coupling in this geometry, which is normal. Moreover the authors developed a Finite Element Method simulation to investigate and confirmed the validity of the magneto-elastic interaction **(d)-(e)**. The differences in the frequency responses for $\phi_u = 0°$ and $\phi_u = 90°$ are primarily due to the initial orientation of the magnetic moments and the resulting dipole fields. If the initial magnetic moment orientation aligns with the applied magnetic field, this leads to a strong magnetoelastic coupling. This alignment enhances the Zeeman, causing significant frequency shifts and observable jumps in the resonance frequency as the magnetic moments flip at the coercive fields. In contrast, for $\phi_u = 90°$, the initial magnetic moment orientation is perpendicular to the applied magnetic field. This orientation results in a large dipole field that counteracts the applied magnetic field. Consequently, the magnetoelastic coupling is significantly attenuated, leading to a much weaker frequency response.

Note, in the eighties, Feng *et al.* also investigated the hysteretic nature of the magnetic susceptibility (parallel and perpendicular to the applied field) and how it impacted the SAW amplitude attenuation on polycrystallline Nickel [196]. The susceptibility calculations were performed using the Stoner-Wohlfarth model. They also investigated this interaction by changing the direction of the applied magnetic field.

In the next section, we go beyong the $\phi_B = 0°$ geometry, and investigate angular-SAW-FMR as well.

5 Angular SAW-FMR at 130°C

In this section, the angular dependence of the SAW-FMR (a-SAW-FMR) interaction is studied. As the SAW propagation direction is fixed by the IDT configuration along the crystallographic [110] direction on GaAs, the magnetic field angle ϕ_B, is taken with respect to [110]. The experiments are measured using the same procedures as before, i.e. by varying the field from an out-of-resonance field and ramping to and out of resonance. Firstly, using the magneto-effective fields derived in Chapter [5], the expected angular dependency is studied. Then, attention is directed towards the a-SAW-FMR data in the fully FM phase (at 130°C) for the 299 MHz SAW. This is followed by the complete analysis and discussion of the amplitude attenuation and relative velocity variations for the three excited SAW frequencies on the Polycrystalline Sample B: FeRh/GaAs.

Note, whereas these experiments were initially meant to check that we have no magneto-elastic coupling (and consequently no SAW-FMR signal), when the field is applied perpendicularly to k_{SAW}, they revealed a very unexpected behaviour which prompted a full angular SAW-FMR study.

5.1 Angular dependency of the magneto-elastic effective fields

The magneto-elastic effective driving fields are recalled here:

$$b_\theta = \underbrace{\frac{2B_2}{M_s}\,\varepsilon_{xz}\,\cos(\phi_M)}_{b\varepsilon_{xz}} + \underbrace{\mu_0\, M_s\, \Omega_{xz}\,\cos(\phi_M)}_{b\Omega_{xz}} \tag{7.12}$$

$$b_\phi = \underbrace{\frac{2B_1}{M_s}\,\sin(\phi_M)\cos(\phi_M)\,\varepsilon_{xx}}_{b\varepsilon_{xx}} \tag{7.13}$$

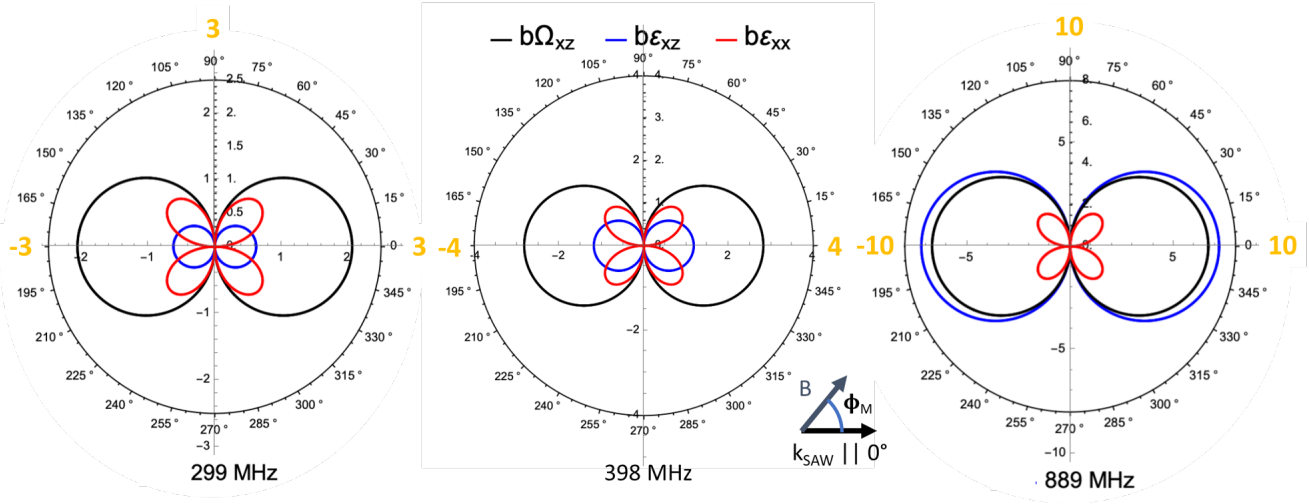

Figure 7.25: Calculation of the angular dependency of each term of the magneto-elastic effective field. Here, the average over the thickness of the FeRh layer, is taken for the linear and rotational components. The major contribution is thus seen to originate from the magneto-rotational term: Ω_{xz}. Parameters: $B_2 = 7.9\times10^6$ J/m^3 and $B_2 = -2B_1$.

The mean values of the strain components are given in Table [7.1]. The different contributions to the magneto-elastic fields coming from each strain components are given on figure [7.25]. Note the difference in scales between the three frequencies (299 MHz [-3,3]; 398 MHz [-4,4] and 889 MHz [-10,10]). For $\phi_B = \phi_M = 0°$, the case studied before, the ε_{xx} contribution is zero. Now, if the field is no longer parallel to k_{SAW}, the ε_{xx} contribution adds up, with a maximum at 45°. However, as seen on the figure, this contribution is of the same order as those coming from the ε_{xz} except in the 889 MHz signal. These aptly illustrate the thickness dependence of the strain components. At f_{SAW}, ε_{xz} contribution is small, while at $3f_{SAW}$, this contribution is no longer negligible. Moreover, at $3f_{SAW}$ even

if ε_{xz} is just 1/6 of Ω_{xz} (c.f. Table [7.1]), their respective contribution to the driving fields are similar, as $B_2 > M_s$. At 889 MHz, this contribution is of the same order as the rotational strain term. Angle wise, for $\phi_B = \phi_M = 90°$, at three contributions go to zero for all three frequencies. Hence, if the field is high enough for the equilibrium magnetisation angle to lie parallel to the field, no magneto-elastic interaction is expected for $\phi_M = 90°$.

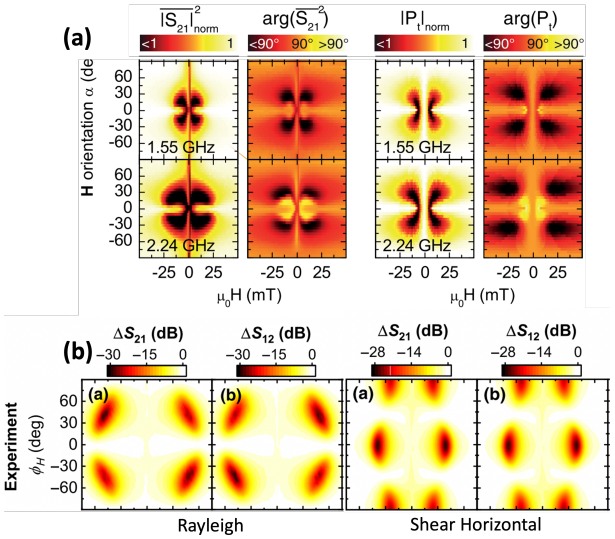

Figure 7.26: **(a)**: SAW transmission versus magnetic field for different magnetic field orientations, in the case of a Rayleigh wave. Adapted from [17]. The first two columns are experimental data, while the last two correspond to a numerical model based on the SAW-FMR power transfer approach. For a Rayleigh wave, considering only the ε_{xx} components, the magneto-elastic interaction has a four-fold symmetry, with maximum at 45°. **(b)**: Similarly, Kuß *et al.* investigated the magneto-elastic field symmetry in the case of Rayleigh and shear-horizontal SAWs, on Nickel. Adapted from [249].

The angular dependency of magneto-elastic interactions is an important feature (c.f. Chapter [5], and has been studied extensively by several groups namely, Weiler *et al.* [17], Dreher *et al.* [18], Thevenard *et al.* [250] and Kuß *et al.* [249]. Figure **(a)** illustrates the SAW transmission as a function of the magnetic filed and its orientation for a 50 nm-thick Ni on LNO sample [17]. On the first two columns are given the experimental data, while the remaining two are numerical calculation of the transmitted SAW power, similar to the power transfer method of SAW-FMR interaction, implemented in this manuscript. The black coloured regions correspond to SAW transmission, i.e. SAW-FMR interactions. Here, only the ε_{xx} contribution was considered. This is reflected on the 4-fold symmetry of the magneto-elastic interaction (c.f. equation [7.13]). Likewise, Kuß *et al.* measured transmission spectra of a 4.47 GHz SAW using vector network analyzer (VNA) on a 10-nm thick Ni film [249]. The transmission spectra of Rayleigh and Shear-Horizontal waves are represented on figure **(b)**. Similar to our magneto-elastic driving fields, for the Rayleigh waves the strain components primarily include ϵ_{xx} and ϵ_{xz}, while for shear horizontal waves, the strain components ϵ_{xy} and ϵ_{yz} are significant. These components lead to different symmetries in the magnetoelastic driving fields as seen. Indeed, the magneto-elastic driving field of a shear horizontal wave is: $b_\theta = B_{yz}\sin(\phi_0)$ and $b_\phi = B_{xy}\cos(2\phi_0)$.
In the rest of the manuscript, we investigate the angular-SAW-FMR interaction on FeRh.

5.2 Amplitude attenuation and relative velocity variations at 299 MHz

In this section is presented the angular-SAW-FMR measurements, first for the 299 MHz frequency. The data at 299 MHz and 889 MHz were measured by T. Tremblais during his M1 internship. On figure [7.27] is represented the SAW amplitude attenuation and on figure [7.28], the corresponding SAW relative velocity variations. The angular variation goes from ϕ_B = - 90° to ϕ_B = + 120° by steps of $\Delta\phi_B = 7.5°$. The reference is taken from the [110] direction of SAW propagation.

The first surprising result is that the angular-SAW-FMR is resonant at all angles, i.e. contrary to the above magneto-elastic effective fields, the interaction does not cancel out at 90°. More so, the interaction does not cancel out at any given angle measured. Secondly, $\phi_B = 45°$ is not the angle to obtain maximum SAW-FMR interaction, although this point was already discussed. Indeed, the introduction of the rotational strain component in the magneto-elastic driving fields pointed more towards a maximum interaction at $\phi_B = 0°$. However, this is not observed in the experimental results.

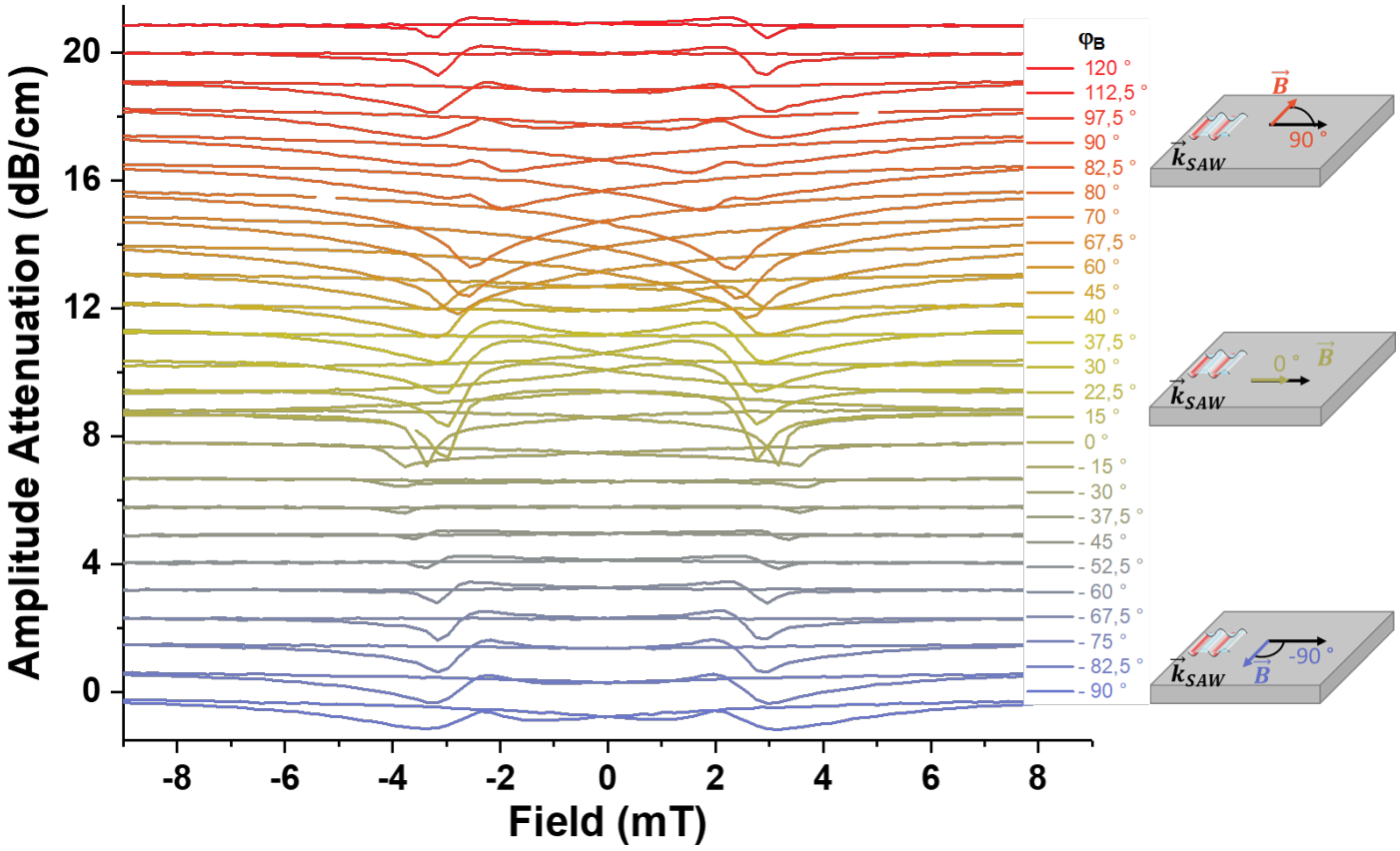

Figure 7.27: Amplitude attenuation for Angular SAW-FMR at 299 MHz.

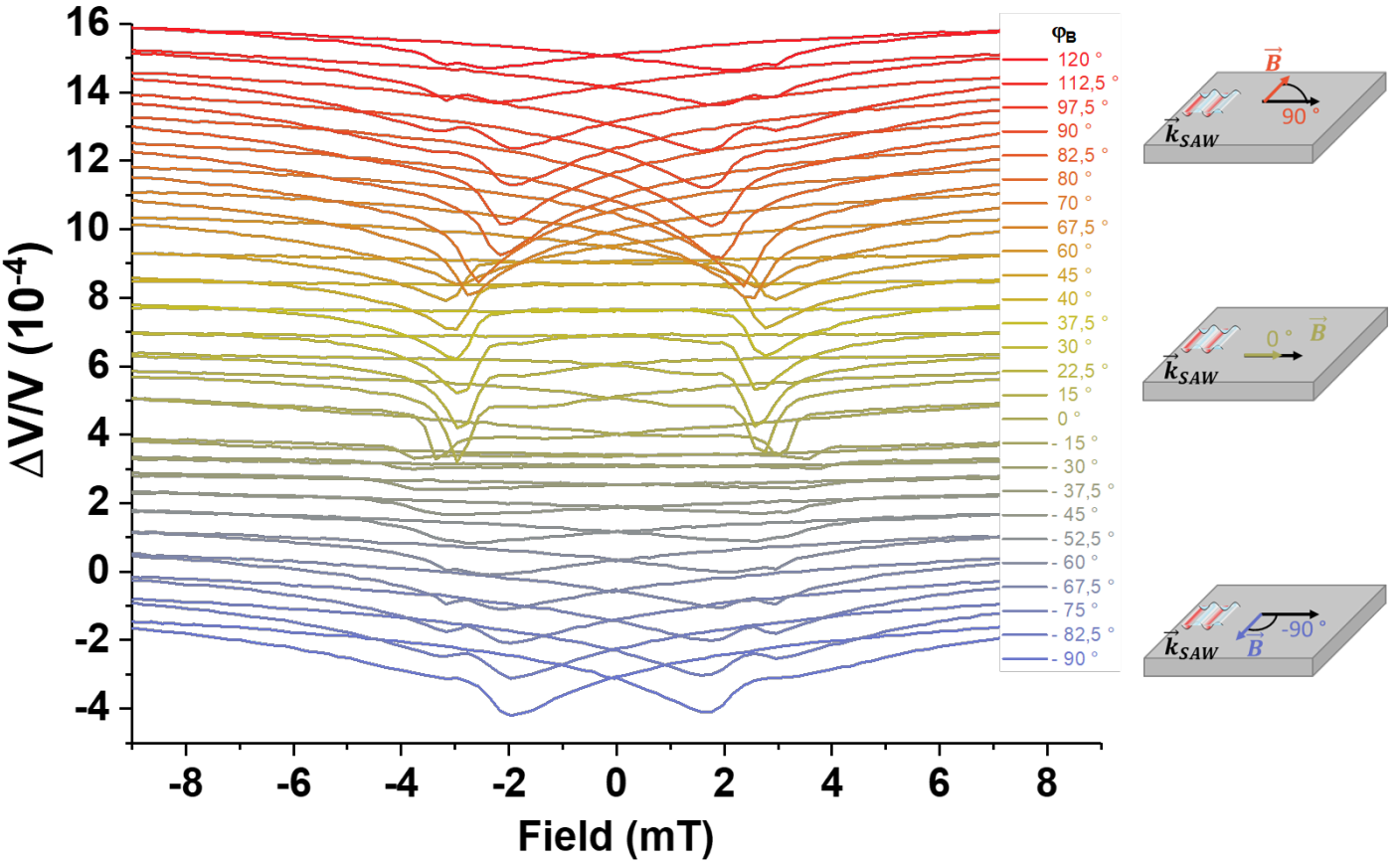

Figure 7.28: Relative velocity variations for Angular SAW-FMR at 299 MHz.

5.2.1 Angular SAW-FMR analysis

On figure [7.29] are represented some particular ϕ_B angles for analysis. On the **left:** are the complete sets of data. It is observed that the shape (defined as the envelop) towards the resonance is different. Starting from - 90° (in blue), the envelop is relatively flat, and the attenuation starts to increase only about ≈ - 50 mT (when coming from - 200 mT). For ϕ_B = - 15° and 0°, the envelop is seen to have the shoulder-like shape. For ϕ_B = 22.5°, on the other hand, this shoulder-like shape is reversed; and this is true until 40° (not-shown). As from ϕ_B = 45° up to 120°, the envelop is observed to remain flat, far from resonance fields. On the **right:** is a zoom around the resonance fields. At ϕ_B = 0°, only one pair of hysteretic resonance fields are seen with $\Delta\Gamma$ = - 1.33 dB/cm. This is true for ϕ_B = 67.5°, with $\Delta\Gamma$ = - 2.82 dB/cm. Surprisingly, at ϕ_B = - 90°, 45°, 82.5°, among others, one observes 2 pairs of hysteretic resonance fields, or in other words, 4 distinct resonance field values. At ϕ_B = 22.5°, the envelop is shaped like the derivative of a Lorentzian function, with a positive SAW attenuation value, followed by a sharp dip towards the resonance field. The SAW-FMR resonance field values, and the SAW attenuation values ($\Delta\Gamma$) with respect to the angular dependency of the magnetic field are discussed in the following sub-sections.

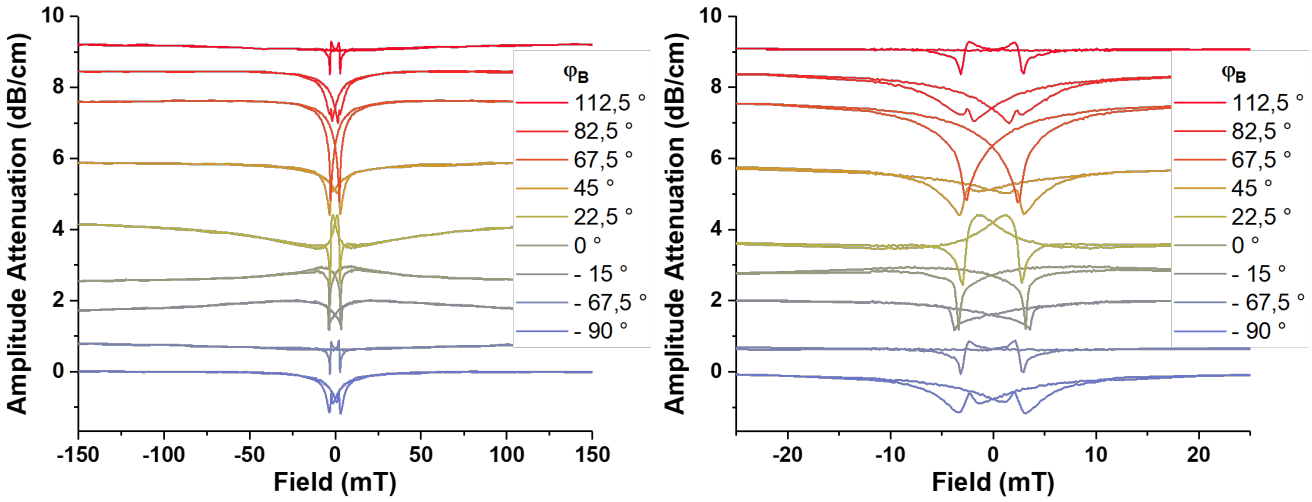

Figure 7.29: Angular SAW-FMR amplitude attenuation for a 299 MHz SAW and at a constant temperature of 130° for specific angles showcasing different SAW-FMR resonance fields and envelop signals. The **right** figure is a zoom around the resonance field values.

Similarly are represented on figure [7.30] the SAW relative velocity variation for the magnetic field applied along different directions.

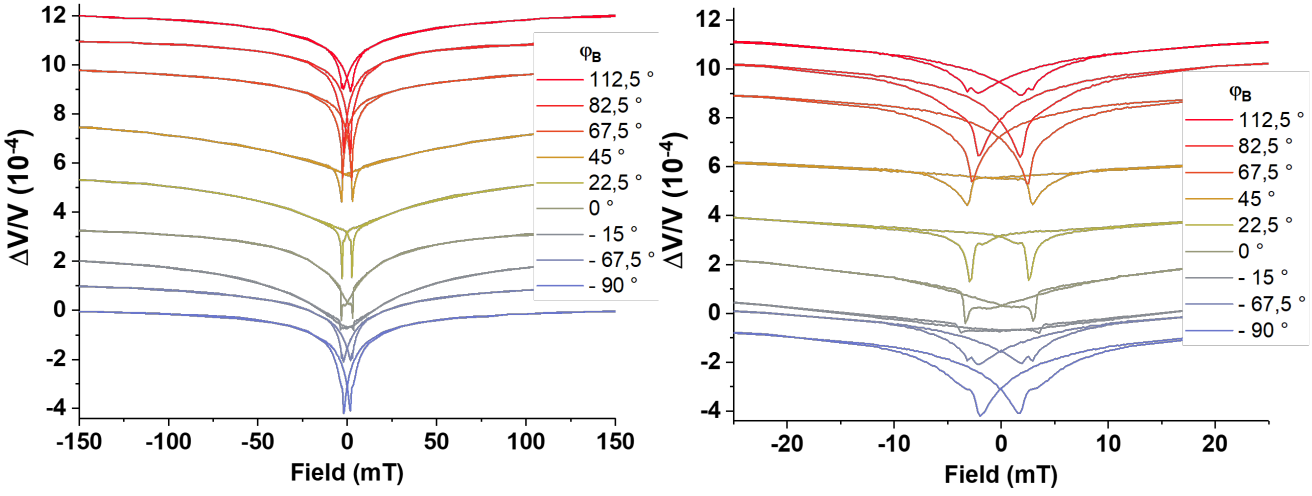

Figure 7.30: Angular SAW-FMR relative velocity variations for a 299 MHz SAW and at a constant temperature of 130° for specific angles showcasing different SAW-FMR resonance fields and envelop signals.

For the complete set of data, and as observed on the SAW-FMR dependency with temperature, there is no shoulder-like shape here. Instead, a gradual increase in the $\Delta V/V$ values are observed close to the resonance fields. This gradual increase is broadest for ϕ_B = - 15°. For the data zoom around the resonance fields, fig. **right**, it is observed that the shapes and the angles at which there are 4 resonance fields are not the same than for the SAW attenuation measurements. This is clearly demonstrated for ϕ_B = - 90°, and by comparing fig. [7.29] and [7.30]. For the amplitude measurements, 4 dips are observed, while on the phase measurements, there is like a plateau/kink following the resonance. The same is demonstrated at ϕ_B = 22.5°. For the amplitude, there is a derivative of the Lorentzian-shape, which is dissimilar to what is seen on the phase variation. It is recalled here, that a measure of the amplitude attenuation is related to the imaginary part of Δk_{SAW}, while the phase variation is related to the real part of Δk_{SAW} (c.f. the SAW-FMR modelling of Chapter [5]). Hence, there is no reasons as to why their envelop signals should be similar.

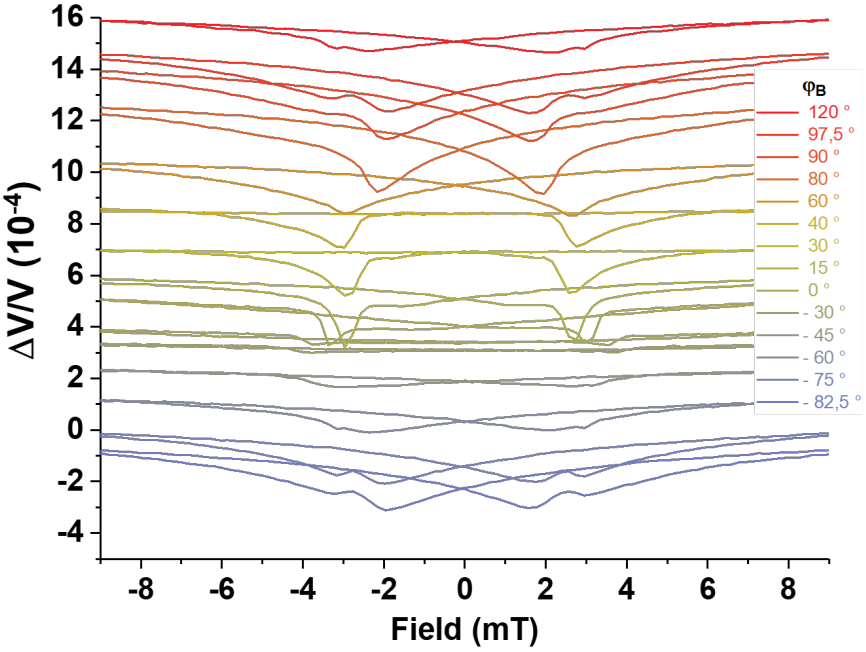

Figure 7.31: Complementary Angular SAW-FMR relative velocity variations data for the 299 MHz SAW. In contrast to the data shown on figure [7.30], the 4 resonance dips are observed. The angles ϕ_B, at which these 4 resonance dips are observed are not similar to those observed on the SAW amplitude attenuation measurements.

On figure [7.31] are represented the complementary set of data for the relative velocity variations. For ϕ_B = - 75°, two mean absolute resonance fields are observed with B_{res} = 1.86 mT ($\Delta\Xi = 3.4\times 10^{-4}$) and B_{res} = 3.06 mT ($\Delta\Xi = 3.2\times 10^{-4}$). As the angle is reduced towards 0°, one of the two resonance vanishes, and only one is observed for ϕ_B between - 60° to 0° and then from 30° to 82.5°. On the SAW relative velocity variation measurements, the four resonance fields are less pronounced compared to the SAW amplitude attenuation measurements. The angular dependence of these resonance fields are studied subsequently.

5.2.2 Angular dependence of the resonance fields measured on the amplitude and phase data sets

Using the data from figures [7.27] and [7.28]- duplicated to be plotted in the full 360° range, the mean resonance field absolute values for the SAW amplitude attenuation (resp. relative velocity variation) are plotted on polar plot in figure [7.32] (resp. [7.33]). On the amplitude measurements, the shape of the resonance field is almost like an 8-shaped with the top and bottom being at respectively, ϕ_B = - 22.5° and 157.5°. Remember, the magnetic anisotropy of this sample is still unknown at this stage. Here, the angular dependency of the resonance field tends towards an uniaxial anisotropy with ϕ_u = - 30°. Moreover, on the amplitude data, the presence of the double resonances are seen for ϕ_B = 37.5°, 45° and for ϕ_B = 82° to 120°. The largest resonant value is measured to be at $\phi_B \approx 330° \pm 7.5°$. The smallest resonance field, excluding the double resonances, is measured to be at ϕ_B = 15°. For the angles where two resonances are present, the smallest resonance field is obtained for ϕ_B = 105°.

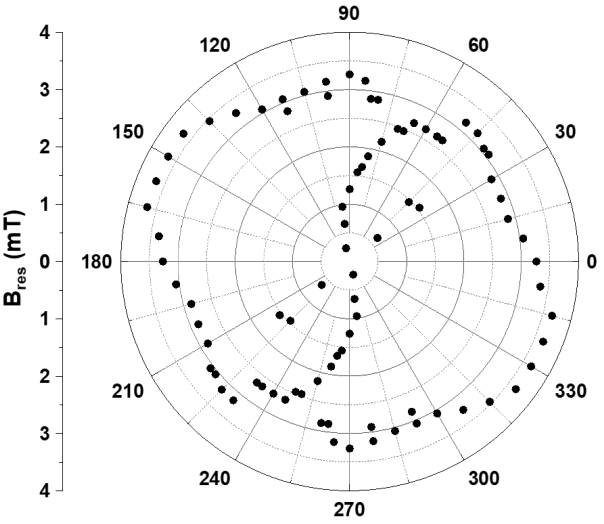

Figure 7.32: Resonance fields measured on the SAW amplitude attenuation measurements with respect to ϕ_B symmetrised over the 4 quadrants. The existence of the second resonance is measured to be exclusively for ϕ_B = 37.5°, 45° and for ϕ_B = 82° to 120°. The field is maximum for $\phi_B \approx$ - 30°.

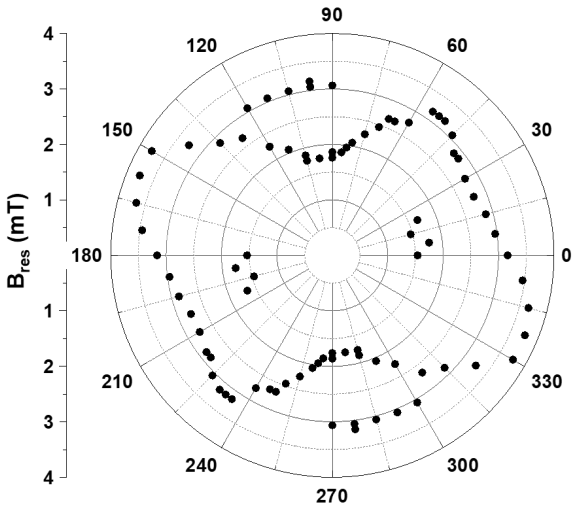

Figure 7.33: SAW Velocity resonance fields with respect to ϕ_B symmetrised. Here the existence of the two resonance fields are for ϕ_B = 0° to 22.5° and for ϕ_B = 90° to 120°. The largest field value is obtained for ϕ_B $\approx$ 337.5° as well, with a clear minimum for ϕ_B = 97.5°, whereby the second resonances are visible.

On the phase measurements, the double resonances are measured on two disjointed angular ranges for ϕ_B = 0° to 22.5° and then for ϕ_B = 90° to 120°. The largest measured resonance field value is for ϕ_B = 337.5° ($\approx$ - 22.5°), while the smallest out of double resonances is measured to be for ϕ_B = 30°. In the presence of double resonances, the smallest resonant field is measured to be at ϕ_B = 97.5°. In order to understand the angular dependencies of the amplitude attenuation and relative velocity variations, the three frequencies are compared with respect to each other, while still in the polar coordinates.

5.3 SAW-FMR attenuation and relative velocity variations for 3 frequencies

In this section, a comparison is done for the three excitable SAW frequencies. First, the raw data are given, then followed by a discussion on the angular variations of $\Delta\Gamma$, $\Delta\Xi$ and B_{res}.

On figure [7.34], it is seen that the three frequencies do not have the same angular dependencies. Note, that the measurements performed at 889 MHz are more noisy, due to recorded amplitude reaching the sensitivity of our oscilloscope (very low signal here). A few remarks from these data are necessary. Let ϕ_B = 67.5°, and compare the 299 and 398 MHz amplitude signals. These corresponds to the maximum dips, and increasing frequency increases the dips. Let ϕ_B = 15°. At 299 MHz, it led to the most prominent shoulder shape before the resonance dips. This particular shape is less prominent at 398 MHz. Let ϕ_B = 45°, a double resonance is seen at 299 MHz, which is less visible on the 398 MHz signal. there seems to be a slight rotation of $\approx$ 7.5-15° between the shape of the envelop at 299 and 398 MHz. This is also visible on the phase measurements. At 398 MHz, double resonances are visible at ϕ_B = 80°. This is not visible at 299 MHz. Moreover, at specific angles, the dips of the amplitude variations and relative velocity consistently increases with frequency, as already discussed before.

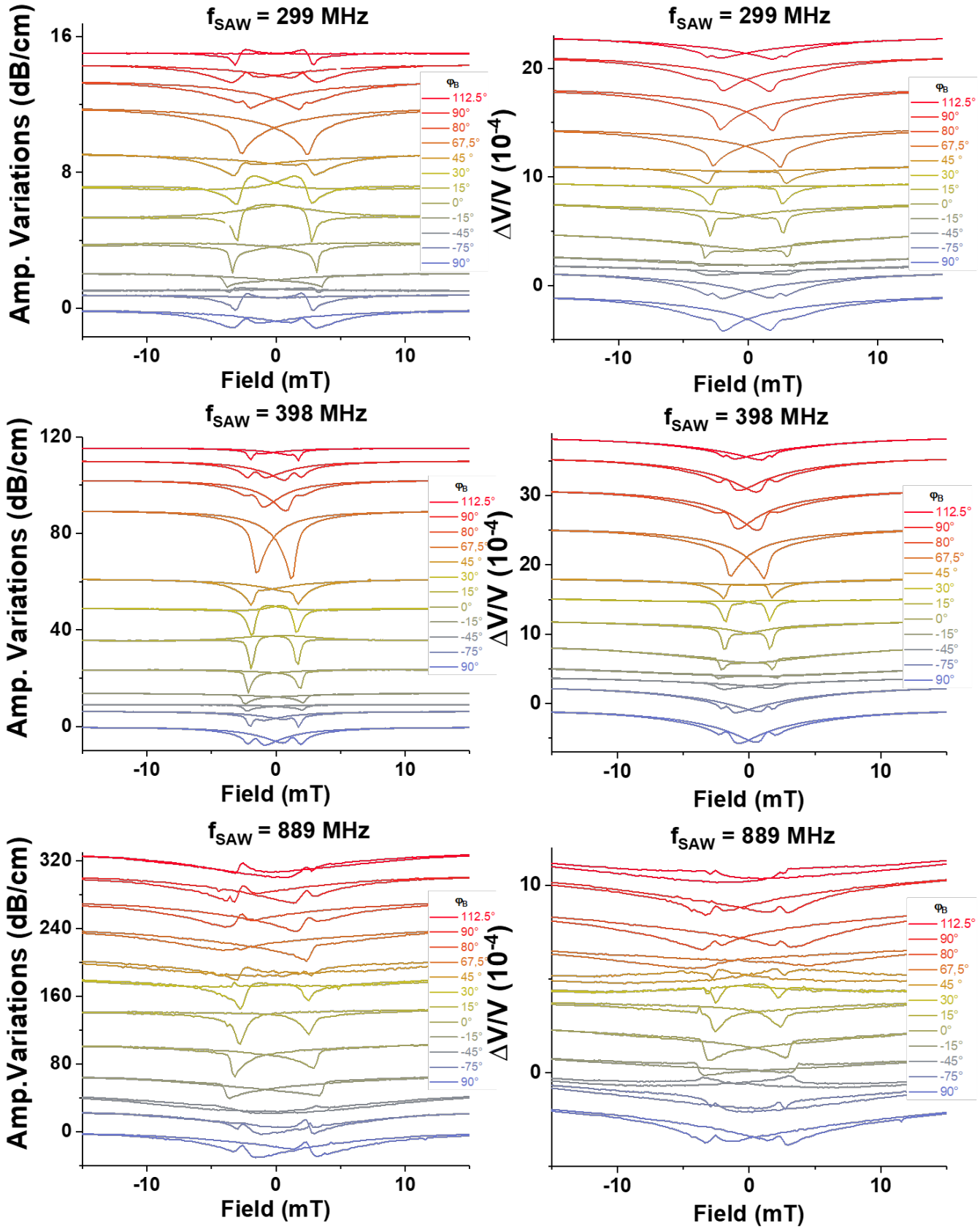

Figure 7.34: Angular-SAW-FMR measurements on the three SAW frequencies.

5.3.1 B_{res} vs ϕ_B

Here is represented the resonance fields with respect to the direction of the applied magnetic field, for the three SAW frequencies. The data set are plotted on the same scale to aid visualisation.

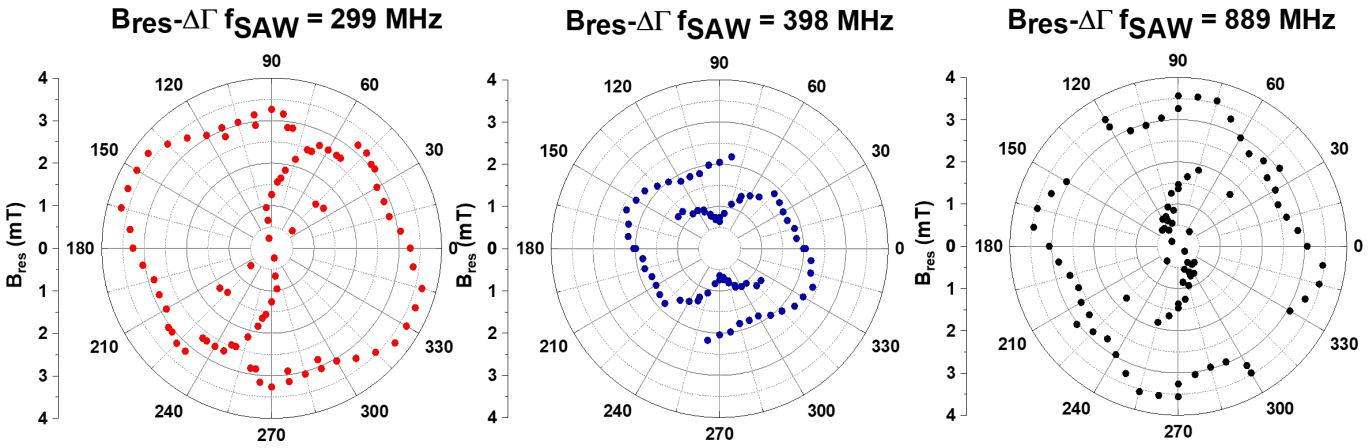

Figure 7.35: Angular dependency of the resonance fields on the SAW amplitude attenuation measurements and for the three SAW frequencies, showcasing the regions with single or double resonance.

On figure [7.35] are represented the resonance fields for the SAW amplitude attenuation. For the 398 MHz frequency, the range on which two consecutive resonance fields are observed, are between $\phi_B = 82.5°$ to 142.5°. On the other hand, there seems to be like a general square boxed shape with corners at 337.5°, around 82.5°, 157.5° and 262.5°. As the resonance fields have been assimilated to the coercivity, i.e. the magnetic switching field, the shape seen at 398 MHz tends to imply the presence of a cubic symmetry, coupled with a region where the switching occurs in two steps, thereby at two different field values. This suggestion is somehow ratified by the angular dependence of the resonance field for the 889 MHz frequency. Here, the two consecutive resonance fields are present for $\phi_B = 75°$ to 120°. The presence of the cubic switching field is seen here, with peaks at 345°, 82.5°, 165° and 262.5°. Finally, comparing the three frequencies, there seems to be a symmetry axis close to $\phi_B = 345°$, and this axis tends to become closer and closer to $\phi_B = 0°$, when the SAW frequency is increased.

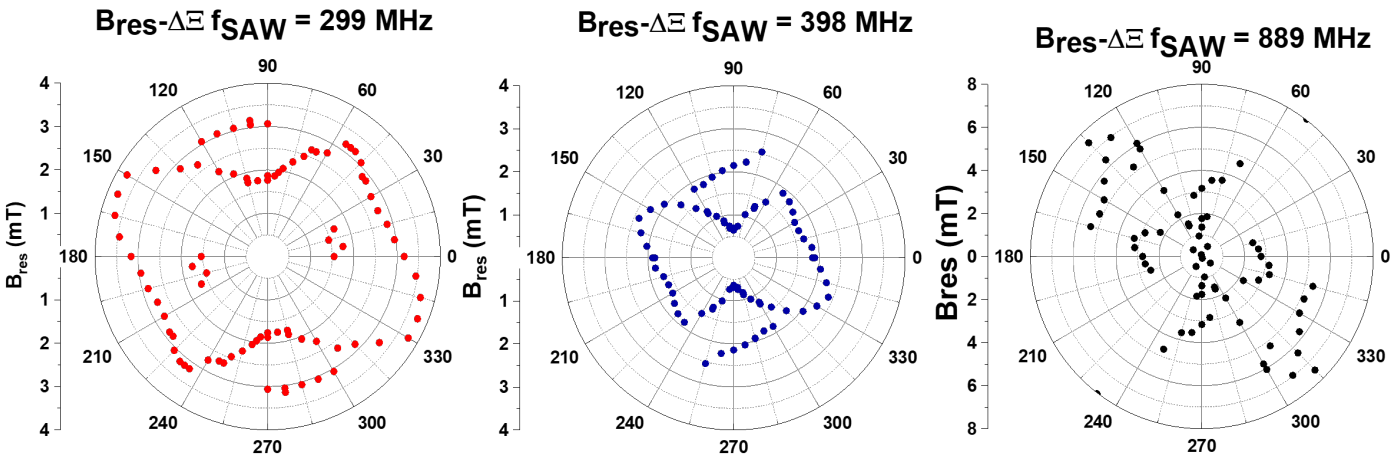

Figure 7.36: Angular dependency of the resonance fields on the SAW relative velocity measurements for the three SAW frequencies, showcasing the regions with single or double resonance. Here, the cubic geometry of the switching field is visually more present.

Likewise, the angular dependency of the relative velocity variation is studied and the resonance fields are presented on figure [7.36]. As the discussion on the 299 MHz has been given before, the focus is on

the remaining two frequencies. Firstly, a quite similar square envelope is seen for the switching field at 398 MHz. Coupled to that, the presence of the consecutive resonance fields are observed for ϕ_B = 75° to 120°, which is quite similar to the amplitude measurements. On the 889 MHz SAW, the data is too noisy. A discussion is necessary before studying the maximum amplitude attenuation $\Delta\Gamma$ and maximum relative velocity variations $\Delta\Xi$. The existence of the symmetry axis is seen here for the first two frequencies as well, with a main axis around $\phi_B = 345°$.

5.3.2 $\Delta\Gamma$ vs ϕ_B

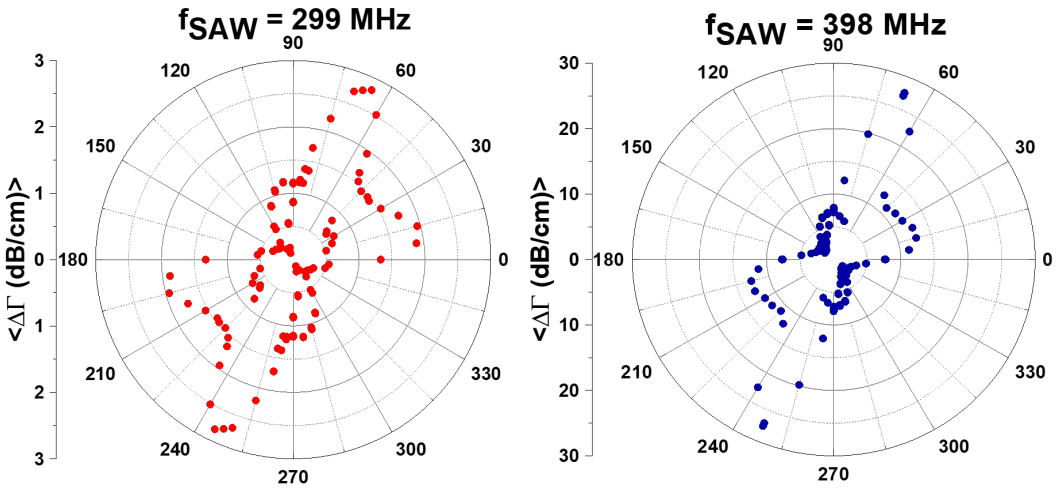

Figure 7.37: Angular dependency of the resonance dips on the SAW amplitude attenuation measurements for the 299 and 398 MHz SAWs.

The maximum and minimum SAW attenuation are observed for fairly close field angles. At 299 MHz, the maximum attenuation corresponds to ϕ_B = 65° to 70°, and the minimum corresponds to ϕ_B = 330°. Note the significant attenuation for ϕ_B = 7.5° to 15°. At 398 MHz, this is more defined. The maximums are at ϕ_B = 67.5° and ϕ_B = 15°, while the minimum lies at ϕ_B = 330°.

So now following the overview of the experimental data, let us now try to understand why we observe this angular dependency.

6 Discussion of the angular SAW-FMR data

Following the overview of the angular-SAW FMR data, the following points can be put forward to summarised the main observations on the three SAW frequencies.

1. The angular SAW-FMR measurements are resonant at all angles ϕ_B, and at the three frequencies;
2. The resonant fields are hysteretic, with different non-hysteretic signal envelopes;
3. The SAW amplitude attenuation and the relative velocity variation do not have strictly similar angular dependencies;
4. For some particular angles ϕ_B, the presence of secondary resonance fields has been recorded. These second resonances are present at all three SAW frequencies, and do not have strictly similar angular dependence, although a cubic geometry in the switching field seems to grow;

In order to discuss those points, it is better to investigate the condition whereby no SAW-FMR interaction is expected. At ϕ_B = 90° and provided that the magnetisation follows the magnetic field (i) The magneto-elastic effective fields driving the magnetisation dynamics are zero; and (ii) The expected spin-wave modes (Damon Esbach), have too high frequencies for matching to occur with the sub-GHz

SAW frequencies.

The starting point of our discussion is to understand the meaning of $\phi_B = \phi_M = 90°$, and how much is this assumption valid in our experiments.

6.1 How are the magneto-elastic torques within the magnetic domains?

The X-Ray diffraction and X-Ray reflectometry measurements performed on the Sample B: FeRh/GaAs have shown that the sample has a polycrystalline structure with no texture (c.f. chapter [2]). However, a crystallographic polycrystalline sample does not imply either that it is magnetically isotropic (i.e. no magnetic anisotropy, or has a rotatable magnetic anisotropy), or that each cristallite within the polycrystal has similar magnetic anisotropy. A discussion is necessary:

(i): If the polycrystal constitutes of big crystallites that each constitutes a magnetic domain. In that case for $\phi_B = 90°$ and B smaller than the anisotropy field, the magnetisation in each crystallite aligns along an easy axis, which results in some cristallites not having a magnetisation at 90° to $\mathbf{k}_{SAW}$.

(ii): If the cristallites are very small compared to the typical magnetic domain size, then the magnetic anisotropy in each cristallite is not relevant but a magnetic anisotropy (not of cristalline origin) might be present and govern the orientation of magnetisation in each magnetic domain close to the coercive field.

One way to investigate this, is to look form the magnetic domains. The Longitudinal-Magneto-Optical Kerr microscopy is performed for two perpendicular geometries:

(i): The magnetic field is parallel to $\mathbf{k}_{SAW}$ with the incident light polarisation being vertical and the light incidence plane horizontal. Here we are sensitive to the magnetisation component parallel to $\mathbf{k}_{SAW}$; and

(ii): the magnetic field is applied at 90° to $\mathbf{k}_{SAW}$ with the incident light polarisation being horizontal and the light incidence plane vertical. Here we are sensitive to the magnetisation component which is at 90° to k_{SAW}.

Recall, as the sample is enclosed inside a cryostat, only these two configurations are possible, since they maximised the already small contrast. For the field parallel to k_{SAW}, the maximum contrast obtained was 0.45%, while for the field perpendicular to k_{SAW} the maximum contrast was measured to be 0.92%. Those values are extremely small! In the remaining sections, only the 398 MHz and thus delay line 2 is under study.

6.1.1 LMOKE Delay line 2- Field $\phi_B = 0°$

Using the Longitudinal Magneto-Optical Kerr microscopy setup presented in chapter [2], the aim of this section is to investigate the magnetic domains. This LMOKE experiment is performed on the delay line 2 and close to the IDT on the left (c.f. figure [7.3]**(a).**). On Figure [7.38] is given the area used to average the LMOKE signal, represented by the red box. This is typically $200 \times 200\ \mu m^2$. Figure [7.39] is the LMOKE signal. Note, in this geometry, the signal has a square shape, and transition, i.e. the magnetic field range for which the magnetisation has switched from $\phi_B = 0°$ to 180° is ≈ 11 mT.

On figure [7.40] are represented the LMOKE images for different magnetic field during the magnetisation switching. The top panel represents the left-to-right magnetisation switching. At 1.7 mT, the regions close to the GaAs edge have already switched. We are looking at darker coloured FM domains (→) in the grey FM matrix (←). At around, 2.3 mT, some darker strips parallel to the field over $\approx$ 70 μm appear. At 2.5 mT, these domain filaments look tilted by $\approx$ - 18°. This maximum tilt is seen

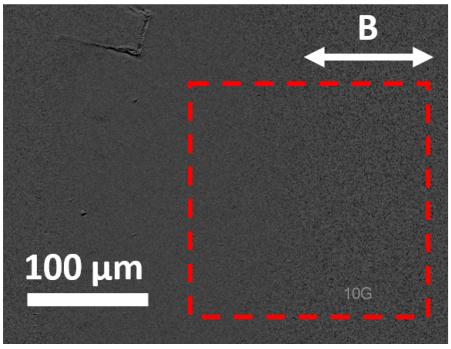

Figure 7.38: Typical LMOKE image, here at high saturation field (± 20 mT). The red square represents the region where an average is performed in order to calculate the LMOKE signal. The field is applied here horizontally, i.e. for $\phi_B = 0°$, which is also parallel to the direction of propagation of the SAW.

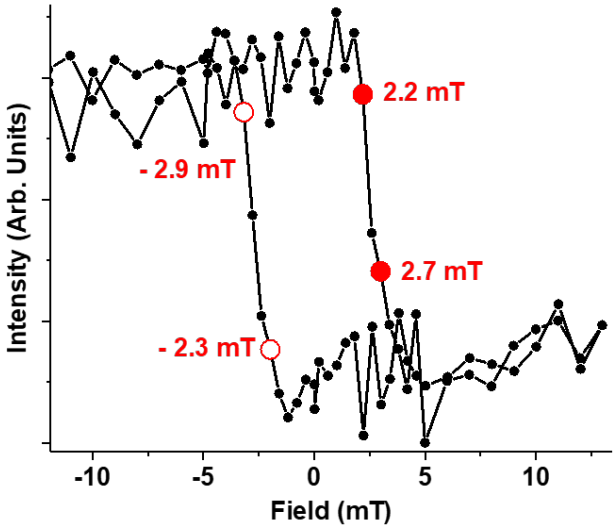

Figure 7.39: Complete LMOKE experiment with respect to field. Note that it takes ≈ 2 mT for the magnetisation switching to occur. Moreover, the LMOKE measurement is well-defined and square shaped, even though that the maximum contrast is only 0.45% here.

at 2.7 mT, where the tilt is - 27°.

Similarly, on the reverse switching, i.e. when going from the right-to-left, we are looking for the appearance of lighter FM domains in the dark FM matrix, as seen first at - 2.3 mT. The domains here are also filament-shape like and goes for up to 100 μm. At - 2.7 mT, the maximum tilt is - 27°. At - 2.9 mT, where most of the observed region has switched, the filaments make an angle of - 33° with the horizontal.

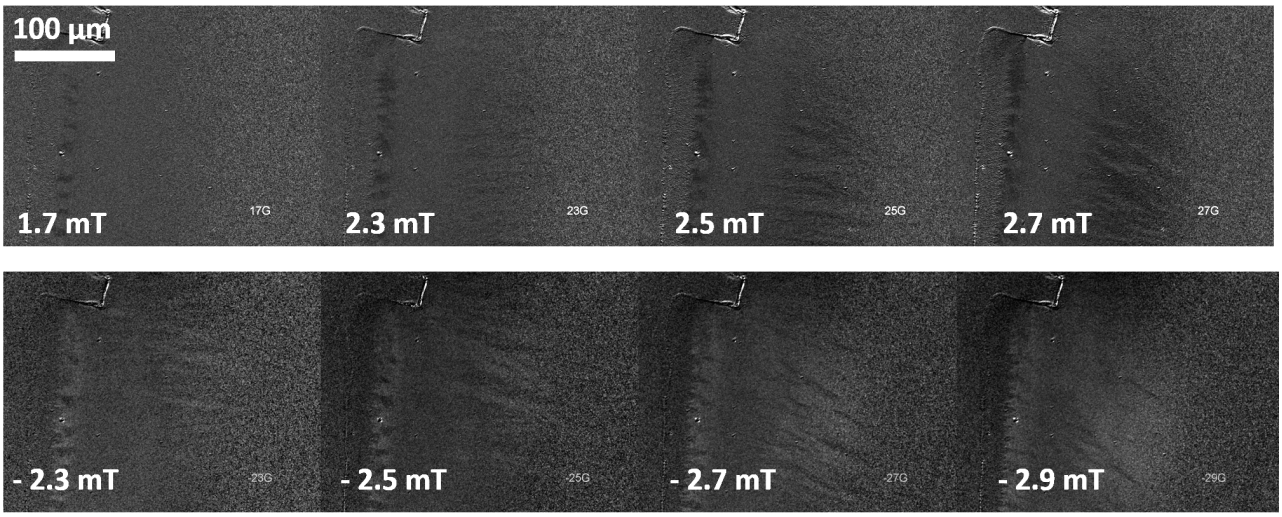

Figure 7.40: Appearance, propagation and disappearance of reversed FM domains on delay line 2, for a magnetic field applied parallel to the direction of propagation of the SAW: for $\phi_B = 0°$. The top panel represents the images in the transition, going from left-to-right. Note the appearance of the darker FM domains in the light FM matrix first horizontally at 2.5 mT. The bottom panel represents the images in the transition going from right-to-left. Here, we are looking at the appearance of darker FM domains.

Two important conclusions can be gathered here:
(i): The FM domains are filament-shape like and are up to 100 μm long.
(ii): There is a residual anisotropy directed approximately around - 31°.

6.1.2 LMOKE Delay line 2- Field $\phi_B = 90°$

Likewise, the experiment is repeated, this time for the magnetic field applied at 90° to k_{SAW} and the plane of incidence also vertical. In this geometry, we are now sensitive to the vertical component of the magnetisation, i.e. at 90° to k_{SAW}. The first difference, is that the LMOKE signal is no longer a straight square shape, but is broader, and the signal does not really overlap following the magnetisation switching. This might be due to the noise signal here. Second remark, the magnetisation switching takes place on a field range twice as large as for the previous geometry. This might be the result of multi-step switching. Indeed, we have represented as before the LMOKE images within the magnetisation switching for particular field values.

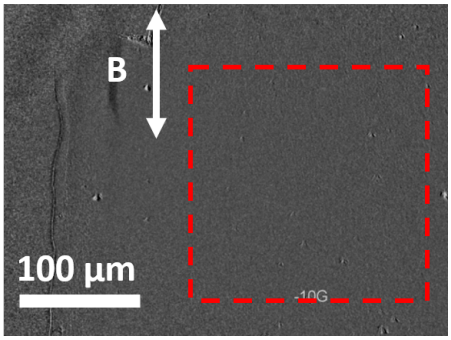

Figure 7.41: Typical LMOKE image, here at high saturation field (± 20 mT) The red square represents the region where an average is performed in order to calculate the LMOKE signal. The field is applied here vertically, i.e. for $\phi_B = 90°$, which is also parallel to the supposed direction where the Rh concentration is assumed to vary.

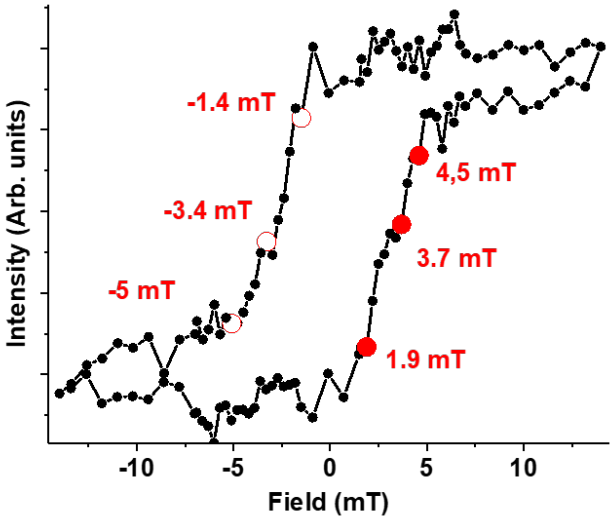

Figure 7.42: Complete LMOKE experiment with respect to field. Note that this cycle has been corrected to remove a slope coming from Faraday effect. Note that it takes now ≈ 4.5 mT for the magnetisation switching to occur. Although the contrast is better here, 0.92%, the signal is noisier.

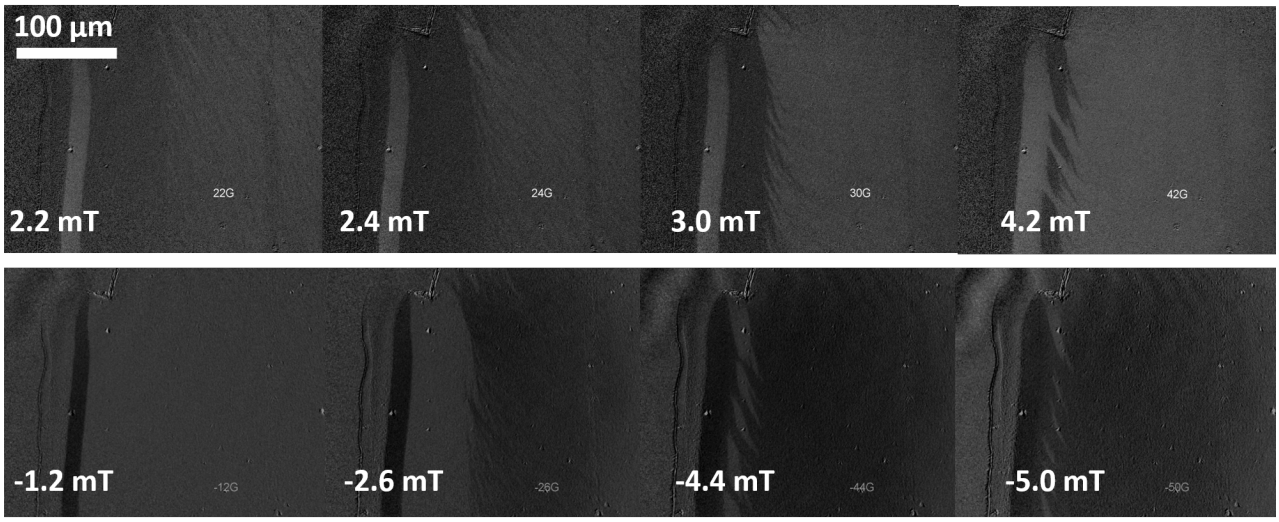

Figure 7.43: Appearance, propagation and disappearance of opposing FM domains on delay line 2, for a magnetic field applied perpendicular to the direction of propagation of the SAW: for $\phi_B = 90°$. The top panel represents the images in the transition, going from the magnetisation ↑ to being ↓.

Let us follow the field going from - 15 mT to + 15 mT. The switching begins at ≈ 1 mT. At 2.2 mT, as seen from the figure, a region close to the left has already switched. Here, we are looking for

lighter FM regions (↑) from the darker matrix (↓). For 2.4 mT to 3.0 mT, we can see the progression of the lighter FM regions (↑). Note here that we have actually 3 level of grey. The darkest matrix with the magnetisation (↓), the lightest grey with magnetisation (↑), and a zone with an intensity in between those two values. Returning to figure [7.43], if we look at 3.7 mT, we can clearly see a small kink, which might be due to this third level of grey. Might be due to the pinning of the propagation of the FM domains, which prevent the magnetisation switching. Note the small tilts on the domain filaments are still visible around -30°.

Two important conclusions can be gathered here:
(i): For a field applied at 90°, the magnetisation is not really at 90°, at least part of the delay line is not at 90°. This imply that the magneto-elastic coupling is not zero. This explains the non-zero SAW-FMR interaction for $\phi_B = 90°$.
(ii): The magnetisation switching is carried out in multi-steps procedure.

6.2 Angular SAW-FMR and LMOKE for $\phi_B = 0°$ and $\phi_B = 90°$

In this section, we aim to compare the LMOKE signal taken on delay line 2, and the SAW amplitude attenuation at 398 MHz. For the field parallel to k_{SAW}, i.e. for $\phi_B = 0°$. This relates to the measurements seen in the previous sections, where we demonstrated that the local coercivity corresponds to the SAW-FMR resonance field.

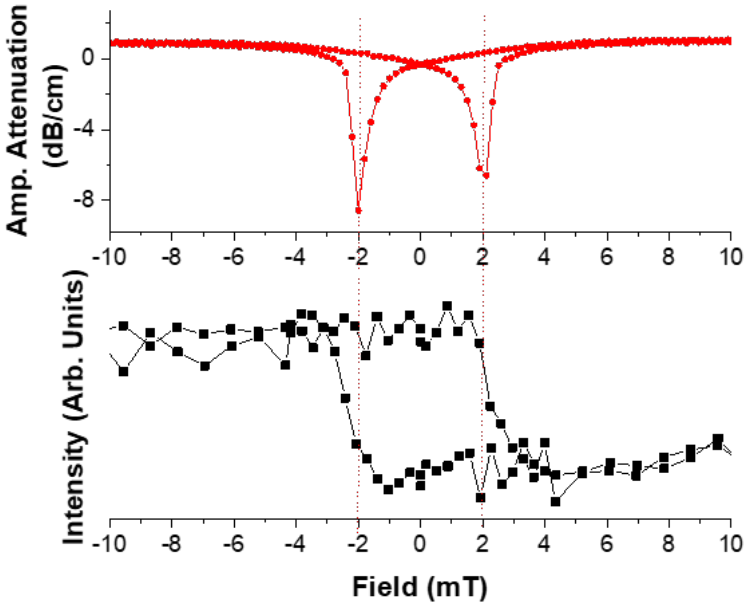

Figure 7.44: The magnetic field is applied along k_{SAW}, i.e. for $\phi_B = 0°$. Correspondence between the SAW amplitude attenuation at 398 MHz and the LMOKE signal taken on delay line 2. In this geometry, as seen before, the local coercive fields match the resonance fields.

Likewise, we represent the SAW amplitude attenuation for $\phi_B = 90°$, and the corresponding LMOKE signal. What we observe is that the larger resonance field actually corresponds to the half-way of the magnetisation switching. Since we know that the LMOKE cannot reproduce multi-step switching, we can only conclude that, for $\phi_B = 90°$, the magnetisation is not at 90°, and the magnetisation switching is in multi-step.

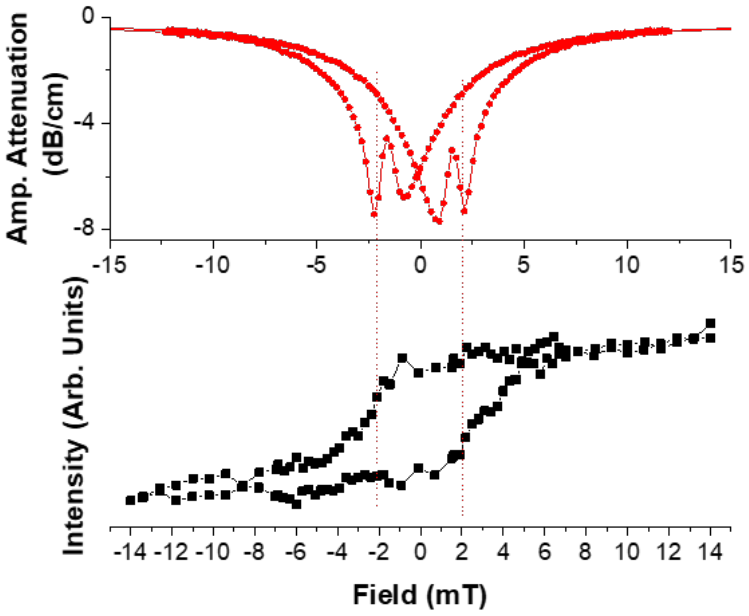

Figure 7.45: The magnetic field is applied perpendicular to k_{SAW}, i.e. for $\phi_B = 90°$. Correspondence between the SAW amplitude attenuation at 398 MHz and the LMOKE signal taken on delay line 2. Here the mid-way to the magnetisation switching correspond to the larger resonance fields. However, we cannot really differentiate between the two resonance fields using the LMOKE signal, since the LMOKE is not sensitive to multi-step magnetisation switching.

6.3 Conundrum

In the previous section, we conclude that the magnetisation is never at 90° to k_{SAW}, hence the magneto-elastic driving field are never completely zero. The is still an unanswered question: what is the correct anisotropy of Polycrystalline Sample B?. As the sample is inside the cryostat, it cannot be rotated while keeping the same LMOKE geometry. Moreover, it is not possible to use the LMOKE setup for angles other than parallel or perpendicular to k_{SAW}.

Idea 1: While fabricating the Polycrystalline Sample B, it was shown that several smaller samples were actually sputtered simultaneously, c.f. figure [2.4]. Recall, the Rhodium concentration varies vertically. So, by taking a second sample adjacent horizontally with Sample B, we suppose having the same magnetic anisotropy, we devised a setup, with the help of D. Ourdani, whereby we glued the sample on a heated copper cylinder, outside of the cryostat, and measured the Longitudinal Kerr Measurements to look for the magnetic anisotropy. Unfortunately, the results were inconclusive. First the contrast was small, C = 0.41%. Secondly, as the sample was glued on a copper cylinder, rotating the sample along its axis meant that we lost focus on the sample almost immediately. Although care was taken to ensure that the LMOKE measurements were taken repeatedly at the same location, the resulting LMOKE signals were extremely noisy. As such, we were not able to measure the remanence, which would have given us a direct measure of the magnetic anisotropy.

Idea 2: D. Ourdani investigated the magnetic anisotropy by performing FMR measurement using a micro-strip line, while rotating the sample at the LSPM[8] [251], [252]. However, the sample broke and this ended our search for the magnetic anisotropy.

6.4 Attempts at modelling the angular-SAW-FMR

Using the numerical SAW-FMR model developed in details in chapter [5], and the conclusive results for $\phi_B = 0°$ (c.f. section [4]), we have tried modelling this angular SAW-FMR without having a clear

[8] Université Sorbonne Paris Nord, Laboratoire des Sciences des Procédés et des Matériaux-LSPM, CNRS, Villetaneuse, France

idea of Sample B anisotropy. Note, this angular modelling is not finished. Hence, i shall explain the different procedures we followed to try to converge towards our experimental measurements, i.e. the existence of two resonance fields for some particular magnetic field directions.

Remarks: Only a macro-spin modelling has been undertaken here, i.e. we have considered the delay line to be a single magnetic domain. We are able numerically to change the value of the anisotropy and the corresponding direction.

Attempt 1: Using the LMOKE measurements whereby we distinguished that the magnetic filaments tend to align at ϕ_B = - 30°. So we modelled using an uniaxial anisotropy directed at this particular angle.
⇒ Here, it was realised that an uniaxial anisotropy only could not lead to the multi-step switching.

Attempt 2: Use the fact that crystalline FeRh has a biaxial anisotropy, we modelled using a bi-axial anisotropy with the presence of a uniaxial anisotropy (which we assumed to be due to graded composition growth). Here, the multi-step switching is possible since the model has two anisotropy in competition with each other. Note, as we are able to change the anisotropy constants, that allowed us to play finely with the angular resonance fields.
⇒ It was not possible to obtain the double resonances at the experimentally observed ϕ_B angles.

Attempt 3: Consider an uniaxial anisotropy with direction close to - 15° (angle where the B_{res} was observed to be maximum before, and a competition from a depinning field.
⇒ This is what give the best result so far. However, since the numerical model is not finished, i refrain from presenting the outputs in the manuscript.

Chapter Summary

1. It has been experimentally demonstrated that SAW-FMR resonance fields occur at local coercivity in the fully ferromagnetic (FM) phase, validating the calculations of chapter [5]. The temperature dependency of SAW-FMR interactions has been also studied down to the AFM phase. This confirmed the SAW-FMR resonance and local coercivity matching for all temperature, and using three different SAW frequencies across two different delay lines.

2. A thorough comparison between experimental data and the Power Transfer SAW-FMR model has been conducted. This comparison validates the model presented in Chapter [5] for parameters such as $\Delta\Gamma$, $\Delta\Xi$, and explores the influence of SAW frequency f_{SAW}, the ferromagnetic fraction (x_{FM}), and SAW velocity (V_{SAW}) on SAW-FMR interactions. Different modelling approaches, including macro-spin and multi-domain models, have been studied to reinforce the theoretical framework, ensuring that the model accurately represents the physical phenomena observed.

3. Studied the contribution of each strain component to the magneto-elastic driving field, and then performed Angular SAW-FMR experiments. This led to the discovery of surprising four hysteretic resonances for some angles, and the presence of resonance at all magnetic field orientations. A comparative analysis of angular variations of $\delta\Gamma$, $\Delta\Xi$, and B_{res} at different frequencies has been provided, highlighting regions with single or double resonance.

4. A method to understand the origin of SAW-FMR resonance across all magnetic orientations has been devised. This firstly involved conducting additional experiments. Reaching a dead-end, we then numerically attempted to model the a-SAW-FMR experiment, to understand our magnetic system.

Chapter 8

SAW-B & -T

Objectives

In this chapter, the interaction of SAWs with the FeRh layer is studied by varying the temperature across the phase transition, while concomitantly applying an external magnetic field. Signs of resonant SAW-FMR interactions, as well as non-resonant interactions, are investigated. Through this a complete picture of the SAW influence on the FeRh layer is sought.

Contents

1 Introduction to SAW-B-T

Pursuant of the previous two chapters: SAW-T (c.f. Chapter [6]) and SAW-B (c.f. Chapter [7]), whereby it has been demonstrated that the SAWs interact both resonantly with field and non-resonantly with temperature (or the corresponding FM fraction), here by applying a magnetic field while varying the temperature, we aim to isolate any resonant conditions. These measurements were taken on the Polycrystalline Sample B: FeRh/GaAs, in-line with chapter [6].

2 Relative velocity variations vs T for a non-zero B field

Similar to chapter [6], the experimental procedure consists in heating the sample from - 40°C, in the fully AFM phase, up to 120°C in the fully FM phase, followed by a cooling down to the initial temperature. Here, in addition, an external magnetic field is applied in the direction of the SAW propagation, i.e. for $\phi_B = 0°$. On figure [8.1] are represented the relative velocity variations for the 299 and 889 MHz frequencies (on delay line 1, c.f. figure [4.22]). The zero-field data are plotted with closed symbols, and non-zero-field data are plotted with open symbols. In the presence of the magnetic field, there is a clear shift in the $\Delta V/V$ in the fully FM phase. Moreover, this shift is larger for the 889 MHz frequency. Note that the shape of the relative velocity variation is relatively unchanged.

On figure [8.2] is represented the average opening at the transition $\Delta\Xi$ (c.f. figure [6.9]), with respect to the three excitable SAW frequencies, in zero-field (c.f. figure [6.13]) and for 50 mT. The application of the field, increases the opening at all frequency with 9% increase at 299 MHz, 3% increase at 398 MHz and a 6% increase at 889 MHz. This is a sign of a small magnetic contribution affecting the velocity measurement, with the maximum effect in the fully ferromagnetic phase.

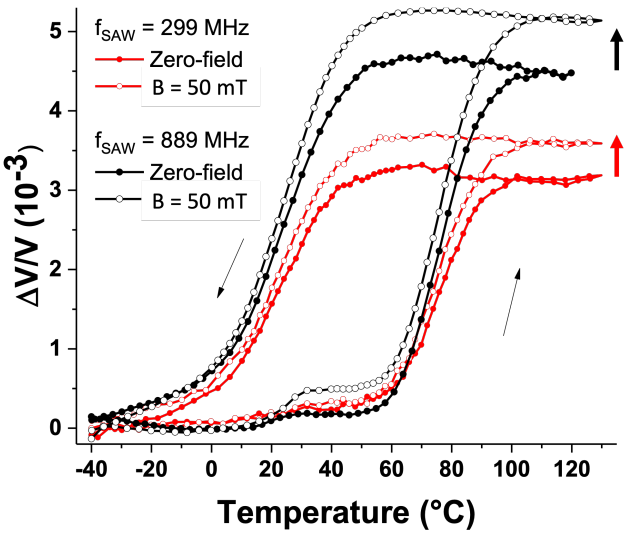

Figure 8.1: Relative velocity variations for the three excited SAW frequencies with respect to temperature, and across the phase transition, and in the absence/presence of a magnetic field parallel to the direction of propagation of the SAW. For 50 mT, there is a clear shift in the relative velocity measurement. The maximum effect is observed in the fully FM phase.

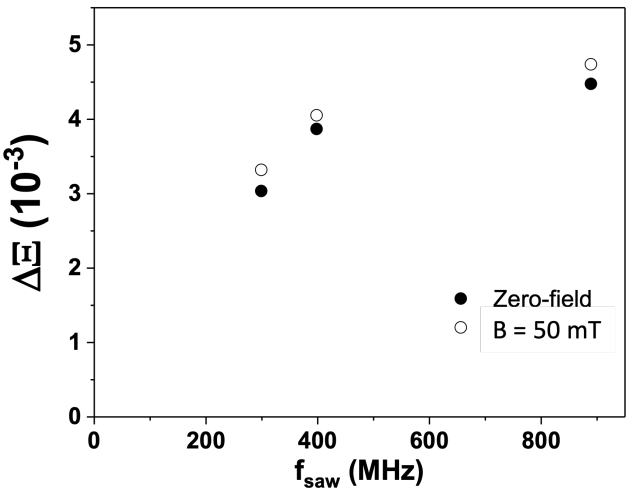

Figure 8.2: Evolution of $\Delta\Xi$ with respect to the SAW frequency. Zero-field measurements are given by full symbols and non-zero-field measurements in open symbols. Here are represented only the average values of the zero-field $\Delta\Xi$ value (c.f. figure [6.13]). The openning at the FM-AFM transition is larger at all frequencies in the presence of a magnetic field.

Conclusion:

Two hypotheses are put forward to explain the increase in $\Delta\Xi$ observed on the relative velocity measurements, in the presence of the magnetic field:

1. We are sensitive to the magneto-striction of FeRh, albeit small,
2. Applying a constant magnetic field, imply that we are no longer in resonant conditions. This increase in $\Delta\Xi$ with respect to T here ($\approx 5\times10^{-4}$), is approximately the change in $\Delta\Xi$ with respect to B-field in chapter [7], figure [7.4] ($\approx$ 3-4$\times10^{-4}$).

3 Amplitude attenuation vs T for a non-zero B field

During the temperature ramps, the SAW amplitude attenuation is also measured. The SAW attenuation is zero-field, seen in chapter [6], is represented on figure [8.3]. The data are stacked for clarity. Recall, we observed that at 299 MHz, two dips at temperatures corresponding to mid-way across the AFM-FM phase transition. For the 889 MHz, a gradual (but very noisy) increase in SAW attenuation was measured with increasing temperature which corresponds to an increase ferromagnetic fraction. We suggested that this variation was due to the SAW interaction with the FM fraction. Moreover at 398 MHz, the measurement was visually like a mix between the two previous frequencies. These measurements are repeated in the presence of a 50 mT magnetic field applied parallel to the SAW propagation direction, i.e. for $k_{SAW} = 0°$, and are represented on figure [8.4]. The data are stacked for clarity.

For the SAW amplitude attenuation in the presence of a magnetic field, we observe that now the three frequencies have similar temperature variations. This can be clearly seen for the 889 MHz SAW. Two dips are now observed compared to the constant increase in SAW attenuation. These dips correspond to temperatures mid-way across the AFM-FM phase transitions. Now, if we look at all three frequencies, we observe that all the dips corresponds to approximately the same temperatures corresponding to 50-50% AFM-FM phases. The temperature dependence of the coercivity (resonance field with respect to B-field) was investigated in the previous chapter and was seen to vary between 2 mT to 16 mT (at 25°C). Thus applying the B-field at 50 mT, ensured we are far from the resonant condition, and effectively kills the SAW-FMR interaction, previously observed at 398 and 889 MHz.

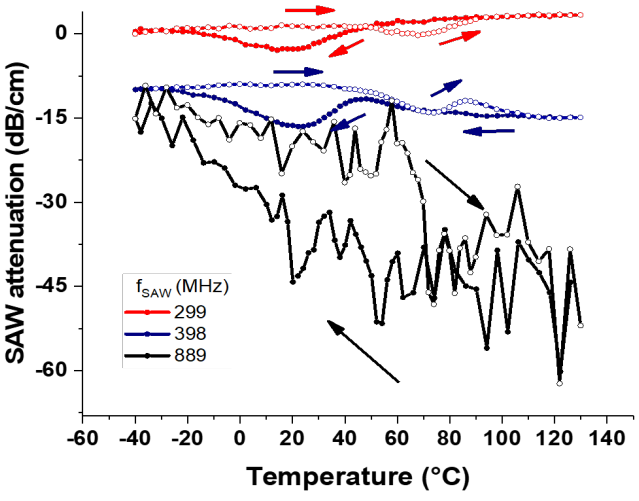

Figure 8.3: SAW amplitude attenuation for zero-field. The data are stacked for clarity. For 299 MHz, two dips are observed, and correspond to temperatures where there is a 50-50% coexistence of the AFM and FM phases. For the 889 MHz SAW, the attenuation increases gradually with the increasing temperature. We suggested this is sign of SAW interaction with the FM fraction.

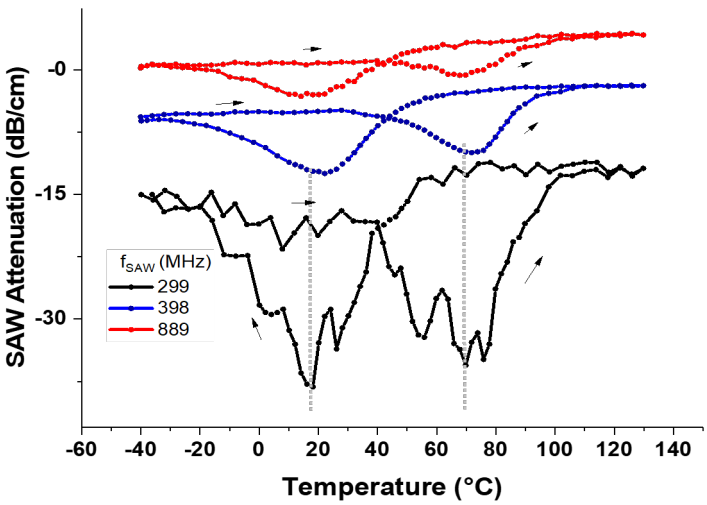

Figure 8.4: SAW amplitude attenuation with a magnetic field applied along $\phi_B = 0°$. The field value is 50 mT. Two dips are now observed for all three SAW frequencies. These dips corresponds to the temperatures whereby there is a 50-50% coexistence between the AFM and FM phases.

Conclusion:

For the SAW-interaction with the FeRh layer, we have two distinct resonance. In SAW-B (SAW interaction with magnetic field, c.f. Chapter [7]), it was demonstrated that the SAW interacted resonantly and that this interaction occurred at the coercivity of the layer. Moreover, the interaction followed the temperature dependence of the coercivity, which matched the FM fraction present in the layer. In SAW-B-T (SAW interaction with temperature in the presence of a magnetic field, c.f. Chapter [8]), by applying a magnetic field larger than the coercivity, this resonant interaction was consequently suppressed. Consequently, this suggest more of an out-of-resonance effect of SAW scattering off AFM-FM domain walls.

Chapter Summary

In this final experimental chapter, the SAW-FMR interaction has been studied across the magnetic phase transition, and under the presence of a magnetic field. In the case of the relative velocity variation, it was demonstrated that the presence of the latter, increased $\Delta\Xi$ across the two phases. For the SAW amplitude variation, an external magnetic field (much larger than the SAW-FMR resonance fields), completely supressed the SAW interaction with the temperature dependent FM fraction. This resulted in maximum SAW attenuation at temperatures mid-way across the transition.

Chapter 9

Setup Improvement: Synchronised Electrical SAW pump and Optical probe

Objectives

This chapter focuses on enhancing the experimental setup for the generation and detection of Surface Acoustic Waves (SAWs) and their interaction with FeRh magnetic thin films. The primary goal is to achieve precise phase synchronisation between the electrical SAW pump and the optical probe. This involves transitioning from a mechanical delay line to a more advanced 1-Master and 2-Slaves electronic configuration. The improvements made to address limitations of the previous setup are explained, and rudimentary measurements of photoelastic effect on Sample B: FeRh/GaAs, demonstrating the effectiveness of the upgraded experimental configuration are given.

Contents

1 Introduction to pump-probe phase synchronisation

As explained in Chapter [4], for the all electrical generation and detection of SAW, c.f. section [8], a square modulated sinusoidal radio-frequency (RF) electronic signal at $f_{SAW} \sim$ GHz, is fed to the exciting IDT. By inverse piezoelectric effect, SAWs are generated towards the FeRh magnetic layer. The SAWs propagate and interact with the magnetic layer and is detected and converted back to an electric signal via direct piezoelectric effect. This signal is displayed on an oscilloscope prior to analysis (c.f. Chapters [6-8]). In this chapter, the SAWs are still generated using the IDT, however the detection is performed using optical probe pulses, phase-locked to the RF pulse. Figure [9.1], is a schematic representation of the general idea behind the electrical pump-signal sent to the IDT (yellow part), which generate a dynamic strain wave via inverse piezoelectricity, represented by the wave-like diagram, and the probe signal, which consists of periodic polarised optical pulses. By performing spatial scanning and/or temporal delay, it is thus possible to reconstruct the magnetisation dynamics.

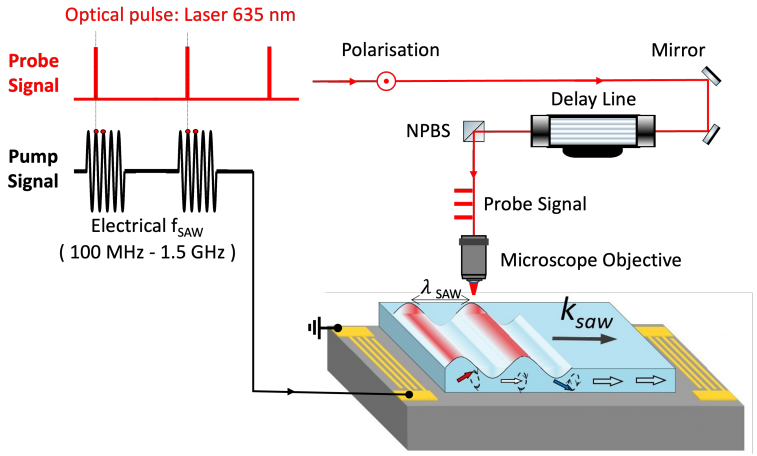

Figure 9.1: General idea behind the phase synchronisation between the RF Pump signal and the optical probe signal.

Achieving stable phase-locking between the excitation and detection signals is fundamental for conducting time-resolved measurements. This holds particular significance in pump-probe experiments, as it guarantees that the probe signal precisely reaches the sample at the intended time stamp after the pump-pulse-induced excitation. Consequently, it solely detects the latter, resulting in an optimised signal-to-noise ratio. During the first-year of the thesis, we have thus improved on the previous optical detection of dynamics[1]. Although we were not able to detect dynamics on FeRh, significant improvements have been made to the setup.

1.1 Limitations of the previous setup

In the previous setup, [26], the phase-lock was ensured by dividing the output of a single Ti:Sapphire femto-second laser source into two distinct optical signals. Firstly, the laser pulses with a 75 MHz repetition rate[2] were sent through a pulse picker, reducing the repetition rate, and served as optical probe. The rest of the optical pulses was electronically filtered, keeping the 75 MHz frequency. Higher harmonics were obtained using RF multipliers and fed to the IDT in order to generate the acoustic waves. A mechanical delay line was used to delay the probing signal which is essential to reconstruct dynamics. Hence, as both the pump-RF and optical-probe signals were derived from the same source, an intrinsic stable phase synchronisation was possible.

However, the experimental configuration posed several stringent limitations. The most inconvenient being the necessity to generate SAWs at frequencies multiple of the laser operating frequency. As such,

[1] By dynamics here, we refer to both magnetisation dynamics and dynamic strain detection using photo-elasticity.
[2] Note that the 75 MHz corresponds to the operating frequency fixed by the laser cavity

generating a 600 MHz SAW frequencies needed 3 RF doublers for example. Additionally, achieving satisfactory acoustic amplitude signals required the use of numerous RF amplifiers and multipliers. Finally, since the optical delay was obtained mechanically using sets of sliding mirrors, the probe signal was prone to divergence and resultant fluctuations in light beam intensities due to minor misalignment. To address these experimental challenges, improvements were made to the pump-probe setup, as detailed below.

2 Elegant Solution: 1-Master and 2-Slaves configuration

In order to satisfy the fundamental requirement of phase synchronisation between the electrical RF pump and the optical probe signal, a new experimental configuration was implemented and tested during the first year of my Ph.D. Figure [9.2], is a schematic representation of the 1-Master and 2-Slaves circuitry and the corresponding modulation of the RF and optical signals at any point in the network.

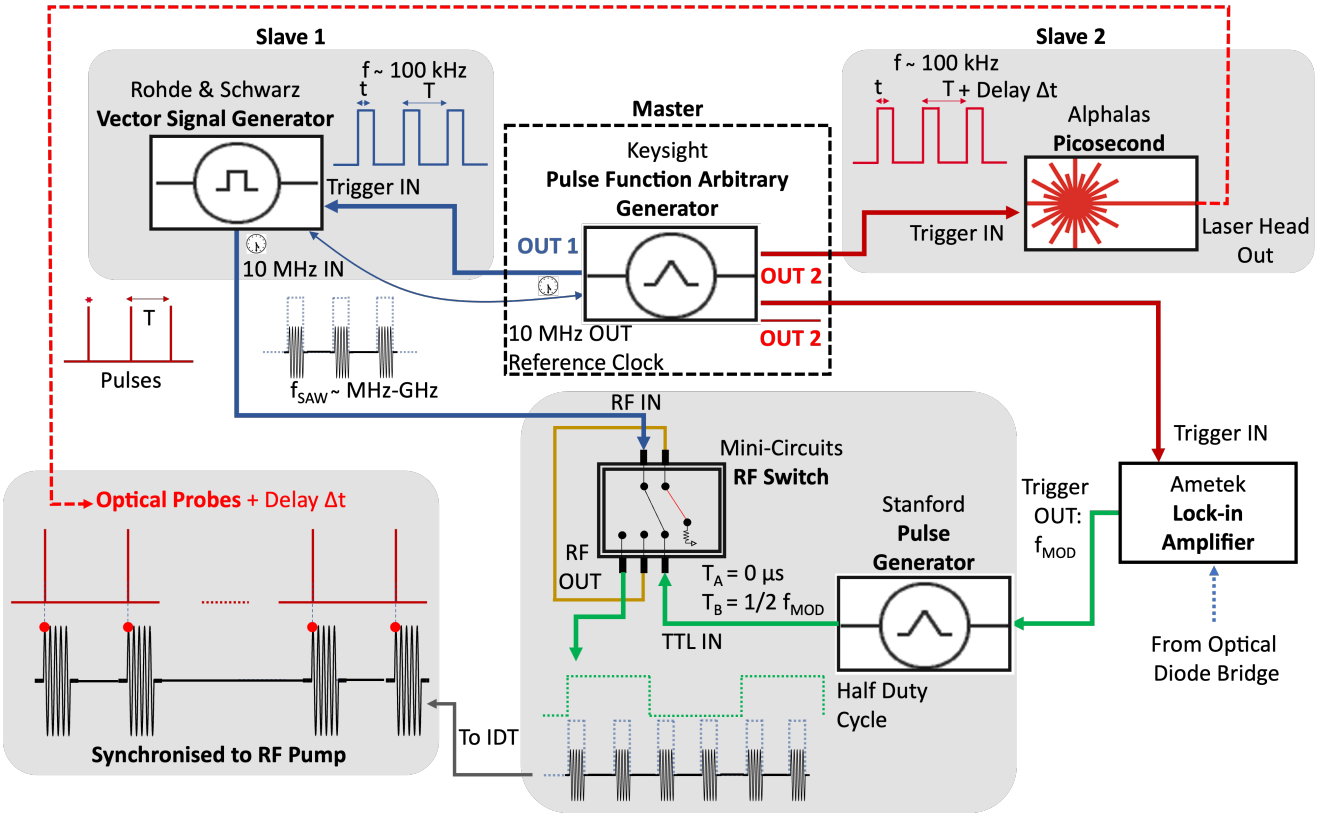

Figure 9.2: 1- Master and 2-Slaves Electronic Circuity. The Master operator is the Pulse function generator, which delivers the trigger signals OUT1, OUT2 and $\overline{\text{OUT2}}$. The two slaves are the Vector Signal Generator and the picosecond laser. The former generates the SAW MHz frequency signal, which is further over-modulated at a frequency of $f_{\text{MOD}} = 11327$ Hz absent in the signal, while the laser head generates optical probes synchronised to the RF excitation. The dynamics is searched for at the frequency of the over-modulation.

A **Keysight** Pulse Function generator is used as the Master source and delivers simultaneously three electrical outputs in the form of repeated pulse-train functions: OUT1, OUT2 and $\overline{\text{OUT2}}$. These serve as external trigger sources for the 2-Slaves: the **Rohde-Schwarz** Vector Signal Generator and the **Alphalas** picosecond laser. Once the trigger level is reached, the latter delivers optical pulses which form part of the probe signal. By electronically delaying the OUT2 signal generated by the Keysight generator, the probing pulses are retarded and dynamics can be reconstructed. As such, the delay is now introduced in the optical pulses electronically, making the mechanical delay line obsolete and thus eliminating any source of beam divergence. It is useful to note that $\overline{\text{OUT2}}$ is simply the inverted signal of OUT2, and is used to balance the optical diode bridge, as detailed in section [3.3.1].

On the other hand, after being externally triggered by the Keysight generator, the Rohde-Schwartz generator, is used to generate the continuous SAW signal in the MHz-GHz regime, modulated by the same pulse-train function. It is important that the pump signal is modulated and not continuous, as it would otherwise be impossible to distinguish between the slower acoustic signal and the electromagnetic leak, consequence of inductive effects within the IDT. In order to reduce electronic noise and improve the detection, a slower envelope modulation at $f_{\mathrm{MOD}} = 11327$ Hz, non-existent in the electronic circuitry, is applied to the RF pump, which will act as the reference signal for demodulation. This carrier wave modulation itself typically does not contain any useful information but serves as a medium to carry the modulated signal. It is represented in figure [9.2] by the green pulse-train, resulting from the convolution of the half-duty cycle signal generated by the Stanford pulse generator and the RF switch. It is noteworthy to grasp that the over-modulation is incorporated solely in the pump signal which generates the SAW. This slower modulation frequency is of utmost importance, as it must not be multiple of any frequency already present in the circuit, and high enough to reduce signal-to-noise ratio (SNR)[3]. The modulated RF electronic signal is then fed to the exciting IDT which generates the SAW. Hence, as the RF pumps driving dynamics and the optical pulses probing dynamics are generated by a unique source, synchronisation is guaranteed. A lock-in demodulation at f_{MOD} is now possible as it is now much smaller than the 250 kHz cut-off frequency. One drawbacks of the current improvements is a lower optical power given by the picosecond laser, as compared to the previous Titanium Sapphire Laser (by comparison with the Ti:Sapphire at 75 MHz, $\mathrm{P_{OUT}} \sim 1$ W, compared to the ps laser at 250 kHz, $\mathrm{P_{OUT}} \sim 3.5\ \mu$W)

On the bottom left of figure [9.2] is represented the phase synchronisation of the optical probe pulse and the RF probe. By delaying electronically OUT2, the pulse probe is delayed in time, and a later dynamics is probed and so on.

2.1 Complete Electrical-Pump and Optical Probe Setup

Figure 9.3, is a schematic representation of the entire pump-probe setup used to detect dynamics. The left-most part illustrates the 1-Master and 2-Slaves electronic circuitry seen previously.

Given that the majority of dynamical interactions we initially wanted to investigate arise from either magneto-optical or photoelastic phenomena, the polarisation of the optical probe signal emerges as a pivotal adjustable parameter. As such, the synchronised optical pulses coming from the picosecond laser are made to pass through a polariser and a half-wave plate and onto the sample placed within the cryostat. For example, in the photoelastic effect, maximising the effect requires that the linearly incident light be oriented at a 45° angle[4] to the direction of SAW propagation. The incoming light is reflected off the sample and directed back through the Non-Polarising Beam-Splitter (NPBS) and onto the optical diode bridge detector. The optical bridge detect the polarisation rotation. The integration of an optical bridge in conjunction with the lock-in detection's amplifier enhances the precision and sensitivity of the measurements and the fine reconstruction of the dynamics. Nonetheless, the magnitude of the dynamics (be it magnetic or photo-elastic) under investigation is still small, and it it still necessary to employ averaging techniques such as accumulation and stroboscopic measurements to enhance signal-to-noise ratio. Using this combined electrical RF pump and optical probe setup offers several advantages. The most important being that the optical detection is spatially separated from the SAW propagation. Indeed, in the case of the all-electrical SAW generation and detection, the whole delay line is probed at all time. Here, using the electrical pump and optical probe, the probing can be made at any point on the delay line. Moreover, by electronically delaying the optical probe, we can reconstruct the strain or magnetisation dynamics anywhere along the delay line for example.

[3] $\mathrm{SNR} = \frac{2\pi A}{\sqrt{f_{\mathrm{MOD}}}}$; A being the amplitude of the signal.

[4] Propagating SAWs modify the refractive index parallel to $\mathrm{k_{SAW}}$. The strain dynamics thus create a birefringence, and if a linearly polarised incident light is sent on the sample, after reflection, its polarisation is changed by: $\beta_{\mathrm{PE}} \propto \varepsilon_{\mathrm{ij}} \sin(2\beta)$, where β is the angle between the polarisation of the incident light and $\mathrm{k_{SAW}}$, and $\varepsilon_{\mathrm{ij}}$ is the strain component parallel to $\mathrm{k_{SAW}}$.

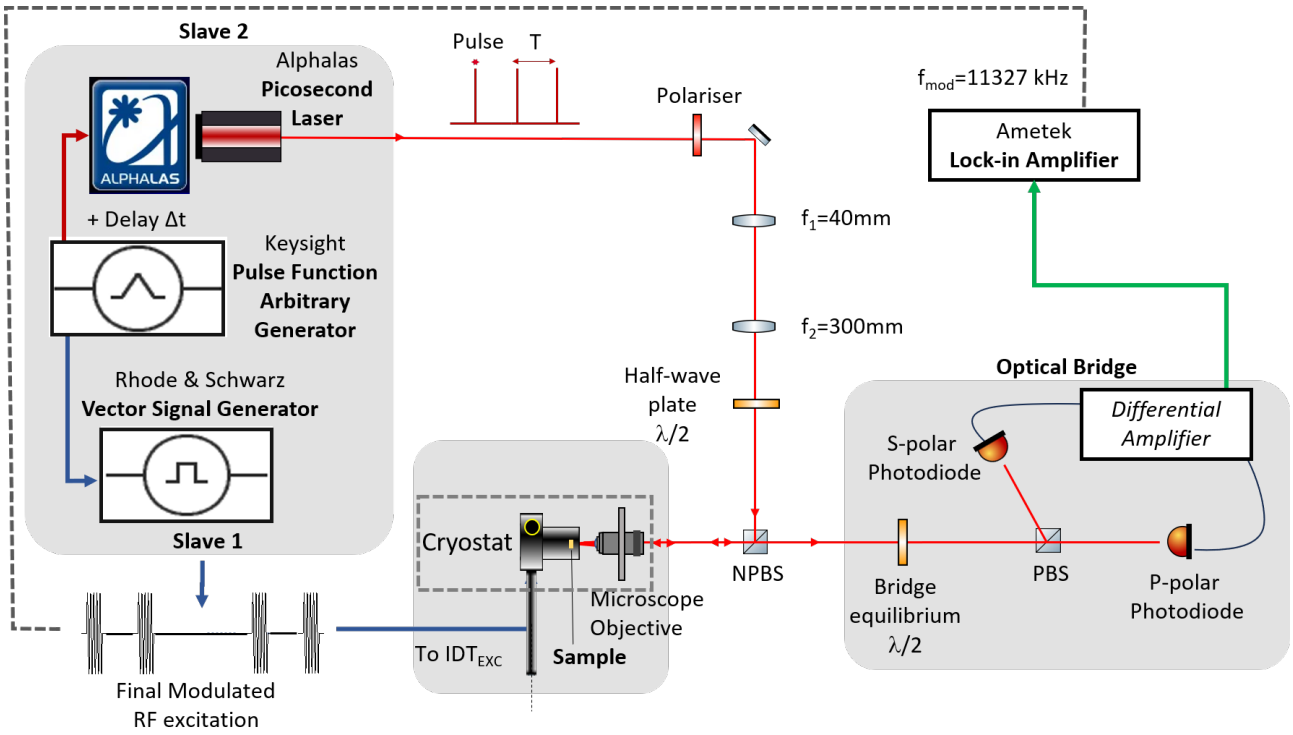

Figure 9.3: Complete Electrical pump and optical probe setup. The modulated RF excitation are fed to the IDT, while the linearly polarised optical probe is made to pass through the microscope objective onto the sample. The laser pulse is reflected and is sent to the optical bridge for detection of its polarisation rotation.

3 Assessing the Improved Experimental upgrade

In this section, the improvements made to the setup are assessed. The spatial and temporal resolution achieved in this configuration are examined, and an example of the photo-elastic effect on Polycrystalline Sample B (FeRh/GaAs) is investigated.

3.1 Spatial and Temporal Resolution

The spatial and temporal resolutions in a pump-probe (be it all optical or as given here an electrical-pump coupled to an optical-probe) experiment, are pivotal factors that determine the ability to investigate and accurately measure the dynamics under scrutiny. These parameters play a crucial role in elucidating intricate temporal variations and spatial distributions of the phenomena, thereby facilitating precise characterisation and analysis.

Time

To assess the stability and accuracy of the experimental setup, edge-to-edge jitter and delay measurements were conducted using an ultrafast **NewFocus** Photodiode (25 GHz Bandwidth). Jitter refers to the brief fluctuations in the positions of the transition edges over time compared to their intended values. It was determined that the temporal jitter between the RF signal and the optical pulse reached a maximum of approximately 15 ps. Furthermore, the minimum temporal delay introduced by the pulse function generator was quantified to be approximately 10 ps.

In our experimental configuration, the measured dynamics are driven by forced excitation, wherein the frequency of the Surface Acoustic Wave (SAW) serves as the driving frequency for the dynamical behaviour. The typical frequency of the SAW, $f_{\mathrm{SAW}} \sim 400$ MHz, imply strain fields oscillating at ~ 2.5 ns. As such, a minimum temporal delay of 10 ps is deemed adequate to satisfy the sampling theorem for accurate reconstruction of the dynamics. Moreover, it is crucial to consider how the inherent characteristics of the pump-probe setup impact the reconstruction of dynamics. To probe

the dynamics, a picosecond laser is used. Following an investigation into the relationship between pulse width and power level, the narrowest temporal profile available has been chosen: $\tau = 67$ ps wide. Again as $\tau << 2.5$ ns, this is amply satisfactory. Consequently, the newly implemented setup facilitates precise measurements within this RF-pulse and optical-probe configuration.

Space

Likewise, in order to obtain an accurate measurement in the spatial regime, the convolution of the laser spot and the SAW wavelength must be taken into account. To be precise, the laser spot does not convolute with the strain but with the sinusoidal variation of the optical index that is modulated at the SAW frequency as it propagates. The laser spot can be approximated to a Gaussian function with measured FWHM equal to 1.5 μm[5] on average. In order to get acceptable measurement, the spot should be smaller than half the wavelength at least. The minimum $\lambda_{SAW} = 3.2$ μm. This is acceptable at the 0.4 numerical aperture being used.

3.2 Testing of the photo-elastic effect on FeRh/GaAs

On figure [9.4] are represented the first evidence of photoelastic effect on the polycrystalline Sample B: FeRh/GaAs. Here, delay line 1 is considered (c.f. figure [4.22] for the sample). Fig. **(a)** shows the edge between the GaAs region (covered by the Kapton tape during sputtering) and the more reflective metallic FeRh region. The horizontal ligne is added to distinguish the region where the IDTs generate the SAWs, to the region where no SAWs propagate. The red-box represents the region where the photoelastic experiment is performed. Figures **(b)** & **(c)** correspond to the red box regions. The SAW is generated at 398 MHz, i.e 7.2 μm. Figure **(b)** is the reflection cartography demodulated at f = 300 kHz (the probe beam modulation). Here the step between the GaAs and the FeRh layer can be clearly seen. This corresponds to the FeRh being more reflective than GaAs. **(c)** is the photoelastic signal demodulated at f_{MOD} (c.f. figure [9.2], i.e. 11327 Hz). This is a spatial scan, i.e. the time is fixed and the scanning along x and y. Hence the reconstruction of the regions of compression and expansion as the SAWs propagate. This is the first result of generation of photo-elastic effect using our new set-up. In order to obtain the photo-elastic rotation, we need to divide figure **(c)** by figure **(b)**. However, this is not the aim here, and i leave it to future students to study the photo-elastic effects on FeRh. This section hence concludes positively the implementation of the improved electrical-pump and optical-probe setup.

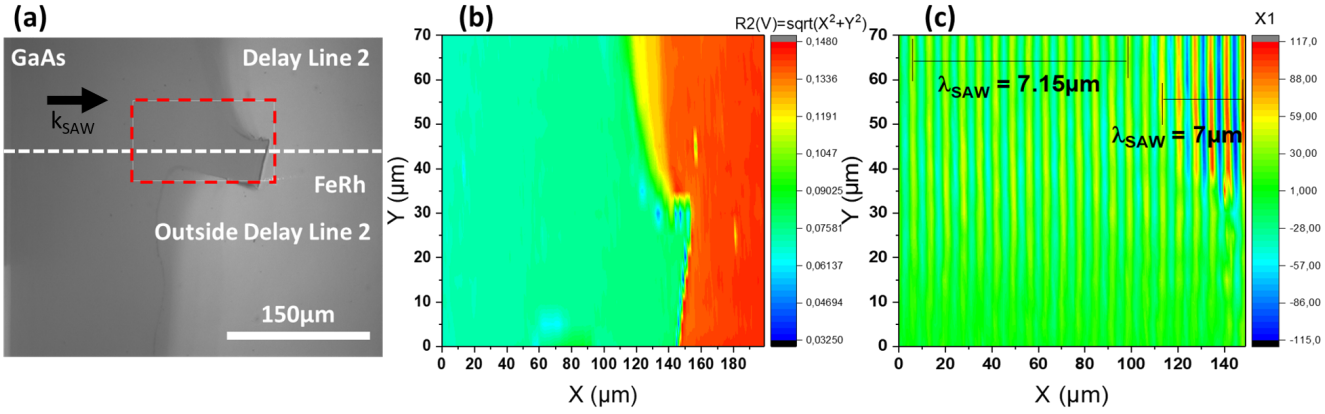

Figure 9.4: **(a)**: Reflectivity image of the GaAs and FeRh regions near the delay line 2, obtained by simply using the CCD camera, c.f. figure [2.15]. The red region is of interest here. **(b)** Reflectivity image obtained from the electrical-pump and optical-probe setup, c.f. figure [9.3]. This reflectivity image is obtained by demodulating the signal at f = 300 kHz. Here, again as FeRh is metallic and is more reflective, there is a different in signal level between FeRh and GaAs. **(c)** This represents the photo-elastic image obtained by demodulating at $f_{MOD} = 11327$ Hz. This is obtained by fixing the time delay, and scanning spatially. We can thus obtain regions of expansion and compression as the SAWs propagate.

[5] FWHM $\approx 2.3548 \times \sigma$

Conclusion and Perspectives

Conclusion

This thesis primarily focused on the investigation of the interaction between Surface Acoustic Waves (SAWs) and magnetic FeRh thin films via magneto-elastic coupling. Although FeRh is an old material, it remains an extremely interesting model material, both for fundamental research and future technological applications. This interest is exacerbated by the lattice, electronic, and magnetic changes in the degree of freedom occurring concomitantly with the antiferromagnetic-ferromagnetic phase transition. In Chapter 2 are presented the two samples over which all the experimental data are taken. Their subsequent characterisation by diffractometry, magnetometry, reflectivity, and magneto-optical techniques served as a starting point for an all-rounded manuscript. After a review of useful theoretical concepts regarding ferromagnetic resonance and linear elasticity in condensed matter, a numerical model based on Farnell-Adler elastic wave propagation in thin films was used to investigate the acoustic eigen-modes and acoustic eigen-values for studying SAW dynamics in the two tri-layered systems: SiO_2/FeRh/MgO and FeRh/Ta/GaAs. In parallel, the elastic constants of FeRh was investigated using BLS, pico-second laser and Farnell-Adler modelling. This collaboration allowed the first determination of the complete set of elastic constants (C_{11}, C_{12} and C_{44}), both in the Antiferromagnetic and Ferromagnetic phases, and resulted in the publication of a scientific paper [168].

The original results I obtained in the course of this work are subsequently reported in Chapters 5 to 9, and are summarised as follows:

- **Chapter 5: SAW-FMR**: Here, we investigated an alternative method to satisfy the resonant conditions of SAW-FMR interaction, when the magnetic field is parallel to k_{SAW}. It was demonstrated, using a mathematical model that spin-waves eigen-frequencies can be softened close to the sample coercivity, opening the perspective to have SAW-FMR coupling using sub-GHz SAWs, even in the absence of a hard-axis of magnetic anisotropy. Additionally, using a power-transfer approach between the propagating SAW and the magnetic layer, a generalised expression of the SAW amplitude attenuation and its relative velocity variation with respect to temperature-dependent parameters such as the ferromagnetic fraction, Rayleigh velocity, and SAW frequency, was derived.

- **Chapter 7: SAW-B**: Here, we demonstrated experimentally that it was indeed possible to have SAW-FMR resonant interaction, in the FM phase, at field values corresponding to the local coercivity. Moreover, by harnessing the FM-to-AFM phase transition occurring close to room temperature, the validity of the model was extended by showing that the SAW-FMR resonance fields and local coercive fields have the same temperature dependency for a magnetic field parallel to k_{SAW}. In the second part of this chapter, we investigated the angular dependence of the magneto-elastic coupling on polycrystalline FeRh. This resulted in the most surprising results of the thesis. It was revealed that the SAW-FMR interaction is non-zero for all magnetic field orientations. This surprising result, opposite to our initial expectations, prompted further investigation. LMOKE measurements subsequently exposed a non-zero magneto-elastic driving field for all magnetic field orientations, as the magnetisation is never orthogonal to k_{SAW}. An on-going

efforts in modelling the angular-SAW-FMR interaction within the observed geometry has been attempted, so as to understand the origin of the double resonance fields and the corresponding SAW-FMR envelopes.

- **Chapter 6: SAW-T and 8: SAW-B-T**: Here, the SAW interaction with the magnetic FeRh layer was investigated with respect to temperature, initially in zero-magnetic field. Attempts were made to harness the change in unit cell volume across the AFM-FM phase transition to shift the transition temperatures non-resonantly. By comparing SAW amplitude attenuation measurements for zero- and non-zero-magnetic field measurements, the existence of both resonant and non-resonant interactions between the SAWs and the FeRh layer was revealed. Several hypotheses, such as AFM-FM domain scattering and domain-wall interactions, were suggested to explain the experimental data. Lastly, using the complete set of elastic constants measured in the AFM and FM phases, the variation of the Rayleigh velocity with respect to temperature was calculated. It was subsequently shown that on relative velocity variation measurements, the opening at the transition is well accounted for by the Rayleigh velocity calculation. It was concluded with fair certainty that a SAW phase variation measurement is a fairly low-cost and easy means to determine the elastic contribution across a magnetic phase transition.

- **Chapter 9**: Here, an improvement of the existing setup for dynamic measurement of SAW interaction with the magnetic layer was described. The ability to induce an electronic delay between the electrical-pump and optical-probe, bypassing the need of a mechanical delay line, significantly reduces the acquisition time and light divergence effects. This will undoubtedly benefit to future experiments.

These results underscore the intriguing physics governing the interactions between SAWs and FeRh thin films, especially concerning phase transition properties and both resonant and non-resonant interactions. FeRh remains a highly promising candidate for spintronics applications, offering potential for advances in data storage, magnetic sensors, and other cutting-edge technologies due to its unique magnetic and electronic properties.

Perspectives

Building on the results and insights obtained in this thesis, several promising directions for future research and development in the field of Surface Acoustic Waves (SAWs) interaction with FeRh thin films via magneto-elastic coupling can be envisioned. These directions aim to deepen our understanding of the underlying physics, explore new applications, and enhance the capabilities of existing technologies. The following perspectives outline potential areas for further investigation:

- **Measuring dynamics**: One of the primary areas of future research involves using the newly implemented electrical-pump and optical-probe setup to investigate both the strain dynamics and magnetisation dynamics in FeRh thin films (c.f. Chapter [9]). Time-resolved studies will allow for detailed insights into the coupling mechanisms between the SAWs and the magnetic properties of FeRh. Specifically, this approach may facilitate the investigation of the double resonance fields observed in polycrystalline FeRh, shedding light on the complex interactions and transitions between the antiferromagnetic and ferromagnetic phases.

- **Enhancing Acoustic Power**: Secondly, one way to increase the SAW-FMR interaction is by either increasing the RF power from the generator or by developing and integrating devices to increase the SAW acoustic power, such as reflectors [253], multi-layered resonators [152] and circular IDTs [254], among others. Implementing acoustic reflectors to confine and redirect SAWs, designing rounded IDTs to focus SAWs into specific regions can only increase the local acoustic power density and strengthening possible magneto-elastic coupling. These developments have similar price tag to our current IDT design, but will significantly advance and improve SAW performance in future experiments.

- **Coupling with Love Waves**: Another promising direction for future research is to explore the interaction between Surface Acoustic Waves (SAWs) and FeRh thin films using Love waves. Unlike Rayleigh waves, which have a more complex elliptical motion and deeper penetration into the material, Love waves are confined to the surface and exhibit a strong horizontal shear component, resulting in a higher acoustic energies concentrated in the thin guiding layer (c.f. Chapter [4]). This confinement makes them particularly sensitive to surface properties and magnetic effects. Integrating Love wave-based technologies could offer improved control over the acoustic wave propagation and improve the magneto-elastic coupling for SAW-FMR interaction [255].

- **Non-Reciprocity SAW-FMR**: A further area of investigation is the detailed exploration of non-reciprocal effects in FeRh and other materials such as synthetic antiferromagnets (SAFs). Despite the extensive body of research on this topic [256]–[258], additional studies could provide valuable insights into the origins and implications of non-reciprocal phenomena. Non-reciprocal effects on FeRh across the FM-AFM phase might allow for a deeper understanding of how magnetic phase transitions influence wave propagation characteristics, and could also reveal new mechanisms for controlling wave propagation at the nano-scale, potentially paving the way for innovative applications

By pursuing these perspectives, the field of magneto-elastic coupling and SAW interactions with FeRh thin films can continue to advance.

Part IV
Appendix

Appendix A

Farnell-Adler 3 layers Matrix

In the case of 3 layers, the determinant seen in equation [4.44] is affected by the second layer and denoted as $.^{layer2}$. Similarly the boundary conditions must include the continuity in the displacements and the normal compression stress at the interface between layer 1 and layer 2.

The full determinant (10×10) taking into account the three layers is given as:

$$
\begin{bmatrix}
1 & 1 & -1 & -1 & -1 \\
r_{s1} & r_{s2} & -r_{11} & -r_{12} & -r_{13} \\
0 & 0 & e^{q_{11}kh_1} & e^{q_{12}kh_1} & e^{q_{13}kh_1} \\
0 & 0 & r_{11}e^{q_{11}kh_1} & r_{12}e^{q_{12}kh_1} & r_{13}e^{q_{13}kh_1} \\
i\dfrac{C_{13,\mathrm{sub}}}{C_{33,\mathrm{sub}}} + q_{s1}r_{s1} & i\dfrac{C_{13,\mathrm{sub}}}{C_{33,\mathrm{sub}}} + q_{s2}r_{s2} & -i\dfrac{C_{12,\mathrm{layer1}}}{C_{33,\mathrm{sub}}} - q_{11}r_{11}\dfrac{C_{11,\mathrm{layer1}}}{C_{33,\mathrm{sub}}} & -i\dfrac{C_{12,\mathrm{layer1}}}{C_{33,\mathrm{sub}}} - q_{12}r_{12}\dfrac{C_{11,\mathrm{layer1}}}{C_{33,\mathrm{sub}}} & -i\dfrac{C_{12,\mathrm{layer1}}}{C_{33,\mathrm{sub}}} - q_{13}r_{13}\dfrac{C_{11,\mathrm{layer1}}}{C_{33,\mathrm{sub}}} \\
-\dfrac{C_{44,\mathrm{sub}}}{C_{44,\mathrm{layer1}}}(q_{s1} + ir_{s1}) & -\dfrac{C_{44,\mathrm{sub}}}{C_{44,\mathrm{layer1}}}(q_{s2} + ir_{s2}) & q_{11} + ir_{11} & q_{12} + ir_{12} & q_{13} + ir_{13} \\
0 & 0 & -ie^{h_1kq_{11}}\left(\dfrac{C_{12,\mathrm{layer1}}}{C_{11,\mathrm{layer1}}} - iq_{11}r_{11}\right) & -ie^{h_1kq_{12}}\left(\dfrac{C_{12,\mathrm{layer1}}}{C_{11,\mathrm{layer1}}} - iq_{12}r_{12}\right) & -ie^{h_1kq_{13}}\left(\dfrac{C_{12,\mathrm{layer1}}}{C_{11,\mathrm{layer1}}} - iq_{13}r_{13}\right) \\
0 & 0 & -e^{h_1kq_{11}}(q_{11} + ir_{11})\dfrac{C_{44,\mathrm{layer1}}}{C_{44,\mathrm{layer2}}} & -e^{h_1kq_{12}}(q_{12} + ir_{12})\dfrac{C_{44,\mathrm{layer1}}}{C_{44,\mathrm{layer2}}} & -e^{h_1kq_{13}}(q_{13} + ir_{13})\dfrac{C_{44,\mathrm{layer1}}}{C_{44,\mathrm{layer2}}} \\
0 & 0 & 0 & 0 & 0 \\
0 & 0 & 0 & 0 & 0
\end{bmatrix}
\cdots\cdots \hookrightarrow
$$

$$
\begin{bmatrix}
-1 & 0 & 0 & 0 & 0 \\
-r_{14} & 0 & 0 & 0 & 0 \\
e^{q_{14}kh_1} & -e^{q_{21}kh_1} & -e^{q_{22}kh_1} & -e^{q_{23}kh_1} & -e^{q_{24}kh_1} \\
r_{14}e^{q_{14}kh_1} & -r_{21}e^{q_{21}kh_1} & -r_{22}e^{q_{22}kh_1} & -r_{23}e^{q_{23}kh_1} & -r_{24}e^{q_{24}kh_1} \\
-i\dfrac{C_{12,\mathrm{layer1}}}{C_{33,\mathrm{sub}}} - q_{14}r_{14}\dfrac{C_{33,\mathrm{layer1}}}{C_{33,\mathrm{sub}}} & 0 & 0 & 0 & 0 \\
q_{14} + ir_{14} & 0 & 0 & e^{h_1kq_{23}}(q_{23} + ir_{23}) & e^{h_1kq_{24}}(q_{24} + ir_{24}) \\
-ie^{h_1kq_{14}}\left(\dfrac{C_{12,\mathrm{layer1}}}{C_{11,\mathrm{layer1}}} - iq_{14}r_{14}\right) & e^{h_1kq_{21}}\left(q_{21}r_{21}\dfrac{C_{11,\mathrm{layer2}}}{C_{11,\mathrm{layer1}}} + i\dfrac{C_{12,\mathrm{layer2}}}{C_{11,\mathrm{layer1}}}\right) & e^{h_1kq_{22}}\left(q_{22}r_{22}\dfrac{C_{11,\mathrm{layer2}}}{C_{11,\mathrm{layer1}}} + i\dfrac{C_{12,\mathrm{layer2}}}{C_{11,\mathrm{layer1}}}\right) & e^{h_1kq_{23}}\left(q_{23}r_{23}\dfrac{C_{11,\mathrm{layer2}}}{C_{11,\mathrm{layer1}}} + i\dfrac{C_{12,\mathrm{layer2}}}{C_{11,\mathrm{layer1}}}\right) & e^{h_1kq_{24}}\left(q_{24}r_{24}\dfrac{C_{11,\mathrm{layer2}}}{C_{11,\mathrm{layer1}}} + i\dfrac{C_{12,\mathrm{layer2}}}{C_{11,\mathrm{layer1}}}\right) \\
-e^{h_1kq_{14}}(q_{14} + ir_{14})\dfrac{C_{44,\mathrm{layer1}}}{C_{44,\mathrm{layer2}}} & e^{h_1kq_{21}}(q_{21} + ir_{21}) & e^{h_1kq_{22}}(q_{22} + ir_{22}) & e^{h_1kq_{23}}(q_{23} + ir_{23}) & e^{h_1kq_{24}}(q_{24} + ir_{24}) \\
0 & e^{(h_1+h_2)kq_{21}}(q_{21}r_{21} + i\dfrac{C_{12,\mathrm{layer2}}}{C_{11,\mathrm{layer2}}}) & e^{(h_1+h_2)kq_{22}}(q_{22}r_{22} + i\dfrac{C_{12,\mathrm{layer2}}}{C_{11,\mathrm{layer2}}}) & e^{(h_1+h_2)kq_{23}}(q_{23}r_{23} + i\dfrac{C_{12,\mathrm{layer2}}}{C_{11,\mathrm{layer2}}}) & e^{(h_1+h_2)kq_{24}}(q_{24}r_{24} + i\dfrac{C_{12,\mathrm{layer2}}}{C_{11,\mathrm{layer2}}}) \\
0 & e^{(h_1+h_2)kq_{21}}(q_{21} + ir_{21}) & e^{(h_1+h_2)kq_{22}}(q_{22} + ir_{22}) & e^{(h_1+h_2)kq_{23}}(q_{23} + ir_{23}) & e^{(h_1+h_2)kq_{24}}(q_{24} + ir_{24})
\end{bmatrix}
\cdots
$$

Appendix B

Expressions of SAW-FMR

1 Introduction

In this Appendix, we will calculate the generalised expressions of the real and imaginary parts of the change in the SAW wave-vector: Δk_{SAW}. Then we will find in the limiting cases, the corresponding formulae of the relative velocity variations and the SAW amplitude attenuation. This will serve to study the experimental data obtained on the Polycrystalline Sample B: FeRh/Ta/GaAs, c.f. Chapters [6-8].
The starting point is the expression of the FMR power given by equation [5.19].

$$\begin{aligned}\Delta P_{FMR} &= \left[\frac{i\,\omega_{SAW}\;M_s}{2}\int_{V_0}(b_\theta, b_\phi)^*\,[\bar{\chi}]\begin{pmatrix}b_\theta\\ b_\phi\end{pmatrix}\,dV\right]\\ &= \frac{i\,\omega_{SAW}\;M_s\,V_0}{2}\left(|b_\theta|^2\chi_{11}+|b_\phi|^2\chi_{22}+\chi_{12}(b_\theta^* b_\phi - b_\phi^* b_\theta)\right)\end{aligned} \tag{B.1}$$

With the Polder matrix given by :

$$\bar{\chi}=\begin{bmatrix}\chi_{11} & \chi_{12}\\ \chi_{21} & \chi_{22}\end{bmatrix}=\frac{\gamma}{D}\begin{bmatrix}\gamma\frac{E_{\phi\phi}}{M_s}\left(\mathbf{k_{SW}}\right)-i\alpha\,\omega_{SAW} & -i\omega_{SAW}\\ i\omega_{SAW} & \gamma\frac{E_{\theta\theta}}{M_s}\left(\mathbf{k_{SW}}\right)-i\alpha\,\omega_{SAW}\end{bmatrix} \tag{B.2}$$

where $E_{\phi\phi}$ and $E_{\theta\theta}$ are the second derivatives of the total magnetic free energy with respect to ϕ_M and θ_M respectively, and

$$\begin{cases} D=-(1+\alpha^2)\left(\omega_{SAW}^2-\omega_0^2+i\kappa\,\omega_{SAW}\right)\\ \omega_0^2\left(\mathbf{k_{SW}}\right)=\dfrac{1}{{M_s}^2}\dfrac{\gamma^2}{\alpha^2+1}\left[E_{\theta\theta}\left(\mathbf{k_{SW}}\right)\times E_{\phi\phi}\left(\mathbf{k_{SW}}\right)\right]\\ \kappa=\dfrac{\gamma}{M_s}\dfrac{\alpha}{\alpha^2+1}\left[E_{\theta\theta}\left(\mathbf{k_{SW}}\right)+E_{\phi\phi}\left(\mathbf{k_{SW}}\right)\right]\end{cases} \tag{B.3}$$

To simplify the notation: $E_{ii}(\mathbf{k_{SW}}) \rightarrow E_{ii}$ and $\omega_{SAW} \rightarrow \omega$. The Polder susceptibility terms are thus written as:

$$\begin{cases}\chi_{11}=\dfrac{\gamma\left(\frac{E_{\phi\phi}\gamma}{M_s}-i\alpha\omega\right)}{-(1+\alpha^2)(i\kappa\omega+\omega^2-\omega_0^2)}\\ \chi_{22}=\dfrac{\gamma\left(\frac{E_{\theta\theta}\gamma}{M_s}-i\alpha\omega\right)}{-(1+\alpha^2)(i\kappa\omega+\omega^2-\omega_0^2)}\\ \chi_{12}=\dfrac{i\gamma\omega}{-(1+\alpha^2)(i\kappa\omega+\omega^2-\omega_0^2)}\end{cases} \tag{B.4}$$

2 Real and Imaginary parts of ΔP_{FMR}

$$\Delta P_{FMR} = \frac{i\,\omega_{SAW}\,M_s\,V_0}{2}\left(|b_\theta|^2\frac{\gamma\left(\frac{E_{\phi\phi}\gamma}{M_s}-i\alpha\omega\right)}{-(1+\alpha^2)(i\kappa\omega+\omega^2-\omega_0^2)}+|b_\phi|^2\frac{\gamma\left(\frac{E_{\theta\theta}\gamma}{M_s}-i\alpha\omega\right)}{-(1+\alpha^2)(i\kappa\omega+\omega^2-\omega_0^2)}+\frac{i\gamma\omega}{-(1+\alpha^2)(i\kappa\omega+\omega^2-\omega_0^2)}(b_\theta^* b_\phi - b_\phi^* b_\theta)\right) \tag{B.5}$$

$$\Delta P_{FMR} = \frac{\omega_{SAW}\,M_s\,V_0\,\gamma}{2\,(1+\alpha^2)(i\kappa\omega+\omega^2-\omega_0^2)}\left(i\frac{\gamma}{M_s}(E_{\phi\phi}|b_\theta|^2+E_{\theta\theta}|b_\phi|^2)-\alpha\omega(|b_\theta|^2+|b_\phi|^2)+\omega(b_\theta^* b_\phi - b_\phi^* b_\theta)\right) \tag{B.6}$$

Replacing the κ term by : $\kappa = \gamma\,\frac{\alpha}{\alpha^2+1}\,[E_{\theta\theta}+E_{\phi\phi}]$

$$\Delta P_{FMR} = \frac{\omega_{SAW}\,M_s\,V_0\,\gamma}{2\left((\alpha^2+1)(\omega^2-\omega_0^2)+i\gamma\alpha\omega(E_{\theta\theta}+E_{\phi\phi})\right)}\left(i\frac{\gamma}{M_s}(E_{\phi\phi}|b_\theta|^2+E_{\theta\theta}|b_\phi|^2)-\alpha\omega(|b_\theta|^2+|b_\phi|^2)+\omega(b_\theta^* b_\phi - b_\phi^* b_\theta)\right) \tag{B.7}$$

Since there is the presence of imaginary terms both in the numerator and denominator, to separate the given expression into its real and imaginary parts, we will first multiply both the numerator and the denominator by the complex conjugate of the denominator.

$$\Delta P_{FMR} = \frac{\left(i\frac{\gamma}{M_s}(E_{\phi\phi}|b_\theta|^2+E_{\theta\theta}|b_\phi|^2)-\alpha\omega(|b_\theta|^2+|b_\phi|^2)+\omega(b_\theta^* b_\phi - b_\phi^* b_\theta)\right)\cdot 2\left((\alpha^2+1)(\omega^2-\omega_0^2)-i\gamma\alpha\omega(E_{\theta\theta}+E_{\phi\phi})\right)}{4\left[\left((\alpha^2+1)(\omega^2-\omega_0^2)\right)^2+(\gamma\alpha\omega(E_{\theta\theta}+E_{\phi\phi}))^2\right]} \tag{B.8}$$

The above expression is expanded, simplified and separated into real and imaginary parts: $\Delta P_{FMR} = \Re\,\Delta P_{FMR} + i\,\Im\Delta P_{FMR}$

$$\Re\Delta P_{FMR} = \frac{2\left[-\alpha\omega(|b_\theta|^2+|b_\phi|^2)(\alpha^2+1)(\omega^2-\omega_0^2)+\omega(b_\theta^* b_\phi - b_\phi^* b_\theta)(\alpha^2+1)(\omega^2-\omega_0^2)\right]}{4\left[\left((\alpha^2+1)(\omega^2-\omega_0^2)\right)^2+(\gamma\alpha\omega(E_{\theta\theta}+E_{\phi\phi}))^2\right]} \tag{B.9}$$

$$\Im\Delta P_{FMR} = \frac{2\left[\frac{\gamma}{M_s}(E_{\phi\phi}|b_\theta|^2+E_{\theta\theta}|b_\phi|^2)(\alpha^2+1)(\omega^2-\omega_0^2)-\gamma\alpha\omega(E_{\theta\theta}+E_{\phi\phi})(\alpha^2+1)(\omega^2-\omega_0^2)\right]}{4\left[\left((\alpha^2+1)(\omega^2-\omega_0^2)\right)^2+(\gamma\alpha\omega(E_{\theta\theta}+E_{\phi\phi}))^2\right]} \tag{B.10}$$

Recall, the SAW amplitude attenuation, $\Delta\Gamma$ and the SAW relative velocity variations are defined as:

$$\Delta\Gamma = 20\log e^{\left[\frac{\Re[\Delta P_{FMR}(B,T)]-\Re[\Delta P_{FMR}(B_0,T_0)]}{2\,P_{SAW}^0}\right]} \tag{B.11}$$

$$\frac{\Delta V}{V} = -\frac{\Im[\Delta P_{FMR}(B,T)]-\Im[\Delta P_{FMR}(B_0,T_0)]}{2\,L\,P_{SAW}^0\,k_{SAW}} \tag{B.12}$$

---

3 Limiting Cases with cubic anisotropy only

We shall now evaluate the corresponding $\Delta\Gamma$ and $\frac{\Delta V}{V}$ dependencies out of the magnetic energies governing our system. We first recall the second derivative of these energies.

$$\begin{cases} E_{\theta\theta} = \mu_0 H M_s\cos(\phi_H\text{-}\phi_M) + K_c\left(2-\sin^2(2\,(\phi_c-\phi_M))\right) \\ \qquad + \mu_0 M_s H_{EX}(k_{SW}a)^2 + \mu_0 {M_s}^2\left(1\text{ - }\frac{dk_{SW}}{2}+\frac{d^2k_{SW}^2}{6}\right) \\ E_{\phi\phi} = \mu_0 H M_s\cos(\phi_H\text{-}\phi_M) + 2K_c\cos(4\,(\phi_c-\phi_M)) \\ \qquad + \mu_0 M_s H_{EX}(k_{SW}a)^2 + \mu_0 {M_s}^2\sin^2(\phi_M)\left(\frac{dk_{SW}}{2}\text{ - }\frac{d^2k_{SW}^2}{6}\right) \end{cases} \tag{B.13}$$

and the magneto-elastic tickles fields given in equations [5.13-5.14] as:

$$b_\theta = i\left(\frac{2B_2}{M_s}\,\varepsilon_{xz} + \mu_0\, M_s\, \omega_{xz}\right)\cos(\phi_M) = iB_{\varepsilon\omega}\cos(\phi_M) \tag{B.14}$$

$$b_\phi = \frac{2B_1}{M_s}\,\sin(\phi_M)\cos(\phi_M)\,\varepsilon_{xx} \tag{B.15}$$

3.1 Field parallel to SAW propagation

3.1.1 At saturation

Here: $\phi_H = 0°$ and the cubic anisotropy is assumed to be aligned with k_{SAW}, $\phi_c = 0°$ leads to:

$$\begin{cases} E_{\theta\theta} = \mu_0 H M_s + 2K_c + \mu_0 M_s H_{EX}(k_{SW}a)^2 + \mu_0 M_s^2\left(1 - \dfrac{dk_{SW}}{2} + \dfrac{d^2k_{SW}^2}{6}\right) \\ E_{\phi\phi} = \mu_0 H M_s + 2K_c + \mu_0 M_s H_{EX}(k_{SW}a)^2 \end{cases} \tag{B.16}$$

$\phi_H = \phi_M = \phi_c = 0°$

i Phase Variations

$$\frac{\Delta V}{V} \approx \frac{\Im[\Delta P_{FMR}]}{2\,L\,P^0_{SAW}\,k_{SAW}} \tag{B.17}$$

Here: $\omega_{SAW} = \omega \ll \omega_0$, $\omega_0 \sim \gamma\mu_0 H$ and $\alpha = 0[1]$ and keep only 1^{st} order terms of k_{SW}. Also, at saturation, $\mu_0 H >> \mu_0 M_s$

$$\frac{\Delta V}{V} \approx \frac{\gamma^2\omega\mu_0 H V_0 (B_{\varepsilon\omega})^2}{2{\omega_0}^2}\frac{1}{2\,L\,P^0_{SAW}\,k_{SAW}} \approx \frac{V_0\,M_s {B_{\varepsilon\omega}}^2\,V_{SAW}}{4\,L\,P^0_{SAW}\,B_{SAT}} \tag{B.18}$$

Thus,

$$\left.\frac{\Delta V}{V}\right|_{B_{SAT}} \approx \frac{V_0\,M_s {B_{\varepsilon\omega}}^2\,V_{SAW}}{4\,L\,P^0_{SAW}\,B_{SAT}} \tag{B.19}$$

Now we develop the expression of P^0_{SAW} found in the denominator. Recall, from equation [5.26],

$$P_{SAW} = \frac{1}{2}\rho\, t\, V_{SAW}\,{\omega_{SAW}}^2 \int_0^d \left[|u_x|^2 + |u_z|^2\right] dz \tag{B.20}$$

Let us consider only solution of the semi-infinite model, the development of partial waves solution lead to the following expressions for the elastic displacements.

$$\vec{u} = \left[\begin{pmatrix} U_1 \\ 0 \\ W_1 \end{pmatrix} e^{(-q_1 z')} + \begin{pmatrix} U_2 \\ 0 \\ W_2 \end{pmatrix} e^{(-q_2 z')}\right] e^{i(\omega\, t - k\, x)} \tag{B.21}$$

Re-writing those elastic displacements lead to:

$$u_x = U\left(e^{-kq_1 z} - \frac{2q_1q_2}{1+q_2^2}e^{-kq_2 z}\right)\cos(kx)$$
$$u_z = iq_1 U\left(\frac{2}{1+q_2^2}e^{-kq_2 z} - e^{-kq_1 z}\right)\cos(kx)$$

From the definition of the linear and rotational strain components, we can write:

$$\varepsilon_{xx} = -kU\left(e^{-kq_1 z} - \frac{2q_1q_2}{1+q_2^2}e^{-kq_2 z}\right)\sin(kx)$$
$$\varepsilon_{zz} = ikq_1U\left(q_1e^{-kq_1 z} - \frac{2q_2}{1+q_2^2}e^{-kq_2 z}\right)\cos(kx)$$
$$\varepsilon_{xz} = \frac{kU}{2}\left(-q_1e^{-kq_1 z} + \frac{2{q_2}^2q_1}{1+q_2^2}e^{-kq_2 z}\right)\cos(kx) - iq_1U\left(\frac{2}{1+q_2^2}e^{-kq_2 z} - e^{-kq_1 z}\right)\sin(kx)$$
$$\omega_{xz} = \frac{kU}{2}\left(-q_1e^{-kq_1 z} + \frac{2{q_2}^2q_1}{1+q_2^2}e^{-kq_2 z}\right)\cos(kx) + iq_1U\left(\frac{2}{1+q_2^2}e^{-kq_2 z} - e^{-kq_1 z}\right)\sin(kx)$$

$$\int_0^d \left(u_x(z)^2 + u_z(z)^2\right)dz = U^2\left(d\left(\frac{-q_1^2(q_2^2-1)^2 + (2q_1q_2 - q_2^2 - 1)^2}{(q_2^2+1)^2}\right) + d^2 f_{q_1,q_2}\right) \tag{B.22}$$

where f_{q_1,q_2} is a function dependent on q_1, q_2. From a development to 0[k], we have:

$$\int_0^d \left(u_x(z)^2 + u_z(z)^2\right)dz \propto U^2 d \tag{B.23}$$

Similarly,

$$< {B_{\varepsilon\omega}}^2 > = \frac{1}{d}\int_0^d \left(\frac{2B_2}{M_s}\,\varepsilon_{xz}(z) + \mu_0\, M_s\, \omega_{xz}(z)\right)^2 dz \propto U^2 {k_{SAW}}^2 \tag{B.24}$$

Coming back to the relative velocity variations at saturation,

$$\begin{aligned}
\left.\frac{\Delta V}{V}\right|_{B_{SAT}} &\approx \frac{V_0\, M_s {B_{\varepsilon\omega}}^2\, V_{SAW}}{4\, L\, P^0_{SAW}\, B_{SAT}} \\
&\approx \frac{V_0\, M_s {B_{\varepsilon\omega}}^2\, V_{SAW}}{2\, L\, B_{SAT}\, \rho\, t\, V_{SAW}\, {\omega_{SAW}}^2 \int_0^d \left[|u_x|^2 + |u_z|^2\right] dz} \\
&\approx \frac{V_0\, M_s U^2 {k_{SAW}}^2}{2\, L\, B_{SAT}\, \rho\, t\, {\omega_{SAW}}^2 U^2 d} \\
&\approx \frac{V_0\, M_s {k_{SAW}}^2}{2\, L\, B_{SAT}\, \rho\, t\, {\omega_{SAW}}^2 d}
\end{aligned} \tag{B.25}$$

So,

$$\left.\frac{\Delta V}{V}\right|_{B_{SAT}} \approx \frac{1}{{V_{SAW}}^2}\frac{V_0}{2\rho V_{DL}}\frac{M_s}{B_{SAT}} \tag{B.26}$$

We define the delay line volume as: V_{DL} = L t d, and the magnetic fraction in the system as: $x_{FM} = V_0/V_{DL}$. Hence we have at the saturation,

$$\left.\frac{\Delta V}{V}\right|_{B_{SAT}} \propto x_{FM}\frac{M_s}{{V_{SAW}}^2\, B_{SAT}} \tag{B.27}$$

ii Amplitude Variations

$$\Delta\Gamma \approx 20\log e^{\left[\frac{\Re[\Delta P_{FMR}]}{2\, P^0_{SAW}}\right]} \tag{B.28}$$

$$\Re\Delta P_{FMR} = \frac{2\left[-\alpha\omega(|b_\theta|^2 + |b_\phi|^2)(\alpha^2+1)(\omega^2-\omega_0^2) + \omega(b_\theta^* b_\phi - b_\phi^* b_\theta)(\alpha^2+1)(\omega^2-\omega_0^2)\right]}{4\left[\left((\alpha^2+1)(\omega^2-\omega_0^2)\right)^2 + (\gamma\alpha\omega(E_{\theta\theta}+E_{\phi\phi}))^2\right]} \tag{B.29}$$

-Replacing the expressions of b_θ, b_ϕ
-Here: $\omega_{SAW} = \omega \ll \omega_0$, $\omega_0 \sim \gamma\mu_0 H$ and $\alpha = 0$[1]

$$\Delta\Gamma \approx 20 \log \exp\left[\frac{1}{2\,P^0_{SAW}}\,\frac{\gamma^2\,M_s\,\alpha\omega {B_{\varepsilon\omega}}^2}{2\omega_0^2}\right] \tag{B.30}$$

Replacing the terms of P^0_{SAW} and $B_{\varepsilon\omega}$ as above we have:

$$\begin{aligned}\Delta\Gamma \propto 20 \log \exp &\left[\frac{1}{\rho\, t\, V_{SAW}\, {\omega_{SAW}}^2 \int_0^d \left[|u_x|^2 + |u_z|^2\right] dz}\,\frac{\gamma^2\,M_s\,\alpha\omega_{SAW} {B_{\varepsilon\omega}}^2}{2\gamma^2 {B_{SAT}}^2}\right] \\ \propto \frac{20}{\ln(10)} &\left[\frac{1}{\rho\, t\, V_{SAW}\, \omega_{SAW} d}\,\frac{M_s\,\alpha\; {k_{SAW}}^2}{2{B_{SAT}}^2}\right]\end{aligned} \tag{B.31}$$

Similarly, using V_{DL} = L t d, and the magnetic fraction in the system as: $\mathrm{x}_{FM} = V_0/V_{DL}$, we have:

$$\Delta\Gamma|_{B_{SAT}} \propto \frac{x_{FM}\,\alpha\,{\omega_{SAW}}^2}{{V_{SAW}}^3\,{B_{SAT}}^2} \tag{B.32}$$

3.1.2 At Coercivity

$\phi_M = \phi_H + \pi$. Here: $\mu_0 H$ = - $\frac{2K_c}{M_s}$ and $\alpha = 0$[1]

$$\begin{cases} E_{\theta\theta} = -\mu_0 H M_s + K_c\left(2 - \sin^2(2(\phi_c - \phi_H))\right) + \mu_0 M_s H_{EX}(k_{SW}a)^2 + \mu_0 M_s^2\left(1 - \dfrac{dk_{SW}}{2} + \dfrac{d^2k_{SW}^2}{6}\right) \\ E_{\phi\phi} = -\mu_0 H M_s + 2K_c\cos(4(\phi_c - \phi_H)) + \mu_0 M_s H_{EX}(k_{SW}a)^2 + \mu_0 M_s^2 \sin^2(\phi_H)\left(\dfrac{dk_{SW}}{2} - \dfrac{d^2k_{SW}^2}{6}\right) \end{cases}$$

$\phi_H = \phi_c = 0$.

i Phase Variations

$$\frac{\Delta V}{V} \approx -\frac{\Im[\Delta P_{FMR}]}{4\,L\,P^0_{SAW}\,k_{SAW}} \tag{B.33}$$

$$\begin{aligned}\frac{\Delta V}{V} \approx -\frac{1}{4LP^0_{SAW}k_{SAW}} &\left(\frac{\gamma\mu_0\omega M_s V_0}{\left((\gamma\alpha\left(-\mu_0 H M_s + 2K_c\right)\omega)^2 + (\omega_0^2 - \omega^2)^2\right)}\right. \\ &\left(\frac{\gamma}{M_s}\left(b_\theta^2\left(-\mu_0 H M_s + 2K_c\right) + b_\phi^2\left(-\mu_0 H M_s + 2K_c\right)\right)\left(\omega_0^2 - \omega^2\right)\right) \\ &\left.-\omega^2\gamma\alpha\left(2b_\theta b_\phi - \alpha(b_\theta^2 + b_\phi^2)\right)\left(-\mu_0 H M_s + 2K_c\right)\right)\end{aligned} \tag{B.34}$$

Replace b_θ and b_ϕ with the condition $\phi_H = \phi_c$= 0° and ϕ_M= $\phi_H and + \pi$

$$\begin{aligned} b_\theta &= -B_{\varepsilon\omega} \\ b_\phi &= 0 \end{aligned} \tag{B.35}$$

$$\begin{aligned}\frac{\Delta V}{V} \approx -\frac{1}{4LP^0_{SAW}k_{SAW}} &\left(\frac{\gamma\mu_0\omega M_s V_0}{\left((\gamma\alpha\left(-\mu_0 H M_s + 2K_c\right)\omega)^2 + (\omega_0^2 - \omega^2)^2\right)} \times\right. \\ &\left.\left(\frac{\gamma}{M_s}B_{\varepsilon\omega}^2\left(-\mu_0 H M_s + 2K_c\right)\left(\omega_0^2 - \omega^2\right)\right) + \omega^2\gamma\alpha^2 B_{\varepsilon\omega}^2\left(-\mu_0 H M_s + 2K_c\right)\right)\end{aligned} \tag{B.36}$$

Here: $\mu_0 H = \frac{2K_c}{M_s}$

$$\left.\frac{\Delta V}{V}\right|_{B_c} = 0 \tag{B.37}$$

ii Amplitude Variations

$$\Delta\Gamma \approx 20\log e^{\left[\frac{\Re[\Delta P_{FMR}]}{2\,P^0_{SAW}}\right]} \tag{B.38}$$

$$\Re\Delta P_{FMR} = \frac{2\left[-\alpha\omega(|b_\theta|^2+|b_\phi|^2)(\alpha^2+1)(\omega^2-\omega_0^2)+\omega(b^*_\theta b_\phi - b^*_\phi b_\theta)(\alpha^2+1)(\omega^2-\omega_0^2)\right]}{4\left[\left((\alpha^2+1)(\omega^2-\omega_0^2)\right)^2+(\gamma\alpha\omega(E_{\theta\theta}+E_{\phi\phi}))^2\right]} \tag{B.39}$$

$$\Delta\Gamma \approx 20\log\exp\left[-\frac{\gamma^2\alpha V_0\omega B^2_{\varepsilon\omega}\cdot 4K_c\cdot\mu_0 M_s^2\cdot dk_{SW}}{16L\,P^0_{SAW}M_s\left(\left(\omega_0^2-\omega^2\right)^2(1+\alpha^2)^2+\left(\gamma\alpha\left[8K_c+\mu_0M_s^2\left(1-\frac{dk_{SW}}{2}\right)\right]\omega\right)^2\right)}\right] \tag{B.40}$$

$$P^0_{SAW}\propto\frac{1}{2}\rho\,t\,V_{SAW}\,\omega^2U^2d \tag{B.41}$$

$${B_{\varepsilon\omega}}^2\propto U^2{k_{SAW}}^2 \tag{B.42}$$

$$\Delta\Gamma|_{B_c} \quad\propto\quad \frac{\alpha\,\gamma^2\,V_0}{{V_{SAW}}^3} \tag{B.43}$$

3.1.3 Amplitude attenuation and Relative velocity variations

i Amplitude attenuation

$$\Delta\Gamma|_{B_{SAT}}-\Delta\Gamma|_{B_c}\propto\quad\frac{\alpha V_0}{{V_{SAW}}^3}\left(\frac{{\omega_{SAW}}^2}{{B_{SAT}}^2}-\gamma^2\right) \tag{B.44}$$

ii Relative velocity variations

$$\left.\frac{\Delta V}{V}\right|_{B_{SAT}}-\left.\frac{\Delta V}{V}\right|_{B_c}=\left.\frac{\Delta V}{V}\right|_{B_{SAT}} \tag{B.45}$$

$$\left.\frac{\Delta V}{V}\right|_{B_{SAT}}-\left.\frac{\Delta V}{V}\right|_{B_c}\propto x_{FM}\frac{M_s}{{V_{SAW}}^2\,B_{SAT}} \tag{B.46}$$

Appendix C

Slope removal on the relative velocity variation

In this appendix is answered the following question: which Temperature slope is removed on GaAs to isolate FeRh contribution with respect to temperature?

From equation [6.5],

$$\frac{\Delta V}{V}_{|FeRh} = \frac{\Delta V}{V}_{|Stack} - \frac{\Delta V}{V}_{|Ta/GaAs} \tag{C.1}$$

where

$$\frac{\Delta V}{V}_{|Ta/GaAs} \sim \frac{\Delta V}{V}_{|GaAs} = \left(\frac{dV_R}{dT}\right) \cdot \left(\frac{\Delta T}{V_R}\right)$$

The parabolic temperature dependence of the Rayleigh velocity is calculated using the elastic constant for the SAW propagating along the [110] direction (c.f. Chapter [4]).

Which temperature slope to remove on Polycrystalline Sample B: FeRh/GaAs?

We consider a linear variation of the Rayleigh velocity with temperature. We can consider only the first order derivative since the temperature considered here is linear over the range considered experimentally.

$$\frac{dV_R}{dT} = a + bT + cT^2 \quad \sim a + bT$$

a = - 0.2 ms^{-1} K^{-1}

Thus, $\frac{\Delta V}{V}_{|Ta/GaAs} \sim$ - 0.2 $\times$ $\frac{250}{<V_R>} \sim$ - 0.0177

Or, from equation [6.3],

$$\frac{\Delta V}{V} = \frac{\Delta \phi}{\omega_{SAW}\, t}$$

Typically, for the 398 MHz SAW, t = 1430 ns. Hence,

$$\Delta\phi = \frac{\Delta V}{V}\omega_{SAW}\, t \sim -63 rad/°C$$

On figure [C.1]**(b)**, a slope of ≈ - 60 rad/°C is seen needed to isolate the FeRh contribution only. Thus, the slope removed on the phase unwrapped corresponds to the correct temperature dependency.

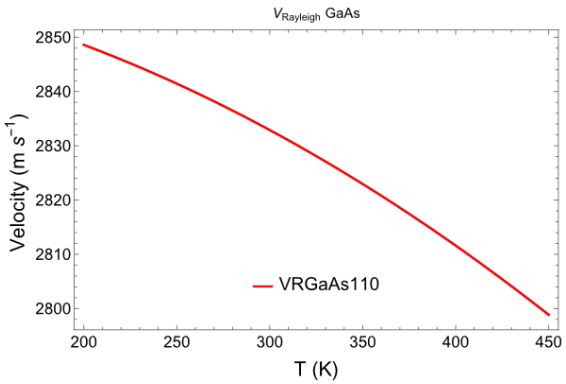

Figure C.1: Temperature evolution of the Rayleigh velocity on GaAs

Bibliography

[1] M. Fowler, *Historical Beginnings of Theories of Electricity and Magnetism*.

[2] I. Žutić, J. Fabian, and S. Das Sarma, "Spintronics: Fundamentals and applications," *Reviews of Modern Physics*, vol. 76, no. 2, pp. 323–410, Apr. 2004, ISSN: 0034-6861. DOI: 10.1103/RevModPhys.76.323. [Online]. Available: https://link.aps.org/doi/10.1103/RevModPhys.76.323.

[3] A. Fert and I. A. Campbell, "Two-Current Conduction in Nickel," *Physical Review Letters*, vol. 21, no. 16, pp. 1190–1192, Oct. 1968, ISSN: 0031-9007. DOI: 10.1103/PhysRevLett.21.1190. [Online]. Available: https://link.aps.org/doi/10.1103/PhysRevLett.21.1190.

[4] A. Fert and I. A. Campbell, "Electrical resistivity of ferromagnetic nickel and iron based alloys," *Journal of Physics F: Metal Physics*, vol. 6, no. 5, pp. 849–871, May 1976, ISSN: 0305-4608. DOI: 10.1088/0305-4608/6/5/025. [Online]. Available: https://iopscience.iop.org/article/10.1088/0305-4608/6/5/025.

[5] M. N. Baibich, J. M. Broto, *et al.*, "Giant Magnetoresistance of (001)Fe/(001)Cr Magnetic Superlattices," *Physical Review Letters*, vol. 61, no. 21, pp. 2472–2475, Nov. 1988, ISSN: 0031-9007. DOI: 10.1103/PhysRevLett.61.2472. [Online]. Available: https://link.aps.org/doi/10.1103/PhysRevLett.61.2472.

[6] S. Natarajan, "Emerging memory technologies," D. Abbott, K. Eshraghian, *et al.*, Eds., Mar. 2004, p. 7. DOI: 10.1117/12.530385. [Online]. Available: http://proceedings.spiedigitallibrary.org/proceeding.aspx?doi=10.1117/12.530385.

[7] B. Das and W. Black, "A generalized HSPICE macro-model for spin-valve GMR memory bits," in *Proceedings of 40th Midwest Symposium on Circuits and Systems. Dedicated to the Memory of Professor Mac Van Valkenburg*, vol. 2, IEEE, pp. 1146–1149, ISBN: 0-7803-3694-1. DOI: 10.1109/MWSCAS.1997.662280. [Online]. Available: http://ieeexplore.ieee.org/document/662280/.

[8] S. S. P. Parkin, C. Kaiser, *et al.*, "Giant tunnelling magnetoresistance at room temperature with MgO (100) tunnel barriers," *Nature Materials*, vol. 3, no. 12, pp. 862–867, Dec. 2004, ISSN: 1476-1122. DOI: 10.1038/nmat1256. [Online]. Available: https://www.nature.com/articles/nmat1256.

[9] T. Na, S. H. Kang, and S.-O. Jung, "STT-MRAM Sensing: A Review," *IEEE Transactions on Circuits and Systems II: Express Briefs*, vol. 68, no. 1, pp. 12–18, Jan. 2021, ISSN: 1549-7747. DOI: 10.1109/TCSII.2020.3040425. [Online]. Available: https://ieeexplore.ieee.org/document/9270597/.

[10] J. M. Slaughter, R. W. Dave, *et al.*, "Fundamentals of MRAM Technology," *Journal of Superconductivity: Incorporating Novel Magnetism*, vol. 15, no. 1, pp. 19–25, 2002, ISSN: 08961107. DOI: 10.1023/A:1014018925270.

[11] A. V. Chumak, V. I. Vasyuchka, *et al.*, "Magnon spintronics," *Nature Physics*, vol. 11, no. 6, pp. 453–461, Jun. 2015, ISSN: 1745-2473. DOI: 10.1038/nphys3347.

[12] A. A. Serga, A. V. Chumak, and B. Hillebrands, "YIG magnonics," *Journal of Physics D: Applied Physics*, vol. 43, no. 26, 2010, ISSN: 00223727. DOI: 10.1088/0022-3727/43/26/264002.

[13] A. V. Chumak, A. A. Serga, and B. Hillebrands, "Magnon transistor for all-magnon data processing," *Nature Communications*, vol. 5, Aug. 2014, ISSN: 20411723. DOI: 10.1038/ncomms5700.

[14] M. P. Kostylev, A. A. Serga, *et al.*, "Spin-wave logical gates," *Applied Physics Letters*, vol. 87, no. 15, Oct. 2005, ISSN: 0003-6951. DOI: 10.1063/1.2089147. [Online]. Available: https://pubs.aip.org/apl/article/87/15/153501/328328/Spin-wave-logical-gates.

[15] A. Khitun, M. Bao, and K. L. Wang, "Magnonic logic circuits," *Journal of Physics D: Applied Physics*, vol. 43, no. 26, p. 264 005, Jul. 2010, ISSN: 0022-3727. DOI: 10.1088/0022-3727/43/26/264005. [Online]. Available: https://iopscience.iop.org/article/10.1088/0022-3727/43/26/264005.

[16] C. Kittel, "Interaction of Spin Waves and Ultrasonic Waves in Ferromagnetic Crystals," *Physical Review*, vol. 110, no. 4, pp. 836–841, May 1958, ISSN: 0031-899X. DOI: 10.1103/PhysRev.110.836. [Online]. Available: https://link.aps.org/doi/10.1103/PhysRev.110.836.

[17] M. Weiler, L. Dreher, *et al.*, "Elastically Driven Ferromagnetic Resonance in Nickel Thin Films," *Physical Review Letters*, vol. 106, no. 11, p. 117 601, Mar. 2011, ISSN: 0031-9007. DOI: 10.1103/PhysRevLett.106.117601. [Online]. Available: https://link.aps.org/doi/10.1103/PhysRevLett.106.117601.

[18] L. Dreher, M. Weiler, *et al.*, "Surface acoustic wave driven ferromagnetic resonance in nickel thin films: Theory and experiment," *Physical Review B*, vol. 86, no. 13, p. 134 415, Oct. 2012, ISSN: 1098-0121. DOI: 10.1103/PhysRevB.86.134415. [Online]. Available: https://link.aps.org/doi/10.1103/PhysRevB.86.134415.

[19] M. Küß, M. Heigl, *et al.*, "Nonreciprocal Dzyaloshinskii–Moriya Magnetoacoustic Waves," *Physical Review Letters*, vol. 125, no. 21, p. 217 203, Nov. 2020, ISSN: 0031-9007. DOI: 10.1103/PhysRevLett.125.217203. [Online]. Available: https://link.aps.org/doi/10.1103/PhysRevLett.125.217203.

[20] L. Thevenard, C. Gourdon, *et al.*, "Surface-acoustic-wave-driven ferromagnetic resonance in (Ga,Mn)(As,P) epilayers," *Physical Review B*, vol. 90, no. 9, p. 094 401, Sep. 2014, ISSN: 1098-0121. DOI: 10.1103/PhysRevB.90.094401. [Online]. Available: https://link.aps.org/doi/10.1103/PhysRevB.90.094401.

[21] J.-Y. Duquesne, P. Rovillain, *et al.*, "Sub-GHz Resonant Magnetoelastic Coupling in Epitaxial Fe Thin Films," Tech. Rep. [Online]. Available: https://hal.archives-ouvertes.fr/hal-02022637.

[22] W. Edrington, U. Singh, *et al.*, "SAW assisted domain wall motion in Co/Pt multilayers," *Applied Physics Letters*, vol. 112, no. 5, Jan. 2018, ISSN: 0003-6951. DOI: 10.1063/1.5000080.

[23] Y. Yang, Y. Ji, *et al.*, "Magnetic skyrmion dynamics induced by surface acoustic waves," *Journal of Physics D: Applied Physics*, vol. 56, no. 8, p. 084 002, Feb. 2023, ISSN: 0022-3727. DOI: 10.1088/1361-6463/acb71f.

[24] P. Rovillain, R. C. De Oliveira, *et al.*, "Nonsymmetric spin pumping in a multiferroic heterostructure," *Physical Review B*, vol. 102, no. 18, Nov. 2020, ISSN: 24699969. DOI: 10.1103/PhysRevB.102.184409.

[25] L. Thevenard, J.-Y. Duquesne, *et al.*, "Irreversible magnetization switching using surface acoustic waves," *Physical Review B*, vol. 87, no. 14, p. 144 402, Apr. 2013, ISSN: 1098-0121. DOI: 10.1103/PhysRevB.87.144402. [Online]. Available: https://link.aps.org/doi/10.1103/PhysRevB.87.144402.

[26] P. Kuszewski, J.-Y. Duquesne, *et al.*, "Optical Probing of Rayleigh Wave Driven Magnetoacoustic Resonance," *Physical Review Applied*, vol. 10, no. 3, p. 034 036, Sep. 2018, ISSN: 2331-7019. DOI: 10.1103/PhysRevApplied.10.034036. [Online]. Available: https://link.aps.org/doi/10.1103/PhysRevApplied.10.034036.

[27] L. Thevenard, I. S. Camara, *et al.*, "Strong reduction of the coercivity by a surface acoustic wave in an out-of-plane magnetized epilayer," *Physical Review B*, vol. 93, no. 14, p. 140 405, Apr. 2016, ISSN: 2469-9950. DOI: 10.1103/PhysRevB.93.140405. [Online]. Available: https://link.aps.org/doi/10.1103/PhysRevB.93.140405.

[28] M. Kraimia, P. Kuszewski, *et al.*, "Time-and space-resolved nonlinear magnetoacoustic dynamics," *Physical Review B: Condensed Matter and Materials Physics*, p. 144 425, 2020. DOI: 10.1103/PhysRevB.101.144425{\"{i}}. [Online]. Available: https://hal.science/hal-02550724.

[29] H. Luo, D. Wang, *et al.*, "Magnetic Cobalt Nanowire Thin Films," *The Journal of Physical Chemistry B*, vol. 109, no. 5, pp. 1919–1922, Feb. 2005, ISSN: 1520-6106. DOI: 10.1021/jp045554t. [Online]. Available: https://pubs.acs.org/doi/10.1021/jp045554t.

[30] M. Yang, S. Lambert, *et al.*, "Laminated CoPtCr/Cr films for low noise longitudinal recording," *IEEE Transactions on Magnetics*, vol. 27, no. 6, pp. 5052–5054, Nov. 1991, ISSN: 0018-9464. DOI: 10.1109/20.278737. [Online]. Available: http://ieeexplore.ieee.org/document/278737/.

[31] A. Chatterjee, D. Das, *et al.*, "Synthesis of nanocrystalline nickel-zinc ferrite by the sol-gel method," *Journal of Magnetism and Magnetic Materials*, vol. 127, no. 1-2, pp. 214–218, Oct. 1993, ISSN: 03048853. DOI: 10.1016/0304-8853(93)90217-P. [Online]. Available: https://linkinghub.elsevier.com/retrieve/pii/030488539390217P.

[32] O. Ushakova, E. Dinislamova, *et al.*, "Structure and magnetic properties of Fe–Cr–Co nanocrystalline alloys for permanent magnets," *Journal of Alloys and Compounds*, vol. 586, S291–S293, Feb. 2014, ISSN: 09258388. DOI: 10.1016/j.jallcom.2012.12.076. [Online]. Available: https://linkinghub.elsevier.com/retrieve/pii/S0925838812023006.

[33] F. Martin-Hernandez and S. Guerrero-Suárez, "Magnetic anisotropy of hematite natural crystals: high field experiments," *International Journal of Earth Sciences*, vol. 101, no. 3, pp. 637–647, Apr. 2012, ISSN: 1437-3254. DOI: 10.1007/s00531-011-0665-z. [Online]. Available: http://link.springer.com/10.1007/s00531-011-0665-z.

[34] E. Haltz, J. Sampaio, *et al.*, "Measurement of the tilt of a moving domain wall shows precession-free dynamics in compensated ferrimagnets," *Scientific Reports*, vol. 10, no. 1, p. 16 292, Oct. 2020, ISSN: 2045-2322. DOI: 10.1038/s41598-020-73049-5. [Online]. Available: https://www.nature.com/articles/s41598-020-73049-5.

[35] M. Fallot, "Les alliages du fer avec les métaux de la famille du platine," *Annales de physique*, vol. 11, no. 10, pp. 291–332, Apr. 1938, ISSN: 0003-4169. DOI: 10.1051/anphys/193811100291. [Online]. Available: http://www.annphys.org/10.1051/anphys/193811100291.

[36] L. J. Swartzendruber, "The FeRh (Iron-Rhodium) system," *Bulletin of Alloy Phase Diagrams*, vol. 5, no. 5, pp. 456–462, Oct. 1984, ISSN: 0197-0216. DOI: 10.1007/BF02872896. [Online]. Available: http://link.springer.com/10.1007/BF02872896.

[37] H. Kumar, D. R. Cornejo, *et al.*, "Strain effects on the magnetic order of epitaxial FeRh thin films," *Journal of Applied Physics*, vol. 124, no. 8, Aug. 2018, ISSN: 0021-8979. DOI: 10.1063/1.5020160. [Online]. Available: https://pubs.aip.org/jap/article/124/8/085306/157026/Strain-effects-on-the-magnetic-order-of-epitaxial.

[38] G. Shirane, C. W. Chen, *et al.*, "Hyperfine Fields and Magnetic Moments in the Fe–Rh System," *Journal of Applied Physics*, vol. 34, no. 4, pp. 1044–1045, Apr. 1963, ISSN: 0021-8979. DOI: 10.1063/1.1729362. [Online]. Available: https://pubs.aip.org/jap/article/34/4/1044/828741/Hyperfine-Fields-and-Magnetic-Moments-in-the-Fe-Rh.

[39] Y. Ohtani and I. Hatakeyama, "Antiferro-ferromagnetic transition and microstructural properties in a sputter deposited FeRh thin film system," *Journal of Applied Physics*, vol. 74, no. 5, pp. 3328–3332, Sep. 1993, ISSN: 0021-8979. DOI: 10.1063/1.354557. [Online]. Available: https://pubs.aip.org/jap/article/74/5/3328/289841/Antiferro-ferromagnetic-transition-and.

[40] J. S. Kouvel and C. C. Hartelius, "Anomalous Magnetic Moments and Transformations in the Ordered Alloy FeRh," *Journal of Applied Physics*, vol. 33, no. 3, pp. 1343–1344, Mar. 1962, ISSN: 0021-8979. DOI: 10.1063/1.1728721. [Online]. Available: https://pubs.aip.org/jap/article/33/3/1343/1812/Anomalous-Magnetic-Moments-and-Transformations-in.

[41] J. S. Kouvel, "Unusual Nature of the Abrupt Magnetic Transition in FeRh and Its Pseudobinary Variants," *Journal of Applied Physics*, vol. 37, no. 3, pp. 1257–1258, Mar. 1966, ISSN: 0021-8979. DOI: 10.1063/1.1708424. [Online]. Available: https://pubs.aip.org/jap/article/37/3/1257/787810/Unusual-Nature-of-the-Abrupt-Magnetic-Transition.

[42] E. F. Bertaut, A. Delapalme, *et al.*, "Magnetic Structure Work at the Nuclear Center of Grenoble," *Journal of Applied Physics*, vol. 33, no. 3, pp. 1123–1124, Mar. 1962, ISSN: 0021-8979. DOI: 10.1063/1.1728627. [Online]. Available: https://pubs.aip.org/jap/article/33/3/1123/1866/Magnetic-Structure-Work-at-the-Nuclear-Center-of.

[43] V. L. Moruzzi and P. M. Marcus, "Antiferromagnetic-ferromagnetic transition in FeRh," *Physical Review B*, vol. 46, no. 5, pp. 2864–2873, Aug. 1992, ISSN: 0163-1829. DOI: 10.1103/PhysRevB.46.2864. [Online]. Available: https://link.aps.org/doi/10.1103/PhysRevB.46.2864.

[44] J. Kim, R. Ramesh, and N. Kioussis, "Revealing the hidden structural phases of FeRh," *Physical Review B*, vol. 94, no. 18, p. 180 407, Nov. 2016, ISSN: 2469-9950. DOI: 10.1103/PhysRevB.94.180407. [Online]. Available: https://link.aps.org/doi/10.1103/PhysRevB.94.180407.

[45] F. De Bergevin and L. Muldawer, "Etude Cristallographique de certains alliages Fer-Rhodium," *Comptes Rendus hebdomadaires des scéances de l'académie des sciences*, vol. 2, no. 252, pp. 1347–1349, 1961. [Online]. Available: https://gallica.bnf.fr/ark:/12148/bpt6k762d.

[46] M. Wolloch, M. E. Gruner, *et al.*, "Impact of lattice dynamics on the phase stability of metamagnetic FeRh: Bulk and thin films," *Physical Review B*, vol. 94, no. 17, p. 174 435, Nov. 2016, ISSN: 2469-9950. DOI: 10.1103/PhysRevB.94.174435. [Online]. Available: https://link.aps.org/doi/10.1103/PhysRevB.94.174435.

[47] A. I. Zakharov, A. M. Kadomtseva, *et al.*, "Magnetic and magneto-elastic properties of a metamagnetic iron-rhodium alloy," Tech. Rep. 6, 1964.

[48] R. Y. Gu and V. P. Antropov, "Dominance of the spin-wave contribution to the magnetic phase transition in FeRh," *Physical Review B*, vol. 72, no. 1, p. 012 403, Jul. 2005, ISSN: 1098-0121. DOI: 10.1103/PhysRevB.72.012403. [Online]. Available: https://link.aps.org/doi/10.1103/PhysRevB.72.012403.

[49] J. A. Arregi, O. Caha, and V. Uhlíř, "Evolution of strain across the magnetostructural phase transition in epitaxial FeRh films on different substrates," *Physical Review B*, vol. 101, no. 17, p. 174 413, May 2020, ISSN: 2469-9950. DOI: 10.1103/PhysRevB.101.174413. [Online]. Available: https://link.aps.org/doi/10.1103/PhysRevB.101.174413.

[50] J. M. Lommel, "Magnetic and Electrical Properties of FeRh Thin Films," *Journal of Applied Physics*, vol. 37, no. 3, pp. 1483–1484, Mar. 1966, ISSN: 0021-8979. DOI: 10.1063/1.1708527. [Online]. Available: https://pubs.aip.org/jap/article/37/3/1483/787971/Magnetic-and-Electrical-Properties-of-FeRh-Thin.

[51] T. Zhou, M. Cher, *et al.*, "On the origin of giant magnetocaloric effect and thermal hysteresis in multifunctional α-FeRh thin films," *Physics Letters A*, vol. 377, no. 42, pp. 3052–3059, Dec. 2013, ISSN: 03759601. DOI: 10.1016/j.physleta.2013.09.027. [Online]. Available: https://linkinghub.elsevier.com/retrieve/pii/S0375960113008554.

[52] J. A. Arregi, M. Horký, *et al.*, "Magnetization reversal and confinement effects across the metamagnetic phase transition in mesoscale FeRh structures," *Journal of Physics D: Applied Physics*, vol. 51, no. 10, p. 105 001, Mar. 2018, ISSN: 0022-3727. DOI: 10.1088/1361-6463/aaaa5a. [Online]. Available: https://iopscience.iop.org/article/10.1088/1361-6463/aaaa5a.

[53] Y. Xie, Q. Zhan, *et al.*, "Effect of epitaxial strain and lattice mismatch on magnetic and transport behaviors in metamagnetic FeRh thin films," *AIP Advances*, vol. 7, no. 5, May 2017, ISSN: 2158-3226. DOI: 10.1063/1.4976301. [Online]. Available: https://pubs.aip.org/adv/article/7/5/056314/629534/Effect-of-epitaxial-strain-and-lattice-mismatch-on.

[54] L. Landau and E. Lifshitz, *Statistical Physics*. Elsevier Science, 1980, vol. 5. [Online]. Available: https://books.google.fr/books?id=D3zjAQAACAAJ.

[55] C. Kittel, "Model of Exchange-Inversion Magnetization," *Physical Review*, vol. 120, no. 2, pp. 335–342, Oct. 1960, ISSN: 0031-899X. DOI: 10.1103/PhysRev.120.335. [Online]. Available: https://link.aps.org/doi/10.1103/PhysRev.120.335.

[56] J. B. McKinnon, D. Melville, and E. W. Lee, "The antiferromagnetic-ferromagnetic transition in iron-rhodium alloys," *Journal of Physics C: Solid State Physics*, vol. 3, no. 1S, S46–S58, May 1970, ISSN: 0022-3719. DOI: 10.1088/0022-3719/3/1S/306. [Online]. Available: https://iopscience.iop.org/article/10.1088/0022-3719/3/1S/306.

[57] J. A. Ricodeau and D. Melville, "Model of the antiferromagnetic-ferromagnetic transition in FeRh alloys," *Journal of Physics F: Metal Physics*, vol. 2, no. 2, pp. 337–350, Mar. 1972, ISSN: 0305-4608. DOI: 10.1088/0305-4608/2/2/024. [Online]. Available: https://iopscience.iop.org/article/10.1088/0305-4608/2/2/024.

[58] P. Tu, A. J. Heeger, *et al.*, "Mechanism for the First-Order Magnetic Transition in the FeRh System," *Journal of Applied Physics*, vol. 40, no. 3, pp. 1368–1369, Mar. 1969, ISSN: 0021-8979. DOI: 10.1063/1.1657670. [Online]. Available: https://pubs.aip.org/jap/article/40/3/1368/5259/Mechanism-for-the-First-Order-Magnetic-Transition.

[59] B. Fogarassy, T. Kemény, *et al.*, "Electronic Specific Heat of Iron-Rhodium and Iron-Rhodium-Iridium Alloys," *Physical Review Letters*, vol. 29, no. 5, pp. 288–291, Jul. 1972, ISSN: 0031-9007. DOI: 10.1103/PhysRevLett.29.288. [Online]. Available: https://link.aps.org/doi/10.1103/PhysRevLett.29.288.

[60] M. E. Gruner, E. Hoffmann, and P. Entel, "Instability of the rhodium magnetic moment as the origin of the metamagnetic phase transition in alpha-FeRh," *Physical Review B*, vol. 67, no. 6, p. 064 415, Feb. 2003, ISSN: 0163-1829. DOI: 10.1103/PhysRevB.67.064415. [Online]. Available: https://link.aps.org/doi/10.1103/PhysRevB.67.064415.

[61] J. Kudrnovský, V. Drchal, and I. Turek, "Physical properties of FeRh alloys: The antiferromagnetic to ferromagnetic transition," *Physical Review B*, vol. 91, no. 1, p. 014 435, Jan. 2015, ISSN: 1098-0121. DOI: 10.1103/PhysRevB.91.014435. [Online]. Available: https://link.aps.org/doi/10.1103/PhysRevB.91.014435.

[62] L. M. Sandratskii and P. Mavropoulos, "Magnetic excitations and femtomagnetism of FeRh: A first-principles study," *Physical Review B*, vol. 83, no. 17, p. 174 408, May 2011, ISSN: 1098-0121. DOI: 10.1103/PhysRevB.83.174408. [Online]. Available: https://link.aps.org/doi/10.1103/PhysRevB.83.174408.

[63] D. W. Cooke, F. Hellman, *et al.*, "Thermodynamic Measurements of Fe-Rh Alloys," *Physical Review Letters*, vol. 109, no. 25, p. 255 901, Dec. 2012, ISSN: 0031-9007. DOI: 10.1103/PhysRevLett.109.255901. [Online]. Available: https://link.aps.org/doi/10.1103/PhysRevLett.109.255901.

[64] C. Koenig, "Self-consistent band structure of paramagnetic, ferromagnetic and antiferromagnetic ordered FeRh," *Journal of Physics F: Metal Physics*, vol. 12, no. 6, pp. 1123–1137, Jun. 1982, ISSN: 0305-4608. DOI: 10.1088/0305-4608/12/6/013. [Online]. Available: https://iopscience.iop.org/article/10.1088/0305-4608/12/6/013.

[65] J.-S. Lee, E. Vescovo, *et al.*, "Electronic structure and magnetic properties of epitaxial FeRh(001) ultrathin films on W(100)," *Physical Review B*, vol. 82, no. 22, p. 224 410, Dec. 2010, ISSN: 1098-0121. DOI: 10.1103/PhysRevB.82.224410. [Online]. Available: https://link.aps.org/doi/10.1103/PhysRevB.82.224410.

[66] F. W. Wu, "Ising Model with Four-Spin Interactions," *Physical Review B*, vol. 4, no. 7, pp. 2312–2314, Oct. 1971, ISSN: 0556-2805. DOI: 10.1103/PhysRevB.4.2312. [Online]. Available: https://link.aps.org/doi/10.1103/PhysRevB.4.2312.

[67] J. Barker and R. W. Chantrell, "Higher-order exchange interactions leading to metamagnetism in FeRh," *Physical Review B - Condensed Matter and Materials Physics*, vol. 92, no. 9, Sep. 2015, ISSN: 1550235X. DOI: 10.1103/PhysRevB.92.094402. [Online]. Available: https://journals.aps.org/prb/abstract/10.1103/PhysRevB.92.094402.

[68] S. Polesya, S. Mankovsky, *et al.*, "Finite-temperature magnetism of FeRh compounds," *Physical Review B*, vol. 93, no. 2, p. 024 423, Jan. 2016, ISSN: 2469-9950. DOI: 10.1103/PhysRevB.93.024423. [Online]. Available: https://link.aps.org/doi/10.1103/PhysRevB.93.024423.

[69] J. B. Staunton, R. Banerjee, *et al.*, "Fluctuating local moments, itinerant electrons, and the magnetocaloric effect: Compositional hypersensitivity of FeRh," *Physical Review B*, vol. 89, no. 5, p. 054 427, Feb. 2014, ISSN: 1098-0121. DOI: 10.1103/PhysRevB.89.054427. [Online]. Available: https://link.aps.org/doi/10.1103/PhysRevB.89.054427.

[70] S. Maat, J.-U. Thiele, and E. E. Fullerton, "Temperature and field hysteresis of the antiferromagnetic-to-ferromagnetic phase transition in epitaxial FeRh films," *Physical Review B*, vol. 72, no. 21, p. 214 432, Dec. 2005, ISSN: 1098-0121. DOI: 10.1103/PhysRevB.72.214432. [Online]. Available: https://link.aps.org/doi/10.1103/PhysRevB.72.214432.

[71] R. C. Wayne, "Pressure Dependence of the Magnetic Transitions in Fe-Rh Alloys," *Physical Review*, vol. 170, no. 2, pp. 523–527, Jun. 1968, ISSN: 0031-899X. DOI: 10.1103/PhysRev.170.523. [Online]. Available: https://link.aps.org/doi/10.1103/PhysRev.170.523.

[72] A. Ceballos, Z. Chen, *et al.*, "Effect of strain and thickness on the transition temperature of epitaxial FeRh thin-films," *Applied Physics Letters*, vol. 111, no. 17, Oct. 2017, ISSN: 0003-6951. DOI: 10.1063/1.4997901. [Online]. Available: https://pubs.aip.org/apl/article/111/17/172401/1019505/Effect-of-strain-and-thickness-on-the-transition.

[73] H. Y. Y. Ko, T. Suzuki, *et al.*, "Magnetic and structural characterizations on nanoparticles of FePt, FeRh and their composites," *Journal of Magnetism and Magnetic Materials*, vol. 320, no. 22, pp. 3120–3123, Nov. 2008, ISSN: 03048853. DOI: 10.1016/j.jmmm.2008.08.089. [Online]. Available: https://linkinghub.elsevier.com/retrieve/pii/S0304885308008780.

[74] L. H. Lewis, C. H. Marrows, and S. Langridge, "Coupled magnetic, structural, and electronic phase transitions in FeRh," *Journal of Physics D: Applied Physics*, vol. 49, no. 32, p. 323 002, Aug. 2016, ISSN: 0022-3727. DOI: 10.1088/0022-3727/49/32/323002. [Online]. Available: https://iopscience.iop.org/article/10.1088/0022-3727/49/32/323002.

[75] V. Uhlíř, J. A. Arregi, and E. E. Fullerton, "Colossal magnetic phase transition asymmetry in mesoscale FeRh stripes," *Nature Communications*, vol. 7, no. 1, p. 13 113, Oct. 2016, ISSN: 2041-1723. DOI: 10.1038/ncomms13113. [Online]. Available: https://www.nature.com/articles/ncomms13113.

[76] D. Weller, G. Parker, *et al.*, "Review Article: FePt heat assisted magnetic recording media," *Journal of Vacuum Science & Technology B, Nanotechnology and Microelectronics: Materials, Processing, Measurement, and Phenomena*, vol. 34, no. 6, Nov. 2016, ISSN: 2166-2746. DOI: 10.1116/1.4965980. [Online]. Available: https://pubs.aip.org/jvb/article/34/6/060801/103138/Review-Article-FePt-heat-assisted-magnetic.

[77] T. J. Zhou, K. Cher, *et al.*, "The concept and fabrication of exchange switchable trilayer of FePt/FeRh/FeCo with reduced switching field," *Journal of Applied Physics*, vol. 111, no. 7, Apr. 2012, ISSN: 0021-8979. DOI: 10.1063/1.3677838. [Online]. Available: https://pubs.aip.org/jap/article/111/7/07C116/399602/The-concept-and-fabrication-of-exchange-switchable.

[78] X. Marti, I. Fina, *et al.*, "Room-temperature antiferromagnetic memory resistor," *Nature Materials*, vol. 13, no. 4, pp. 367–374, Apr. 2014, ISSN: 1476-1122. DOI: 10.1038/nmat3861. [Online]. Available: https://www.nature.com/articles/nmat3861.

[79] *Greenhouse-gas-emissions-carbon-data-centres-cloud-computing*. [Online]. Available: https://www.climatiq.io/blog/measure-greenhouse-gas-emissions-carbon-data-centres-cloud-computing.

[80] *HDD-drives*.

[81] S. Xiong, R. Smith, *et al.*, "Setting Write Spacing in Heat Assisted Magnetic Recording," *IEEE Transactions on Magnetics*, vol. 54, no. 8, pp. 1–7, Aug. 2018, ISSN: 0018-9464. DOI: 10.1109/TMAG.2018.2841367.

[82] R. M. Tom, R. Smith, *et al.*, "Optical forces in heat-assisted magnetic recording head-disk interface," *Scientific Reports*, vol. 13, no. 1, p. 8451, May 2023, ISSN: 2045-2322. DOI: 10.1038/s41598-023-35126-3.

[83] J.-U. Thiele, S. Maat, and E. E. Fullerton, "FeRh/FePt exchange spring films for thermally assisted magnetic recording media," *Applied Physics Letters*, vol. 82, no. 17, pp. 2859–2861, Apr. 2003, ISSN: 0003-6951. DOI: 10.1063/1.1571232. [Online]. Available: https://pubs.aip.org/apl/article/82/17/2859/513896/FeRh-FePt-exchange-spring-films-for-thermally.

[84] M. Sharma, H. M. Aarbogh, *et al.*, "Magnetotransport properties of epitaxial MgO(001)/FeRh films across the antiferromagnet to ferromagnet transition," *Journal of Applied Physics*, vol. 109, no. 8, Apr. 2011, ISSN: 0021-8979. DOI: 10.1063/1.3573503. [Online]. Available: https://pubs.aip.org/jap/article/109/8/083913/929460/Magnetotransport-properties-of-epitaxial-MgO-001.

[85] T. Moriyama, N. Matsuzaki, *et al.*, "Sequential write-read operations in FeRh antiferromagnetic memory," *Applied Physics Letters*, vol. 107, no. 12, Sep. 2015, ISSN: 0003-6951. DOI: 10.1063/1.4931567. [Online]. Available: https://pubs.aip.org/apl/article/107/12/122403/29012/Sequential-write-read-operations-in-FeRh.

[86] N. Matsuzaki, T. Moriyama, *et al.*, "Current induced antiferro–ferromagnetic transition in FeRh nanowires," *Japanese Journal of Applied Physics*, vol. 54, no. 7, p. 073 002, Jul. 2015, ISSN: 0021-4922. DOI: 10.7567/JJAP.54.073002. [Online]. Available: https://iopscience.iop.org/article/10.7567/JJAP.54.073002.

[87] R. O. Cherifi, V. Ivanovskaya, *et al.*, "Electric-field control of magnetic order above room temperature," 2014. DOI: 10.1038/NMAT3870{\"{i}}. [Online]. Available: www.nature.com/naturematerials.

[88] S. P. Bennett, A. T. Wong, *et al.*, "Giant Controllable Magnetization Changes Induced by Structural Phase Transitions in a Metamagnetic Artificial Multiferroic," *Scientific Reports*, vol. 6, no. 1, p. 22 708, Mar. 2016, ISSN: 2045-2322. DOI: 10.1038/srep22708. [Online]. Available: https://www.nature.com/articles/srep22708.

[89] J. Chen, J. Ma, *et al.*, "Strain modulated ferromagnetic to antiferromagnetic transition in FeRh/BaTiO3 (001) heterostructures," *Journal of Applied Physics*, vol. 121, no. 19, May 2017, ISSN: 0021-8979. DOI: 10.1063/1.4983361. [Online]. Available: https://pubs.aip.org/jap/article/121/19/194101/1006216/Strain-modulated-ferromagnetic-to.

[90] Z. Q. Liu, L. Li, *et al.*, "Full Electroresistance Modulation in a Mixed-Phase Metallic Alloy," *Physical Review Letters*, vol. 116, no. 9, p. 097 203, Mar. 2016, ISSN: 0031-9007. DOI: 10.1103/PhysRevLett.116.097203. [Online]. Available: https://link.aps.org/doi/10.1103/PhysRevLett.116.097203.

[91] Y. Lee, Z. Q. Liu, *et al.*, "Large resistivity modulation in mixed-phase metallic systems," *Nature Communications*, vol. 6, no. 1, p. 5959, Jan. 2015, ISSN: 2041-1723. DOI: 10.1038/ncomms6959. [Online]. Available: https://www.nature.com/articles/ncomms6959.

[92] A. B. Mei, I. Gray, *et al.*, "Local Photothermal Control of Phase Transitions for On-Demand Room-Temperature Rewritable Magnetic Patterning," *Advanced Materials*, vol. 32, no. 22, p. 2 001 080, Jun. 2020, ISSN: 0935-9648. DOI: 10.1002/adma.202001080. [Online]. Available: https://onlinelibrary.wiley.com/doi/abs/10.1002/adma.202001080.

[93] J. M. Bartell, D. H. Ngai, *et al.*, "Towards a table-top microscope for nanoscale magnetic imaging using picosecond thermal gradients," *Nature Communications*, vol. 6, no. 1, p. 8460, Sep. 2015, ISSN: 2041-1723. DOI: 10.1038/ncomms9460. [Online]. Available: https://www.nature.com/articles/ncomms9460.

[94] I. Fina, N. Dix, *et al.*, "Flexible Antiferromagnetic FeRh Tapes as Memory Elements," *ACS Applied Materials & Interfaces*, vol. 12, no. 13, pp. 15 389–15 395, Apr. 2020, ISSN: 1944-8244. DOI: 10.1021/acsami.0c00704. [Online]. Available: https://pubs.acs.org/doi/10.1021/acsami.0c00704.

[95] J. M. Lommel and J. S. Kouvel, "Effects of Mechanical and Thermal Treatment on the Structure and Magnetic Transitions in FeRh," *Journal of Applied Physics*, vol. 38, no. 3, pp. 1263–1264, Mar. 1967, ISSN: 0021-8979. DOI: 10.1063/1.1709570. [Online]. Available: https://pubs.aip.org/jap/article/38/3/1263/693004/Effects-of-Mechanical-and-Thermal-Treatment-on-the.

[96] J. van Driel, R. Coehoorn, *et al.*, "Compositional dependence of the giant magnetoresistance in FexRh1x thin films," *Journal of Applied Physics*, vol. 85, no. 2, pp. 1026–1036, Jan. 1999, ISSN: 0021-8979. DOI: 10.1063/1.369224. [Online]. Available: https://pubs.aip.org/jap/article/85/2/1026/289417/Compositional-dependence-of-the-giant.

[97] *Rf-sputtering-process*. [Online]. Available: https://www.phasis.ch/products/more-about-epitaxial-gold-au-111/more-about-rf-sputtering.

[98] D. Nguyen Ba, "A study of the FM-AFM phase transition in FeRh : compositionally graded films and strain control," Tech. Rep., 2017. [Online]. Available: https://theses.hal.science/tel-02418509v2.

[99] Y. Hong, I. de Moraes, *et al.*, "A high throughput study of both compositionally graded and homogeneous Fe–Pt thin films," *Journal of Materials Research and Technology*, vol. 18, pp. 1245–1255, May 2022, ISSN: 22387854. DOI: 10.1016/j.jmrt.2022.03.055.

[100] V. Saidl, M. Brajer, *et al.*, "Investigation of magneto-structural phase transition in FeRh by reflectivity and transmittance measurements in visible and near-infrared spectral region," *New Journal of Physics*, vol. 18, no. 8, p. 083 017, Aug. 2016, ISSN: 1367-2630. DOI: 10.1088/1367-2630/18/8/083017. [Online]. Available: https://iopscience.iop.org/article/10.1088/1367-2630/18/8/083017.

[101] M. Eddrief, Y. Zheng, *et al.*, "Metastable tetragonal structure of Fe <math display="inline"> <msub> <mrow/> <mrow> <mn>100</mn> <mo></mo> <mi>x</mi> </mrow> </msub> </math> Ga <math display="inline"> <msub> <mrow/> <mi>x</mi> </msub> </math> epitaxial thin films on ZnSe/GaAs(001) substrate," *Physical Review B*, vol. 84, no. 16, p. 161 410, Oct. 2011, ISSN: 1098-0121. DOI: 10.1103/PhysRevB.84.161410.

[102] G. C. Han, J. J. Qiu, *et al.*, "Suppression of low-temperature ferromagnetic phase in ultrathin FeRh films," *Journal of Applied Physics*, vol. 113, no. 12, Mar. 2013, ISSN: 0021-8979. DOI: 10.1063/1.4798275. [Online]. Available: https://pubs.aip.org/jap/article/113/12/123909/400965/Suppression-of-low-temperature-ferromagnetic-phase.

[103] Q. J. Yap, J. J. Qiu, *et al.*, "Phase ordering and its effect on magnetic and structural properties of FeRh ultrathin films," *Journal of Applied Physics*, vol. 116, no. 4, Jul. 2014, ISSN: 0021-8979. DOI: 10.1063/1.4890032. [Online]. Available: https://pubs.aip.org/jap/article/116/4/043902/282943/Phase-ordering-and-its-effect-on-magnetic-and.

[104] M. Mansuripur, *The Physical Principles of Magneto-optical Recording*. Cambridge University Press, Apr. 1995, ISBN: 9780521461245. DOI: 10.1017/CBO9780511622472. [Online]. Available: https://www.cambridge.org/core/product/identifier/9780511622472/type/book.

[105] A. Zvezdin and V. Kotov, *Modern Magnetooptics and Magnetooptical Materials*. CRC Press, Jan. 1997, ISBN: 9780367802608. DOI: 10.1201/9780367802608. [Online]. Available: https://www.taylorfrancis.com/books/9781420050844.

[106] B. Sepúlveda, Y. Huttel, *et al.*, "Linear and quadratic magneto-optical Kerr effects in continuous and granular ultrathin monocrystalline Fe films," *Physical Review B*, vol. 68, no. 6, p. 064 401, Aug. 2003, ISSN: 0163-1829. DOI: 10.1103/PhysRevB.68.064401. [Online]. Available: https://link.aps.org/doi/10.1103/PhysRevB.68.064401.

[107] J. A. Arregi, P. Riego, and A. Berger, "What is the longitudinal magneto-optical Kerr effect?" *Journal of Physics D: Applied Physics*, vol. 50, no. 3, 03LT01, Jan. 2017, ISSN: 0022-3727. DOI: 10.1088/1361-6463/aa4ea6. [Online]. Available: https://iopscience.iop.org/article/10.1088/1361-6463/aa4ea6.

[108] C.-Y. You and S.-C. Shin, "Derivation of simplified analytic formulae for magneto-optical Kerr effects," *Applied Physics Letters*, vol. 69, no. 9, pp. 1315–1317, Aug. 1996, ISSN: 0003-6951. DOI: 10.1063/1.117579. [Online]. Available: https://pubs.aip.org/apl/article/69/9/1315/518657/Derivation-of-simplified-analytic-formulae-for.

[109] C.-Y. You and S.-C. Shin, "Simplified Analytic formulae for magneto-optical kerr effects in general cases," *Journal of the Magnetics Society of Japan*, vol. 22, no. S_2_MORIS_97, pp. 189–190, 1998, ISSN: 1880-4004. DOI: 10.3379/jmsjmag.22.S2{_}189. [Online]. Available: http://www.jstage.jst.go.jp/article/jmsjmag/22/S_2_MORIS_97/22_S_2_MORIS_97_S2_189/_article.

[110] C.-Y. You and S.-C. Shin, "Generalized analytic formulae for magneto-optical Kerr effects," *Journal of Applied Physics*, vol. 84, no. 1, pp. 541–546, Jul. 1998, ISSN: 0021-8979. DOI: 10.1063/1.368058. [Online]. Available: https://pubs.aip.org/jap/article/84/1/541/491208/Generalized-analytic-formulae-for-magneto-optical.

[111] S. Inoue, N. N. Phuoc, *et al.*, "Structural and magneto-optical properties of FeRh thin films," *Journal of Applied Physics*, vol. 103, no. 7, Apr. 2008, ISSN: 0021-8979. DOI: 10.1063/1.2834446. [Online]. Available: https://pubs.aip.org/jap/article/103/7/07B312/895711/Structural-and-magneto-optical-properties-of-FeRh.

[112] S. P. Bennett, M. Currie, *et al.*, "Spectral reflectivity crossover at the metamagnetic transition in FeRh thin films," *Optical Materials Express*, vol. 9, no. 7, p. 2870, Jul. 2019, ISSN: 2159-3930. DOI: 10.1364/OME.9.002870. [Online]. Available: https://opg.optica.org/abstract.cfm?URI=ome-9-7-2870.

[113] V. Saidl, P. Němec, *et al.*, "Optical determination of the Néel vector in a CuMnAs thin-film antiferromagnet," *Nature Photonics*, vol. 11, no. 2, pp. 91–96, 2017, ISSN: 1749-4885. DOI: 10.1038/nphoton.2016.255. [Online]. Available: http://www.nature.com/doifinder/10.1038/nphoton.2016.255.

[114] R. C. O'Handley, *Modern magnetic materials : principles and applications*. Wiley, 2000, p. 740, ISBN: 978-0-471-15566-9. [Online]. Available: https://edisciplinas.usp.br/pluginfile.php/6916190/mod_resource/content/1/Robert%20C.%20OHandley-Modern%20Magnetic%20Materials_%20Principles%20and%20Applications%20%20-Wiley-Interscience%20%281999%29.pdf.

[115] S. O. Mariager, L. L. Guyader, *et al.*, "Imaging the antiferromagnetic to ferromagnetic first order phase transition of FeRh," Jan. 2013. [Online]. Available: http://arxiv.org/abs/1301.4164.

[116] P. Zeeman, "Archives_néerlandaises_des_sciences_exactes_et_naturelles," 1896. [Online]. Available: https://books.google.fr/books?id=_AkWAAAAYAAJ&pg=PA217&hl=fr&source=gbs_toc_r&cad=2#v=onepage&q&f=false.

[117] D. Suess, J. Fidler, and T. Schrefl, "chapter 2 Micromagnetic Simulation of Magnetic Materials," in 2006, pp. 41–125. DOI: 10.1016/S1567-2719(05)16002-8. [Online]. Available: https://linkinghub.elsevier.com/retrieve/pii/S1567271905160028.

[118] W. Pauli, "Über den Zusammenhang des Abschlusses der Elektronengruppen im Atom mit der Komplexstruktur der Spektren," *Zeitschrift für Physik*, vol. 31, no. 1, pp. 765–783, Feb. 1925, ISSN: 0044-3328. DOI: 10.1007/BF02980631.

[119] W. Heisenberg, "Uber quantentheoretische Umdeutung kinematischer und mechanischer Beziehungen.," *Zeitschrift fr Physik*, vol. 33, no. 1, pp. 879–893, Dec. 1925, ISSN: 1434-6001. DOI: 10.1007/BF01328377.

[120] L. LANDAU and E. LIFSHITZ, "On the theory of the dispersion of magnetic permeability in ferromagnetic bodies," in *Perspectives in Theoretical Physics*, vol. 8, Elsevier, 1992, pp. 51–65. DOI: 10.1016/B978-0-08-036364-6.50008-9. [Online]. Available: https://linkinghub.elsevier.com/retrieve/pii/B9780080363646500089.

[121] T. Gilbert, "A Lagrangian formulation of the gyromagnetic equation of the magnetic field," *Physical Review*, vol. 100, no. 4, pp. 1235–1235, Nov. 1955, ISSN: 0031-899X. DOI: 10.1103/PhysRev.100.1235.

[122] G. V. Skrotskiĭ, "The Landau-Lifshitz equation revisited," *Soviet Physics Uspekhi*, vol. 27, no. 12, pp. 977–979, Dec. 1984, ISSN: 0038-5670. DOI: 10.1070/PU1984v027n12ABEH004101. [Online]. Available: https://iopscience.iop.org/article/10.1070/PU1984v027n12ABEH004101.

[123] V. Kamberský, "On ferromagnetic resonance damping in metals," *Czechoslovak Journal of Physics*, vol. 26, no. 12, pp. 1366–1383, Dec. 1976, ISSN: 0011-4626. DOI: 10.1007/BF01587621.

[124] K. Gilmore, Y. U. Idzerda, and M. D. Stiles, "Spin-orbit precession damping in transition metal ferromagnets (invited)," in *Journal of Applied Physics*, vol. 103, 2008. DOI: 10.1063/1.2832348.

[125] R. Arias and D. L. Mills, "Extrinsic contributions to the ferromagnetic resonance response of ultrathin films," *Physical Review B*, vol. 60, no. 10, pp. 7395–7409, Sep. 1999, ISSN: 0163-1829. DOI: 10.1103/PhysRevB.60.7395. [Online]. Available: https://link.aps.org/doi/10.1103/PhysRevB.60.7395.

[126] F. Bloch, "Zur Theorie des Ferromagnetismus," *Zeitschrift fr Physik*, vol. 61, no. 3-4, pp. 206–219, Mar. 1930, ISSN: 1434-6001. DOI: 10.1007/BF01339661.

[127] P. Pirro, V. I. Vasyuchka, *et al.*, *Advances in coherent magnonics*, Dec. 2021. DOI: 10.1038/s41578-021-00332-w.

[128] J. R. Eshbach and R. W. Damon, "Surface Magnetostatic Modes and Surface Spin Waves," *Physical Review*, vol. 118, no. 5, pp. 1208–1210, Jun. 1960, ISSN: 0031-899X. DOI: 10.1103/PhysRev.118.1208.

[129] R. W. Damon, "Relaxation Effects in the Ferromagnetic Resonance," *Reviews of Modern Physics*, vol. 25, no. 1, pp. 239–245, Jan. 1953, ISSN: 0034-6861. DOI: 10.1103/RevModPhys.25.239. [Online]. Available: https://link.aps.org/doi/10.1103/RevModPhys.25.239.

[130] J. H. E. GRIFFITHS, "Anomalous High-frequency Resistance of Ferromagnetic Metals," *Nature*, vol. 158, no. 4019, pp. 670–671, Nov. 1946, ISSN: 0028-0836. DOI: 10.1038/158670a0. [Online]. Available: https://www.nature.com/articles/158670a0.

[131] S. Sievers, J. Kurda, *et al.*, "Microwave Interferometry for High Sensitivity VNA-FMR Measurements," *IEEE Transactions on Magnetics*, vol. 53, no. 4, Apr. 2017, ISSN: 00189464. DOI: 10.1109/TMAG.2016.2623839.

[132] I. S. Maksymov and M. Kostylev, *Broadband stripline ferromagnetic resonance spectroscopy of ferromagnetic films, multilayers and nanostructures*, 2015. DOI: 10.1016/j.physe.2014.12.027.

[133] V. Flovik, "Magnetization dynamics in nanostructures," Ph.D. dissertation, 2016. [Online]. Available: http://hdl.handle.net/11250/2430044.

[134] K. Vogt, F. Y. Fradin, *et al.*, "Realization of a spin-wave multiplexer," *Nature Communications*, vol. 5, Apr. 2014, ISSN: 20411723. DOI: 10.1038/ncomms4727.

[135] F. Kargar and A. A. Balandin, *Advances in Brillouin–Mandelstam light-scattering spectroscopy*, Oct. 2021. DOI: 10.1038/s41566-021-00836-5.

[136] J. Stigloher, T. Taniguchi, *et al.*, "Observation of a Goos-Hänchen-like Phase Shift for Magnetostatic Spin Waves," *Physical Review Letters*, vol. 121, no. 13, p. 137 201, Sep. 2018, ISSN: 0031-9007. DOI: 10.1103/PhysRevLett.121.137201. [Online]. Available: https://link.aps.org/doi/10.1103/PhysRevLett.121.137201.

[137] J. Stigloher, M. Decker, *et al.*, "Snell's Law for Spin Waves," *Physical Review Letters*, vol. 117, no. 3, p. 037 204, Jul. 2016, ISSN: 0031-9007. DOI: 10.1103/PhysRevLett.117.037204. [Online]. Available: https://link.aps.org/doi/10.1103/PhysRevLett.117.037204.

[138] S. Mansfeld, J. Topp, *et al.*, "Spin wave diffraction and perfect imaging of a grating," *Physical Review Letters*, vol. 108, no. 4, Jan. 2012, ISSN: 00319007. DOI: 10.1103/PhysRevLett.108.047204.

[139] V. E. Demidov, S. O. Demokritov, *et al.*, "Mode interference and periodic self-focusing of spin waves in permalloy microstripes," *Physical Review B - Condensed Matter and Materials Physics*, vol. 77, no. 6, Feb. 2008, ISSN: 10980121. DOI: 10.1103/PhysRevB.77.064406.

[140] Á. Papp, W. Porod, *et al.*, "Nanoscale spectrum analyzer based on spin-wave interference," *Scientific Reports*, vol. 7, no. 1, Dec. 2017, ISSN: 20452322. DOI: 10.1038/s41598-017-09485-7.

[141] Á. Papp, W. Porod, and G. Csaba, "Nanoscale neural network using non-linear spin-wave interference," *Nature Communications*, vol. 12, no. 1, p. 6422, Nov. 2021, ISSN: 2041-1723. DOI: 10.1038/s41467-021-26711-z. [Online]. Available: https://www.nature.com/articles/s41467-021-26711-z.

[142] D. D. Awschalom, C. R. Du, *et al.*, "Quantum Engineering With Hybrid Magnonic Systems and Materials," *IEEE Transactions on Quantum Engineering*, vol. 2, 2021, ISSN: 26891808. DOI: 10.1109/TQE.2021.3057799.

[143] Y. Zhao, Q. Song, *et al.*, "Experimental Investigation of Temperature-Dependent Gilbert Damping in Permalloy Thin Films," *Scientific Reports*, vol. 6, no. 1, p. 22 890, Mar. 2016, ISSN: 2045-2322. DOI: 10.1038/srep22890. [Online]. Available: https://www.nature.com/articles/srep22890.

[144] *https://awetech8.com/site/*. [Online]. Available: https://awetech8.com/site/.

[145] *Types-of-waves-and-laws-of-propagation-of-acoustic-waves-acoustic-field*. [Online]. Available: http://novotest.biz/basics-of-acoustics-1-4-types-of-waves-and-laws-of-propagation-of-acoustic-waves-acoustic-field/.

[146] H. Farhat, "Failure analysis," in *Operation, Maintenance, and Repair of Land-Based Gas Turbines*, Elsevier, 2021, pp. 197–221. DOI: 10.1016/B978-0-12-821834-1.00005-8. [Online]. Available: https://linkinghub.elsevier.com/retrieve/pii/B9780128218341000058.

[147] S. Lago, S. Brignolo, *et al.*, "Application of acoustic methods for a non-destructive evaluation of the elastic properties of several typologies of materials," *Applied Acoustics*, vol. 75, no. 1, pp. 10–16, Jan. 2014, ISSN: 0003682X. DOI: 10.1016/j.apacoust.2013.07.006. [Online]. Available: https://linkinghub.elsevier.com/retrieve/pii/S0003682X13001564.

[148] B. Masserey, C. Raemy, and P. Fromme, "High-frequency guided ultrasonic waves for hidden defect detection in multi-layered aircraft structures," *Ultrasonics*, vol. 54, no. 7, pp. 1720–1728, Sep. 2014, ISSN: 0041624X. DOI: 10.1016/j.ultras.2014.04.023. [Online]. Available: https://linkinghub.elsevier.com/retrieve/pii/S0041624X14001140.

[149] D. Mandal and S. Banerjee, "Surface Acoustic Wave (SAW) Sensors: Physics, Materials, and Applications," *Sensors*, vol. 22, no. 3, p. 820, Jan. 2022, ISSN: 1424-8220. DOI: 10.3390/s22030820. [Online]. Available: https://www.mdpi.com/1424-8220/22/3/820.

[150] A. Slobodnik, "Surface acoustic waves and SAW materials," *Proceedings of the IEEE*, vol. 64, no. 5, pp. 581–595, 1976, ISSN: 0018-9219. DOI: 10.1109/PROC.1976.10180. [Online]. Available: http://ieeexplore.ieee.org/document/1454449/.

[151] R. Banu Priya and T. Venkatesan, "A Short Review of SAW Sensors," *Journal of Environmental Nanotechnology*, vol. 4, no. 4, pp. 15–22, Dec. 2015, ISSN: 22790748. DOI: 10.13074/jent.2015.12.154171. [Online]. Available: http://www.nanoient.org/JENT/Volume4/Issue4/A-Short-Review-of-SAW-Sensors/432#.V0kElDV9600.

[152] H. Mishra, J. Streque, *et al.*, "Temperature compensated magnetic field sensor based on Love waves," DOI: 10.1088/1361-665X/ab7857{\"{i}}. [Online]. Available: https://hal.science/hal-02865495.

[153] F. Hadj-Larbi and R. Serhane, "Sezawa SAW devices: Review of numerical-experimental studies and recent applications," *Sensors and Actuators A: Physical*, vol. 292, pp. 169–197, Jun. 2019, ISSN: 09244247. DOI: 10.1016/j.sna.2019.03.037. [Online]. Available: https://linkinghub.elsevier.com/retrieve/pii/S0924424718311786.

[154] P. Kuszewski, I. S. Camara, *et al.*, "To cite this article: P Kuszewski et al," *Journal of Physics: Condensed Matter*, vol. 30, no. 24, p. 244 003, 2018. DOI: 10.1088/1361-648X/aac152{\"{i}}. [Online]. Available: https://doi.org/10.1088/1361-648X/aac152.

[155] *royer_ dieulesait_ Tome 1*. [Online]. Available: https://books.google.fr/books?id=SzwQ1UYspyQC&lpg=PA1&ots=WLZxzYEoGS&dq=elastic%20waves%20royer%20dieulesaint&lr&pg=PR4#v=onepage&q=elastic%20waves%20royer%20dieulesaint&f=false.

[156] J. Lubliner, *Plasticity Theory Revised Edition*. 1990, ISBN: 9780486462905. [Online]. Available: https://books.google.fr/books?id=MkK-BLbHtcAC.

[157] *https://en.wikipedia.org/w/index.php?title=Cauchy_ stress_ tensor&oldid=1210275569*. [Online]. Available: https://en.wikipedia.org/w/index.php?title=Cauchy_stress_tensor&oldid=1210275569.

[158] C. Hepburn, "Dynamic interplay between the magnetization and surface acoustic waves in magnetostrictive Fe1-xGax thin films," Ph.D. dissertation. [Online]. Available: https://theses.hal.science/tel-02411563v2.

[159] D. Sander, "The correlation between mechanical stress and magnetic anisotropy in ultrathin films," *Reports on Progress in Physics*, vol. 62, no. 5, pp. 809–858, May 1999, ISSN: 0034-4885. DOI: 10.1088/0034-4885/62/5/204. [Online]. Available: https://iopscience.iop.org/article/10.1088/0034-4885/62/5/204.

[160] G. Farnell and E. Adler, "Elastic wave propagation in thin layers," in 1972, pp. 35–127. DOI: 10.1016/B978-0-12-395670-5.50007-6. [Online]. Available: https://linkinghub.elsevier.com/retrieve/pii/B9780123956705500076.

[161] V. M. Bright, Y. Kim, and W. D. Hunt, "Study of surface acoustic waves on the {110} plane of gallium arsenide," *Journal of Applied Physics*, vol. 71, no. 2, pp. 597–605, Jan. 1992, ISSN: 0021-8979. DOI: 10.1063/1.350412. [Online]. Available: https://pubs.aip.org/jap/article/71/2/597/394384/Study-of-surface-acoustic-waves-on-the-110-plane.

[162] J. Soderkvist and K. Hjort, "The piezoelectric effect of GaAs used for resonators and resonant sensors," *Journal of Micromechanics and Microengineering*, vol. 4, no. 1, pp. 28–34, Mar. 1994, ISSN: 0960-1317. DOI: 10.1088/0960-1317/4/1/004. [Online]. Available: https://iopscience.iop.org/article/10.1088/0960-1317/4/1/004.

[163] V. Voigt, *Lehrbuch der Kristallphysik*. 1928. [Online]. Available: https://archive.org/details/bub_gb_SvPPAAAAMAAJ/page/n3/mode/2up.

[164] A. Reuss, "Berechnung der Fließgrenze von Mischkristallen auf Grund der Plastizitätsbedingung für Einkristalle .," *ZAMM - Journal of Applied Mathematics and Mechanics / Zeitschrift für Angewandte Mathematik und Mechanik*, vol. 9, no. 1, pp. 49–58, Jan. 1929, ISSN: 0044-2267. DOI: 10.1002/zamm.19290090104. [Online]. Available: https://onlinelibrary.wiley.com/doi/10.1002/zamm.19290090104.

[165] R. Hill, "The Elastic Behaviour of a Crystalline Aggregate," *Proceedings of the Physical Society. Section A*, vol. 65, no. 5, pp. 349–354, May 1952, ISSN: 0370-1298. DOI: 10.1088/0370-1298/65/5/307. [Online]. Available: https://iopscience.iop.org/article/10.1088/0370-1298/65/5/307.

[166] U. Aschauer, R. Braddell, *et al.*, "Strain-induced structural instability in FeRh," Mar. 2016. DOI: 10.1103/PhysRevB.94.014109. [Online]. Available: http://arxiv.org/abs/1603.01827%20http://dx.doi.org/10.1103/PhysRevB.94.014109.

[167] W. He, H. Huang, and X. Ma, "First-principles calculations on elastic and entropy properties in FeRh alloys," *Materials Letters*, vol. 195, pp. 156–158, May 2017, ISSN: 0167577X. DOI: 10.1016/j.matlet.2017.02.043. [Online]. Available: https://linkinghub.elsevier.com/retrieve/pii/S0167577X17302239.

[168] D. Ourdani, A. Castellano, *et al.*, "Experimental determination of the temperature- and phase-dependent elastic constants of FeRh," *Physical Review B*, vol. 110, no. 1, p. 014 427, Jul. 2024, ISSN: 2469-9950. DOI: 10.1103/PhysRevB.110.014427. [Online]. Available: https://link.aps.org/doi/10.1103/PhysRevB.110.014427.

[169] E. Péronne, N. Chuecos, *et al.*, "Acoustic solitons: A robust tool to investigate the generation and detection of ultrafast acoustic waves," *Physical Review B*, vol. 95, no. 6, p. 064 306, Feb. 2017, ISSN: 2469-9950. DOI: 10.1103/PhysRevB.95.064306. [Online]. Available: https://link.aps.org/doi/10.1103/PhysRevB.95.064306.

[170] F. Knoop, N. Shulumba, *et al.*, "TDEP: Temperature Dependent Effective Potentials," *Journal of Open Source Software*, vol. 9, no. 94, p. 6150, Feb. 2024, ISSN: 2475-9066. DOI: 10.21105/joss.06150. [Online]. Available: https://joss.theoj.org/papers/10.21105/joss.06150.

[171] Y. Sumino, O. L. Anderson, and I. Suzuki, "Temperature Coefficients of Elastic Constants of Single Crystal MgO between 80 and 1,300 K," *Phys Chem Minerals*, vol. 9, pp. 38–47, 1983.

[172] A. Polian, D. Vo-Thanh, and P. Richet, "Elastic properties of a-SiO2 up to 2300 K from Brillouin scattering measurements," *Europhysics Letters (EPL)*, vol. 57, no. 3, pp. 375–381, Feb. 2002, ISSN: 0295-5075. DOI: 10.1209/epl/i2002-00470-4. [Online]. Available: https://iopscience.iop.org/article/10.1209/epl/i2002-00470-4.

[173] R. G. Leisure, D. K. Hsu, and B. A. Seiber, "Elastic properties of tantalum over the temperature range 4-300 K," *Journal of Applied Physics*, vol. 44, no. 8, pp. 3394–3397, 1973, ISSN: 00218979. DOI: 10.1063/1.1662772.

[174] M. Powlowski, F. Sfigakis, and N. Y. Kim, "Temperature dependent angular dispersions of surface acoustic waves on GaAs," *Japanese Journal of Applied Physics*, vol. 58, no. 3, Mar. 2019, ISSN: 13474065. DOI: 10.7567/1347-4065/ab0008.

[175] R I Cottam and G A Saunders, "The elastic constants of GaAs from 2 K to 320 K," *Journal of Physics C: Solid State Physics*, vol. 6, no. 13, pp. 2105–2118, Jul. 1973, ISSN: 0022-3719. DOI: 10.1088/0022-3719/6/13/011. [Online]. Available: https://iopscience.iop.org/article/10.1088/0022-3719/6/13/011.

[176] A. Neubrand and P. Hess, "Laser generation and detection of surface acoustic waves: Elastic properties of surface layers," *Journal of Applied Physics*, vol. 71, no. 1, pp. 227–238, 1992, ISSN: 00218979. DOI: 10.1063/1.350747.

[177] S. Büyükköse, B. Vratzov, *et al.*, "Ultrahigh-frequency surface acoustic wave transducers on ZnO/SiO ₂ /Si using nanoimprint lithography," *Nanotechnology*, vol. 23, no. 31, p. 315 303, Aug. 2012, ISSN: 0957-4484. DOI: 10.1088/0957-4484/23/31/315303. [Online]. Available: https://iopscience.iop.org/article/10.1088/0957-4484/23/31/315303.

[178] J. Zheng, J. Zhou, *et al.*, "30 GHz surface acoustic wave transducers with extremely high mass sensitivity," *Applied Physics Letters*, vol. 116, no. 12, Mar. 2020, ISSN: 0003-6951. DOI: 10.1063/1.5142673. [Online]. Available: https://pubs.aip.org/apl/article/116/12/123502/570975/30-GHz-surface-acoustic-wave-transducers-with.

[179] S. Katzir, "The discovery of the piezoelectric effect," in *The beginning of piezoelectricity*, Dordrecht: Springer Netherlands, pp. 15–64. DOI: 10.1007/978-1-4020-4670-4{_}2. [Online]. Available: http://link.springer.com/10.1007/978-1-4020-4670-4_2.

[180] Piceramic, *Piezoelectricity fundamentals*. [Online]. Available: https://www.piceramic.com/en/expertise/piezo-technology/fundamentals.

[181] B. Hailu, A. Gachacan, *et al.*, "Embedded piezoelectric transducers for structural health monitoring," in *1999 IEEE Ultrasonics Symposium. Proceedings. International Symposium (Cat. No.99CH37027)*, IEEE, 1999, pp. 735–738, ISBN: 0-7803-5722-1. DOI: 10.1109/ULTSYM.1999.849506. [Online]. Available: https://ieeexplore.ieee.org/document/849506/.

[182] F. J. R. Schülein, E. Zallo, *et al.*, "Fourier synthesis of radiofrequency nanomechanical pulses with different shapes," *Nature Nanotechnology*, vol. 10, no. 6, pp. 512–516, Jun. 2015, ISSN: 1748-3387. DOI: 10.1038/nnano.2015.72. [Online]. Available: https://www.nature.com/articles/nnano.2015.72.

[183] R. Ramesh and S. Manipatruni, *Electric field control of magnetism*, Jul. 2021. DOI: 10.1098/rspa.2020.0942.

[184] Z. Budrikis, "Magnetism: Doping rehabilitates failed materials," *Nature Reviews Materials*, vol. 3, no. 4, p. 18018, Mar. 2018, ISSN: 2058-8437. DOI: 10.1038/natrevmats.2018.18. [Online]. Available: https://www.nature.com/articles/natrevmats201818.

[185] S. A. Chambers, "Ferromagnetism in doped thin-film oxide and nitride semiconductors and dielectrics," *Surface Science Reports*, vol. 61, no. 8, pp. 345–381, Oct. 2006, ISSN: 01675729. DOI: 10.1016/j.surfrep.2006.05.001. [Online]. Available: https://linkinghub.elsevier.com/retrieve/pii/S0167572906000446.

[186] H. Shokrollahi, "The magnetic and structural properties of the most important alloys of iron produced by mechanical alloying," *Materials & Design*, vol. 30, no. 9, pp. 3374–3387, Oct. 2009, ISSN: 02613069. DOI: 10.1016/j.matdes.2009.03.035. [Online]. Available: https://linkinghub.elsevier.com/retrieve/pii/S0261306909001423.

[187] S. A. Wolf, D. D. Awschalom, *et al.*, "Spintronics: A Spin-Based Electronics Vision for the Future," *Science*, vol. 294, no. 5546, pp. 1488–1495, Nov. 2001, ISSN: 0036-8075. DOI: 10.1126/science.1065389. [Online]. Available: https://www.science.org/doi/10.1126/science.1065389.

[188] M. C. Prestgard, G. P. Siegel, and A. Tiwari, "Oxides For Spintronics: A Review Of Engineered Materials For Spin Injection," *Advanced Materials Letters*, vol. 5, no. 5, pp. 242–247, May 2014, ISSN: 0976-397X. DOI: 10.5185/amlett.2014.amwc1032. [Online]. Available: https://aml.iaamonline.org/article_14510.html.

[189] J. Ryu, S. Lee, *et al.*, "Current-Induced Spin–Orbit Torques for Spintronic Applications," *Advanced Materials*, vol. 32, no. 35, Sep. 2020, ISSN: 0935-9648. DOI: 10.1002/adma.201907148. [Online]. Available: https://onlinelibrary.wiley.com/doi/10.1002/adma.201907148.

[190] C. Song, R. Zhang, *et al.*, "Spin-orbit torques: Materials, mechanisms, performances, and potential applications," *Progress in Materials Science*, vol. 118, p. 100761, May 2021, ISSN: 00796425. DOI: 10.1016/j.pmatsci.2020.100761. [Online]. Available: https://linkinghub.elsevier.com/retrieve/pii/S0079642520301250.

[191] R. Ramaswamy, J. M. Lee, *et al.*, "Recent advances in spin-orbit torques: Moving towards device applications," *Applied Physics Reviews*, vol. 5, no. 3, p. 031107, Sep. 2018, ISSN: 1931-9401. DOI: 10.1063/1.5041793. [Online]. Available: https://pubs.aip.org/aip/apr/article/123945.

[192] E. Haltz, "Domain wall dynamics drivenby spin-current in ferrimagnetic alloys," Ph.D. dissertation, 2019. [Online]. Available: https://tel.archives-ouvertes.fr/tel-02903018.

[193] E. H. Gregory and H. E. Bömmel, "Acoustic Excitation of Nuclear Spin Resonance in Single-Crystal Metallic Tantalum," *Physical Review Letters*, vol. 15, no. 9, pp. 404–406, Aug. 1965, ISSN: 0031-9007. DOI: 10.1103/PhysRevLett.15.404. [Online]. Available: https://link.aps.org/doi/10.1103/PhysRevLett.15.404.

[194] M. Pomerantz, "Excitation of Spin-Wave Resonance by Microwave Phonons," *Physical Review Letters*, vol. 7, no. 8, pp. 312–313, Oct. 1961, ISSN: 0031-9007. DOI: 10.1103/PhysRevLett.7.312. [Online]. Available: https://link.aps.org/doi/10.1103/PhysRevLett.7.312.

[195] T. Kobayashi, R. C. Barker, and A. Yelon, "Ferromagnetoelastic Resonance in Thin Films. II. Application to Nickel," *Physical Review B*, vol. 7, no. 7, pp. 3286–3297, Apr. 1973, ISSN: 0556-2805. DOI: 10.1103/PhysRevB.7.3286. [Online]. Available: https://link.aps.org/doi/10.1103/PhysRevB.7.3286.

[196] I. A. Feng, M. Tachiki, *et al.*, "Mechanism for the interaction of surface waves with 200-Å nickel films," *Journal of Applied Physics*, vol. 53, no. 1, pp. 177–193, 1982, ISSN: 00218979. DOI: 10.1063/1.331582.

[197] A. K. Ganguly, K. L. Davis, *et al.*, "Magnetoelastic surface waves in a magnetic film–piezoelectric substrate configuration," *Journal of Applied Physics*, vol. 47, no. 6, pp. 2696–2704, Jun. 1976, ISSN: 0021-8979. DOI: 10.1063/1.322991. [Online]. Available: https://pubs.aip.org/jap/article/47/6/2696/8794/Magnetoelastic-surface-waves-in-a-magnetic-film.

[198] N. Ekreem, A. Olabi, *et al.*, "An overview of magnetostriction, its use and methods to measure these properties," *Journal of Materials Processing Technology*, vol. 191, no. 1-3, pp. 96–101, Aug. 2007, ISSN: 09240136. DOI: 10.1016/j.jmatprotec.2007.03.064. [Online]. Available: https://linkinghub.elsevier.com/retrieve/pii/S0924013607002889.

[199] A. J. Gualdi, F. L. Zabotto, *et al.*, "Stress magnetization model for magnetostriction in multiferroic composite," *Journal of Applied Physics*, vol. 114, no. 5, Aug. 2013, ISSN: 0021-8979. DOI: 10.1063/1.4816785. [Online]. Available: https://pubs.aip.org/jap/article/114/5/053913/377177/Stress-magnetization-model-for-magnetostriction-in.

[200] M. P. Ruffoni, S. Pascarelli, *et al.*, "Direct Measurement of Intrinsic Atomic Scale Magnetostriction," *Physical Review Letters*, vol. 101, no. 14, p. 147 202, Oct. 2008, ISSN: 0031-9007. DOI: 10.1103/PhysRevLett.101.147202.

[201] P. Delsing, A. N. Cleland, *et al.*, "The 2019 surface acoustic waves roadmap," *Journal of Physics D: Applied Physics*, vol. 52, no. 35, p. 353 001, Aug. 2019, ISSN: 0022-3727. DOI: 10.1088/1361-6463/ab1b04. [Online]. Available: https://iopscience.iop.org/article/10.1088/1361-6463/ab1b04.

[202] G. Paria, "Magneto-Elasticity and Magneto-Thermo-Elasticity," in 1966, pp. 73–112. DOI: 10.1016/S0065-2156(08)70394-6. [Online]. Available: https://linkinghub.elsevier.com/retrieve/pii/S0065215608703946.

[203] F. Claeyssen, N. Lhermet, *et al.*, "Actuators, transducers and motors based on giant magnetostrictive materials," *Journal of Alloys and Compounds*, vol. 258, no. 1-2, pp. 61–73, Aug. 1997, ISSN: 09258388. DOI: 10.1016/S0925-8388(97)00070-4. [Online]. Available: https://linkinghub.elsevier.com/retrieve/pii/S0925838897000704.

[204] A. S. Almansouri, K. N. Salama, and J. Kosel, "Magneto-Acoustic Resonator for Aquatic Animal Tracking," *IEEE Transactions on Magnetics*, vol. 55, no. 2, pp. 1–4, Feb. 2019, ISSN: 0018-9464. DOI: 10.1109/TMAG.2018.2861980. [Online]. Available: https://ieeexplore.ieee.org/document/8438510/.

[205] J. Li, T. Li, *et al.*, "Magneto–Acoustic Hybrid Nanomotor," *Nano Letters*, vol. 15, no. 7, pp. 4814–4821, Jul. 2015, ISSN: 1530-6984. DOI: 10.1021/acs.nanolett.5b01945. [Online]. Available: https://pubs.acs.org/doi/10.1021/acs.nanolett.5b01945.

[206] du Tremolet de la Lacheisserie -, *Magnetisme-chap-magneto-elasticite*.

[207] R. Hasegawa, "Static bubble domain properties of amorphous Gd-Co films," *Vacuum*, vol. 25, no. 2, p. 87, Feb. 1975, ISSN: 0042207X. DOI: 10.1016/0042-207X(75)91359-7. [Online]. Available: https://linkinghub.elsevier.com/retrieve/pii/0042207X75913597.

[208] H. Szymczak and R. Żuberek, "Surface Magnetostriction," *Acta Physica Polonica A*, vol. 83, no. 5, pp. 651–659, May 1993, ISSN: 0587-4246. DOI: 10.12693/APhysPolA.83.651. [Online]. Available: http://przyrbwn.icm.edu.pl/APP/PDF/83/a083z5p11.pdf.

[209] A. Clark, "Chapter 7 Magnetostrictive rare earth-Fe2 compounds," in Wolfhart Edition Publisher, vol. 1, 1980, pp. 531–589. DOI: 10.1016/S1574-9304(05)80122-1. [Online]. Available: https://linkinghub.elsevier.com/retrieve/pii/S1574930405801221.

[210] E. R. Callen, A. E. Clark, *et al.*, "Magnetostriction in cubic néel ferrimagnets, with application to YIG," *Physical Review*, vol. 130, no. 5, pp. 1735–1740, 1963, ISSN: 0031899X. DOI: 10.1103/PhysRev.130.1735.

[211] E. Callen, "Magnetostriction," *Journal of Applied Physics*, vol. 39, no. 2, pp. 519–527, Feb. 1968, ISSN: 0021-8979. DOI: 10.1063/1.2163507. [Online]. Available: https://pubs.aip.org/jap/article/39/2/519/4802/Magnetostriction.

[212] E. Klokholm and J. A. Aboaf, "The saturation magnetostriction of permalloy films," *Journal of Applied Physics*, vol. 52, no. 3, pp. 2474–2476, Mar. 1981, ISSN: 0021-8979. DOI: 10.1063/1.328971. [Online]. Available: https://pubs.aip.org/jap/article/52/3/2474/10522/The-saturation-magnetostriction-of-permalloy-films.

[213] A. E. Clark, K. B. Hathaway, *et al.*, "Extraordinary magnetoelasticity and lattice softening in bcc Fe-Ga alloys," *Journal of Applied Physics*, vol. 93, no. 10, pp. 8621–8623, May 2003, ISSN: 0021-8979. DOI: 10.1063/1.1540130. [Online]. Available: https://pubs.aip.org/jap/article/93/10/8621/530752/Extraordinary-magnetoelasticity-and-lattice.

[214] S. Maekawa and M. Tachiki, "Surface acoustic attenuation due to surface spin wave in ferro- and antiferromagnets," in *AIP Conference Proceedings*, vol. 29, AIP, Aug. 1976, pp. 542–543. DOI: 10.1063/1.30437. [Online]. Available: https://pubs.aip.org/aip/acp/article/29/1/542-543/626917.

[215] M. Xu, K. Yamamoto, *et al.*, "Nonreciprocal surface acoustic wave propagation via magneto-rotation coupling," *Science Advances*, vol. 6, no. 32, eabb1724, Aug. 2020, ISSN: 2375-2548. DOI: 10.1126/sciadv.abb1724. [Online]. Available: http://arxiv.org/abs/2001.05135%20http://dx.doi.org/10.1126/sciadv.abb1724%20https://advances.sciencemag.org/lookup/doi/10.1126/sciadv.abb1724.

[216] A. Adhikari, E. R. Gilroy, *et al.*, "Surface acoustic wave assisted depinning of magnetic domain walls," *Journal of Physics: Condensed Matter*, vol. 33, no. 31, 31LT01, Aug. 2021, ISSN: 0953-8984. DOI: 10.1088/1361-648X/ac02e4. [Online]. Available: https://iopscience.iop.org/article/10.1088/1361-648X/ac02e4.

[217] A. Adhikari and S. Adenwalla, "Surface acoustic waves increase magnetic domain wall velocity," *AIP Advances*, vol. 11, no. 1, Jan. 2021, ISSN: 21583226. DOI: 10.1063/9.0000159.

[218] P. Kuszewski, I. S. Camara, *et al.*, "Resonant magneto-acoustic switching: influence of Rayleigh wave frequency and wavevector," *Journal of Physics: Condensed Matter*, vol. 30, no. 24, p. 244 003, Jun. 2018, ISSN: 0953-8984. DOI: 10.1088/1361-648X/aac152. [Online]. Available: https://iopscience.iop.org/article/10.1088/1361-648X/aac152.

[219] J. Dean, M. T. Bryan, *et al.*, "A sound idea: Manipulating domain walls in magnetic nanowires using surface acoustic waves," *Applied Physics Letters*, vol. 107, no. 14, Oct. 2015, ISSN: 0003-6951. DOI: 10.1063/1.4932057.

[220] A. Rivelles, R. Yanes, *et al.*, "Mechanism to transfer linear momentum from a Surface Acoustic Wave to a Magnetic Domain Wall," Tech. Rep.

[221] M. Weiler, H. Huebl, *et al.*, "Spin Pumping with Coherent Elastic Waves," *Physical Review Letters*, vol. 108, no. 17, p. 176 601, Apr. 2012, ISSN: 0031-9007. DOI: 10.1103/PhysRevLett.108.176601. [Online]. Available: https://link.aps.org/doi/10.1103/PhysRevLett.108.176601.

[222] C. Berk, M. Jaris, *et al.*, "Strongly coupled magnon–phonon dynamics in a single nanomagnet," *Nature Communications*, vol. 10, no. 1, p. 2652, Jun. 2019, ISSN: 2041-1723. DOI: 10.1038/s41467-019-10545-x. [Online]. Available: https://www.nature.com/articles/s41467-019-10545-x.

[223] F. Godejohann, A. V. Scherbakov, *et al.*, "Magnon polaron formed by selectively coupled coherent magnon and phonon modes of a surface patterned ferromagnet," *Physical Review B*, vol. 102, no. 14, Oct. 2020, ISSN: 24699969. DOI: 10.1103/PhysRevB.102.144438.

[224] L. J. Cornelissen, K. Oyanagi, *et al.*, "Nonlocal magnon-polaron transport in yttrium iron garnet," *Physical Review B*, vol. 96, no. 10, p. 104 441, Sep. 2017, ISSN: 2469-9950. DOI: 10.1103/PhysRevB.96.104441. [Online]. Available: https://link.aps.org/doi/10.1103/PhysRevB.96.104441.

[225] K. An, C. Kim, *et al.*, "Optimizing the Magnon-Phonon Cooperativity in Planar Geometries," *Physical Review Applied*, vol. 20, no. 1, Jul. 2023, ISSN: 23317019. DOI: 10.1103/PhysRevApplied.20.014046.

[226] P. J. Shah, D. A. Bas, *et al.*, "Giant nonreciprocity of surface acoustic waves enabled by the magnetoelastic interaction," *Science Advances*, vol. 6, no. 49, Dec. 2020, ISSN: 2375-2548. DOI: 10.1126/sciadv.abc5648. [Online]. Available: https://www.science.org/doi/10.1126/sciadv.abc5648.

[227] R. E. Camley and K. L. Livesey, "Consequences of the Dzyaloshinskii-Moriya interaction," *Surface Science Reports*, vol. 78, no. 3, p. 100 605, Aug. 2023, ISSN: 01675729. DOI: 10.1016/j.surfrep.2023.100605.

[228] P. G. Gowtham, D. Labanowski, and S. Salahuddin, "Mechanical back-action of a spin-wave resonance in a magnetoelastic thin film on a surface acoustic wave," *Physical Review B*, vol. 94, no. 1, Jul. 2016, ISSN: 24699969. DOI: 10.1103/PhysRevB.94.014436.

[229] A. Hernández-Mínguez, F. Macià, *et al.*, "Large Nonreciprocal Propagation of Surface Acoustic Waves in Epitaxial Ferromagnetic/Semiconductor Hybrid Structures," *Physical Review Applied*, vol. 13, no. 4, p. 044 018, Apr. 2020, ISSN: 2331-7019. DOI: 10.1103/PhysRevApplied.13.044018. [Online]. Available: https://doi.org/10.1103/PhysRevApplied.13.044018%20https://link.aps.org/doi/10.1103/PhysRevApplied.13.044018.

[230] P. Rovillain, J. Y. Duquesne, *et al.*, "Impact of Spin-Wave Dispersion on Surface-Acoustic-Wave Velocity," *Physical Review Applied*, vol. 18, no. 6, Dec. 2022, ISSN: 23317019. DOI: 10.1103/PhysRevApplied.18.064043.

[231] J. Shuai, M. Ali, *et al.*, "Local anisotropy control of Pt/Co/Ir thin film with perpendicular magnetic anisotropy by surface acoustic waves," *Applied Physics Letters*, vol. 120, no. 25, p. 252 402, Jun. 2022, ISSN: 0003-6951. DOI: 10.1063/5.0097172.

[232] H. Wu, Q. Liu, *et al.*, "Acoustic Wave-Induced FeRh Magnetic Phase Transition and Its Application in Antiferromagnetic Pattern Writing and Erasing," *ACS Nano*, vol. 18, no. 19, pp. 12 134–12 145, May 2024, ISSN: 1936-0851. DOI: 10.1021/acsnano.3c11619. [Online]. Available: https://pubs.acs.org/doi/10.1021/acsnano.3c11619.

[233] X. Liu, H. Wu, *et al.*, "The Magnetic Phase Transition of FeRh Modulated by AC Magnetic Field," *physica status solidi (RRL) – Rapid Research Letters*, vol. 16, no. 12, Dec. 2022, ISSN: 1862-6254. DOI: 10.1002/pssr.202200238. [Online]. Available: https://onlinelibrary.wiley.com/doi/10.1002/pssr.202200238.

[234] K. Fossheim, "Electromagnetic Shear-Wave Interaction in a Superconductor," *Physical Review Letters*, vol. 19, no. 2, pp. 81–85, Jul. 1967, ISSN: 0031-9007. DOI: 10.1103/PhysRevLett.19.81. [Online]. Available: https://link.aps.org/doi/10.1103/PhysRevLett.19.81.

[235] R. Hemphill, "Effect of a Thin-Film Phase-Transition Material on Surface Acoustic Wave Propagation," in *IEEE 1984 Ultrasonics Symposium*, IEEE, 1984, pp. 1006–1002. DOI: 10.1109/ULTSYM.1984.198455. [Online]. Available: http://ieeexplore.ieee.org/document/1535395/.

[236] W. Rehwald, "The study of structural phase transitions by means of ultrasonic experiments," *Advances in Physics*, vol. 22, no. 6, pp. 721–755, Nov. 1973, ISSN: 0001-8732. DOI: 10.1080/00018737300101379. [Online]. Available: http://www.tandfonline.com/doi/abs/10.1080/00018737300101379.

[237] B. Lüthi, T. Moran, and R. Pollina, "Sound propagation near magnetic phase transitions," *Journal of Physics and Chemistry of Solids*, vol. 31, no. 8, pp. 1741–1758, Aug. 1970, ISSN: 00223697. DOI: 10.1016/0022-3697(70)90164-2. [Online]. Available: https://linkinghub.elsevier.com/retrieve/pii/0022369770901642.

[238] K. Fossheim, "Ultrasonic Investigations of Structural Phase Transitions," *Physica Scripta*, vol. 25, no. 6A, pp. 665–670, Jun. 1982, ISSN: 0031-8949. DOI: 10.1088/0031-8949/25/6A/001. [Online]. Available: https://iopscience.iop.org/article/10.1088/0031-8949/25/6A/001.

[239] J. Worgull, E. Petti, and J. Trivisonno, "Behavior of the elastic properties near an intermediate phase transition in Ni2MnGa," *Physical Review B*, vol. 54, no. 22, pp. 15 695–15 699, Dec. 1996, ISSN: 0163-1829. DOI: 10.1103/PhysRevB.54.15695. [Online]. Available: https://link.aps.org/doi/10.1103/PhysRevB.54.15695.

[240] M. Rosen, "Elastic Moduli and Ultrasonic Attenuation of Gadolinium, Terbium, Dysprosium, Holmium, and Erbium from 4.2 to 300°K," *Physical Review*, vol. 174, no. 2, pp. 504–514, Oct. 1968, ISSN: 0031-899X. DOI: 10.1103/PhysRev.174.504. [Online]. Available: https://link.aps.org/doi/10.1103/PhysRev.174.504.

[241] A. E. Petrova and S. M. Stishov, "Ultrasonic studies of the magnetic phase transition in MnSi," *Journal of Physics: Condensed Matter*, vol. 21, no. 19, p. 196 001, May 2009, ISSN: 0953-8984. DOI: 10.1088/0953-8984/21/19/196001. [Online]. Available: https://iopscience.iop.org/article/10.1088/0953-8984/21/19/196001.

[242] Y. Au, O. S. Latcham, *et al.*, "Resonant scattering of surface acoustic waves by arrays of magnetic stripes," *Journal of Applied Physics*, vol. 134, no. 23, Dec. 2023, ISSN: 0021-8979. DOI: 10.1063/5.0170498. [Online]. Available: https://pubs.aip.org/jap/article/134/23/233904/2930333/Resonant-scattering-of-surface-acoustic-waves-by.

[243] L. Thevenard, C. Gourdon, *et al.*, "Domain wall propagation in ferromagnetic semiconductors: Beyond the one-dimensional model," *Physical Review B*, vol. 83, no. 24, p. 245 211, Jun. 2011, ISSN: 1098-0121. DOI: 10.1103/PhysRevB.83.245211. [Online]. Available: https://link.aps.org/doi/10.1103/PhysRevB.83.245211.

[244] J. Rhensius, L. Heyne, *et al.*, "Imaging of Domain Wall Inertia in Permalloy Half-Ring Nanowires by Time-Resolved Photoemission Electron Microscopy," *Physical Review Letters*, vol. 104, no. 6, p. 067 201, Feb. 2010, ISSN: 0031-9007. DOI: 10.1103/PhysRevLett.104.067201. [Online]. Available: https://link.aps.org/doi/10.1103/PhysRevLett.104.067201.

[245] M. Kraimia, "Magnéto-élasticité et magnéto-acoustique dans le semi-conducteur ferromagnétique (Ga,Mn)As," Tech. Rep. [Online]. Available: https://theses.hal.science/tel-03369755.

[246] E. Mancini, F. Pressacco, *et al.*, "Magnetic phase transition in iron-rhodium thin films probed by ferromagnetic resonance," *Journal of Physics D: Applied Physics*, vol. 46, no. 24, Jun. 2013, ISSN: 00223727. DOI: 10.1088/0022-3727/46/24/245302.

[247] K. Maaz, A. Mumtaz, *et al.*, "Temperature dependent coercivity and magnetization of nickel ferrite nanoparticles," *Journal of Magnetism and Magnetic Materials*, vol. 322, no. 15, pp. 2199–2202, Aug. 2010, ISSN: 03048853. DOI: 10.1016/j.jmmm.2010.02.010.

[248] W. Hu, M. Huang, *et al.*, "Self-Biased Magnetic Field Sensors Based on Surface Acoustic Waves through Angle-Dependent Magnetoacoustic Coupling," *Physical Review Applied*, vol. 19, no. 1, Jan. 2023, ISSN: 23317019. DOI: 10.1103/PhysRevApplied.19.014010.

[249] M. Küß, M. Heigl, *et al.*, "Symmetry of the Magnetoelastic Interaction of Rayleigh and Shear Horizontal Magnetoacoustic Waves in Nickel Thin Films on LiTa03," *Physical Review Applied*, vol. 15, no. 3, p. 034 046, Mar. 2021, ISSN: 2331-7019. DOI: 10.1103/PhysRevApplied.15.034046. [Online]. Available: https://link.aps.org/doi/10.1103/PhysRevApplied.15.034046.

[250] L. Thevenard, I. S. Camara, *et al.*, "Precessional magnetization switching by a surface acoustic wave," *Physical Review B*, vol. 93, no. 13, p. 134 430, Apr. 2016, ISSN: 2469-9950. DOI: 10.1103/PhysRevB.93.134430. [Online]. Available: https://link.aps.org/doi/10.1103/PhysRevB.93.134430.

[251] M. Belmeguenai, M. S. Gabor, *et al.*, "Perpendicular Magnetic Anisotropy in Co₂ FeAl Thin Films: Effect of Annealing Temperature," *IEEE Transactions on Magnetics*, vol. 51, no. 11, pp. 1–4, Nov. 2015, ISSN: 0018-9464. DOI: 10.1109/TMAG.2015.2435815. [Online]. Available: http://ieeexplore.ieee.org/document/7111291/.

[252] I. Benguettat-El Mokhtari, Y. Roussigné, *et al.*, "Interface phenomena in ferromagnet/ <math> <mrow> <mi>Ta</mi> <msub> <mi mathvariant="normal">O</mi> <mi>x</mi> </msub> </mrow> </math> -based systems: Damping, perpendicular magnetic anisotropy, and Dzyaloshinskii-Moriya interaction," *Physical Review Materials*, vol. 4, no. 12, p. 124 408, Dec. 2020, ISSN: 2475-9953. DOI: 10.1103/PhysRevMaterials.4.124408. [Online]. Available: https://link.aps.org/doi/10.1103/PhysRevMaterials.4.124408.

[253] Y. Liu, B. Lin, *et al.*, "Boosting Performance of SAW Resonator via AlN/ScAlN Composite Films and Dual Reflectors," *IEEE Transactions on Ultrasonics, Ferroelectrics, and Frequency Control*, vol. 70, no. 10, pp. 1239–1245, Oct. 2023, ISSN: 0885-3010. DOI: 10.1109/TUFFC.2023.3247902. [Online]. Available: https://ieeexplore.ieee.org/document/10050094/.

[254] M. K. Tan, J. R. Friend, and L. Y. Yeo, "Interfacial Jetting Phenomena Induced by Focused Surface Vibrations," *Physical Review Letters*, vol. 103, no. 2, p. 024 501, Jul. 2009, ISSN: 0031-9007. DOI: 10.1103/PhysRevLett.103.024501. [Online]. Available: https://link.aps.org/doi/10.1103/PhysRevLett.103.024501.

[255] N. K. Babu, A. Trzaskowska, *et al.*, "The Interaction between Surface Acoustic Waves and Spin Waves: The Role of Anisotropy and Spatial Profiles of the Modes," *Nano Letters*, vol. 21, no. 2, pp. 946–951, Jan. 2021, ISSN: 15306992. DOI: 10.1021/acs.nanolett.0c03692.

[256] R. Bläsing, T. Ma, *et al.*, "Exchange coupling torque in ferrimagnetic Co/Gd bilayer maximized near angular momentum compensation temperature," *Nature Communications*, vol. 9, no. 1, 2018, ISSN: 20411723. DOI: 10.1038/s41467-018-07373-w. [Online]. Available: http://dx.doi.org/10.1038/s41467-018-07373-w.

[257] H. Matsumoto, T. Kawada, *et al.*, "Large surface acoustic wave nonreciprocity in synthetic antiferromagnets," *Applied Physics Express*, vol. 15, no. 6, Jun. 2022, ISSN: 18820786. DOI: 10.35848/1882-0786/ac6da1.

[258] R. Verba, V. Tiberkevich, and A. Slavin, "Wide-Band Nonreciprocity of Surface Acoustic Waves Induced by Magnetoelastic Coupling with a Synthetic Antiferromagnet," *Physical Review Applied*, vol. 12, no. 5, p. 054 061, Nov. 2019, ISSN: 2331-7019. DOI: 10.1103/PhysRevApplied.12.054061. [Online]. Available: https://link.aps.org/doi/10.1103/PhysRevApplied.12.054061.